

Altimeter Retrievals of Sea Ice, Lake Ice and Snow Properties

by

Justin Francis Beckers

A thesis submitted in partial fulfillment of the requirements for the degree of

Doctor of Philosophy

Department of Earth and Atmospheric Sciences

University of Alberta

© Justin Francis Beckers, 2018

Abstract

Lake and sea ice and their snow covers are major components of Earth's cryosphere and act to strongly modify climatic and biological systems. Both ice types serve as an important habitat for micro-fauna and support macro-fauna and strongly modify the exchange of energy, gases, and momentum between the atmosphere and the underlying water. Observations of areal properties of ice and snow have been widely available for the past 40 years, allowing for monitoring of the long term decreases in e.g. ice extent, duration and age. Unfortunately, observations of other ice properties remain limited, due to reductions in monitoring programs, operational and logistical limitations such as cost and remoteness and technological limitations such as the absorption of EM radiation by water. Laser and radar altimeters can provide measurements of the surface properties of the ice cover and snow covers such as roughness and thickness but have traditionally suffered from the same issues of poor spatial resolution or coverage. In 2010, The European Space Agency launched CryoSat-2 carrying SIRAL, a pulse-limited Delay-Doppler Synthetic Aperture and Interferometric radar altimeter with improved spatial coverage and along-track resolution and across-track position information using dual antennae. We provide several analyses of CryoSat-2 radar altimeter data over sea ice and lake ice using on-ice manual and autonomous measurements, airborne laser and radar altimetry and electromagnetic sounding and satellite radar imagery. First, a method to produce airborne roughness from a laser scanner without complicated inertial navigation data is presented and shown to better represent the roughness of sea ice and to better highlight differences in roughness between different types of ice, smooth first-year ice (FYI) north of Svalbard, rough drifting multi-year ice (MYI) and FYI in Fram Strait and very rough landfast ice off the eastern

coast of Greenland than a single-beam laser altimeter. Second, the first retrievals of lake ice thickness using CryoSat-2, or any radar altimeter, are presented. The retrievals are able to reproduce the seasonal development in ice thickness observed by drill holes and model data ($r > 0.65$) and with low uncertainty ($RMSE < 0.33$ m) given that the minimum thickness that can be sensed is 0.26 m. Three studies into the response of CryoSat-2 over sea ice are presented using comparisons with ground and airborne data in the Arctic and Antarctica. The first of these studies highlighted errors with the early versions of CryoSat-2 data. The modal laser and radar freeboards and their latitudinal gradients were found to be the same despite the fact that the CryoSat-2 radar freeboard is assumed to come from the ice surface and the laser freeboard is representative of the snow surface. The agreement between the two freeboard measures may indicate incomplete radar penetration into the snow and the complicating issue of surface roughness and differences in spatial coverage. The second CryoSat-2 study highlighted the influence of snow depth on the retracking of CryoSat-2 radar echoes and the resulting freeboard results over sea ice with thick and thin snow covers. Lastly, the third study compares all available coincident CryoSat-2 and airborne laser and radar altimeter, and EM sounding data collected between 2010 and 2014. Results show low correlations (< 0.3) between CryoSat-2 and airborne data at the scale of individual CryoSat-2 footprints but higher correlations ($0.3 < r < 0.6$) when averaged along 50km sections of the orbit. Higher correlations are observed between modal airborne freeboard and CryoSat-2 freeboard than between mean airborne freeboard and CryoSat-2 freeboard, possibly indicating that CryoSat-2 is more sensitive to modal freeboard than mean freeboard. The three CryoSat-2 and airborne data comparison studies show that CryoSat-2 can accurately capture large areal averages of sea ice freeboard. This study contributes to the

understanding of altimeter data over sea ice and lake ice and identifies the need for improved data on snow thickness on sea ice as a major challenge to improve altimetric sea ice products.

Preface

Chapter 5 of this thesis has been published as J. F. Beckers, A. H. H. Renner, G. Spreen, S. Gerland, and C. Haas (2015). Sea-ice surface roughness estimates from airborne laser scanner and laser altimeter observations in Fram Strait and north of Svalbard. *Annals of Glaciology*, **56 (69)**: 235–244, doi: 10.3189/2015AoG69A717. I was responsible for the project development, data collection, data analysis, and manuscript composition. C. Haas contributed to the manuscript edits, was the supervisory author and played a large role in developing the project. A. H. H. Renner was involved with data collection, developing the project, and with manuscript edits. G. Spreen was involved with developing the project and manuscript edits. S. Gerland contributed to developing the project, manuscript edits, and acted as a supervisory author. Reprinted with permission of the International Glaciological Society.

Chapter 6 was published as: J. F. Beckers, J. A. Casey, and C. Haas. (2017). Retrievals of lake ice thickness from Great Slave and Great Bear Lakes using CryoSat-2. *IEEE Transactions on Geoscience and Remote Sensing*, **55 (7)**, 3708-3720, doi: 10.1109/TGRS.2017.2677583. I was responsible for the project development, data collection, data analysis, and manuscript composition. C. Haas contributed to the manuscript edits and was the supervisory author. J. A. Casey contributed to the manuscript edits and was involved with developing the project. Reprinted with permission from IEEE.

Chapter 7 has been published as: J. F. Beckers, J. A. Casey, S. Hendricks, R. Ricker, V. Helm, and C. Haas. Characteristics of CryoSat-2 signals over multi-year and seasonal sea ice. In *2013 IEEE International Geoscience and Remote Sensing Symposium - IGARSS*, pages 220–223, July 2013. I was responsible for project development, data analysis, and manuscript composition. C. Haas contributed to the manuscript edits, was the supervisory author and was involved with developing the project. J. A. Casey contributed to the manuscript edits and was involved with developing the project. R. Ricker, S. Hendricks and V. Helm provided data and manuscript input. Reprinted with permission from IEEE.

Chapter 8 was published as D. Price, J. F. Beckers, R. Ricker, N. Kurtz, W. Rack, C. Haas, V. Helm, S. Hendricks, G. Leonard, and P. J. Langhorne (2015). Evaluation of CryoSat-2 derived sea-ice freeboard over fast ice in McMurdo Sound, Antarctica. *Journal of Glaciology*, **61 (226)**, 285-300, doi:/10.3189/2015JoG14J157. Daniel Price and I developed the project, collected the data, and performed data analysis. I contributed to the manuscript and was responsible for the analysis of several sections of data and coding for other sections. R. Ricker, V. Helm, and S. Hendricks provided AWI CryoSat-2 data and analysis and contributed to the manuscript. N. Kurtz provided analysis using his CryoSat-2 algorithms. G. Leonard, P. J. Langhorne, W. Rack and C. Haas helped develop and guide the project, and contributed to the manuscript reviews. Reprinted with Permission of the International Glaciological Society.

Chapter 9 of this thesis will be submitted as J. F. Beckers, C. Haas, S. Hendricks, R. Ricker, S. Baker, M. Davidson, S. Farrell, R. Forsberg, S. Gerland, S. M. Hvidegaard, J. King, H. Skourup, G. Spreen. Validation of CryoSat-2 freeboard retrievals with coincident airborne measurements. C. Haas was the scientific principal investigator and lead scientist and contributed to the data collection, processing and manuscript edits. I performed data collection, analysis and the manuscript composition. All other authors contributed to the data processing, to manuscript edits and to the development of the project.

Acknowledgements

The Arctic is a beautiful and captivating place but research there is remote, challenging and expensive; as a result, I have often thought of research in the Arctic much like the widely-used proverb that it takes a village to raise a child. In the past four or so years of research for this doctoral degree I have had the privilege of working with an entire village of dedicated polar scientists, all of whom deserve thanks or some other acknowledgement, not only for their contribution to my research and career but for their friendship, mentoring, teaching, and general kindness. I apologize in advance for not mentioning you all, but brevity precludes an exhaustive list.

First off, I must thank my family for supporting me in this endeavor. To my wife, Nicole, this thesis would simply not have been possible without your love and support. You put with my long hours and months of absences with amazing grace and always encouraged me to say yes to the opportunities that came up over the years. Damian my son, you reminded me of why I was doing this and always provided me with a welcome distraction.

Next, of course, is my (nearly) fearless supervisor, Christian Haas. Christian, I am not sure that I will ever be able to properly express my thanks for your guidance, mentorship, lessons and ideas, leadership, insight, and for the opportunities you have given me. I hope to give such support to others in the future.

I am grateful to my supervisory committee, Dr. Christian Haas, Dr. Martin Sharp, and Dr. Paul Myers for their guidance and support over the years.

Alec: Thank you so much for all the hours spent discussing sea ice, and for being the whiteboard for my projects that our office never had. I have thoroughly enjoyed working with you on our numerous projects and in the field and hope to continue doing so.

Stefan and Robert: thank you for the amazing times on Polarstern, for the lively discussions of sea ice, EM induction, and for your CryoSat insights.

To Benjamin A. Lange, Angelika H. H. Renner, Harvey Goodwin, Gunnar Spreen, Sebastian Gerland, Bruce Elder, Chris Hiemstra, Wolfgang Rack, Anne Bublitz, Josh King, Arvids Silis, Daniel Price, Ido Hatam, the CryoVal team, the CryoVEx teams, all the staff at Kenn Borek, Polar Continental Shelf Resolute, CFS Alert.... Thank you!

The research presented in this thesis would not have been possible without the financial or logistical support of many scholarships and grants including but not limited to the Queen Elizabeth II Graduate Student Scholarship, the University of Alberta Northern Research Award, the Northern Scientific Training Program, the Norwegian Research Council Leiv Eiriksson Mobility Fellowship Programme, the George Hobson Award, the NSERC CREATE Mobility Fellowship, NSERC CREATE Oral Communication prize, a University of Alberta Education Abroad Individual Award, the European Space Agency CryoVEx project, the European Space Agency CryoVal-SI project, Dr. Haas' Albertina Ingenuity, Canada Research Chair, NSERC Discovery, Alberta Ingenuity-Technology Innovates and the Canadian Foundation for Innovation funding as well as funding and support from other granting agencies and projects.

Finally, the work of this thesis would not be possible without the work of countless researchers across the world who collected ground and airborne data of snow and sea ice properties and making those data available.

Table of Contents

ABSTRACT	II
PREFACE	V
ACKNOWLEDGEMENTS	VII
TABLE OF CONTENTS	IX
LIST OF TABLES	XIV
LIST OF FIGURES	XVI
1. GENERAL INTRODUCTION	1
1.1. MOTIVATION	1
1.2. OBJECTIVES	2
1.3. STRUCTURE	3
2. BACKGROUND	4
2.1. SEA ICE	4
2.1.1. GROWTH AND MELT	4
2.1.2. PHYSICAL AND DIELECTRIC PROPERTIES	8
2.1.3. IMPORTANCE OF SEA ICE	14
2.1.4. CURRENT STATE AND PREDICTIONS	16
2.2. FRESHWATER ICE	18
2.2.1. GROWTH	18
2.2.2. PHYSICAL AND DIELECTRIC PROPERTIES	19
2.2.3. IMPORTANCE	20
2.2.4. CURRENT STATE AND PREDICTIONS	21
2.3. SNOW	23
2.3.1. PHYSICAL AND DIELECTRIC PROPERTIES	23
2.3.2. IMPORTANCE	29
2.3.3. CURRENT STATE AND PREDICTIONS	30

2.4. SUMMARY	31
<u>3. ALTIMETER MEASUREMENTS OF SEA ICE, LAKE ICE, AND SNOW</u>	<u>32</u>
3.1. TYPES OF ALTIMETERS	32
3.1.1. LASER ALTIMETERS	32
3.1.2. RADAR ALTIMETERS	34
3.2. FREEBOARD RETRIEVAL	38
3.2.1. METHOD	38
3.2.2. UNCERTAINTIES	42
3.3. THICKNESS RETRIEVAL	51
3.3.1. METHOD	52
3.3.2. UNCERTAINTIES	52
3.3.3. FUTURE CHANGES AND CHALLENGES	56
3.4. SUMMARY	57
<u>4. LINKS BETWEEN THESIS CHAPTERS</u>	<u>58</u>
<u>5. SEA ICE SURFACE ROUGHNESS ESTIMATES FROM AIRBORNE LASER SCANNER AND LASER ALTIMETER OBSERVATIONS IN FRAM STRAIT AND NORTH OF SVALBARD</u>	<u>63</u>
5.1. ABSTRACT	63
5.2. INTRODUCTION	63
5.3. MEASUREMENTS AND METHODS	67
5.4. SOURCES OF UNCERTAINTY	70
5.5. RESULTS	71
5.6. DISCUSSION	77
5.6.1. ALTIMETER VS. SCANNER	77
5.6.2. REGIONAL COMPARISON	79
5.7. CONCLUSIONS	81
5.8. ACKNOWLEDGEMENTS	82
5.9. REFERENCES	83
<u>6. RETRIEVALS OF LAKE ICE THICKNESS FROM GREAT SLAVE LAKE AND GREAT BEAR LAKE USING CRYOSAT-2</u>	<u>87</u>

6.1. ABSTRACT	87
6.2. INTRODUCTION	87
6.3. RADAR PENETRATION INTO SNOW AND ICE	89
6.4. DATA AND METHODS	90
6.4.1. STUDY AREA	90
6.4.2. DATA	91
6.4.2.1. CS2 Data	91
6.4.2.2. In Situ Ice Thickness Data	92
6.4.2.3. Auxiliary	92
6.5. PHENOLOGY OF SEASONAL CS2 WAVEFORM SHAPES OVER LAKES	93
6.5.1. CHARACTERISTIC CRYOSAT-2 WAVEFORMS OVER LAKE ICE	97
6.6. ICE THICKNESS RETRIEVAL ALGORITHM	99
6.6.1. FULL-RESOLUTION PEAK SELECTION	100
6.6.2. ALONG-TRACK AVERAGE WAVEFORM PEAK SELECTION	101
6.6.3. ICE THICKNESS CALCULATION	102
6.7. ALGORITHM VALIDATION AND ANALYSIS	103
6.7.1. IMPACT OF ICE PROPERTIES	103
6.8. THICKNESS RETRIEVAL RESULTS AND VALIDATION	104
6.8.1. VALIDATION OF THICKNESS RETRIEVALS FROM INDIVIDUAL WAVEFORMS	105
6.8.2. VALIDATION OF THICKNESS RETRIEVALS FROM 10-KM MEAN WAVEFORMS	109
6.9. DISCUSSION AND CONCLUSION	111
6.10. ACKNOWLEDGEMENT	116
6.11. REFERENCES	117
<u>7. CHARACTERISTICS OF CRYOSAT-2 SIGNALS OVER MULTI-YEAR AND SEASONAL SEA ICE</u>	<u>122</u>
7.1. ABSTRACT	122
7.2. INTRODUCTION	122
7.3. DATA AND METHODS	124
7.4. RESULTS AND DISCUSSION	125
7.4.1. BALTIC SEA	125
7.4.2. ARCTIC	127
7.5. CONCLUSIONS AND RECOMMENDATIONS	130

7.6. REFERENCES	131
8. EVALUATION OF CRYOSAT-2 DERIVED SEA-ICE FREEBOARD OVER FAST ICE IN MCMURDO SOUND, ANTARCTICA	133
<hr/>	
8.1. ABSTRACT	133
8.2. INTRODUCTION	133
8.3. CRYOSAT-2 ASSESSMENT IN MCMURDO SOUND	138
8.3.1. IN SITU INVESTIGATIONS	140
8.3.2. CRYOSAT-2	140
8.4. TRACKING SURFACE HEIGHT FROM CS-2 WAVEFORMS	141
8.4.1. EUROPEAN SPACE AGENCY LEVEL 2 DATA PRODUCT (ESAL2)	142
8.4.2. WAVEFORM FITTING PROCEDURE DATA PRODUCT (WFF)	142
8.4.3. THRESHOLD-FIRST-MAXIMUM-RETRACKER-ALGORITHM 40 (TFMRA40)	143
8.4.4. TRACKING OF SEA SURFACE HEIGHT	143
8.5. SUPERVISED FREEBOARD RETRIEVAL	144
8.5.1. SUPERVISED FREEBOARD RETRIEVAL RESULTS	147
8.6. AUTOMATIC FREEBOARD RETRIEVAL PROCEDURE	154
8.6.1. ESAL2 AUTOMATIC SSH IDENTIFICATION	155
8.6.2. WFF AUTOMATIC SSH IDENTIFICATION	158
8.6.3. TFMRA40 AUTOMATIC SSH IDENTIFICATION	158
8.6.4. AUTOMATIC RESULTS	159
8.7. DISCUSSION	161
8.8. CONCLUSION	167
8.9. ACKNOWLEDGEMENTS	168
8.10. REFERENCES	169
9. VALIDATION OF CRYOSAT FREEBOARD RETRIEVALS WITH COINCIDENT AIRBORNE MEASUREMENTS	174
<hr/>	
9.1. ABSTRACT	174
9.2. INTRODUCTION	175
9.2.1. METHODS AND MEASUREMENTS	179
9.2.2. AIRBORNE MEASUREMENTS	180

9.2.2.1. OIB	180
9.2.2.2. ALS	181
9.2.2.3. ASIRAS	181
9.2.2.4. AEM	182
9.2.3. CRYOSAT DATA PRODUCTS	183
9.2.3.1. AWI product	183
9.2.3.2. ESA product	184
9.2.4. RESAMPLING AIRBORNE DATA TO CRYOSAT FOOTPRINTS	184
9.3. RESULTS	186
9.3.1. ILLUSTRATION OF DETAILED ANALYSIS OF DATA ALONG ONE ORBIT	186
9.3.2. ANALYSIS OF COMPLETE FREEBOARD DATASET AND IMPROVEMENT BY ALONG-TRACK AVERAGING	191
9.3.3. DIFFERENCES OVER FIRST- AND MULTIYEAR ICE	193
9.3.4. DIFFERENCES BETWEEN MEAN AND MODAL FREEBOARD	195
9.3.5. COMPARISON OF AEM ICE THICKNESS WITH CRYOSAT ICE THICKNESS	196
9.3.6. COMPARISON OF OIB WITH CRYOSAT ICE THICKNESS	198
9.4. DISCUSSION	200
9.5. ACKNOWLEDGEMENTS	206
9.6. REFERENCES	207
9.7. APPENDIX: OVERVIEW OF GOLDEN DAYS	212
10. SUMMARY AND CONCLUSIONS	213
10.1. SUMMARY	213
10.2. LIMITATIONS	217
10.3. FUTURE WORK	218
REFERENCES	222
APPENDIX A: OTHER PUBLICATIONS	253

List of Tables

Table 3.1: Published CryoSat-2 Waveform classification parameters. Note that Ricker et al. 2014 and Kurtz et al. 2014 use different formulations of pulse peakiness (PP) than Laxon et al. 2015.	44
Table 3.2: Sea ice, snow, and water density and snow depth data utilized in studies of altimetric retrievals of sea ice thickness. *Kwok modified the Warren et al. 1999 snow density climatology (W99). MX.XW99 is a modified version of the Warren et al. (1999) where X.X is the multiplication factor applied to W99 over FYI. ¹Zygmuntowska et al. (2014) apply an additional correction of ½ the multi-year ice fraction to the modified Warren et al. (1999) climatology over FYI.	54
Table 3.3: Summary of CryoSat ice thickness validation results using NASA Operation IceBridge (OIB) ice thickness retrievals resampled onto monthly 25 x25 km² grids. Table shows correlation coefficients (r), mean differences (MD), and RMS differences (RMSD) between CryoSat and OIB data.	56
Table 5.1: Riegl LMS Q120 laser scanner characteristics. Data adapted from scanner settings used during study and the scanner specifications (Riegl, 2010).	66
Table 5.2: Total thickness and roughness data measured over the sea ice north of Svalbard, the drift ice in Fram Strait, and the fast ice in Fram Strait. AEM statistics calculated using data coincident with laser scanner observations.	75
Table 6.1: CORRELATION (R) AND RMSE OF THE INDIVIDUAL FULL-RESOLUTION CS2 ICE THICKNESS RETRIEVALS (SEE SECTION 6.6.1) AND THE FDD MODEL AND DRILL HOLE THICKNESS DATA OVER GSL AND GBL. TWO SETS OF STATISTICS ARE PROVIDED: ONE FOR THE FULLRESOLUTION INDIVIDUAL CS2 WAVEFORMS (SCALE = IND.) AND THE OTHER FOR THE ORBIT MEANS OF THOSE WAVEFORMS (SCALE = ORBIT). FOR THE ORBIT MEANS, IF AN ORBIT CONTAINED LESS THAN 33 WAVEFORMS (WHICH IS APPROXIMATELY ONE COMPLETE 10-km MEAN WAVEFORM), IT WAS NOT INCLUDED IN THE CALCULATED STATISTICS. RMSE IS IN METERS AND N IS THE NUMBER OF POINTS IN THE COMPARISON. THE 2010/2014 ENTRY COMBINES THE DATA FROM ALL STUDY YEARS	106
Table 6.2: CORRELATION (R) AND RMSE OF THE 10-km MEAN WAVEFORM CS2 ICE THICKNESS RETRIEVALS (SEE SECTION 6.6.2) AND THE FDD MODEL AND DRILL HOLE THICKNESS DATA OVER GSL AND GBL. TWO SETS OF STATISTICS ARE PROVIDED: THE RESULTS FOR THE INDIVIDUAL 10-km MEAN WAVEFORMS (SCALE = 10 km) AND ORBIT MEANS OF THOSE 10-km MEAN WAVEFORMS (SCALE = ORBIT) WHERE AN ORBIT CONTAINED MORE THAN ONE 10-km MEAN WAVEFORM. RMSE IS IN METERS AND N IS THE NUMBER OF POINTS IN THE COMPARISON. THE 2010/2014 ENTRY COMBINES THE DATA FROM ALL STUDY YEARS	109
Table 8.1: Mean freeboard values, standard deviations and sample sizes (n) derived by each retracker by the supervised procedure in austral spring (November and December) 2011 and 2013 and comparison to interpolated in situ mean ice (F_i) and snow freeboards (F_s). The satellite tracks from which each F_{sup} mean is derived are displayed in blue in Figure 8.3.	146

- Table 8.2: Mean automatic procedure freeboard values and standard deviations derived by each technique for each year for the entire study area and fast ice only (bold). The total number of measurements (n) for each year is also displayed. The spatial distribution of the satellite tracks from which the Fb_{auto} means are derived are shown in orange in Figure 8.3. 159**
- Table 8.3: Mean automatic procedure freeboard values (m), standard deviations and number of measurements (in parentheses) used to derive the statistics for each technique in each year over the fast-ice area. The data are binned into calendar months. The day corresponding approximately to the middle of each calendar month from the start of the analysis (day zero = 1 March) is also displayed. 161**
- Table 9.1: Previous CryoSat ice thickness validation results using NASA Operation IceBridge (OIB) ice thickness retrievals resampled onto monthly 25 x25 km² grids. Table shows correlation coefficients (r), mean differences (MD), and RMS differences (RMSD) between CryoSat and OIB data. 177**
- Table 9.2: Different definitions of freeboard required for discussion of comparison of altimeter freeboard retrievals and conversion to ice thickness. 179**
- Table 9.3: Waveform parameters and ice concentration thresholds used in the AWI and ESA CryoSat-2 processing algorithms to discriminate between the surface types: “ocean”, “lead” and “sea ice”: pulse peakiness (PP), stack kurtosis (K), standard deviation (SSD), peakiness left of the power maximum (PP_l), peakiness right of the power maximum (PP_r), sea-ice concentration (IC) and the width of the OCOG box (OCOG WIDTH). 184**

List of Figures

Figure 2.1: Common features of Arctic sea ice including those that form through convergence, divergence and shear. Adapted from Wikipedia: “Sea Ice,” Creative Commons Attribution-Share Alike Unported 3.0 License. Modified and provided by J. Alec Casey.....	5
Figure 2.2: Row 1: Travel through and on sea ice. Row 2: Rafted and ridged sea ice. Row 3: Ridged ice and melt ponds. Row 4: Jumbled and rafted thin sea ice. Photo in bottom left courtesy of M. Hoppmann.....	6
Figure 2.3: Sea ice floe near Cape Josef Henry on Ellesmere Island, Nunavut in various stages of melt. All images are of the same floe and taken within 6 days, (top left): June 14, 2011 at 11:00, (top right): June 17, 2011 at 11:00, (bottom left): June 19, 2011 at 11:00, and (bottom right): June 20, 2011 at 06:00.	7
Figure 2.4: Example ice salinity profiles from cores of FYI and MYI self-collected in the Lincoln Sea in 2012. Note the typical “C” shaped curve for FYI and the low surface salinity of the MYI.	9
Figure 2.5: Example sea ice core salinity and density profile for sea ice at the end of summer melt self-collected in the central Arctic Ocean during RV Polarstern Cruise PS94. Error bars show minimum and maximum values of density estimated using mass/volume and liquid/solid volume methods.	10
Figure 2.6: Penetration depth into sea ice at different frequencies for different ice types and snow showing the IEEE definitions of the C, X, and Ku-bands. Adapted with permission from Shokr and Sinha, 2015. Copyright American Geophysical Union 2015.	12
Figure 2.7: Arctic sea ice thickness and snow depth from CryoSat-2 and the modified Warren climatology for April 2017 as produced by AWI (Hendricks, 2015). Note the thin smooth ice in the Laptev Sea. The Beaufort Gyre (BG) is more visible in the snow depth map than the ice thickness map and the Trans-Polar Drift (TPD) can be seen in both the ice thickness and snow depth maps.	14
Figure 2.8: Maps (left) and time series (right) of sea ice age (top), sea ice extent (middle) and sea ice thickness (bottom). Sea ice age is a useful proxy for thickness as older ice is generally thicker.....	17
Figure 2.9: Boxplots (quartiles, with deciles as whiskers) and histograms of 21000 snow depth measurements from the Lincoln Sea and Beaufort Sea self-collected between 2010 and 2014 during CASIMBO and CryoVEx field campaigns.	26
Figure 2.10: Example snow pit profile from CryoVEx 2017 showing snow density where S.M.P. is Snow Micro-penetrator estimate of snow density based on force needed to push sensor through the snow and Samples is from a 100 cc sample of snow (a), temperature (b), salinity (c), grain size (d) and the snow pack layers (f) from the Arctic Ocean in April 2017. S.M.P. Force is presented in (e).....	27
Figure 2.11: Approximate maximum penetration depth for L- (ALOS PALSAR), C- (Envisat ASAR and RadarSat), X- (TerraSAR-X) and Ku- (CryoSat-2) band radar waves for snow densities of 100 kgm ⁻³ , 325 kgm ⁻³ and 500 kgm ⁻³	29
Figure 3.1: Left: CryoSat-2 footprint and waveform representation showing Pulse-Doppler- and Pulse-limited footprints and the waveform components; Adapted from Rosmorduc et al. (2016). Right: CryoSat-2 Beam-,	

Pulse-, and Pulse-Doppler-limited footprints shown to scale. The beam-limited footprint is roughly 15 km wide across track and 13.5 km along-track, the pulse limited footprint is 1.67 km in diameter, and the pulse-Doppler-limited footprint is 1.67 km wide across-track and 0.3 km along-track. 36

Figure 3.2: Schematic of CryoSat-2 Doppler waveform stacking. Waveforms from different Doppler beams that look at the same area (a) are stacked to produce the CryoSat-2 L1B waveforms (b). From Rosmorduc et al. (2016). 37

Figure 3.3: Flowchart for altimetric retrievals of sea ice freeboard and thickness from Ricker et al., 2014 (Creative Commons Attribution 3.0 License)..... 39

Figure 3.4: Process of converting CryoSat-2 surface elevation heights to freeboard. a) Mean sea surface height (MSSH) and CryoSat-2 retrieved surface elevations. b) Relative elevation after removing the MSSH from the CryoSat-2 elevations. Shows the location of valid echoes identified as ice, unknown waveforms flagged as invalid, and lead waveforms. The sea surface height anomaly (SSHA) is created by interpolating between leads. c) The radar freeboard determined after removing the SSHA from the elevation of the valid echoes. Negative freeboards exist but are not shown in c). Provided by Robert Ricker. 41

Figure 3.5: Example retracking points on the leading edge for different retrackers from Ricker et al. (2014) in blue, Kurtz et al. (2014) in green and the ESA CryoSat L2I product in orange. Figure from Price et al. (2015). Reprinted from the Journal of Glaciology with permission of the International Glaciological Society..... 43

Figure 3.6: Lead fraction (a) and sea ice freeboard (b) from Ricker et al. 2016 showing high lead fractions in November 2015 in the CAA and still showing some areas with high lead fractions in March 2015. 46

Figure 3.7: Averaged waveforms for different ice types showing the backscattered power (a) and the normalized power (b). a) highlights differences in returned power while b) highlights differences in waveform shape. From Zygmontowska et al. 2013. Creative Commons License 3.0. 47

Figure 3.8: Mean Sea Surface Height Model comparison from S. Hendricks (unpublished, 2016). Left: Maps of sea ice freeboard, sea ice surface height anomaly and sea ice thickness derived using the (top to bottom) EGM 2008, DTU10, DTU13, and UCL13 MSS models. Right: Along-track sea surface height anomaly, freeboard and MSS difference between DTU13 and the EGM2008, DTU10 and UCL13 MSS models. Red and blue boxes indicate the location of subsea features not detected in EGM2008 and how these are mapped or not mapped directly into freeboards depending on the presence of sea ice leads. 51

Figure 3.9: Altimetric retrievals over snow-covered sea-ice showing the retrieval surfaces of laser and radar altimeters as well as the instantaneous (MSS + SSA) and mean sea surfaces (MSS). Figure adapted from Ricker et al. 2014. Creative Commons Attribution 3.0 License. Equations from Giles et al. (2007). 52

Figure 5.1: Map of study region overlain on ASCAT C-band scatterometer backscatter data from 6 September 2010. Backscatter variations over sea ice correspond to different ice concentration, ice type distribution and ice roughness. Over open water, backscatter varies with wind speed and direction..... 65

Figure 5.2: Laser-scanner results from example section of sea ice north of Svalbard. (a) Example curve-fit procedure for scanner line 1255; (b) laser return strength; (c) nadir photograph taken from helicopter; (d) raw laser scanner range measurements; (e) estimated flat surface; (f) relative elevation of measurements (d) to flat surface in (e). 68

Figure 5.3: Comparison of standard deviation of relative surface elevation from the laser scanner and laser altimeter for two short sections of sea ice in Fram Strait from flight FS20100906f1. Adjacent photographs were taken from the helicopter and show the AEM sensor. The scanner standard deviation is the standard deviation of relative surface elevation of all beams in a single scan line. The laser altimeter standard deviation is computed using a running five-point along-track window..... 72

Figure 5.4: (a-c) Change in distribution of surface roughness for different window sizes (box-car filter length (m)) used to calculate the surface roughness. PDF: probability density function. The profiles represented are 38km, 40km and 45km long flight sections for the ice north of Svalbard, in Fram Strait and over the fast ice in Fram Strait, respectively. (d-f) High-elevation fraction (HEF) is the number of points higher than 0.8m divided by the total number of points in an increasing length of a profile, represented by the number of scan lines, for the altimeter for all measurements in each region. 74

Figure 5.5: (a-c) Statistical distributions of surface roughness for all data collected over the three observed ice regimes, seasonal ice north of Svalbard, FYI/MYI mixture in Fram Strait, and fast ice in Fram Strait. (d, e) Distribution of surface roughness for data collected while flying in different cardinal directions (north, south, east and west). (f) Statistical distribution of total thickness measured by the AEM sensor for the three study regions. (g-i) Comparison of surface roughness and total thickness (snow plus ice thickness) for the three observed ice regimes using average values from successive 1 km sections of flight..... 76

Figure 6.1: Map of GSL and GBL. The locations of weather stations used for FDD ice thickness modeling are shown by crosses. Tracks of four CS2 orbits plotted in Figure 6.2, Figure 6.3, and Figure 6.5 are shown by the black lines. Shoreline and islands data are from the GSHHG database v2.2 [37]. 91

Figure 6.2: CS2 L1B waveform data from four orbits over GSL on (a) January 12, (b) April 7, (c) May 6, and (d) July 1, 2013, representing early season ice, late season ice, early snow/ice melt, and open water, respectively. The normalized power from 0.0 to 1.0 is displayed by the color scale with white representing 1.0. The one-way travel distance of the signal is displayed on the y-axis and the distance in kilometers along the track is displayed on the x-axis. The one-way travel distance is determined using the speed of light in free space and is calculated for range bins 140 (0 m) to 200 (14 m)..... 94

Figure 6.3: Maximum power (watts) of each waveform for the CS2 orbits shown in Figs. 1 and 2. Only a subset of the waveforms in each orbit is shown for clarity. 96

Figure 6.4: Six waveforms (a-f) from the CS2 L1B SARIN mode pass over GSL on April 7, 2013, illustrating the variability in relative power of the peaks, peak and signal noise, and the resulting challenges to retrieving the location of the power peaks originating from the ice surface and ice bottom. The normalized power is

displayed on the y-axis and the one-way travel distance of the signal is displayed on the x-axis. The one-way travel distance is determined using the speed of light in free space and is calculated for range bins 140 (0 m) to 200 (14 m). 97

Figure 6.5: Mean waveforms from each of the four orbits over GSL presented in Figure 6.2, January 12, April 7, May 6, and July 1, 2013, representing (a) early season ice, (b) late season ice, (c) early ice melt, and (d) open water, respectively. The mean normalized power is displayed on the y-axis and the one-way travel distance of the signal is displayed on the x-axis. The one-way travel distance is determined using the speed of light in free space and is calculated for range bins 140 (0 m) to 200 (14 m). The horizontal lines in (a) and (b) indicate how ice thickness is calculated as the difference in the one way-travel distance of the peaks. 98

Figure 6.6: Envisat ASAR image of GBL acquired on March 15, 2012 overlain with the 10-km-long, 1.65-km-wide CS2 10 km mean waveform footprints from March 17, 2012. Subplots surrounding the map present the selected CS2 10-km mean normalized power waveforms and Envisat ASAR backscatter histograms for the pixels within the footprint of each CS2 10-km mean waveform. In the ASAR image, high backscatter is bright and low backscatter is dark. The circular markers in the normalized power waveform plots indicate the peaks in power used to calculate ice thickness. (Top right) Inset value within each histogram and waveform subplot is the retrieved ice thickness. 100

Figure 6.7: Validation results for ice thickness retrievals over GBL and GSL derived from the full-resolution CS2 data described in Section 6.6.1. (Top) Scatter plot of CS2 versus in situ ice thickness measurements. The blue line shows the linear regression with slope 1.10 ± 0.01 for GBL and 0.78 ± 0.01 for GSL. The black line is a one-to-one line. (Bottom) Comparison of time series of lake ice thickness from CS2, the FDD model, and in situ measurements. 105

Figure 6.8: Validation results for ice thickness retrievals over GBL and GSL derived from the orbit means of the 10-km along-track averaged CS2 waveforms described in Section 6.6.2. (Top) Scatter plot of CS2 versus in situ ice thickness measurements. The blue line shows the linear regression with slope 1.12 ± 0.05 for GBL and 0.90 ± 0.06 for GSL. The black line shows a one-to-one line. (Bottom) Comparison of time series of lake ice thicknesses from CS2, the FDD model, and in situ measurements. 108

Figure 7.1: Maps showing examined Cryosat-2 tracks in the Arctic Ocean (a) and Baltic Sea (b). Thin lines represent airborne data..... 124

Figure 7.2: Examples of extreme across-track snagging in CryoSat-2 L2 SARM data (March 4, 11:55). The L2 surface height profile (top right) and waveforms (bottom right) are shown for measurements 400-500. The CryoSat-2 data are overlaid on an Envisat ASAR image (Mar 4, 09:16 UTC) (left). In the ASAR image, wind-roughened open water appears white, and the ice appears dark. 7 km wide footprints are drawn for distance reference purposes..... 126

Figure 7.3: Normalized power waveforms from the extreme across-track snagging example in Figure 2 containing a) ice at nadir, b) open water at nadir, c) open water at nadir with a smooth reflector off-nadir (leading to

snagging), and d) open water at nadir with a smooth reflector off-nadir (no snagging). The vertical dashed line indicates the position within the waveforms selected by the CryoSat-2 L2 retracker. X and + represent the location of the first peak and retracked power threshold value identified by a retracker under development at the University of Alberta. 127

Figure 7.4: a) Normalized power waveforms from CryoSat-2 L1B data over the Lincoln Sea in the Arctic Ocean on April 3, 2012. b) Profile of the surface height from the L2 product (black) and after retracking the Level 1B waveforms (grey)..... 128

Figure 7.5: Comparison of the CryoSat-2 sea ice thickness estimates produced by AWI and AEM sea ice thickness measurements for CryoSat-2 SAR mode acquisitions from 2012/04/03 and 2012/04/04 over the Lincoln Sea. 129

Figure 7.6: Comparison of CryoSat-2 freeboard produced by AWI and NASA OIB quick look freeboard for a CryoSat-2 SARIn mode pass from 2012/03/26 in the Arctic Ocean. OIB freeboard is the height of the snow surface above the water. 130

Figure 8.1: Components relating to the interpretation of CryoSat-2 freeboard data. The reception period is maintained by a range window (RW; 120m in SIN mode) which is constantly adjusted in the vertical dimension to receive echoes from the surface. The transmitted power (P_t) is subject to interaction at the surface from the air/snow interface, volume of the snow cover and snow/ice interface which all influence the power returned to the satellite (P_r). The dominant backscattering surface is variable and is displaced by varying snow depth (s_h), snow layering and snow and ice properties. The retracking procedure is completed, resulting in a range (R) between r_1 and r_2 over sea ice (r_3 over water) dependent upon the assumptions of the respective retracking technique. This range is subtracted from the satellite altitude above the ellipsoid to provide uncorrected height. After application of geophysical corrections, freeboard is obtained by discerning the difference between local sea surface height (SSH) and an interface in the range of the ice freeboard (F_{bi}) and the snow freeboard (F_{bs}) as measured by the satellite. 135

Figure 8.2: (a) Typical CryoSat-2 SIN mode waveform over snow-covered sea ice in McMurdo Sound with labelling of characteristics mentioned in the text. (b) An expanded view of the outlined grey area in (a) from range bins 140–170 (1 bin = 0.234 m) and the expected retracking points on the leading edge for the techniques described here: ESAL2 (40–70% orange), WfF (50–90% green) and TFMRA40 (40% blue). 137

Figure 8.3: (a) Location of the study area within the Antarctic. (b, c) McMurdo Sound and the study area for 2011 (b) and 2013 (c), showing the distribution of CryoSat-2 tracks for those used in the supervised analysis (blue lines), the automatic study period (orange lines) and locations of in situ measurement sites (white dots). The November fast-ice edge is displayed for each year (white line). The full study area for each annual automatic analysis is outlined in green. The validation line in Figure 8.4 is highlighted by the black rectangle and expanded in (d) to show each in situ measurement point (light blue dots) along the CryoSat-2 track. 139

Figure 8.4: Comparison of each method along a validation line coincident with a CryoSat-2 overpass on 27 November 2013 for (a) ESAL2, (b) WfF and (c) TFMRA40. In situ measured ice and snow freeboards are shown as blue and grey horizontal lines respectively. Segments 3 (S3) and 4 (S4) in Figure 8.5 are also shown. Sea surface height was identified using the supervised procedure. The CryoSat-2 height profile begins in the north over open water and progresses south over the fast-ice edge at the beginning of segment 3. The freeboard retrievals for each respective retracker are displayed as orange circles, and the validation line statistics describe the sea-ice area only. S3 and S4 means are also displayed for each technique, along with the ice freeboard and snow freeboard measured in situ..... 149

Figure 8.5: (a) Segments 1–4 over the first-year sea-ice area (bounded by white dotted line) overlaid upon a TerraSAR-X radar image from 28 November 2013. TerraSAR-X image (courtesy DLR (German Aerospace Center)). (b) Mean waveforms from these segments plotted as power for multiple sea-ice surface conditions with variable geometric roughness (GR), radar roughness (RR) and snow depth (s_h)..... 151

Figure 8.6: Mean waveform examples for sea ice in 2011 with significant snow cover (circles and blue fits) and minimal snow cover (crosses and orange fits). The area with significant snow cover had a mean snow depth of 0.20m with consistent coverage. Over the minimal area a mean snow depth of 0.07m was measured with a patchy distribution. (a) The retracking points for ESAL2 with linear fits between each bin; (b) the retracking points for WfF with respective model fits; and (c) the retracking points for TFMRA40 with interpolated curves..... 153

Figure 8.7: Surface type discrimination as indicated by Level 2 parameter peakiness (P) displayed as a cumulative percentage. Surface types, open water, fast ice and developing floes are displayed for 2011 (a) and 2013 (b). In 2011, surface conditions made the discrimination of open water and fast ice more difficult. This resulted in a change in the thresholds between the years. The expected inclusion of sea ice in the open-water surface type is indicated by the percentage overlaps..... 157

Figure 8.8: The development of the McMurdo Sound fast-ice cover from mean automatic procedure freeboard values for each month for 2011 and 2013 over the expected sea-ice growth period (day zero = 1 March) for ESAL2 (a), WfF (b) and TFMRA40 (c). A linear fit from the beginning of mid-March (~day 15) to mid-December (~day 290) defines the expected sea-ice growth period. Mean in situ measured ice and snow freeboards measured in November/December of each year are shown by the blue and grey lines respectively. The standard deviations for each mean value are provided in Table 8.3..... 162

Figure 9.1: Map of all coincident laser (OIB and ALS), radar (ASR), and AEM flights used in this study (see flight list in Appendix 9.1). Note that flight tracks overlap and therefore not all sensor’s tracks are visible on the map. Freeboard retrievals along one coincident CryoSat ground track between Canada and Siberia (orbit 021011 on March 26, 2014) are also shown as example. Background shows radar backscatter on March 26, 2014 (from ASCAT; Long et al., 2001) chosen to represent typical ice conditions during CryoVEx campaigns, with first-year ice indicated by low (darker) and multiyear ice by high backscatter (bright). 180

Figure 9.2: Example for the averaging of OIB freeboard data to the beam-sharpened CryoSat footprints (large rectangles). Black circles are 40 m in diameter and show the OIB freeboard retrieval locations and the values for each measurement. Triangles and left labels show the averaged OIB freeboard data in each footprint. 185

Figure 9.3: a) Typical 10 km section of the full resolution airborne data collected along CryoSat Orbit 21011 on March 26, 2014, showing OIB and ALS snow freeboard, ASIRAS (ASR) radar freeboard, and AWI and ESA CryoSat freeboard. b) Airborne data resampled to the CryoSat footprints. 188

Figure 9.4: Example of the comparison between airborne and CryoSat freeboard retrievals along complete flight tracks for orbit 021011 on March 26, 2014 (see Figure 9.1). Left column shows comparisons between mean airborne data in individual CryoSat footprints. Right column shows data averaged along-track over 50 km. The scatter plots show the correlation coefficient r , Mean Difference and RMS Difference (RMSD, in parentheses) in the bottom right. N is the number of CryoSat footprints with coincident measurements (left column), or of coincident 50 km sections (right column). Bold correlations have a p -value less than 0.01 (statistically significant) and r is significantly different from 0. 190

Figure 9.5: Summary of results of the comparison of airborne and CryoSat freeboard over different along-track averaging distances. Percentile analysis of a) correlation coefficient r , b) RMSD, and c) the mean difference (MD) between the resampled airborne data and the CryoSat freeboard data. Full denotes the footprint averaged results and 50 km is the 50 km along track average of the footprint resampled results. The boxes present the 25th and 75th percentiles, the horizontal line within the box is the median (50th percentile) and the whiskers end at the 10th and 90th percentiles. Circles show mean value. 192

Figure 9.6: Summary of results of the comparison of airborne and CryoSat freeboard over FYI and MYI. Shown are results for 50 km along-track mean data. Percentile analysis of a) correlation coefficient r , b) RMSD, and c) the mean difference (MD) between the airborne and CryoSat freeboard data. The boxes present the 25th and 75th percentiles, the horizontal line within the box is the median (50th percentile) and the whiskers end at the 10th and 90th percentiles. Circles show mean value. 194

Figure 9.7: Comparison of airborne ALS and ASIRAS (ASR) fb_{mean} and fb_{mode} (see text) with 50 km along-track mean CryoSat freeboard. Percentile analysis of a) correlation coefficient r , b) RMSD, and c) the mean difference (MD) between the resampled airborne data and the CryoSat freeboard data. The boxes present the 25th and 75th percentiles, the horizontal line within the box is the median (50th percentile) and the whiskers end at the 10th and 90th percentiles. Circles show mean value. 196

Figure 9.8: Comparison of the AEM and AWI CryoSat thickness, showing the effect of along-track averaging distance (left column), differences over different ice types (center column), and differences between the modal and mean thickness (right column; cf. Figure 9.5, Figure 9.6, Figure 9.7 for freeboard). The figure shows percentile analysis of a) correlation coefficient r , b) RMSD, and c) the mean difference (MD) between the resampled AEM thickness and CryoSat thickness. The boxes present the 25th and 75th percentiles, the

horizontal line within the box is the median (50th percentile) and the whiskers end at the 10th and 90th percentiles. Circles show mean value. 198

Figure 9.9: Comparison of the OIB and AWI CryoSat thickness, showing the effect of along-track averaging distance (left column) and differences over different ice types (right column; cf. Figure 9.5, Figure 9.6). The figure shows percentile analysis of a) correlation coefficient r , b) RMSD, and c) the mean difference (MD) between the resampled OIB thickness and the CryoSat thickness. The boxes present the 25th and 75th percentiles, the horizontal line within the box is the median (50th percentile) and the whiskers end at the 10th and 90th percentiles. Circles show mean value. 200

1. General Introduction

1.1. Motivation

Research over the past decade has provided strong evidence that the Arctic is undergoing dramatic changes associated with the observed increasing global average temperature: sea ice extent and thickness are decreasing, variability in winter air temperatures is increasing, and there have been strong changes in the depth of snow and duration of snow cover over Arctic sea ice and land (Vaughan et al. 2013). Changes in ice and snow properties have been observed throughout the central Arctic and sub-Arctic, affecting glaciers, the tundra, sea ice, and sub-Arctic lakes.

Advances in airborne and satellite remote sensing in the past four decades have improved our knowledge of the Arctic and its snow and ice fields; sea ice extent, age, and drift vectors are now routinely observable by satellites (e.g. Maslanik et al., 2011; Kwok et al., 2013; Serreze et al., 2015). In 2010, the European Space Agency launched CryoSat-2, a new generation of radar altimeter mission to measure the changes in Arctic sea ice thickness.

Despite the advances made using satellite sensors, including pan-Arctic sea ice thickness estimates from CryoSat-2, challenges and uncertainties remain in our ability to measure the changes in the physical properties of sea ice and lake ice and snow cover and make predictions about its future. We are faced with the usual trade-off of highly certain measurements with limited spatial and temporal extent or large areal coverage, high temporal resolution data with reduced certainty. The difficulty of collecting physical measurements and in retrieving certain physical properties from airborne or satellite data makes combined in-situ, airborne, and satellite data highly valuable.

The thickness of the ice remains especially difficult to retrieve at a sufficient spatial and temporal resolution and scale to make accurate long-term (annual or longer) or even short term (seasonal) predictions. Current altimeter retrievals of ice freeboard and thickness have poorly quantified and limited certainty and are influenced by a wide variety of physical processes and properties of the ice and, especially, the snow.

Our ability to measure the physical properties of snow remains limited over sea ice, lake ice and even in certain land environments. Like sea ice, snow has high spatial and temporal variability

at multiple scales. Current airborne measurements of snow thickness on sea ice have low certainty stemming from a range of issues (discussed further on) and are not pan-Arctic. Snow is extremely important for the retrieval of remotely sensed sea ice thickness and freeboard estimates as well as lake ice thickness. Current altimeter retrievals of sea ice freeboard and thickness are either using adjusted or unadjusted climatological snow depth and density data developed in 1999 (Warren et al., 1999) using data from the 1950s – 1990s, or are using non-validated atmospheric reanalysis outputs.

Additional data on the thickness and freeboard of sea ice, snow depth and assessments of our current attempts to measure these properties are urgently needed to improve our knowledge of these fields for remote sensing retrievals of snow and ice, for improved local and regional forecasting of sea ice conditions, to provide accurate initialization data for seasonal and longer coupled and non-coupled ice, ocean and climate models, and for assessing the parameterization of these variables in said models.

1.2. Objectives

The primary objectives of this thesis are to further our ability to measure, and to provide new measurements of, the physical properties of sea and lake ice and their snow covers using satellite and airborne altimeter data. To achieve these objectives, numerous measurements of sea ice, lake ice and snow have been performed, new algorithms have been developed, and comparisons between existing data from on-ice, airborne, and satellite sensors have been made. This thesis examines several questions: 1) Can new insight into the properties of snow depth, ice thickness and surface roughness be achieved with additional ground, satellite and airborne altimetry measurements? 2) Can Cryosat-2 provide measurements of lake ice thickness; and 3) Are CryoSat-2 measurements of Arctic sea ice freeboard and thickness valid.

Throughout my doctoral program, I have also sought to support and collaborate with other related studies that have similar or complementary goals. A list of other publications that I have been involved in throughout this doctoral program is provided in Appendix A and these are discussed briefly in Chapter 4.

1.3. Structure

This manuscript-based thesis is comprised of 10 chapters: four background chapters, 4 published publications, 1 unpublished chapter, and a conclusions chapter. I have examined sea ice, lake ice, and snow using in-situ, airborne and satellite data, especially altimeters. This chapter has introduced the main motivation, objectives, and structure. Chapter 2 describes the relevant physical and dielectric properties of sea ice, lake ice and snow as well as summarizes our current knowledge of these properties. Chapter 3 describes radar and laser altimeter measurements of the ice (and snow) and uncertainty. Chapters 5 through 9 are the journal articles that compose the main scientific work of my thesis; all chapters but Chapter 9 have been published in peer-reviewed journals. Chapter 5 examines airborne laser scanner data without the need for an inertial navigation system/inertial measurement unit. Chapter 6 examines CryoSat-2 radar altimetry data over lake ice and presents, to my best knowledge, the first retrievals of lake ice thickness using radar altimetry. Finally, Chapters 7, 8, and 9 examine various aspects of CryoSat-2 data, freeboard and thickness retrievals over Arctic and Antarctic sea ice and comparisons with airborne data.

2. Background

The objectives described in Chapter 1, and the publications presented in Chapters 5 through 9 require some understanding of the physical and dielectric properties of sea ice, lake ice and snow. While each article provides the necessary background information, this chapter provides a quick summary of the physical and dielectric properties of sea ice (2.1), lake ice (2.2) and snow (2.3). For each medium, the physical and dielectric properties are presented along with a brief description of their importance to climate and remote sensing. Each section ends with a short review of the changes being observed now and predicted for the future.

2.1. Sea Ice

Sea ice, the frozen ocean cover found in the Arctic Ocean, the northern reaches of the Atlantic and Pacific Oceans and the waters around Antarctica, covers some 16 and 28 million km² of the earth's surface at its annual minimum and maximum extents, respectively. Sea ice makes up a large part of the cryosphere and plays an important role in climate dynamics and is an important habitat to a wide variety of fauna, including e.g. algae, polar cod, seals, polar bears. Changes in the ice cover's thickness and extent will also have important geopolitical and environmental ramifications as access to the Arctic basin is predicted to become more common. In this section, we briefly review the growth and melt of sea ice, summarize some of the key physical and electrical properties of sea ice before discussing the importance of sea ice. We finish with a brief review of the current state of the sea ice cover and the predictions for the near future. For comprehensive reviews of sea ice properties, the reader is pointed to e.g. Timco and Weeks (2010), the textbooks *Sea Ice* edited by D. Thomas (2010, 2017), *Field Techniques for Sea Ice Research* edited by H. Eicken et al. (2009) and *Sea Ice: Physics and Remote Sensing* edited by M. Shokr and N. Sinha (2015).

2.1.1. Growth and melt

Sea ice formation in the Arctic begins in late August or September when the upper ocean is cooled to the freezing point, around -1.8°C (Petrich and Eicken, 2010). Ice formation begins with frazil ice crystals suspended in the water. In calm conditions, continuous sheets called nilas are formed as the frazil crystals combine; in rough seas, the frazil freezes together as pancake ice, rounded ice pans with raised edges resulting from wave action and collisions between frazil and,

eventually, between pans. Pancake ice grows larger with the accretion of frazil ice and additional pancakes. Ice thickening occurs as columnar crystals, i.e. congelation ice, grow downward from the bottom of the ice (Petrich and Eicken, 2010). The accumulation of frazil crystals and platelet ice to the bottom of the ice, or in gaps between rafted pancakes can also increase the thickness and the size of the ice floes. Thermodynamic ice growth decreases with increasing ice thickness due to reduced thermal gradient between the atmosphere and the ocean. Once ice floes have formed, snow can accumulate on the surface and further reduce the thermal heat flux between the cold atmosphere and warm ocean. However, snow may be transformed into snow ice by flooding, liquid precipitation, or melt events; snow ice has a higher thermal conductivity than snow. In addition to dynamic growth, sea ice can also thicken through dynamic processes.

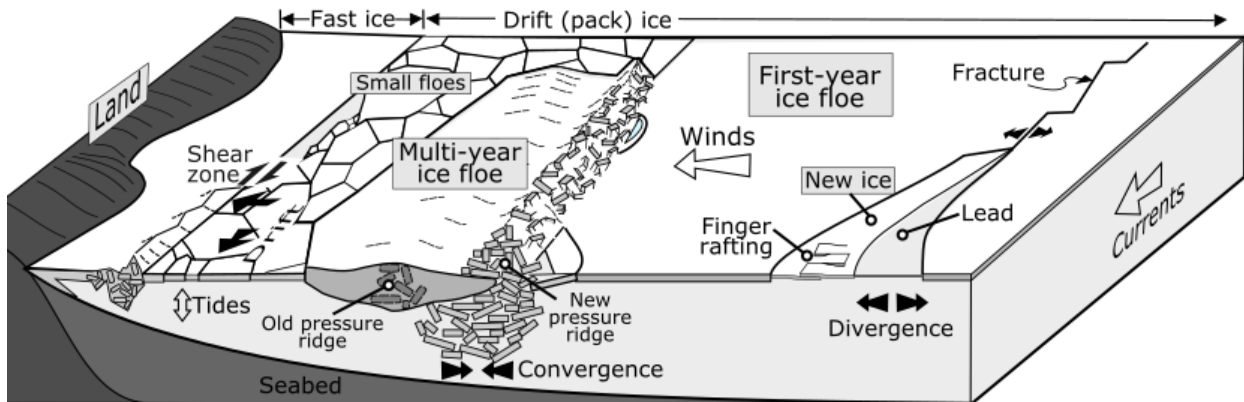


Figure 2.1: Common features of Arctic sea ice including those that form through convergence, divergence and shear. Adapted from Wikipedia: “Sea Ice,” Creative Commons Attribution-Share Alike Unported 3.0 License. Modified and provided by J. Alec Casey.

Dynamic growth, which occurs through the convergence or shear of ice floes can cause ice thicknesses much greater than the thermodynamic limit (Figure 2.1). Compression, when sea ice floes collide or are driven together near boundaries such as shore lines or fast ice, can result in ridging or rafting and increases in local thickness (Figure 2.1). Over time, compressive features such as ridges and rafted ice blocks consolidate as water between the ice blocks freezes and snow accumulates. Shear, when two ice floes slide along each other, can also result in significant deformation, ridging, and rafting. Dynamic features influence the distribution of snow and the atmospheric and ocean forces acting on the ice through the sail (above water ridge) and keel (below water ridge). Furthermore, ridges, and the snow drifts that develop on the leeward side

of ridges, provide shelter for seals and thus hunting grounds for polar bears. Ridges are also a major obstacle for travel through the ice for ships (Kubat and Timco, 2003; Timco and Weeks, 2010; Pizzolato et al., 2014); however, the associated snow drifts can ease travel on the ice with a snow machine or skis (Figure 2.2).

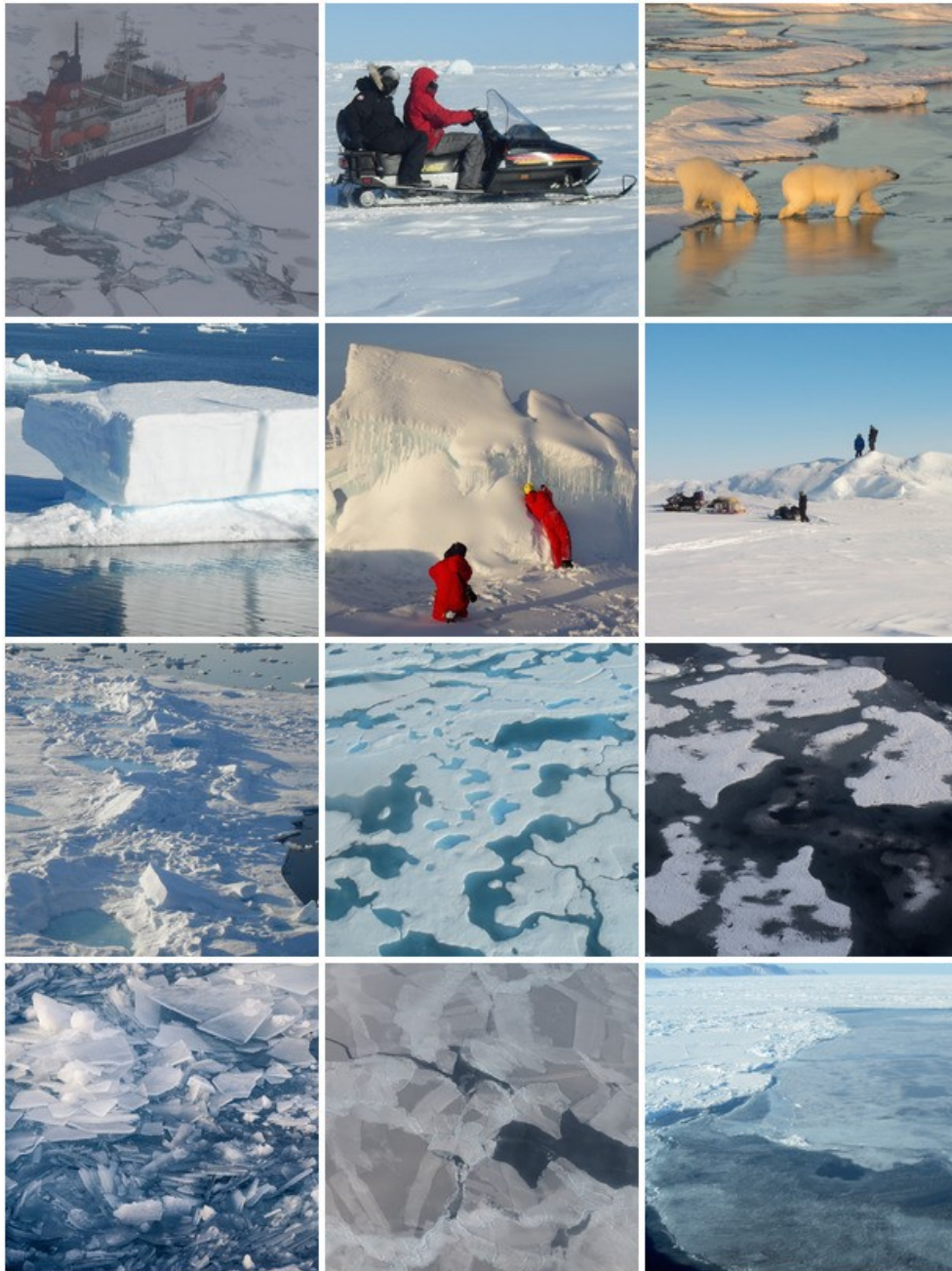


Figure 2.2: Row 1: Travel through and on sea ice. Row 2: Rafted and ridged sea ice. Row 3: Ridged ice and melt ponds. Row 4: Jumbled and rafted thin sea ice. Photo in bottom left courtesy of M. Hoppmann.

Sea ice retreat begins in late March or April, depending on latitude, when solar radiation returns to the Arctic. Snow and ice melt water can pool in depressions to form melt ponds. Wet snow and melt ponds have low albedo (see Figure 2.3) and thus wet snow and ice beneath melt ponds melt more quickly than bare ice or dry snow; this leads to the hummocky topography of MYI. Inclined ice features such as ridge flanks, rafted ice blocks and the slope of MYI hummocks also experience enhanced melt. Ice melt can also occur on the underside or sides of ice floes due to lateral heating from solar input which reaches the ocean and ice floe sides through the open water leads between the ice floes. Recently, Perovich et al. (2007, 2011) and Steele et al. (2010) highlighted the important role of solar heat input to the oceans and bottom melt of sea ice to the changing sea ice mass balance. Their results show stronger correlation between the input of heat to the ocean and the heat used in bottom melt than the heat input to the ice and heat used in surface melt (Perovich et al. 2007, 2011). New work by Steele and Dickinson (2016) shows that the timing of ice retreat is important to the amount of upper ocean warming as retreat that is early for a region but still late in the season does not lead to significant warming.



Figure 2.3: Sea ice floe near Cape Josef Henry on Ellesmere Island, Nunavut in various stages of melt. All images are of the same floe and taken within 6 days, (top left): June 14, 2011 at 11:00, (top right): June 17, 2011 at 11:00, (bottom left): June 19, 2011 at 11:00, and (bottom right): June 20, 2011 at 06:00.

As the ice and snow melt, some melt water drains through the ice or through thaw holes where melt ponds melt completely through the ice. In addition to solar radiation and upper surface melt, the heat content of the upper ocean can also play a role in the growth and melt of ice as it provides a large source of heat to melt ice in the summer and delay freeze up in the winter (Polyakov et al. 2017). Recent work by Polyakov et al. (2017) provides evidence that increased ocean heat content and release has reduced winter ice-growth by amounts comparable to the effect of enhanced summer melt due to atmospheric forcing and increased solar input to the upper ocean.

2.1.2. Physical and Dielectric Properties

Sea ice is a mixture of pure ice, brine, and air. Salt is rejected to the ice crystal boundaries during ice formation but can be trapped between crystals forming brine pockets. The brine content depends on the ice growth rate and on the temperature of the ice and age; as soon as sea ice forms, it begins to desalinate through gravity drainage (Petrich and Eicken, 2010). The melt, freeze, and dynamic processes affecting sea ice play an important role in modifying the physical, thermal and dielectric properties of the ice. The salinity, density, electromagnetic and thermal properties of the ice are briefly reviewed here as these properties influence sea ice thickness retrievals from altimeter sensors.

Ice salinity depends on the growth rate and the salinity of the formative water. FYI has higher salinity than MYI as the amount of time that has passed for brine drainage to occur is less. Furthermore, during summer melt, freshwater from snow melt can drain through the ice and further freshen the ice cover. Typical salinity profiles for FYI and MYI collected in the Lincoln Sea during fieldwork performed in 2012 are provided in Figure 2.4. FYI has a typical “C” shaped profile with high salinities at the top and bottom and slightly lower values elsewhere. MYI salinity is typically low at the surface and increases towards the bottom. However, MYI may also show several C-shaped profiles representing individual years, with a final increase in salinity towards the bottom where the ice is near the water. Salinity typically ranges from 4 parts per thousand (ppt) to 12 ppt for FYI and from 0 ppt to 6 ppt for MYI.

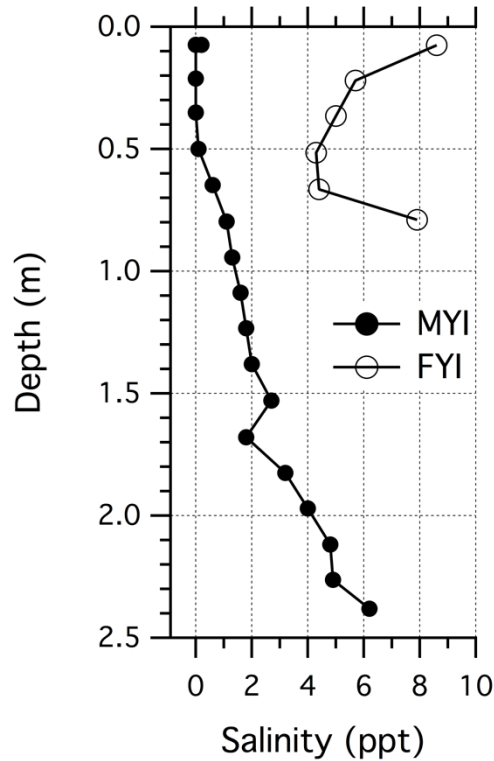


Figure 2.4: Example ice salinity profiles from cores of FYI and MYI self-collected in the Lincoln Sea in 2012. Note the typical “C” shaped curve for FYI and the low surface salinity of the MYI.

The salinity of the ice affects many physical properties of the ice including e.g. the dielectric properties and ice density, key variables in the retrieval of ice thickness and properties from altimeter data.

Sea ice density depends on the structure of the ice and brine content. FYI is denser than MYI because it contains more salt; during summer melt, brine is drained from FYI and MYI resulting in a lower mean density and salinity as presented in Figure 2.5. The surface of MYI is often of much lower density than the rest of the ice due to the presence of air bubbles that are left behind after the summer melt and drainage. Ice density estimates were reviewed by Timco and Weeks (2010) who give a range of 720 kg m^{-3} to 940 kg m^{-3} , depending on ice type, and if one considers ice above or below water. The normal range of ice density values is $840 - 910 \text{ kg m}^{-3}$ for FYI above water, 720 kg m^{-3} to 910 kg m^{-3} for MYI above water, and $900 - 940 \text{ kg m}^{-3}$ for both ice types below water. Alexandrov et al. (2010) summarized measurements from the Russian drifting ice stations and other in-situ measurements collected in the 1980s and found mean values of 916.7 kg m^{-3} for FYI and 882 kg m^{-3} for MYI. Other estimates of sea ice density typically fall in the ranges

summarized in Timco and Weeks (2010); however, some studies suggest much lower ice density, 500-600 kg m⁻³ for air bubble rich hummocks of multiyear ice (see Alexandrov et al., 2010). The salinity and density of the ice and the brine discussed here largely control the dielectric properties of the ice and therefore influence interactions with EM radiation such as from radar altimeters.

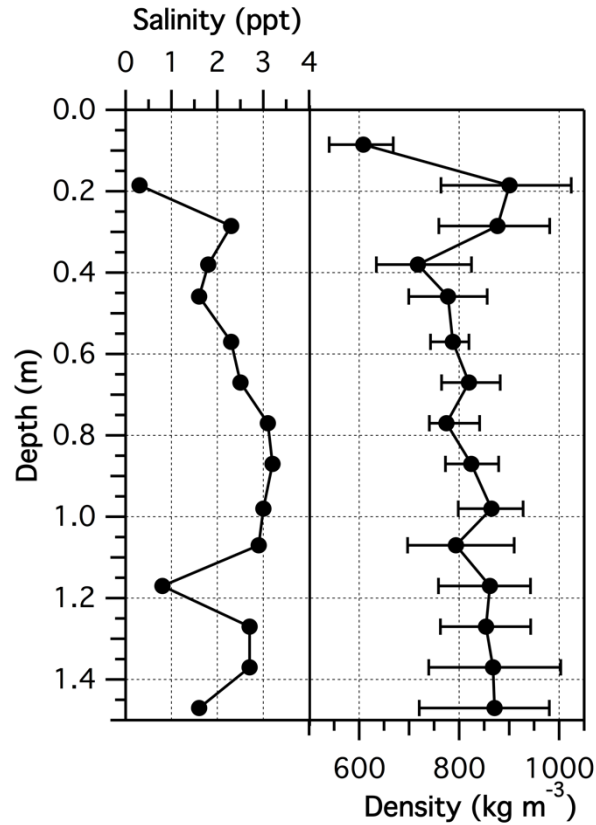


Figure 2.5: Example sea ice core salinity and density profile for sea ice at the end of summer melt self-collected in the central Arctic Ocean during RV Polarstern Cruise PS94. Error bars show minimum and maximum values of density estimated using mass/volume and liquid/solid volume ratio methods.

EM radiation incident upon a material can be reflected or scattered, absorbed, or transmitted. The dielectric permittivity and loss factors, ϵ' and ϵ'' , control the amount of energy that is transmitted through, absorbed by, or reflected from a medium and are dependent on the frequency of the interacting wave and the physical properties of the ice, e.g. the temperature, salinity, brine/air volume, brine salinity, and brine orientation. High dielectric loss (absorption) will result in weak or no signal from the medium and therefore also limits penetration of the signal through the layer. Sea ice is dielectrically lossy at most microwave frequencies.

The depth of penetration or transmission into a material indicates the maximum depth of the medium that contributes to the backscatter coefficient (Hallikainen and Winebrenner, 1992). Equation 1 provides for a first-order calculation of the penetration depth of EM radiation in a medium where λ_0 is the wavelength of the EM wave in vacuum, and ϵ' and ϵ'' are the dielectric permittivity and loss factors of the medium in question.

$$\delta_p = \frac{\lambda_0}{4\pi} \left\{ \frac{\epsilon'}{2} \left[\left(1 + \left(\frac{\epsilon''}{\epsilon'} \right)^2 \right)^{1/2} - 1 \right] \right\}^{-1/2} \quad \text{Eq. 2.1}$$

Penetration into sea ice at the Ku-band signal used by CryoSat-2 is limited due to the brine content but can also be reduced by the snow cover. Penetration depth curves for MYI, FYI, and dry and wet snow are presented in Figure 2.6 below using standard models for the FYI and MYI air bubble/brine channel shape, ice salinity, temperature and density (Shokr and Sinha, 2015).

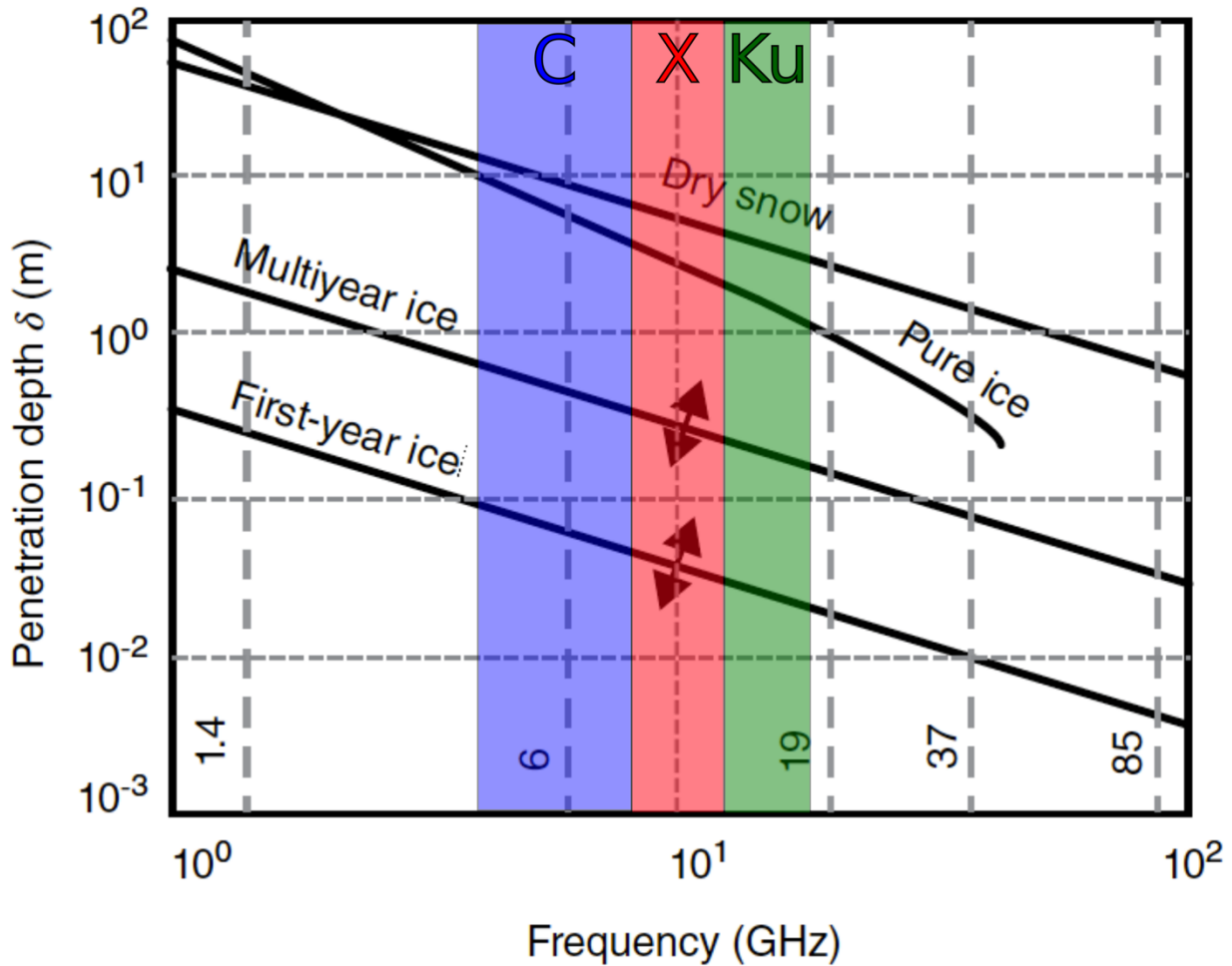


Figure 2.6: Penetration depth into sea ice at different frequencies for different ice types and snow showing the IEEE definitions of the C, X, and Ku-bands. Adapted with permission from Shokr and Sinha, 2015. Copyright American Geophysical Union 2015.

Figure 2.6 suggests that the Ku-band signal used by CryoSat-2 (13.65GHz) will not penetrate more than a few centimeters into FYI and not more than few tenths of a meter into multiyear ice. Ku-band signals can penetrate several meters into dry snow and freshwater ice. However, Eq. 1 is only valid for homogeneous media while the snow pack on sea ice and lake ice is normally composed of multiple layers. These layers will strongly influence scattering and thus the penetration of microwaves. Interestingly, some recent work has suggested that CryoSat-2 Ku-band signals can be strongly influenced by snow (Kwok and Haas, 2015, Kurtz et al. 2014, Price et al. 2015), and may not penetrate completely through snow (c.f. Ricker et al. 2015; Willatt et al. 2010, Willatt et al. 2011). Dielectric properties of the freshwater ice and snow are discussed in Chapter 2.2 and 2.3.

As with the dielectric properties, the thermal conductivity of sea ice is dependent on the mixture of the brine, air and ice, and therefore on the salinity and temperature of the ice (Pringle et al., 2007). The thermal conductivity of brine is approximately 25% that of pure ice. Additionally, as the temperature increases and the brine volume of the ice increases, the thermal conductivity decreases (Pringle et al. 2007). Changes in the thermal conductivity of the ice will influence properties such as ice growth, thermal modification of the snow, and the exchange of energy between the atmosphere and the ocean.

One simple way of estimating ice thickness is based on cumulative freezing degree days, the product of the cumulative number of days that air temperature is below the freezing point of ice and the difference in temperature of the air and the ice freezing point. Freezing degree days are usually related to ice thickness with a calibration factor that accounts for, among other things, the thermal conductivity of the ice and any overlying snow and the heat flux from the underlying water. Freezing degree days can provide a rapid, first-order estimate of ice thickness and can be used as a method for assessing satellite retrievals, a technique used in Chapter 6.

Sea ice thickness ranges from millimeters to tens of meters thick depending on age and state of deformation. Figure 2.7 presents an estimate of sea ice thickness and snow depth in the Arctic from the AWI CryoSat-2 sea ice thickness product. The thickness data are generated from isostatic equilibrium assumptions and measurements of sea ice freeboard, the height of the ice above water; these data and the method are discussed in further detail in Chapter 3. Figure 2.7 illustrates some of the main features of Arctic sea ice including: 1) regions with extensive compression and shear north the Canadian Arctic Archipelago (CAA), 2) land-fast ice within the CAA and the Laptev Sea where there are no thickness retrievals due to the lack of leads, 3) the Beaufort Gyre which can transport old ice that drifts along the northern boundary of the CAA to the Beaufort Sea and then along the Alaskan Coast and into the Canada Basin or into 4) the Trans-Polar Drift which exports ice from the Russian shelves and central Arctic to Fram Strait and also drives the compressive action along the northern coast of the CAA. Figure 2.7 shows that the estimated CryoSat-2 thickness ranges from 0 to over 5 m; the actual maximum is 17 m and the mean is 1.92 m. Figure 2.7 also presents snow depth from the modified Warren et al. (1999) climatology where the depth over FYI has been reduced by 50% over FYI; thus, the map also

illustrates the OSI-SAF sea ice type product used by AWI, where MYI is shown in oranges and FYI is purple shades. The snow depth map also shows the Beaufort Gyre (BG) and Trans-Polar Drift (TPD).

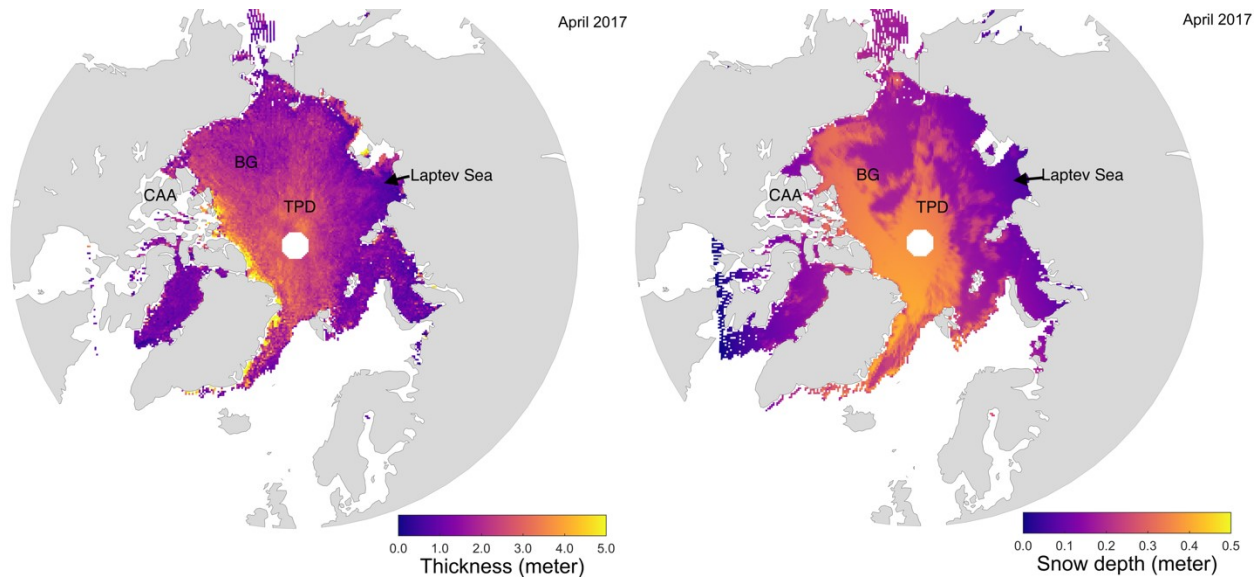


Figure 2.7: Arctic sea ice thickness and snow depth from CryoSat-2 and the modified Warren climatology for April 2017 as produced by AWI (Hendricks, 2015). Note the thin smooth ice in the Laptev Sea. The Beaufort Gyre (BG) is more visible in the snow depth map than the ice thickness map and the Trans-Polar Drift (TPD) can be seen in both the ice thickness and snow depth maps.

2.1.3. Importance of Sea Ice

Changes in the properties of Arctic sea ice such as thickness, areal extent, and mobility affect the biogeochemical and energy balance of the planet. Because ice floats and has strength, the ice cover decreases the exchange of water, energy, and gases between the atmosphere and ocean. Sea ice reflects sixty to eighty percent of incoming short-wave radiation while open water reflects just 10% or so. Arndt and Nicolaus (2014) found a 63% increase in the potential for bottom ice melt due to 1.5%/year increase in solar heat input through sea ice associated with the decrease in ice thickness and other ice property changes between 1979 and 2011. Furthermore, several studies have implicated decreasing ice extent with increased ocean melt and ocean heat content due to increased solar radiation input to the ocean (Steele et al. 2010, Perovich et al. 2008, 2011) and due to increased temperatures in the Arctic Ocean (Polyakov et al. 2017). Recent work by Francis et al. has implicated the role of sea ice extent changes in changes in the variability

in meander patterns and stability of the jet stream (Francis and Skific 2015). The flux of freshwater from the Arctic to deep-water formation sites in the Greenland and Labrador Seas could have important implications for the connected, temperature and salinity driven circulation of Earth's oceans (see e.g. Aagaard and Carmack, 1989, Morison et al. 2012 and references therein). Changes in ice type, roughness and ice thickness are linked (see Chapter 2.1.1), and strongly influence the strength of ice which will in turn influence maritime safety, and the linkages between sea ice, the ocean and the atmosphere.

Numerous studies have shown the link between sea-ice and atmospheric circulation patterns. Recent work implicates the loss of sea ice and Arctic warming with an increase in severe weather events and changes in the meander pattern of the jet stream at mid-latitudes (Walsh 2014; Francis and Skific, 2015). The loss of sea ice correlates with changes in the hydrology and airflow in the north-Central USA (Budikova et al. 2017). Work by Screen (2017) highlights the effects of regional ice loss on atmospheric circulation and how they differ from those of pan-Arctic loss. Sea ice also affects ocean circulation and water mass formation as salt and brine are rejected during freeze-up and cold fresh water is released during melt.

Accurate sea ice and snow data are essential to ensure accurate initial conditions and spin-up in sea ice models used for short term predictions and as a validation set for global climate and coupled ice-ocean models (Stroeve et al., 2007; Hunke, 2014). Limited sea ice thickness information, especially sub-grid cell resolution ice thickness distributions, has several times been highlighted as a major challenge in accurate sea ice modelling (Stroeve et al. 2007, Stroeve et al. 2012).

In addition to its role in Earth's climate, the loss of sea ice implies loss of habitat for ice-associated fauna such as polar bears, narwhals, and seals (de la Guardia et al., 2013; Hamilton et al., 2014); however, reduced ice extent may allow for the expansion of the habitat of other species of whales, fish, birds, phytoplankton (Hollowed et al., 2013, Lange et al., 2015, Lange et al., 2017). Recent work has shown that the primary productivity of sea ice may be greater and more important than previously assumed (Assmy et al. 2017; Pavlov et al., 2017; Arrigo et al., 2012; Arrigo et al., 2017; Hatam et al., 2016; Lange et al., 2015; Lange et al., 2017). Furthermore, several of these studies (Lange et al. 2015, 2017) show that the continued decrease in the extent

of MYI will have important implications for the primary productivity and entire food web of the Arctic Ocean.

Sea ice is also a primary factor of consideration for maritime operations in the Arctic as it poses a hazard to shipping, as exemplified by Kubat and Timco (2003), Mussells et al. (2017) and even by the recent cancelation of the ArcticNet BaySys research cruise which was severely delayed due to extensive multiyear ice export out of the Arctic Ocean through Nares Strait and Baffin Bay. Sea ice is also a hazard to resource extraction activities such of offshore oil and gas but can serve as a platform for hunting and travel. Changes in the presence and thickness of sea ice have socio-economic and geopolitical ramifications as many countries claim or desire access to the Arctic for: mineral and energy resources (Mussells et al., 2017), use as a trade route between Europe and Asia (e.g. Aksenov et al., 2017), tourism activities including the Crystal Serenity cruises through the Northwest Passage (Stephenson et al., 2013; Smith and Stephenson, 2013; Pizzolato et al., 2014; Pizzolato et al. 2016), and as a potential fishery (Hollowed et al., 2013).

2.1.4. Current State and Predictions

In the Antarctic, sea ice extent ranges from 2 to 20 million km²; most of the sea ice forms and melts each summer thus there are only small regions of multi-year ice (MYI). Although MYI is much more abundant in the Arctic than the Antarctic with the annual extent of sea ice ranging from 4 to 17 million km², the fraction of the ice covered by MYI has decreased rapidly since the 1980s (Maslanik et al., 2011; Tschudi et al., 2016; Figure 2.8). MYI is also not being fully replaced by seasonal, first year ice (FYI) growth, as the maximum extent of sea ice at the end of winter in March is decreasing at a rate of 2.7% per decade; the lowest March extent in the 38-year satellite record occurred in 2017 (NSIDC, 2017). The volume of Arctic sea ice has decreased by ~7700 km³/decade (Kwok and Cunningham, 2015) as September ice-extent has decreased by ~13 %/decade (Serreze and Stroeve, 2015) and mean Arctic ice thickness decreased by 0.08 – 0.2 m/decade between the late 1960s and 2009 (Kwok and Rothrock, 2009; Kwok and Cunningham, 2015; Figure 2.8). Since 2010/11, Cryosat-2 (CS2) ice thickness retrievals for 2011-2014 by Kwok and Cunningham (2015) and Tilling et al. (2015) indicate further decreases in volume but also show considerable inter-annual variability.

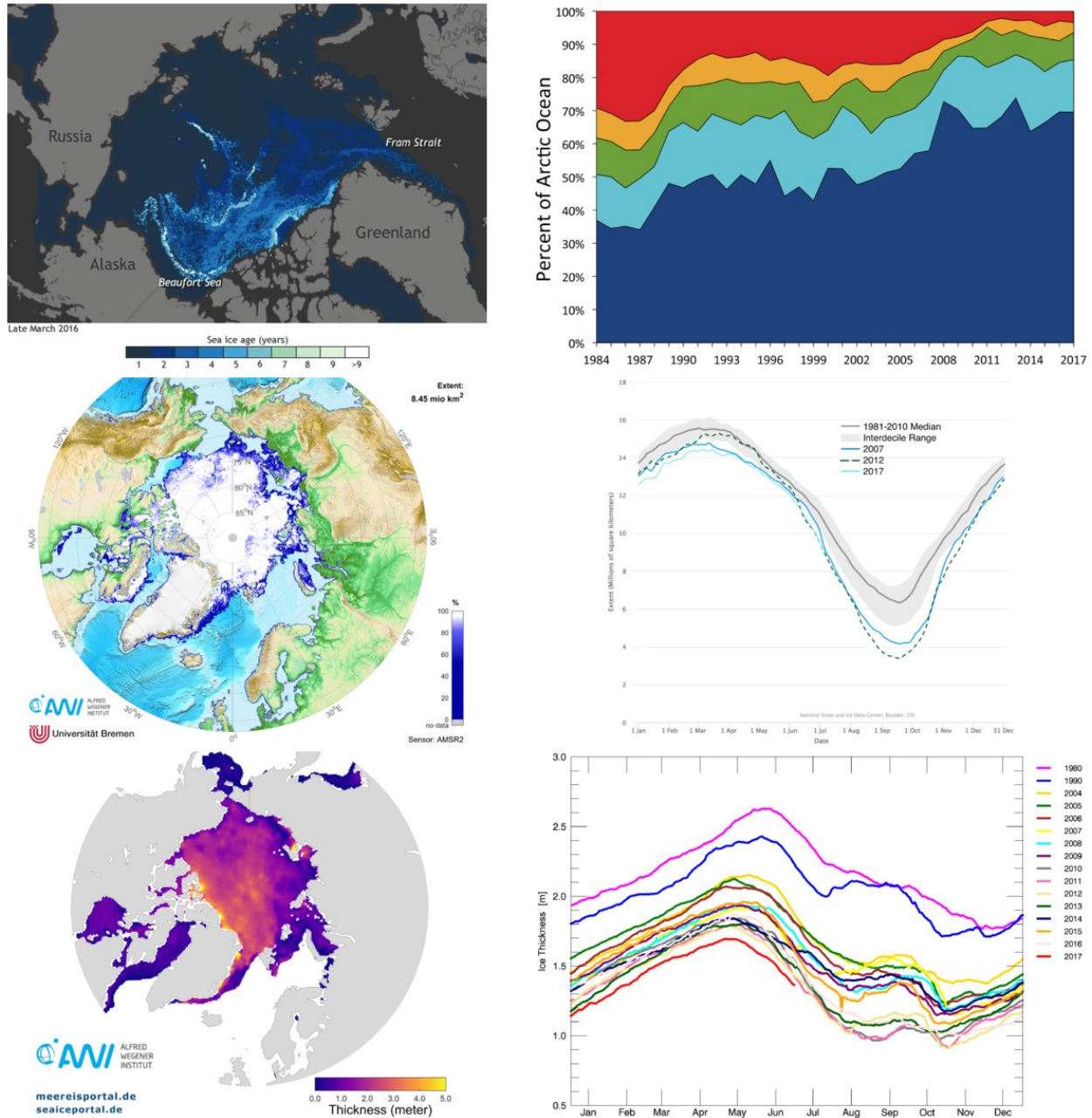


Figure 2.8: Maps (left) and time series (right) of sea ice age (top), sea ice extent (middle) and sea ice thickness (bottom). Sea ice age is a useful proxy for thickness as older ice is generally thicker.

Concurrently, the mean age of the ice has decreased (Maslanik et al., 2011; Tschudi et al., 2016; Figure 2.8) and ice drift has increased (Girard et al., 2009; Rampal et al., 2009; Spreen et al., 2011; Kwok et al. 2013); these changes have resulted in more open water and a thinner, weaker, and more mobile ice pack. Some studies have also found that deformation of sea ice, ridging and rafting, may be increasing with the observed increase in ice mobility and decrease in

thickness (i.e. Kwok and Cunningham, 2015). There has been increased lateral warming and melt from solar radiation input into open water in the marginal ice zone and in leads (Steele et al., 2010; Perovich et al., 2008; Perovich et al., 2011) and increased heat content in the ocean is now having as large an effect in winter as solar radiation in summer (Polyakov et al. 2017). Predictions of sea ice extent, thickness, and volume by ice-ocean models and global climate models using business as usual and increased CO₂ concentration forcing are variable but show continued decrease of sea ice volume over the next century (c. f. Jahn et al., 2011; Stroeve et al., 2012; Wang and Overland, 2012; Hu and Myers, 2014). Recent results continue to show that models fail to capture the full magnitude of thickness decrease in the Arctic (Wang et al., 2016). A recent study has also linked changes in sea ice in the Beaufort Sea to changes in lake ice in Alaska (Alexeev et al. 2016).

2.2. Freshwater Ice

Seasonally ice-covered lakes and rivers are common throughout the world, covering up to 2% of the world's land surface (Brown and Duguay, 2010). The ice cover controls the amount of evaporation and precipitation and the heat budget of the lake and influences the surrounding environment (Brown and Duguay, 2010, Rouse 2008). Accurate representations of river and lake ice extent, thickness and snow cover are critical to accurate weather climate model, and hydrological forecasts (Duguay et al. 2015). Lake ice cover duration has decreased over the past decades, a trend linked to increasing air temperatures and to large scale atmospheric patterns such as the AO (Brown and Duguay, 2010). In this section, we briefly review the growth and melt of lake ice, examine the relevant physical and dielectric properties of freshwater ice and highlight our current state of understanding of lake ice and the predictions for its future. For some properties and processes we compare lake ice to sea ice.

2.2.1. Growth

The primary differences between sea ice growth and freshwater ice growth in lakes are the result of the salinity difference. The temperature of maximum water density is reached at 4°C in freshwater allowing the surface water to stratify and cool more rapidly than in the ocean. Furthermore, the freshwater ice has no salt. The detailed formation of ice growth in freshwater lakes has been thoroughly presented in Michel and Ramseier (1971). Lake ice formation is

generally assumed to occur under more calm conditions than sea ice due to the relative rarity of swell and waves, as well as the lack of significant tidal motion; however, large lakes such as the Great Lakes in northern Canada can be subjected to significant wave action and can exhibit pancake ice formation and deformation as is observed for sea ice. More commonly, ice growth on lakes begins as a thin, smooth layer like nilas and is called skim ice (Brown and Duguay, 2010). Ice thickens similarly to the thermodynamic growth of sea ice (Michel and Ramseier, 1971).

Lake ice melt occurs similarly to sea ice through a combination of surface and bottom melt. Lateral melt can occur once the shoreline ice melts. Lake ice often melts from the edges inwards, as the shallow water along the shoreline can be warmed more rapidly and may interact with meltwater input from the surrounding land. Lake ice bottom melt can occur when ice thickness is sufficient to allow for the melt of the snow cover and allow for warming of the ice and the water below the ice to occur before the ice melts from the surface.

2.2.2. Physical and Dielectric Properties

Unlike sea ice, freshwater ice is considered to have low dielectric loss at microwave frequencies. While air bubbles can become trapped in lake ice and enhance scattering loss, recent work by Gunn et al. (2015) and Atwood et al. (2015) has shown that ice interface roughness is the primary mechanism for scattering. Bubbles at depth may act to enhance the apparent interface roughness, depending on the wavelength of the signal being studied.

Freshwater ice density has a small range as is also observed for sea ice below the water line. Freshwater ice density is typically taken to be 917 kg m^{-3} ; however, the density will decrease with increases in air bubble content.

The dielectric constant for freshwater ice is largely independent of frequency in the microwave range and is only weakly affected by ice temperature:

$$\varepsilon'_i = \begin{cases} 3.1884 + (9.1 \cdot 10^{-4}) \cdot T_i, & -30^\circ\text{C} < T_i \leq 0^\circ\text{C} \\ 3.1 & , T_i \leq -30^\circ\text{C} \end{cases} \quad \text{Eq. 2.2}$$

The dielectric loss is frequency and temperature dependent (Mätzler, 2006).

$$e''_i = \frac{\alpha}{f} + \beta f \quad \text{Eq. 2.3}$$

$$\alpha = \left(0.00504 + 0.0062 \cdot \left(\frac{300}{T} - 1 \right) \right) \cdot \exp \left(-22.1 \cdot \frac{300}{T} - 1 \right) \quad \text{Eq. 2.4}$$

$$\beta = \left(\frac{B_1}{T} \cdot \frac{\exp\left(\frac{b}{T}\right)}{\left(\exp\left(\frac{b}{T}\right) - 1\right)^2} + B_2 f^2 \right) + \left(\exp(-9.963 + 0.0372 \cdot (T - 273.16)) \right) \quad \text{Eq. 2.5}$$

where f is the frequency in GHz, T is the temperature in Kelvin, $b = 335\text{K}$, $B_1 = 0.0207 \text{ KGHz}^{-1}$, $B_2 = 1.16 \cdot 10^{-11} \text{ GHz}^{-3}$.

Using the equations of Mätzler (2006) for the dielectric constant and loss for pure ice above, and Eq. 2.1 to calculate the penetration depth (Chapter 2.1.2), one finds that the penetration depth through freshwater ice for the 13.65 GHz signal used by CryoSat-2 is more than 4 m at 0 °C and 8 m at -30 °C; these penetration depths may be reduced in the presence of air bubbles and snow cover as energy is lost through scattering. The presence of wet snow or roughness at the ice top or bottom surfaces can also reduce penetration through absorption or scattering (Howell et al., 2009; Gunn et al, 2015; Atwood et al., 2015).

The thermal conductivity of freshwater ice is greater than that of sea ice due to the lack of brine pockets. The thermal conductivity of freshwater ice will be reduced by density variations caused by air bubbles as air bubbles are poor thermal conductors.

Snow on freshwater lakes is similar to snow on sea ice but may begin to accumulate earlier as lake ice freeze up occurs more rapidly as only the surface water must be cooled. Additionally, unlike snow on sea ice, snow on freshwater lakes will never contain salt or brine. Like the ocean, lakes and rivers provide a large source of heat that results in rapid metamorphism of snow grains. Snow depth on lake ice is highly dependent on the surrounding environment and on wind redistribution and the conversion of snow to snow-ice. Modelling work by Brown and Duguay (2011) suggests that predicted increases in snow precipitation result in increased snow-ice formation which offsets the increased insulation effect that deeper snow would have on lake ice growth rates.

2.2.3. Importance

Freshwater lakes and rivers influence the surrounding environment through the release of moisture, heat and by reflecting more solar radiation than the surrounding land in late spring when lakes remain partly or fully ice covered and the snow on land has melted. The high evaporation rates from lakes can result in down-wind precipitation or fog (lake-effect fog and

snow), and can moderate the local climate (Brown and Duguay, 2010). The winter ice cover on lakes limits the exchange of gases with the atmosphere which are then released upon melt (Brown and Duguay, 2010). As northern lakes often overlies permafrost, warming lakes and permafrost may result in an increase in carbon dioxide and methane emissions from northern lakes (Brown and Duguay 2010). Jeffries and Morris (2006) have also shown that conductive heat fluxes through the ice cover of large lakes may be more important than previously thought. Besides modifying the local and regional climate, lakes and rivers are important sources of freshwater, fish and are widely used for hydroelectric power generation. Furthermore, ice roads on lakes and rivers are vital to travel between communities and for resource extraction activities in Canada's north.

2.2.4. Current State and Predictions

Since the 1980s there has been a strong decline in direct measurements of lake ice and snow in Canada and around the world even as changes in lake ice and snow have been recognized as sensitive indicators of climate changes (Duguay et al., 2015). Lake ice cover duration, freeze onset and melt onset have been closely linked to air temperature in the prior weeks to months (Duguay et al. 2006, Kouraev et al. 2007). A review by Prowse et al. (2011) found that the average ice duration in the Northern hemisphere has already decreased by ~17 days per century and that this rate is even larger for high-latitude lakes in Northern Canada. The review by Brown and Duguay (2010) also provides ample evidence for the linkage between lake ice and large scale atmospheric pattern indices such as the North Atlantic Oscillation (NAO), Pacific Decadal Oscillation (PDO), and the Pacific/North America Pattern (PNA) but also highlights the interactions and moderations of multiple indices. Recently, Brown and Duguay (2011) modelled predicted changes in lake ice phenology of North American Arctic lakes for 2041-2070 in comparison to measurements and modelled results from 1961-1990. Their results suggest continued delays in freeze up of 0 - 15 days and earlier ice break up of 10-25 days. Their results also showed that ice duration may be more strongly reduced over large deep lakes and in coastal regions than in the continental interior of Canada to variations in the amount and timing of warming and snow depth changes.

As direct measurements of lake ice and snow in Canada have decreased there has been an increase in satellite observations of lake ice and its phenology. Howell et al. (2009) developed a method to retrieve ice phenology information from the QuikScat Ku-band scatterometer data over Great Slave and Great Bear Lakes and found that the ice cover duration on Great Bear Lake can be 3 to 5 weeks longer than on Great Slave Lake. More recently, Kang et al. (2012) have shown that 18 GHz microwave data from AMSR-E are sensitive to ice phenology and found similar differences in ice cover duration between the two northern Great Lakes as Howell et al. (2009). Du et al. (2017) showed a decrease in ice cover duration in the Northern hemisphere between 2002 and 2015 using AMSR/AMSR-E. These results agree with the findings of Surdu et al. (2016) who also showed shorter ice cover duration for high latitude lakes in Canada from SAR image analysis. Surdu et al. (2016) also showed that some perennially covered lakes in the Canadian Arctic Archipelago may be transitioning to a seasonal ice cover.

Finally, along with changes in ice cover duration, the modelled results of Brown and Duguay (2011) suggest that ice thickness will decrease between 0.05 and 0.6 m and that an increase in the contribution of snow-ice to the total ice thickness can be expected as snow depth increases were also predicted. The increased melt associated with higher temperatures, and the decrease in ice growth associated with thicker snow cover is compensated by the conversion of snow to snow-ice as the deeper snow would result in negative freeboards and flooding of the lake ice surface.

Unfortunately, lakes are rarely monitored for snow and ice thickness and until recently satellite-based estimates of lake ice thickness were not possible. Kang et al. (2010) first showed that AMSR-E data are strongly correlated with ice thickness change on the northern Great Lakes; Kang et al. (2014) found similar results. The first retrievals of lake ice thickness from radar altimeter data are presented in Chapter 6 (Beckers et al., 2017). However, the AMSR-E and CryoSat-2 thickness results are influenced by the snow overlying the lake ice. Snow is difficult to measure remotely, has high spatial and temporal variability and a strong impact on remote sensing measurements of both sea ice and lake ice.

2.3. Snow

Over the past few years our limited knowledge of snow has emerged as a critical knowledge gap in terms of its role in climate dynamics and its influence on the retrieval of remotely sensed sea and lake ice thickness and sea ice freeboard estimates from e.g. laser and radar altimeters. Snow is also critical to hydrological forecasts of ground water recharge and lake and river discharge. Snow strongly modifies the exchange of energy between the atmosphere and underlying media (lake ice and water, sea ice and ocean, land). The thickness of the snow cover on ice also has important implications for the activity of primary producers that drive the entire marine food web as it strongly modifies the availability of light under the ice (Lange et al., 2015; 2017; Assmy et al., 2017).

As sea and lake ice are usually at least partly covered by snow, signals from satellite and airborne sensors of the ice first interact with the snow and are thus influenced by the snow. As indicated above, the snow also modifies the underlying ice and water below. As this thesis is solely focused on sea and lake ice, the discussion of the properties of snow, its importance, and the current state and predictions for the future are all presented in the context of lake and sea ice; the properties and role of snow cover on land and glaciers are not discussed.

2.3.1. Physical and Dielectric Properties

The physical properties of the snow: depth, density, grain size and structure, influence the thermal and dielectric properties of the snow. Snow depth on sea and lake ice varies in space and time at multiple scales. Snow depth on lake ice depends strongly on the surrounding environment as seasonally ice-covered lakes can be found in regions with highly varying precipitation regimes, including polar deserts, polar oases, mountainous regions as well as the sub-Arctic tundra and plains. In Canada, several Arctic and sub-Arctic lakes are monitored for snow depth and ice thickness as part of the Canadian Ice Service Ice Thickness Program; however, these measurements reflect just a single location. Snow depth on lake ice is only very sparsely measured, both temporally and spatially, but is critical to remote sensing measurements of i.e. ice thickness.

Snow depth measurements on Arctic sea ice have a long history, having been measured in-situ at Russian drifting ice-stations across the Arctic since the 1960s (Warren et al. 1999). These

measurements were still fairly sparse but form the basis for the Warren et al. (1999) snow depth climatology. There have also been numerous other field campaigns in the Arctic such as CryoVEx, CASIMBO, the AWI RV PolarStern and NPI RV Lance cruises, among others, during which snow depth data were collected (e.g. Figure 2.9), however these have never been systematically combined and analyzed. Figure 2.9 presents the snow depth data collected by author as part of the Canadian Arctic Sea Ice Mass Balance Observatory measurements including during this PhD thesis over FYI and MYI in the Beaufort Sea, within the Canadian Archipelago and in the Lincoln Sea between 2010 and 2014. Median FYI snow depth and the inter-quartile-range (IQR) is less than over MYI. In 1998 Markus and Cavalieri presented an algorithm to retrieve snow depth from SSM/I passive microwave data over Antarctic sea ice. In 2003, the algorithm was adapted to AMSR-E and for use in the Arctic but only over FYI as MYI has a similar signature to snow at the 19 and 37 GHz channels used. The AMSR-E/2 snow depth data over FYI has not seen widespread use in altimetric studies of sea ice. Besides being affected by snow grain size (Comiso et al. 2003), it is also strongly influenced by surface roughness (Stroeve et al. 2006).

More recently snow depth data has been retrieved by airborne snow depth radar by NASA's Operation IceBridge since 2009. Webster et al. (2014) found that the OIB snow depth retrievals over FYI were nearly half of that found in the Warren et al. (1999) climatology, although there have been some questions about the accuracy of the snow depth retrievals over MYI (King et al. 2015, Kwok and Haas 2015). Kwok et al. (2017) compared the five main NSIDC OIB snow depth retrieval algorithms which shows that several algorithms consistently underestimate snow depth and that all algorithms are sensitive to surface roughness as suggested by King et al. (2015). The OIB snow depth retrievals are often used as validation data for other remote sensing estimates of snow depth such as those from SMOS (Maas et al., 2013) and Altika (Armitage and Ridout, 2015; Guerreiro et al., 2016).

Retrievals of snow depth using the Soil Moisture and Ocean Salinity L-band radiometer were made over thick multiyear ice by Maas et al. (2013). While comparisons with NASA OIB data suggested that the SMOS retrievals are reasonable over thick MYI and for snow depths up to 0.35m, the uncertainty in the validity of OIB snow depth retrievals over MYI needs to be considered.

Finally, estimates of snow depth over Arctic sea ice have also been generated using a combination of Ku- and Ka-band radar altimeter data from CryoSat-2 and AltiKa by Guerreiro et al. (2016). Their work builds upon observations by Armitage and Ridout (2015) and Maheshwari et al. (2015) who found some agreement between the difference in CryoSat-2 and AltiKa freeboards and AltiKa and NASA OIB ice freeboards and the expected range of snow depths for Arctic sea ice. The results of Guerreiro et al. (2016) also used the NASA OIB data as validation data and found that the average snow depth on FYI and MYI was lower than the Warren et al. (1999) climatology by $63 - 75\% \pm 20\%$ and $32 - 57\% \pm 8\%$, respectively. However, all three studies make different assumptions about penetration of the Ka-band signal with Armitage and Ridout (2015) finding that the Ka-band penetrates 45% of the snow, Maheshwari et al. (2015), assuming that it penetrates the complete snowpack, and Guerreiro et al. (2016) assuming that it does not penetrate the snowpack.

All the studies agree that snow depth on FYI is typically less than over MYI, simply because snow fall early in the season can land on MYI when FYI has not yet formed. Furthermore, the rough topography of MYI results in wind driven redistribution and accumulation. Clearly additional studies into Ka-band penetration are required before dual frequency altimetric retrievals of snow depth can be considered accurate. However, altimeter retrievals of snow depth are, like passive microwave retrievals, dependent on snow density and grain size and possibly surface roughness. Despite the uncertainty as to the validity of the OIB snow depth data and the use of the Warren climatology, these two products are the most widely used in altimetric studies of sea ice with the OIB data being used to adjust the Warren climatological snow depth; the climatological snow density remains unmodified.

Snow density plays an important role in the thermal and dielectric properties of the snow pack. The density of snow ranges from around 100 kg m^{-3} for freshly fallen snow in calm conditions to more than 450 kg m^{-3} for slabs of wind compressed snow (Sturm et al. 2002a, Figure 2.10). Constructive metamorphism of the snow grains into larger grains called depth hoar occurs due to the steep thermal gradient between the cold atmosphere and the warm ocean and lake water and ice below the snow pack (Sturm et al. 2002).

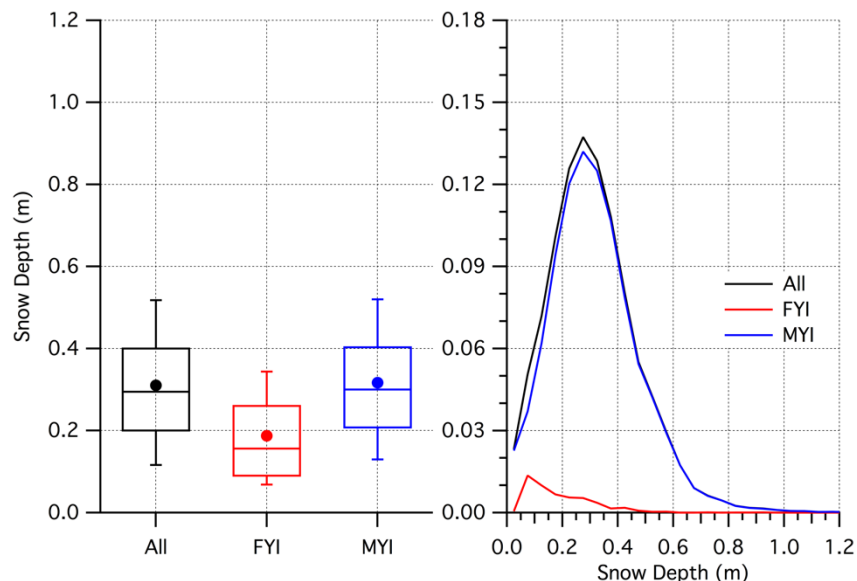


Figure 2.9: Boxplots (quartiles, with deciles as whiskers) and histograms of 21000 snow depth measurements from the Lincoln Sea and Beaufort Sea self-collected between 2010 and 2014 during CASIMBO and CryoVEx field campaigns.

The snow pack on sea ice and lake ice can generally be divided into just two layers, depth hoar and wind slab which forms from wind redistribution and snow deposition under windy conditions (Sturm et al. 2002). Other possible features of snow packs on Arctic include ice lenses from either early season liquid precipitation or melt and refreeze events, new snow, or saline snow. Saline snow typically occurs over first year ice when brine rejected from the sea ice is wicked upwards into the snow pack (Barber et al. 1995). The density of the snow and presence of saline snow impact the dielectric properties of the snow and therefore affect radar altimeter measurements of sea and lake ice. Dense layers such as ice lenses may limit penetration and cause strong scattering from above the snow/ice interface. Snow volume scattering can affect identification of the snow/ice surface returns in radar altimeter measurements of sea and lake ice. Saline snow will also limit penetration through the snow and can cause scattering from the upper saline snow boundary and thereby bias radar altimeter measurements of the snow/ice interface.

Snow density and grain size are linked through metamorphism. Small snow grains are transformed into large grains through a series of temperature-drive metamorphic steps through moisture transfer and processes such as sintering. Small grains, <2mm, deposited under windy conditions or that have experienced wind redistribution can be transformed into larger, 2 – 15

mm grains. Large depth hoar grains are formed from metamorphism of smaller grains and thus represent a decrease in density as the air/void space between grains must increase (Figure 2.10). Grain size plays an important role in microwave remote sensing as large depth hoar can be similar in size to the radar wavelength and thus act as a rough scattering surface or as a source for volume scatter. The density and grain size also strongly influence the thermal conductivity of the snow, with denser layers composed of smaller grains having a higher thermal conductivity than large grained less dense layers such as depth hoar. The thermal conductivity of snow is about 10% to 30% that of sea or lake ice (Sturm et al. 2002, Shokr and Sinha, 2015). Measurements from snow pit data, like those from the 2017 CryoVEx experiments presented in Figure 2.10, including density samples and a snow micro-penetrometer are providing new high vertical-resolution insights to the interaction of radar waves with snow over sea ice.

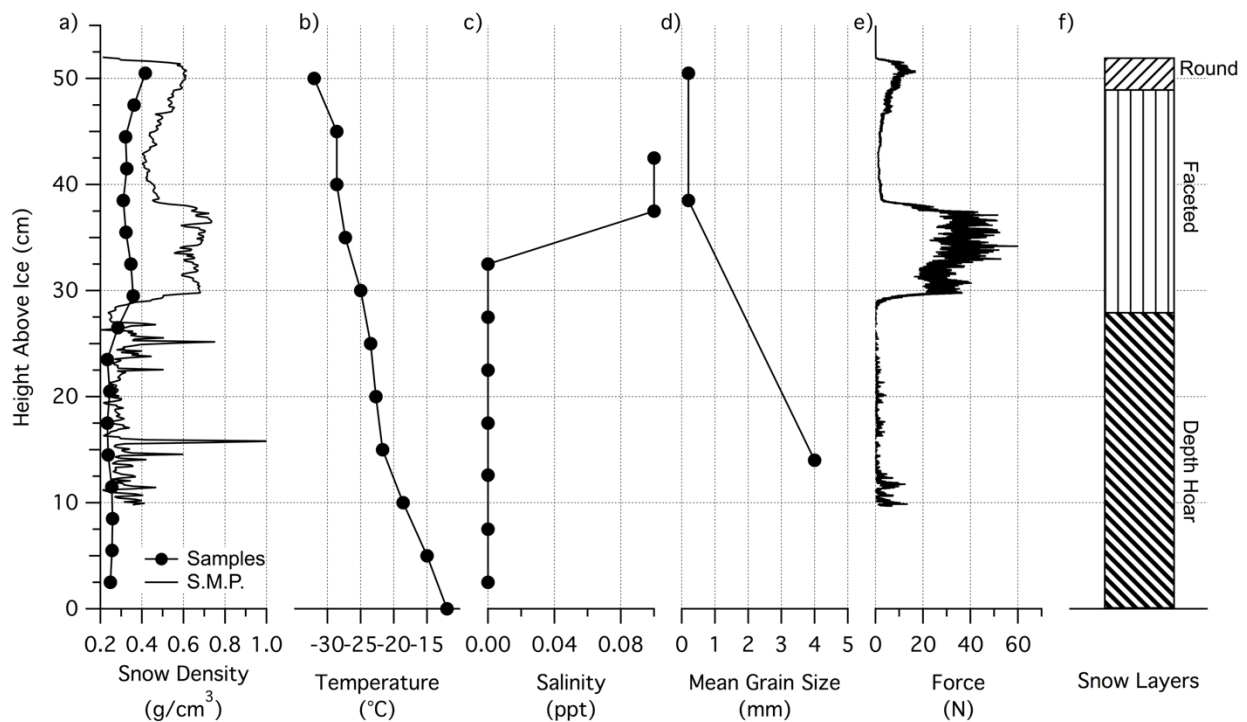


Figure 2.10: Example snow pit profile from CryoVEx 2017 showing snow density where S.M.P. is Snow Micro-penetrometer estimate of snow density based on force needed to push sensor through the snow and Samples is from a 100 cc sample of snow (a), temperature (b), salinity (c), grain size (d) and the snow pack layers (f) from the Arctic Ocean in April 2017. S.M.P. Force is presented in (e).

Finally, the dielectric properties of the snow ultimately control the interaction of EM radiation with the snowpack and determine if the signal penetrates and how far and whether or not there is significant volume scatter or surface scattering. For dry snow with a density of less than 500 kgm⁻³, the dielectric permittivity is:

$$\varepsilon'_{ds} = 1 + 1.9\rho_{ds} \quad \text{Eq. 2.6}$$

where ρ_{ds} is the snow density in gcm⁻³ (Hallikainen et al., 1986). The dielectric loss factor for dry snow is related to the density of the snow through the ice volume fraction of the snow according to the review performed by Hallikainen and Winebrenner (1992):

$$\varepsilon''_{ds} = \frac{0.34V_i\varepsilon''_i}{(1-0.417\cdot V_i)^2} \quad \text{Eq. 2.7}$$

$$V_i = \frac{\rho_{ds}}{0.916}. \quad \text{Eq. 2.8}$$

Wet snow is essentially a mixture of air, ice and water. The dielectric permittivity and loss factors for wet snow can be represented by the semi-empirical model of Hallikainen et al. (1986):

$$\varepsilon'_{ws} = A + \frac{Bm_v^x}{1+(f/f_0)^2} \quad \text{Eq. 2.9}$$

$$\varepsilon''_{ws} = \frac{C(f/f_0)m_v^x}{1+(f/f_0)^2} \quad \text{Eq. 2.10}$$

where f is the frequency in GHz, f_0 is 9.07 GHz, m_v is the liquid water content and x is 1.31. A , B , C are determined using the following equations:

$$A = 1.0 + 1.83\rho_{ds} + 0.02A_1m_v^{1.015} + B_1 \quad \text{Eq. 2.11}$$

$$B = 0.073A_1 \quad \text{Eq. 2.12}$$

$$C = 0.073A_2, \quad \text{Eq. 2.13}$$

where if $f < 15$ GHz, $A_1=A_2 = 1.0$ and $B_1 = 0$, else:

$$A_1 = 0.78 + 0.03f - 0.58 \times 10^{-3}f^2 \quad \text{Eq. 2.14}$$

$$A_2 = 0.97 - 0.39f \times 10^{-2} + 0.39 \times 10^{-3}f^2 \quad \text{Eq. 2.15}$$

$$B_1 = 0.31 - 0.05f + 0.87 \times 10^{-3}f^2. \quad \text{Eq. 2.16}$$

Because the dielectric permittivity of water is nearly 40 times that of dry snow, even small amounts of liquid water within the snow (i.e. 1%) will limit penetration through the snow to less than 0.15 m at Ku-band (Hallikainen et al. 1986, Howell et al. 2009). Using equations 2.1 – 2.16, Figure 2.11 shows the rapid decrease in penetration depth with increasing volumetric

water content and with increasing frequency (decreasing wavelengths) and decreasing snow density for different radar bands and snow densities.

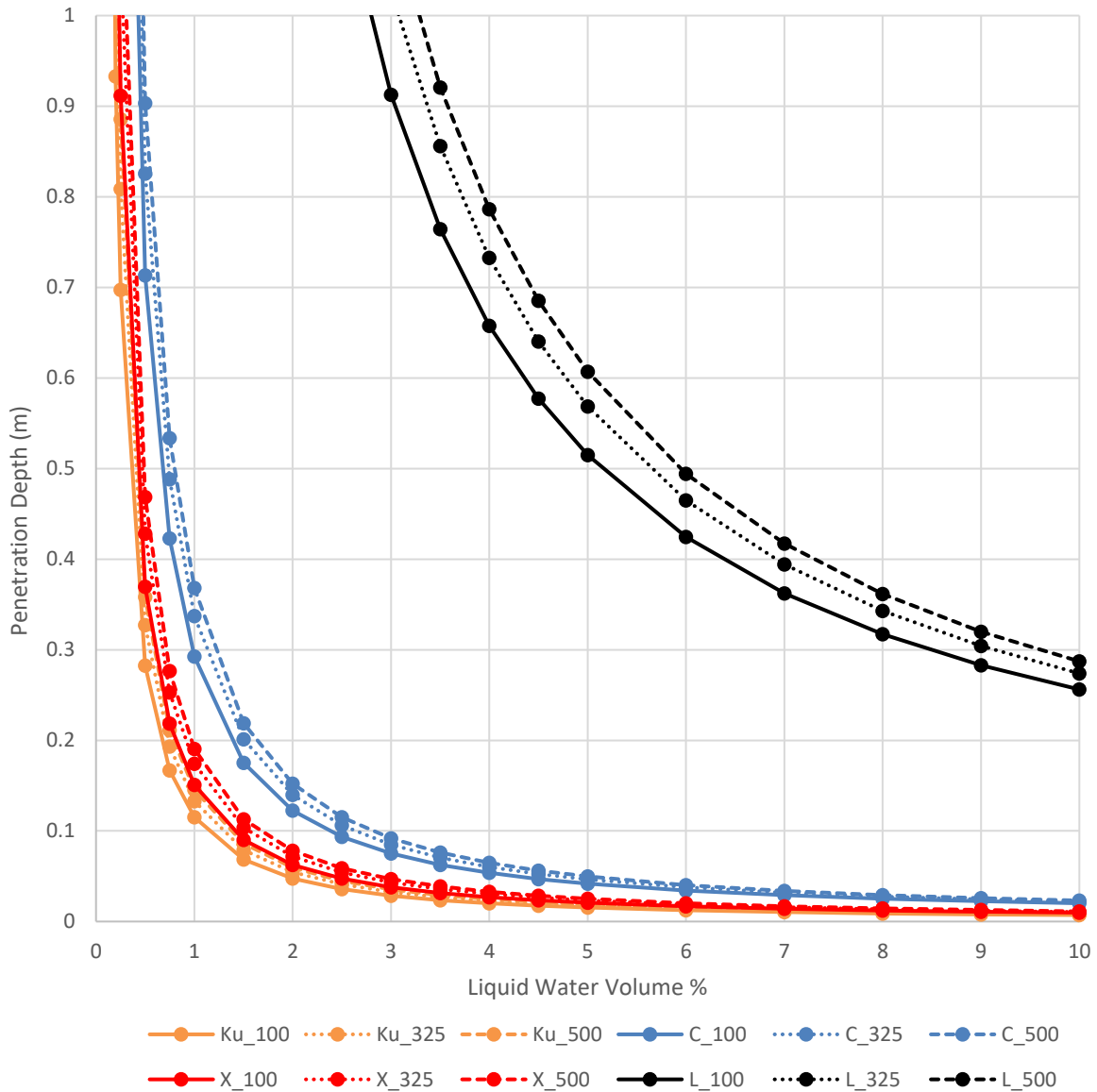


Figure 2.11: Approximate maximum penetration depth for L- (ALOS PALSAR), C- (Envisat ASAR and RadarSat), X- (TerraSAR-X) and Ku- (CryoSat-2) band radar waves for snow densities of 100 kgm^{-3} , 325 kgm^{-3} and 500 kgm^{-3} .

2.3.2. Importance

Ice is strongly modified by its snow cover, the high albedo and low thermal conductivity of snow (Perovich et al., 2008; Perovich and Richter-Menge, 2015; Sturm et al., 2002) reduces the flow of energy between the atmosphere and lake/ocean/ground, decreasing ice growth and melt

rates. As snow lies over the ice, it is the first layer of interaction for remote sensing applications of ice. Furthermore, snow modifies the physical properties of ice currently utilized by many remote sensing methods to estimate ice properties such as type or thickness. Snow is redistributed over the rough ice surface and can act to smooth the surface to any sensor that cannot penetrate the snow (i.e. lidar). The weight of the snow on sea ice reduces ice freeboard and can cause flooding and snow ice formation. In addition, brine can be wicked up into the snow and cause high dielectric loss from within the snow pack instead of at the ice surface. For some sensors, snow can cause a significant and detectable volume scattering that is either indistinguishable from the ice surface or reduces certainty (e.g. in radar altimetry). Although several studies have recently presented ice thickness results, uncertainties remain in their validation and calibration due to these and other errors as is discussed in Chapter 3.

Besides its influence on the physical properties and remote sensing of ice, snow has important consequences for primary productivity in the Arctic Ocean as it strongly attenuates the light that could otherwise pass through the ice (Lange et al. 2015, Lange et al. 2017). Work by Lange et al. (2017) shows that the thin snow cover on MYI hummocks allows for more light and under ice primary production than previously assumed. Clearly, current and continued changes in snow cover duration and depth will have important climatic and biological consequences.

2.3.3. Current State and Predictions

Concurrent with changes in sea and lake ice properties are decreases in depth of snow on sea ice and increases in melt season duration. A recent study of NASA OIB snow depth data concluded that snow depth on Arctic sea ice has decreased by 37% to 56% since the early 1990s (Webster et al., 2014). It should be noted that several studies have called into question the accuracy of some of the data over MYI that was used in Webster et al. (2014); however, the largest decrease in mean snow depth was observed over FYI, not MYI. These studies (Kwok and Haas, 2015; King et al., 2015) suggest that the NASA OIB data used in Webster et al. (2014) may not provide accurate measurements of snow depth, especially over multi-year ice, due to e.g. side-lobes in the snow radar being mistaken for the air-snow interface and more. Furthermore, while 2013 and 2014 were lower melt years (as measured over sea ice using melting-degree-days; Tilling et al., 2015), the general trend in melt season duration is an increasing trend; e.g. Howell et al.

(2009) noted an increase in melt season duration between 1979 and 2008 of +7%/decade within the CAA. Derksen et al. (2015) showed that snow cover in the Arctic is melting earlier in spring and has a delayed onset in fall resulting in a 3-5 day per decade decrease in snow cover duration. Furthermore, Brutel-Vuilmet et al. (2013) showed that CMIP5 models underestimate the observed reduction in spring snow cover over the satellite record and underestimate the relationship between air temperature and spring snow cover extent. A review by Bokhorst et al. (2016) found that CMIP5 models diverged most during the snow melt period (c.f. Fletcher et al. 2015) and reiterated the findings of Duguay et al. (2015) that snow and lake-ice remain underrepresented in the literature.

2.4. Summary

The current changes in sea ice, lake ice and snow properties such as thickness, extent or duration are well documented and predicted to show continued changes as earth's climate responds to warming and Arctic amplification. Many of the physical and dielectric properties of snow, freshwater and sea ice have large spatial and temporal variability at scales relevant to remote sensing and climate modelling. This chapter has reviewed the major properties of snow and ice that are relevant to their measurement by laser and radar altimeters and other remote sensing methods such as synthetic aperture radar and passive microwave imaging. Chapter 3 presents the method and uncertainties associated with altimeter measurements of snow, sea ice and lake ice and reiterates and discusses their influence on the certainty of the retrievals.

3. Altimeter Measurements of Sea Ice, Lake Ice, and Snow

Altimeter measurements of snow and ice have become more common over the past decade as the technology has matured. Airborne platforms such as helicopters, airplanes and more recently, unmanned airborne vehicles (UAVs) are widely used to scale between ground and satellite measurements by acquiring data over larger areas than typical in-situ surveys. Satellite based altimetry over Arctic sea ice also has a long lineage, dating from the early 1970s with Skylab. Satellite altimetry data of the Arctic has only been available since the early 1990s with ERS-1, though the first sea ice measurements of freeboard/thickness were only published in 2003 by Seymour Laxon (Laxon et al., 2003). In this chapter laser and radar altimetry are briefly described along with a brief review of the history of each sensor over sea ice and lake ice. The processing methodologies for laser and radar altimetry retrievals of sea ice freeboard and ice thickness and lake ice thickness are also described along with a discussion of the uncertainties in each of the processing steps.

3.1. Types of Altimeters

3.1.1. Laser Altimeters

LIDAR (Light Detection and Ranging) sensors typically use near-infrared or green wavelength light to measure the distance or range between the sensor and surface using the two-way travel time between transmission of the signal and reception of the signal reflected back from the surface. Scanning altimeters utilize a moving beam or mirror to direct the collocated light beam from the sensor across the surface. Single beam altimeters do not use a mirror to move the beam across the footprint and thus record a single point below the sensor. In traditional LIDAR systems, the laser pulse is emitted and the sensor then waits a predetermined amount of time to detect the return before firing the next laser pulse. Most LIDAR systems do not store the returned energy as a function of time but simply detect the returned signal and keep track of the time of flight, and the power of the returned signal. New laser sensors such as photon counting and waveform-storing laser altimeters allow for retrievals from multiple surfaces and are able to keep track of multiple “in the air” pulses. These new sensors are providing higher spatial density than existing technologies; sensors with pulse rates of 1 - 2 MHz are now readily available.

Laser altimetry over sea ice started in the mid-1960s when Rempel and Parker (1964) described a gas-laser system for airborne profiling of micro-relief. In 1971, Robert Ketchum described the first laser altimeter measurements over an Arctic ice island and sea ice using a differential barometer to measure the aircraft's altitude; both the laser range and the signal intensity were recorded and compared to photographs of the ice island and used to determine the mean thickness of the ice island (Ketchum, 1971). Hibler (1972a) proposed a method of removing aircraft altitude variations from the laser altimeter data using high and low pass filters, a method which is still used today (e.g. von Saldern et al., 2006; Fors et al., 2016). Around this time, numerous studies of sea ice surface roughness and ridge morphology were performed by e.g. Hibler and others (1972b, 1972c), and others, e.g. Wadhams et al., 1992 and references therein. In 1976, the first joint airborne laser and submarine measurements of sea ice freeboard and draft were performed (e.g. Lowry and Wadhams, 1979). Airborne laser scanner systems were developed in the late-1970s, e.g. NASA's Airborne Oceanographic Lidar system. However, most studies in the 1980s continued to use single beam laser altimeters, or did not utilize the 2D nature of the laser scanner swath (e.g. Wadhams et al., 1992). Most studies of laser altimeter and swath data focused on sea ice topography or relative elevation or roughness measurements until Forsberg et al. (2001) provided the first examples of laser scanner swath freeboard data. Part of the reason for the delay in using the 2D swath of scanners may be the limitations in recording the attitude of the sensor, information needed to process the swath data. Following the launch of ICESAT carrying the Geoscience Laser Altimeter System (GLAS), the first satellite laser altimeter, numerous studies provided estimates of Arctic sea ice freeboard (e.g. Kwok et al., 2004; Forsberg and Skourup, 2005; Kwok et al., 2006; Kwok and Cunningham, 2008; Kurtz et al. 2011) based on work performed by the radar altimetry community just a few years prior. Even though the GLAS laser sensors stopped operating in 2009, studies of ICESAT data continue to this day (e.g. Khvorostovsky and Rampal, 2016). Before the loss of ICESAT, NASA launched Operation IceBridge (OIB), a large airborne campaign to bridge the gap between ICESAT and the already discussed follow-on mission, ICESAT-2. OIB uses the next generation of the Airborne Oceanographic Lidar system, called the Airborne Topographic Mapper (ATM). ATM measurements had been made since the 1990s over glaciers (Krabill et al. 1995, 2002) but was

not used over sea ice; the first OIB measurements occurred in 2009 and featured both land ice and sea ice missions. OIB has provided fundamental monitoring of Arctic sea ice and is easily the largest Arctic airborne measurement campaign of all time. Data from OIB have provided new insights into sea ice topography (e.g. Petty et al., 2016, 2017), the ice thickness and age relationship (Tschudi et al., 2016), ice freeboard (e.g. Farrell et al. 2012) and have been used as validation and calibration data for the European Space Agency's CryoSat-2 radar altimeter (e.g. Chapters 7, 8, and 9; Kwok et al. 2015). With a planned launch of 2018, ICESAT-2 will use a modern photon-counting laser system to provide enhanced spatial resolution and measurement density in comparison to ICESAT (Abdalati et al., 2010).

Two sets of airborne laser scanner sensors are used in this study, Riegl laser scanners and the NASA OIB ATM. The Riegl scanners use a rotating mirror to sweep a near-infrared laser beam across the 60 or 80° field of view at up to 50 to 150 Hz (i.e. the scan rate). The Riegl scanners used have a pulse rate, i.e. the number of individual laser measurements, of 10 kHz to 100 kHz. The NASA OIB ATM is a conical laser scanner that conically rotates a green laser to produce overlapping ellipses of laser measurements on the ground as the NASA OIB aircraft moves forward. The ATM has a pulse rate of 5 kHz, a scan rate of 20 Hz and a nominal scan width of 22.5° (Martin et al., 2012).

Airborne altimetry normally requires additional data from GPS and inertial measurement units (IMU) in order to determine and account for changes in the position and attitude (yaw, pitch and roll) of the sensor as the aircraft moves. The processing of this data is non-trivial and often requires special surveys of well-known targets, such as runway passes, or passes over buildings. Chapter 5 presents airborne scanning laser altimeter data over sea ice that were collected without an IMU and thus would normally be discarded; however, we use the theoretical flat-surface response of the altimeter to estimate roll and thus correct the laser altimeter data and provide measurements of sea ice relative elevation and surface roughness (Beckers et al., 2015).

3.1.2. RADAR Altimeters

Like LIDAR, Radio Detection and Ranging (RADAR) sensors measure the distance between the sensor and target using the time of flight of an emitted pulse of electromagnetic waves at radar

frequencies, typically Ku-band (13 GHz). Radar altimetry can trace its roots back to the 1970s with satellite sensors on board Skylab and numerous ocean altimeter satellite missions (e.g. GEOS 3, SEASAT, and GEOSAT), and airborne campaigns (e.g. Drinkwater, 1991). However, these sensors did not provide measurements over the Arctic and thus satellite radar altimetry of sea ice begins with ERS-1 in 1991. In the late 1980s and early 1990s, radar altimeter observations of sea ice were mainly focused on ice type, extent and in understanding the backscatter response of Ku-band altimeter signals over sea ice (e.g. Chase and Holyer, 1990; Drinkwater, 1991; Dwyer and Godin, 1980; Laxon, 1990; Rapley, 1984, Ulander, 1987). In 2003, Laxon et al. provided the first freeboard data from ERS-1 and ERS-2. Since then, retrievals of sea surface height, mean dynamic topography, and sea ice freeboard (e.g. Laxon et al. 2013; Ricker et al. 2014, Kurtz et al. 2014; Kwok and Cunningham, 2015; Price et al. 2015; Tilling et al. 2015) have been generated from the radar altimeter onboard Envisat, AltiKA, and CryoSat-2.

Until the results published in Chapter 6, radar altimeter measurements of lake ice have been limited to detecting the presence or absence of ice when studying lake water levels, e.g. Cretaux and Birkett, 2006, Kouraev et al., 2007, 2007b). Recent advances in altimeter design such as synthetic aperture and interferometric processing are providing exciting new opportunities for the study of sea and lake ice.

Today, there are two main types of satellite radar altimeters, pulse-limited such as AltiKa and Jason-2, and the two delay-Doppler sensors CryoSat-2 and Sentinel-3. In pulse-limited altimetry, a short, frequency modulated signal, or pulse is sent to the surface at NADIR. The radar signal is a circular or elliptical pulse that spreads with time (Figure 3.1). The signal interacts with the surface and is returned to the sensor. Multiple pulses are averaged and split into discrete time samples, or range bins, to form a radar waveform. For example, in CryoSat-2 Low-Resolution Mode (LRM, pulse-limited), the pulse repetition rate is 1.97 kHz and the pulses are averaged to 20Hz; each 20Hz waveform is discretized into 128 samples or range bins.

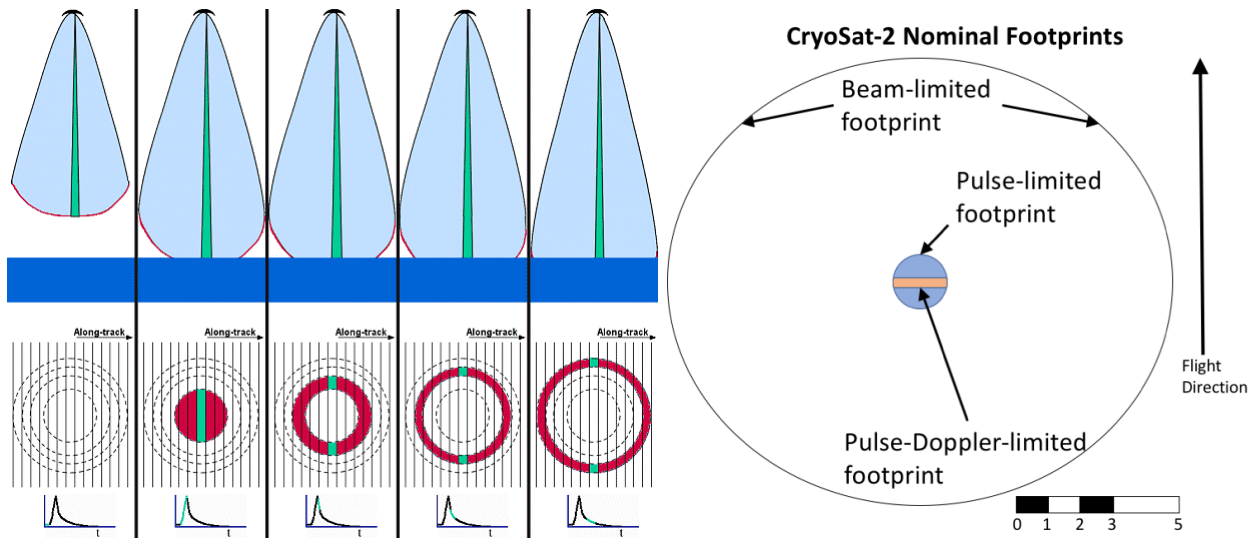


Figure 3.1: Left: CryoSat-2 footprint and waveform representation showing Pulse-Doppler- and Pulse-limited footprints and the waveform components; Adapted from Rosmorduc et al. (2016). Right: CryoSat-2 Beam-, Pulse-, and Pulse-Doppler-limited footprints shown to scale. The beam-limited footprint is roughly 15 km wide across track and 13.5 km along-track, the pulse limited footprint is 1.67 km in diameter, and the pulse-Doppler-limited footprint is 1.67 km wide across-track and 0.3 km along-track.

In delay-Doppler/SAR radar altimetry, non-coherent bursts of coherent pulses are transmitted to the surface and returned to the sensor. For CryoSat-2, each burst consists of 64 coherent pulses sent at 18.181 kHz (ESA, 2013). The pulses within a burst must be coherent to determine the Doppler frequency shifts of the pulses and bursts must be incoherent in order to separate the bursts from each other. The bursts are transmitted at 85.7 Hz in SAR mode and 21.7Hz in Synthetic Aperture Radar/Interferometric mode (SARIN; CryoSat Product Handbook). The phase information/Doppler information is used to split the pulses into Doppler beams (Figure 3.2a). All the Doppler beams from all bursts that look at the same point on the surface are then stacked and averaged to form a SAR/SARIN waveform (Figure 3.2b).

The previous generation of radar altimeters (ERS-1/2, Envisat RA-2, Jason, TOPEX/POSEIDON, and some current altimeters (Jason-2, AltiKa) are pulse-limited systems. Only two scientific pulse-limited delay-Doppler satellite altimeters are now in operation, CryoSat-2's SIRAL and Sentinel-3's SARAL sensor. This thesis is focused on CryoSat-2 and the airborne equivalent/validation sensor, ASIRAS, which operates similarly but from just 500 m elevation and thus has a much smaller footprint (nominally 3 m x 12 m).

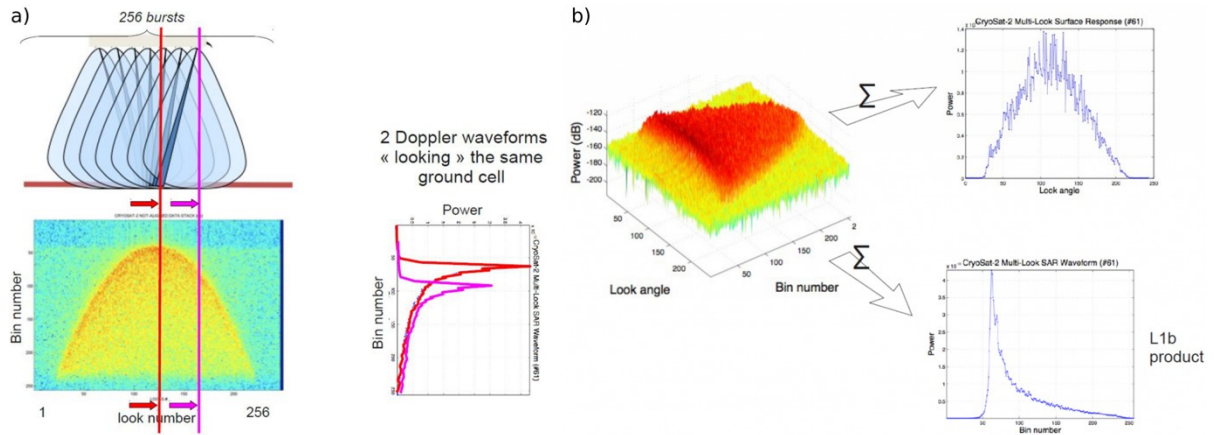


Figure 3.2: Schematic of CryoSat-2 Doppler waveform stacking. Waveforms from different Doppler beams that look at the same area (a) are stacked to produce the CryoSat-2 L1B waveforms (b). From Rosmorduc et al. (2016).

The altimeter waveform contains information on the returned power for multiple time steps resulting from the various interactions with the surface. Points near nadir or that are closer to the sensor are returned first. Multiple reflections from the same surface level/range will result in higher power for a given travel time. Specular reflectors, corner-type reflectors and other strong scatterers can also result in high returned power (backscatter). For CryoSat-2, the waveforms are discretized into different waveform sizes/range bin widths depending on the operating mode. CryoSat-2's SARIN mode, used over coastal regions with highly varying topography, has 1024 range bins that are 0.2342 m (or 1.5625 ns) wide; SAR mode has 512 such range bins and LRM mode waveforms are discretized into 128 range bins that are 0.4684 m (3.125 ns) wide. Features such as leads have a very different waveform shape than the sea ice and can be classified based on standard shape parameters such as kurtosis and skewness, and peak width and height or power.

Due to the Doppler processing, the CryoSat-2 waveforms represent smaller spatial footprints than traditional pulse-limited sensors. However, it is important to note that both types of sensors can receive data from the beam-limited footprint of the sensor. Returns from the beam-limited footprint can occur when the surface is highly varying, such as with off-nadir specular features or other strong scatterers. The vast difference in the scale of the footprints of the LRM and SAR CryoSat-2 footprints and the beam-limited footprint from which surface returns can contribute are presented to scale in Figure 3.1. These footprints are valid for the assumed radar height of

730 km and for a flat surface approximation; the elliptical geometry of Earth and the CryoSat-2 satellite orbit as well surface roughness variations will influence the size of the footprints with increasing footprint sizes observed for rougher/farther surfaces. Footprint size is extremely important in sea ice altimetry as it strongly influences the detection of leads and open water between ice floes needed to calculate sea ice freeboard and thickness (see Chapters 3.2, 3.3). Increased spatial resolution provides a higher likelihood that a footprint will come from a homogeneous surface or at least from a footprint that is dominated by one surface type over the others. Recent work by Egidio and Smith (2017) highlighted the advantages of increased spatial resolution of CryoSat-2 by providing fully-focused CryoSat-2 SAR data with 0.5 m along-track resolution. Their work showed increased lead and water feature detection and much higher multi-looking capability, which reduces noise (by $\sqrt{2}$), than the delay-doppler SAR mode employed in the standard CryoSat-2 product. Fully-focused SAR may provide improved retrievals of sea ice freeboard and thickness from CryoSat-2 and the Sentinel 3 and 6 radar altimeter sensors.

3.2. Freeboard Retrieval

The main focus of this thesis is altimeter measurements of sea ice and lake ice. One of the primary variables of interest is ice thickness, as it is the vital and difficult to observe component of ice volume change and energy balance change (see Chapter 2.1). As neither the Ku-band radar waves emitted by CryoSat-2 nor the laser beam from altimeters can penetrate into sea ice or sea water and measure ice thickness directly, this section discusses the necessary steps and assumptions to retrieve ice freeboard from laser and radar altimetry data. The uncertainties of each of the steps and parameters needed to retrieve freeboard are also briefly discussed. Furthermore, while we discuss most of the steps in terms of CryoSat-2 and radar altimetry, many of the same issues affect laser altimetry.

3.2.1. Method

Freeboard is the height of the ice surface above the local, instantaneous water surface. Freeboard depends on the density of the ice and water, the thickness of the ice, and on the mass of any overlying snow. Laser altimeters do not penetrate snow and thus measure the snow freeboard or the height of the snow surface above the local water surface. As discussed in

Chapters 2 and 3, it is unclear if the signal from Ku-band radar altimeters like CryoSat-2 consistently penetrates to the ice surface or not and thus the term radar freeboard is usually used to denote the radar retrieval level. Radar freeboard may represent the ice surface or some level within the snowpack. Radar-derived freeboard is the radar freeboard corrected for the reduced speed of propagation of the radar wave within the snow and can also be extended to correct for incomplete penetration through the snowpack. Figure 3.3 presents an example flowchart of the CryoSat-2 freeboard and thickness processing chain, from Ricker et al. (2014). Each of the main processing steps is discussed below.

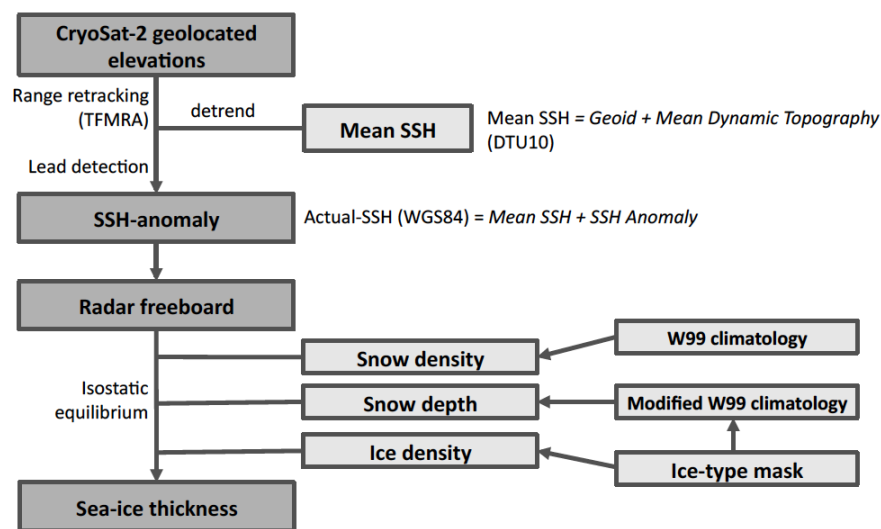


Figure 3.3: Flowchart for altimetric retrievals of sea ice freeboard and thickness from Ricker et al., 2014 (Creative Commons Attribution 3.0 License).

CryoSat-2 geo-located range retrievals are used to calculate freeboard. The first step, referred to as retracking, calculates the height of the surface for each waveform or measurement above some reference ellipsoid by identifying the surface return in the CryoSat-2 waveform. The surface return is represented in a waveform as the leading edge of the main peak in power found in the waveform, see e.g. the waveforms in Figure 3.1 and Figure 3.2. The various CryoSat-2 freeboard and thickness products use different retrackers and different assumptions about what point of the leading edge represents the surface. Values retrieved from lower on the leading edge will be higher in elevation.

In addition to retracking the waveform, geophysical corrections need to be applied to the range measured by CryoSat-2. These corrections include atmospheric and ionospheric delays, the

influence of atmospheric pressure on the sea surface and a variety of tidal components. These corrections are included with the CryoSat-2 waveform product but other tidal or atmospheric path delay models can be used to correct the range of the CryoSat-2 waveform.

The next step is usually the removal of the mean sea surface height, this detrends the slope in SSH elevation due to the geoid and removes the main features of the mean sea surface (see Figure 3.4). This step is necessary to constrain the instantaneous sea surface height where open water leads between ice floes are not detected.

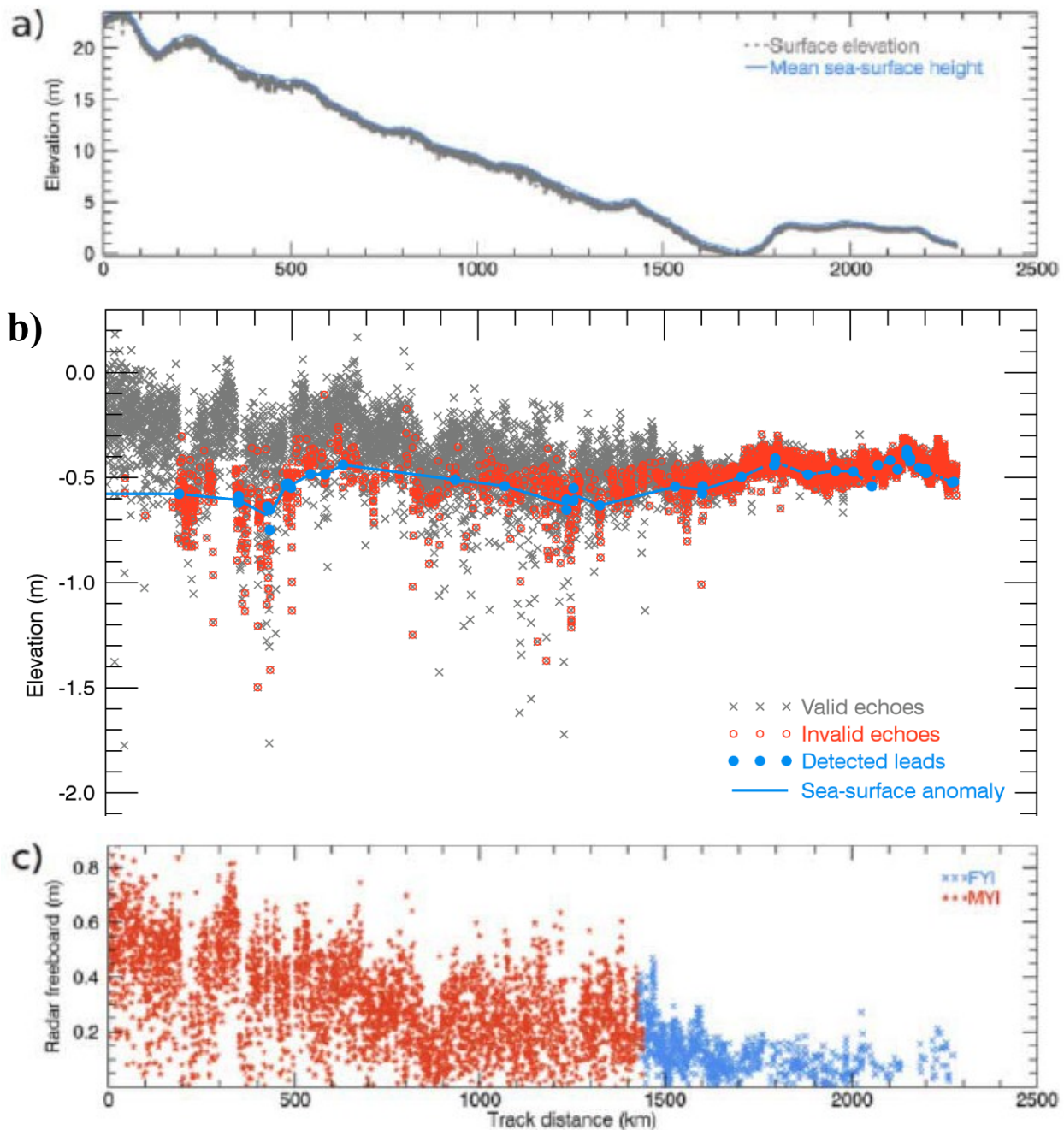


Figure 3.4: Process of converting CryoSat-2 surface elevation heights to freeboard. a) Mean sea surface height (MSSH) and CryoSat-2 retrieved surface elevations. b) Relative elevation after removing the MSSH from the CryoSat-2 elevations. Shows the location of valid echoes identified as ice, unknown waveforms flagged as invalid, and lead waveforms. The sea surface height anomaly (SSHA) is created by interpolating between leads. c) The radar freeboard determined after removing the SSHA from the elevation of the valid echoes. Negative freeboards exist but are not shown in c). Provided by Robert Ricker.

Retrieving freeboard from altimetry data requires classifying the returns into ice, leads, and open water. Usually another class (unknown) is used for radar waveforms where the waveform shape does not fit into the aforementioned categories. This step can happen before or after the mean surface height removal and surface height retrieval. Leads are identified from a variety of waveform shape parameters such as the peakiness of the waveform, a measure of the width of the primary peak in the waveform, the waveform's kurtosis, ice concentration as well as some information about the beam forming and SAR multilooking process.

After retracking and removing the mean sea surface height and classifying waveforms, the sea surface height anomaly (SSHA), the difference between the instantaneous sea surface height and the mean sea surface height is retrieved from the detected leads. The SSHA differs from the MSS due to tides, eddies and even atmospheric pressure. As the freeboard measurement requires a sea surface height for each ice measurement, the lead elevations are often interpolated and often smoothed to reduce noise.

Freeboard can then be retrieved by removing the sea surface height anomaly from the surface height elevations for sea ice classified waveforms, providing the mean sea surface height has already been removed from these waveforms. All of the above steps are also required for laser altimetry, except where the sensor is performing the range determination internally or in the case of airborne altimetry where the uncertainty due to atmospheric delays is reduced.

3.2.2. Uncertainties

The numerous processing steps presented in Chapter 3.2.1 illustrated some of the uncertainties and assumptions required for the retrieval of freeboard from satellite altimetry. The uncertainties, including retracking, sea surface height retrieval, snow penetration and snow loading, and waveform classification are presented in more detail here.

Retrieving the ellipsoidal surface elevation from altimeter data requires identifying the surface from the time-discretized power signal (the waveform), a process known as retracking. Retracking is essentially sub range-bin interpolation of the waveform to increase the vertical resolution. There are a variety of different methods for retracking, e.g. threshold first maximum (e.g. Ricker et al., 2014; Figure 3.5), offset center of gravity, and numerical waveform fitting (e.g. Kurtz et al., 2014; Figure 3.5).

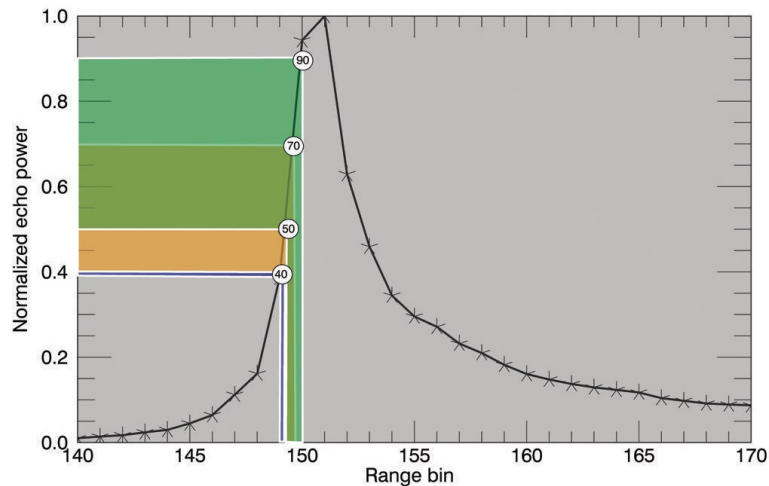


Figure 3.5: Example retracking points on the leading edge for different retracers from Ricker et al. (2014) in blue, Kurtz et al. (2014) in green and the ESA CryoSat L2I product in orange. Figure from Price et al. (2015). Reprinted from the Journal of Glaciology with permission of the International Glaciological Society.

Different methods are based on different parameters of the waveform or on threshold levels along the leading edge of the waveform, some methods such as offset center of gravity and numerical waveform fitting account for the shape of the leading and trailing edge of the waveform, while others are only concerned with the leading-edge slope. All waveform fitting and leading edge retracers identify the surface as occurring on some point of the leading edge; different retracers place the surface higher or lower on the leading edge, i.e. arriving sooner or later (e.g. Figure 3.5). For example, retracking lower on the leading edge, i.e. an earlier return time and higher elevation thus puts the retracked surface closer to the snow surface and means that the radar freeboard is less likely to represent the true ice freeboard. Furthermore, some sea ice freeboard products use different retracers or different thresholds for different surfaces, i.e. for sea ice and for leads; this can introduce a bias that needs to be accounted for. These biases and issues also exist for laser altimeter retracking data if the laser system provides range waveforms; some sensors do the surface range detection internally and only provide range.

Geophysical corrections for tides, ionospheric and tropospheric delays are provided in the CryoSat-2 waveform product and are based on a combination of models. Theoretically, these geophysical corrections have no impact on freeboard as they are applied to both the measurements of the ice and sea surface height. However, as the true instantaneous sea surface

height is not available for each position but is interpolated from detected open water leads, the geophysical corrections added to the ice are not equally compensated (Ricker et al. 2016). Ricker et al. (2016) also showed that the impact of geophysical corrections on freeboard is spatially and temporally variable and inversely correlated with the distribution of leads; regions with few leads, such as the convergent MYI zone North of the Canadian Arctic Archipelago (CAA) and over the thin, land-fast ice in the Laptev Sea were more affected by the geophysical corrections than the central Arctic Basin. Interestingly, the MYI zone north of the CAA is also home to some of the oldest and thickest ice in the Arctic (Haas et al. 2010); in contrast, the Laptev Sea is home to large regions of thermodynamically grown first year ice and extensive sea ice export (e.g. Krumpen et al. 2013). Thus, while geophysical corrections will have a negligible impact over most of the Arctic, Ricker et al. (2016) concluded that in regions with few leads, the ocean tides and barometric pressure corrections can have an important impact. The identification of leads (and ice) is therefore critical to the freeboard retrieval method.

Classification of the sea ice waveforms is typically performed using a variety of waveform shape parameters that are either provided in the CryoSat-2 data product or were developed for pulse-limited altimeter retrievals of sea ice, such as pulse peakiness (Laxon and Peacock, 2003). Different products use different criteria and thresholds to distinguish between open water, leads, sea ice and usually an unknown class. Furthermore, some CryoSat-2 freeboard products also utilize external data, such as the OSI-SAF sea ice type data product, to separate between FYI and MYI in order to apply different ice densities and to adjust the snow depth.

Table 3.1 summarizes the different surface type classifications used by the main CryoSat-2 freeboard studies.

Table 3.1: Published CryoSat-2 Waveform classification parameters. Note that Ricker et al. 2014 and Kurtz et al. 2014 use different formulations of pulse peakiness (PP) than Laxon et al. 2015.

Study/Product	Classification Fields: PP = Pulse Peakiness, SSD = Stack Standard Deviation, IC = Ice Concentration (%), K = Kurtosis, PP _L = left pulse peakiness, PP _R = right pulse peakiness, OCOG Width = Offset Center of Gravity Retracker Width, P _C = Power of the Peak, W _C = Width of the centroid relative to the peak
Tilling et al. 2015	PP: No values provided; Same as Laxon et al. 2013? SSD: No values provided; Same as Laxon et al. 2013?

Laxon et al. 2013	Leads: $PP > 18$ and $SSD < 4$. Ice: $PP < 9$ and $SSD > 4$.
Ricker et al. 2014*	Ocean: $0 \leq PP \leq 10$, $SSD \geq 18.5$, $IC \leq 5$, OCOG Width ≥ 38 Leads: $PP \geq 40$, $K \geq 40$, $PP_L \geq 40$, $PP_R \geq 30$, $IC \geq 70$ Sea Ice: $K \leq 8$, $PP_R \leq 15$, $IC \geq 70$
Kurtz et al. 2014 ⁺	Leads: $PP > 0.18$, $SSD < 4$ Ice: $PP < 0.09$, $SSD > 4$ (3 in SARIN mode areas)
Kwok and Cunningham, 2015	Leads: $P_C > 40$, W_c criterion presented graphically

Table 3.1 reveals that each study is using different parameters or criteria for classifying sea ice and leads. The classification by Ricker et al. (2014) uses more parameters than the other studies but includes some of the same parameters. Kwok and Cunningham (2015) use different parameters than the other studies but the parameters are thematically related to their retracking method. Despite the different parameters, few studies have assessed the accuracy of lead detections; and those that have are often limited in extent, the relatively coarse spatial resolution of available imagery for validation, or by temporal offsets between the imagery and CryoSat-2 data. However, even simple examinations such as the lead fraction maps in Figure 3.6 illustrate some of the issues with current lead detections. Figure 3.6 shows numerous lead detections within the fast-ice covered CAA in November and March 2015 and illustrates the resulting freeboard maps from Ricker et al. (2016). While some open water can be found in the CAA in winter in latent and sensible heat polynyas, there are also detections of leads near shorelines that may indicate land contamination or very flat ice thermodynamically grown ice that result in peaky, lead-like waveforms. Furthermore, these relatively sparse detections, if true, lead to far more widely distributed freeboard estimates due to the interpolation of the SSHA in a region where the sea surface height and tides are poorly constrained.

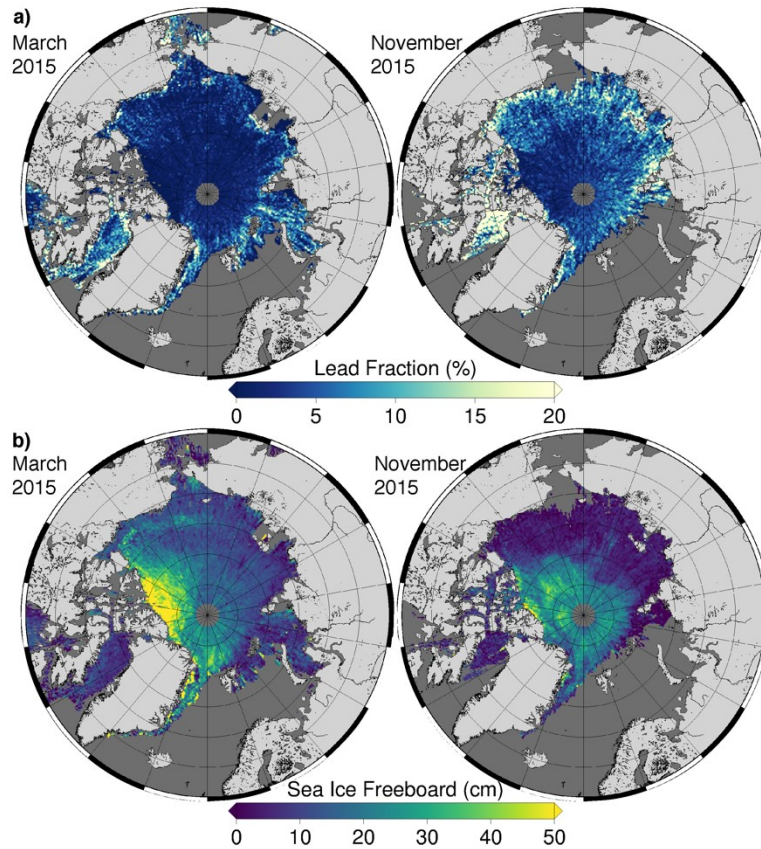


Figure 3.6: Lead fraction (a) and sea ice freeboard (b) from Ricker et al. 2016 showing high lead fractions in November 2015 in the CAA and still showing some areas with high lead fractions in March 2015.

Recently Lee et al. (2017) used machine-learning based classification of leads to separate leads, sea ice, and ocean and found higher accuracy than using the criteria specified by Laxon et al. (2013) and Rose (2013). Their classification used SSD, stack skewness, pulse peakiness, stack kurtosis, and radar backscatter (σ°); however, it is unclear if the validation of the algorithms includes the footprint size or if it only accounts for nadir position. Furthermore, the classification and validation are limited to leads larger than 250 m, and likely even larger, as the MODIS 250m product was used to visually detect leads for both training and validation. The study by Lee et al. (2017), Wernecke and Kaleshke (2015) show that there are significant differences in the lead detections among the methods presented in Table 3.1.

Another significant and under-utilized study is that of Zygmontowska et al. (2013) who classified airborne ASIRAS radar altimeter waveforms using waveform shape parameters and

both rule-based threshold and Bayesian probabilistic classification. They were able to show reliable classification of leads and sea ice, and distinguish between FYI and MYI using parameters such as pulse peakiness, leading edge width, trailing edge slope, trailing edge width, and maximum power; no other studies have shown or attempted to classify ice types using CryoSat-2 waveform parameters (see Figure 3.7). Figure 3.7 shows that the different ice types are separable by waveform power, and other parameters such as width of the peak and the length of the trailing edge; it appears that separating flat FYI and leads may be more difficult due to their similar width and power levels. Figure 3.7 suggests that flat FYI may indeed be flagged as leads in Figure 3.6.

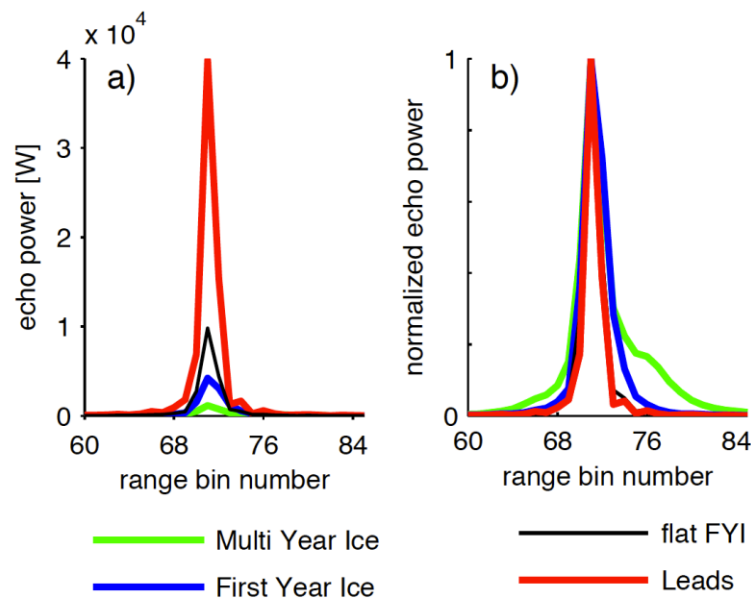


Figure 3.7: Averaged waveforms for different ice types showing the backscattered power (a) and the normalized power (b). a) highlights differences in returned power while b) highlights differences in waveform shape. From Zygmuntowska et al. 2013. Creative Commons License 3.0.

The work by Zygmuntowska et al. (2013) also confirms that classifying normalized power waveforms may lead to misidentification of flat FYI as leads. However, by classifying ice type from the CryoSat-2 waveforms, instead of the widely used OSI-SAF sea ice type (available at <http://www.osi-saf.org/?q=content/global-sea-ice-type-c>), the discrimination between FYI and MYI may improve, as the OSI-SAF product has a coarse spatial resolution of 10 km. Significant work and validation of the classification of surface types in the CryoSat-2 footprint using waveform parameters and external data is still required. However, once the surface type can be

accurately identified, there remain numerous other significant sources of uncertainty, especially snow.

Significant uncertainty exists regarding the consistency of penetration of the CryoSat-2 radar signal through the snow on sea ice. Evidence (e.g. Chapter 8) suggests that the snowpack on sea ice may influence the shape of the leading edge of the CryoSat-2 waveforms (Kwok and Haas, 2015; Kwok 2014; Price et al. 2015; Ricker et al. 2015; Kurtz et al. 2014; Ricker et al. 2014; Willatt et al. 2010, Willatt et al. 2011) and that the snow pack may act as the main scattering horizon (Ricker et al. 2015; Willatt et al. 2010; Willatt et al. 2011)). The main source of argument for complete penetration are the laboratory experiments by Beaven et al. 1995 with some additional support from Willatt et al. 2010. However, as numerous other studies have found evidence of incomplete penetration, there is still considerable uncertainty regarding penetration and its spatial and temporal variability. If the radar signal does not scatter mainly from the ice surface but from within the snow pack the freeboards will be artificially high and thus over estimate ice thickness. Furthermore, if one wishes to convert radar freeboard to actual ice freeboard, one should account for the change in the speed of light within the snow. Even if accurate snow depth is available, if the scattering horizon is not consistently at the ice surface, there will be additional error when correcting for the change in propagation velocity of the wave in the snow.

Currently, accurate correction of propagation speed changes within the snow are not possible as there is no accurate, pan-Arctic snow depth product. Current data products from e.g. Ricker et al. 2014, or Tilling et al. (2015) utilize either an outdated climatology (Warren et al., 1999) with or without correction factors based on NASA OIB snow depth estimates, or have used reanalysis precipitation data. While NASA OIB snow depth data may help to constrain differences between the Warren et al. (1999) climatology and today's climatological snow pack on sea ice, recent work by Kwok and Haas (2015) has shown that the radar side-lobes are often mistaken for the air – snow interface and may influence previous results from the OIB snow radar (i.e. Webster et al., 2014). King et al., (2015) have also shown disagreements between the OIB quick-look product snow depths and in-situ transect measurements over FYI and MYI in the Arctic, with the differences between the two being larger over MYI. Ricker et al., 2015 suggest that incomplete penetration, and spatial and temporal variability explain observations of freeboard increase

observed by both CryoSat-2 and snow-depth measuring buoys in fall of 2013. These results also agree with several unpublished comparisons of satellite and airborne radar and airborne laser altimeter data that show higher than expected radar freeboards, i.e. similar to the laser snow freeboard. Snow is also a major consideration for laser altimeters as signals are reflected from the snow surface and thus the laser freeboard includes snow depth. In order to determine ice thickness, independent information on snow thickness is therefore required. The NASA OIB sensor suite provides both snow depth and laser snow freeboard measurements, though the aforementioned studies call into question the accuracy of the snow depth data and thus the ice thickness results. Furthermore, the green laser used by IceSat/IceBridge may be able to penetrate open water and thus will be subject to bias due to the assumed height of the sea surface.

Although snow plays a critical role in the freeboard error budget, other steps in radar altimeter processing, such as the choice of mean sea surface are also critical to accurately retrieving freeboard. The mean sea surface used to de-trend the geolocated ellipsoidal surface heights and to constrain the sea surface height anomaly (SSHA) interpolation is critical to the retrieval of freeboard. As the SSHA is also tied to the open water leads detected from the altimeter data itself, the MSS error is convolved with the classification of leads. In areas where few leads are detected, the MSS provides information on changes in the sea level due to local geoid/gravity features. The higher gravity around e.g. sea floor features such as ridges can pull water towards them, raising the sea surface. If the MSS contains these features, the interpolated SSHA can be reasonably well constrained, even without leads in the area. However, if these subsea features are not represented in the MSS, or if other artefacts are found in the MSS, the increase in surface height in the sea surface cannot be separated into MSS or SSHA and thus will map directly into the freeboard retrievals if there are no open water leads.

Various mean sea surface products/geoid products have been used in satellite altimetry retrievals of sea ice including the EGM2008 geoid (e.g. Farrell et al., 2012; 2015; Kwok et al. 2012; Kwok and Cunningham, 2015), the Danish Technical University mean sea surface versions 2010, 2013 and 2015 (e.g. AWI CryoSat-2 Products: Ricker et al., 2014), and the University College London 2004 and 2013 mean sea surfaces included in the ESA CryoSat-2 Baseline B and C data versions, respectively. However, each of these geoids is produced using different data and with

different algorithms and thus have different issues. The UCL13 MSS uses two years of CryoSat-2 data to produce an MSS north of 60°, while the DTU MSS models use a combination of previous pulse-limited altimeter data, IceSat and in DTU13 and DTU15, three and five years of CryoSat-2 data. The EGM2008 geoid mainly used gravimetric data but also utilized altimetry data where no other data were available. Recent work in the CryoVal project by Skourup et al. (submitted 2017) highlights how critical the selection of the mean sea surface can be. Interestingly they found that over 70% of studies that have provided information on the MSS model used were using the ArcGP and EGM2008 geoid models, even studies as recent as those by Kwok and Cunningham 2015 and Farrell et al. 2015. However, their results also show that numerous sub-sea ridges and sea mounts are not observed in the EGM2008 model. Their results also show some issues with the DT MSS models related to spatial extent of altimeter missions (81.5N/S from ERS-1/2/Envisat, and at 86N from IceSat. The change in MSS around these features can directly map into freeboard when there are no leads in the vicinity as can be seen in Figure 3.8. The work by Skourop et al. (submitted) clearly shows that reprocessing of past altimetric retrievals of freeboard that use ArcGP or EGM2008 geoid modelled MSS height is required and that more modern MSS models such as DTU15 or UCL13 should be used.

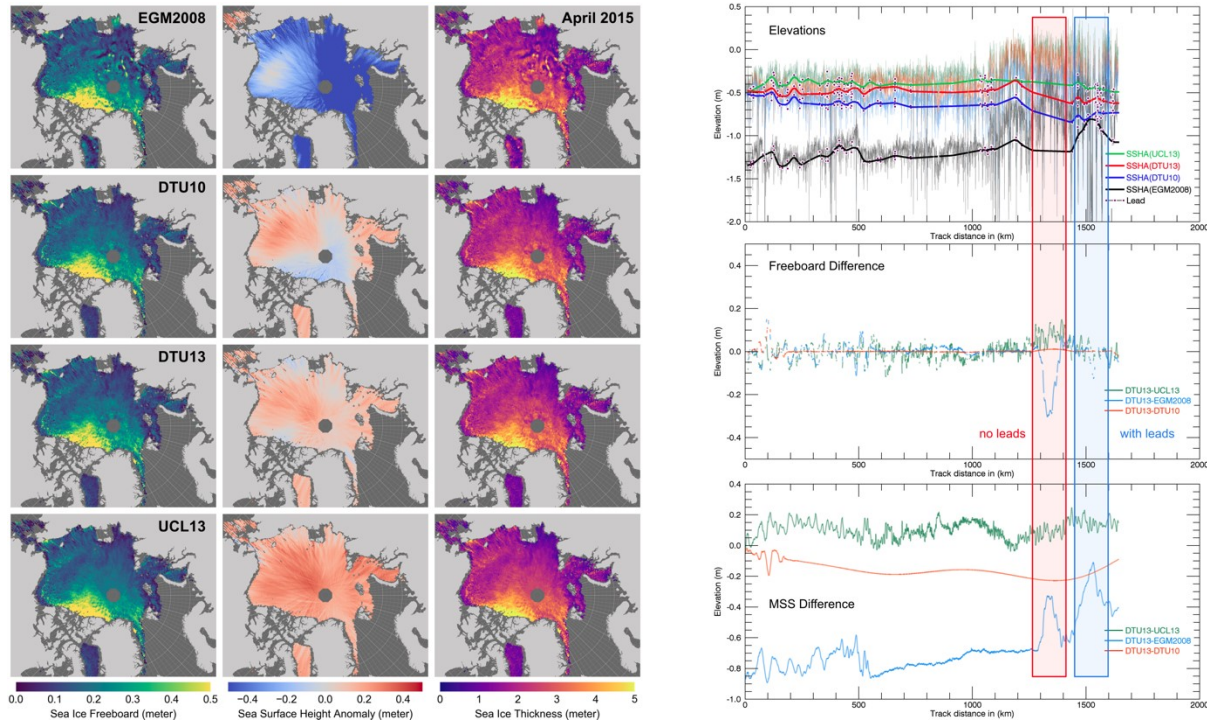


Figure 3.8: Mean Sea Surface Height Model comparison from S. Hendricks (unpublished, 2016). Left: Maps of sea ice freeboard, sea ice surface height anomaly and sea ice thickness derived using the (top to bottom) EGM 2008, DTU10, DTU13, and UCL13 MSS models. Right: Along-track sea surface height anomaly, freeboard and MSS difference between DTU13 and the EGM2008, DTU10 and UCL13 MSS models. Red and blue boxes indicate the location of subsea features not detected in EGM2008 and how these are mapped or not mapped directly into freeboards depending on the presence of sea ice leads.

3.3. Thickness Retrieval

All of the processing steps and uncertainties discussed in Chapter 3.2 introduce spatially and temporally changing uncertainties to altimeter freeboard retrievals. Current retrievals of Arctic sea ice freeboard have all been focussed on pan-Arctic results with a spatially and temporally consistent processing scheme. While pan-Arctic solutions are valuable in many contexts, regional freeboard products may be of more interest and offer higher certainty. Unfortunately, freeboard retrievals are usually just an intermediate step in altimeter-based studies of sea ice as the parameter of interest is usually ice volume change and the determination e.g. the fluxes of atmospheric and ocean energy and momentum; ice volume information requires converting the freeboard to thickness. This section discusses the necessary steps and assumptions to retrieve sea ice thickness from laser and radar altimetry data. The uncertainties associated with each of the steps and parameters needed to retrieve thickness are also briefly discussed.

3.3.1. Method

Moving from altimetric retrievals of freeboard to sea ice thickness requires additional information in order to solve the isostatic balance equations. Snow depth, snow density, ice density, and water density are required for each freeboard measurement in order to calculate thickness. As discussed above, snow depth influences laser and radar altimeter freeboard calculations differently, and thus also affect ice thickness calculations differently (Figure 3.9).

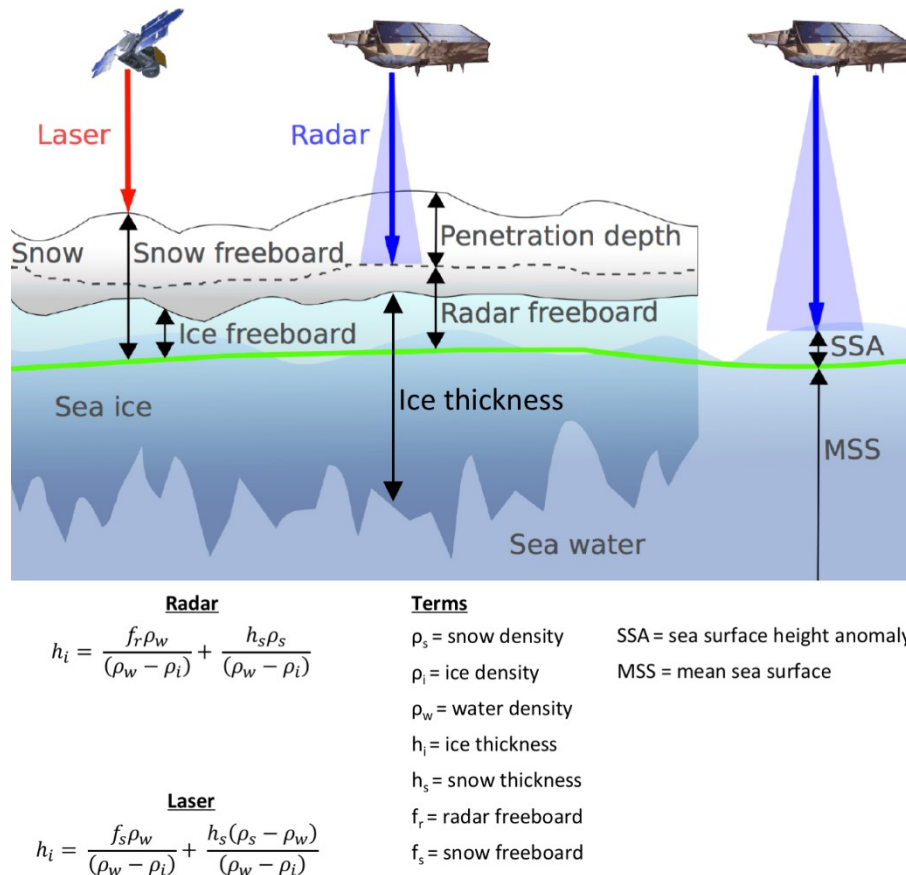


Figure 3.9: Altimetric retrievals over snow-covered sea-ice showing the retrieval surfaces of laser and radar altimeters as well as the instantaneous (MSS + SSA) and mean sea surfaces (MSS). Figure adapted from Ricker et al. 2014. Creative Commons Attribution 3.0 License. Equations from Giles et al. (2007).

3.3.2. Uncertainties

Sea ice thickness retrievals are subject to all the uncertainties as freeboard but also have additional uncertainties that arise from the isostatic balance assumption (Figure 3.9). These uncertainties include the snow loading, and water displacement effects.

The only available pan-Arctic snow thickness and density dataset is the Warren et al. (1999) snow climatology based on data from Russian ice camps and measurements from the 1950s to the 1990s. These data are thus based on an Arctic sea ice pack that was predominantly old-MYI, a stark contrast to today's mainly seasonal and two-year-old ice cover. Numerous studies (Table 3.2; e.g. Laxon et al. 2013, Ricker et al. 2014, Kurtz et al., 2014, Kwok 2015,) have used a modified version of the Warren et al. (1999) climatology where the snow depth on FYI was reduced by 30% or 50% to match the snow depths by NASA OIB. Melt season duration has increased over the past decades, pushing the formation date of the ice later into the fall and limiting the beginning of snow accumulation. Furthermore, the Warren et al. (1999) snow depth climatology does not provide inter-annual variability. However, as aforementioned, besides the high spatial and temporal variability of snow depth, the NASA OIB snow depth data may be erroneous.

Snow density values in sea ice altimetry studies are either fixed (e.g. Kurtz et al. 2014 used 320 kg m^{-3}), or use the Warren et al. (1999) snow density climatology. There has been little concentrated effort to retrieve or apply other spatial or temporally varying snow density data (see Table 3.2). However, it is also widely assumed that snow density on sea ice has not changed significantly over the past decade or two, though this has not been verified.

Ice density assumptions appear to have converged within the CryoSat-2 publication record (Table 3.2), with most studies using the same values for FYI (916.7 kgm^{-3}) and MYI (882 kgm^{-3}), based on the study by Alexandrov et al. (2010) who examined isostatically derived ice thickness and freeboard data from Russian drifting stations. Interestingly, different studies have assigned different uncertainties to the ice density data based on various methods of calculations. Tilling et al. (2015) used an uncertainty value of 7.6 kg m^{-3} based on the Alexandrov study and using the standard deviation of 18 monthly averages of the isostatically calculated ice density from drill hole data, after removing density values outside the range $860 - 970 \text{ kg m}^{-3}$; they suggest that 7.6 kg m^{-3} is likely an overestimate of the density uncertainty. Other work by Hutchings et al. (2015) showed that the uncertainty in measured ice density is typically $40\text{-}50 \text{ kg m}^{-3}$. Furthermore, Hutchings et al. (2015) and Price et al (2014) found that isostatic derivations of ice density, those from freeboard and thickness measurements, are higher than other methods such as mass/volume and solid/liquid volume estimates. Given that ice density uncertainty in radar

altimetry retrievals of ice thickness will also include misclassification of FYI/MYI and uncertainty due to the inclusion of deformed ice, the value for uncertainty in many studies may be underestimated. Additionally, it is not known if the values from Alexandrov et al. (2010) are the most accurate or representative solution. Kwok and Cunningham (2015) presented the large discrepancies between several other parameterizations of ice density based on thickness.

Ultimately the uncertainty in the ice density value used depends on 1) true error in density of FYI/MYI, related to the range in values observed as well as 2) the uncertainty in the measurement of density. Furthermore, when ice is separated into different types, even the coarse FYI/MYI classification applied in many recent altimeter studies, classification error also should be considered in ice density uncertainty determination.

Table 3.2: Sea ice, snow, and water density and snow depth data utilized in studies of altimetric retrievals of sea ice thickness. ⁺Kwok modified the Warren et al. 1999 snow density climatology (W99). MX.XW99 is a modified version of the Warren et al. (1999) where X.X is the multiplication factor applied to W99 over FYI. ¹Zygmuntowska et al. (2014) apply an additional correction of ½ the multi-year ice fraction to the modified Warren et al. (1999) climatology over FYI.

Article	Sea Ice Density (FYI, MYI) (kg m ⁻³)	Snow Density (kg m ⁻³)	Water Density	Snow Depth Schema
Ricker et al., 2014	916.7, 882.0	W99	1024	M0.5W99
Laxon et al., 2013	916.7, 882.0	W99		M0.5W99
Kurtz et al., 2014	915, 915	320	1024	OIB snow depth
Kwok et al. 2015	917, 882	W99	1025	M0.5W99; M0.7W99
Zygmuntowska et al., 2014	900, 916 925, 882	270 (Fall), 330 (Spring)	1024	M0.5W99 ¹
Tilling et al., 2015	916.7, 882.0	W99	1023.8	M0.5W99
Kurtz et. al. 2011	915, 915	W99	1024	ECMWF ERA-Interim
Kern et al. 2015	917, 882	240, 340	1030	OIB, AMSR-E, W99
Kwok et al. 2009, Kwok et al. 2008	925	MW99 ⁺	1024	ECMWF ERA-Interim
Spreen et. al. 2009	910, 887	330	1023.9	0.3m
Laxon and Peacock, 2003	915.1	W99	1023.9	W99
Zwally et al. 2008	915.1	300	1023.9	
Kwok 2004	928	300		W99

Finally, water density is also consistent in the altimetric literature, with the most commonly used value being 1024 kg m^{-3} (Table 3.2). However, some studies use more precision (e.g. 1023.8 kg m^{-3} in Tilling et al. 2015), while others have used higher values: 1025 (Kwok and Cunningham 2015) and even 1030 kg m^{-3} (Kern et al. 2015). Interestingly, most altimetric sea ice thickness retrieval studies assign an error value of just 0.5 kg m^{-3} for water density even though the spread in values used in literature would suggest that the actual uncertainty is larger.

The theoretical error formulation for radar and laser altimeter sea ice thickness retrievals is presented in Equations 3.1 and 3.2 from Giles et al. (2007), where F_i is ice freeboard, Z_s is snow depth, and ρ_w , ρ_i , ρ_s are the densities of water, ice and snow, and ϵ is the uncertainty of each parameter; equations 3.1 and 3.2 assume that the uncertainties are uncorrelated. Almost all current sea ice thickness studies have used the Giles et al. (2007) formulation of uncertainty for radar, ϵ_r , and laser, ϵ_L , altimetry:

$$\epsilon_r = \epsilon_{F_i}^2 \left(\frac{\rho_w}{\rho_w - \rho_i} \right)^2 + \epsilon_{Z_s}^2 \left(\frac{\rho_s}{\rho_w - \rho_i} \right)^2 + \epsilon_{\rho_s}^2 \left(\frac{Z_s}{\rho_w - \rho_i} \right)^2 + \epsilon_{\rho_w}^2 \left(\frac{F_i}{\rho_w - \rho_i} - \frac{F_i \rho_w}{(\rho_w - \rho_i)^2} - \frac{Z_s \rho_s}{(\rho_w - \rho_i)^2} \right)^2 + \epsilon_{\rho_i}^2 \left(\frac{F_i \rho_w}{(\rho_w - \rho_i)^2} + \frac{Z_s \rho_s}{(\rho_w - \rho_i)^2} \right)^2 \quad \text{Eq. 3.17}$$

$$\epsilon_L = \epsilon_{F_s}^2 \left(\frac{\rho_w}{\rho_w - \rho_i} \right)^2 + \epsilon_{Z_s}^2 \left(\frac{\rho_s}{\rho_w - \rho_i} - \frac{\rho_w}{\rho_w - \rho_i} \right)^2 + \epsilon_{\rho_s}^2 \left(\frac{Z_s}{\rho_w - \rho_i} \right)^2 + \epsilon_{\rho_w}^2 \left(\frac{F_s}{\rho_w - \rho_i} - \frac{Z_s}{\rho_w - \rho_i} - \frac{F_s \rho_w}{(\rho_w - \rho_i)^2} - \frac{Z_s \rho_s}{(\rho_w - \rho_i)^2} + \frac{Z_s \rho_w}{(\rho_w - \rho_i)^2} \right)^2 + \epsilon_{\rho_i}^2 \left(\frac{F_s \rho_w}{(\rho_w - \rho_i)^2} + \frac{Z_s \rho_s}{(\rho_w - \rho_i)^2} - \frac{Z_s \rho_w}{(\rho_w - \rho_i)^2} \right)^2, \quad \text{Eq. 3.18}$$

where i, s, and w refer to ice, snow, and water and Z refers to thickness, F to freeboard, ρ is density and ϵ is uncertainty.

Only a few studies have provided uncertainty calculations for their ice thickness retrievals and most use different values for the uncertainty in each parameter, and often different parameter values as outlined above. For example, Giles et al (2007) assigned an uncertainty of 0.5 kg m^{-3} to water density while Kurtz et al. (2011) and Ricker et al. (2014) suggested that it is so small that it can be ignored; water density error has less importance than snow loading error though variations in the used values for water density suggest that the error may be larger than has been estimated so far. The uncertainty in other parameters may also need to be revisited and updated. Finally, as some groups assign multiyear and first year ice classes to the CryoSat-2 data using

external ice type products such as OSI-SAF, additional uncertainty resulting from misclassification can result and thus increase the uncertainty terms of e.g. ice density and snow depth.

In addition to uncertainty estimates several studies have also performed comparisons between CryoSat-2 and airborne data from laser and radar altimeters, electromagnetic induction sensors, and with underwater upward-looking sonar (ULS) sensors (Table 3.3). However, unlike the study presented in Chapter 9 which uses footprint scale data and along-track averages only, the studies in

Table 3.3 have all used gridded data and monthly averages.

Table 3.3: Summary of CryoSat ice thickness validation results using NASA Operation IceBridge (OIB) ice thickness retrievals resampled onto monthly 25 x25 km² grids. Table shows correlation coefficients (r), mean differences (MD), and RMS differences (RMSD) between CryoSat and OIB data.

	r	MD (m)	RMSD (m)
Laxon et al. (2013)	0.61	0.05	0.72
Kurtz et al. (2014)*	0.57	0.11	0.69
Kwok and Cunningham (2015)	0.53	-0.16	0.87
Tilling et al. (2015)	0.67	0.00	0.66

*Best results from March 2013.

3.3.3. Future Changes and Challenges

Evidence that snow and ice properties are changing were presented throughout Chapter 2. Altimeter retrievals of sea ice freeboard and thickness will be influenced by these changes in the snow and ice properties. For example, while current assumptions are that snow density has not changed significantly one can argue that the mean snow density on sea ice has changed, based on changes in ice season duration for FYI. If FYI forms later and snow depth accumulation cannot begin until later in the year, then it also holds that the period for thermal modification of the snow pack, i.e. metamorphism, is reduced. Furthermore, mid-winter warm periods, as have been observed in the winters of 2015/16 and 2016/17, may result in winter-time liquid precipitation events, further modifying the snow density. Additionally, thinner FYI will result from a reduced ice growth season and thus result in stronger thermal gradients through the snow influencing the thermal metamorphism of the snow cover. As the amount of MYI is decreasing, this may lead to changes in mean snow density within the Arctic. Changes in the frequency of storms, amount of precipitation may also influence future Arctic snow density. Another example can be found in the

variations in freshwater content of the Arctic Ocean. Given the variability in storage of freshwater in the Beaufort Sea Gyre (e.g. Morison et al. 2012, Kwok et al. 2016), and large freshwater inputs in the Russian seas, some regional variability in water density may be expected and should be explored for altimetric retrievals of sea ice.

3.4. Summary

Altimetric retrievals of sea ice freeboard and thickness are dependent on numerous parameters and assumptions as well as external data, each with their own uncertainty and spatial and temporal variability. Understanding how altimeters respond to changes and variability in these parameters and how the method is influenced by each of the processing steps is critical to achieving the highest accuracy. The work presented in Chapters 5 through 9 contributes to our knowledge of how altimeter geophysical retrievals perform over sea and lake ice and the uncertainty in the measurements retrieved by altimeters.

4. Links between thesis chapters

The publications in this thesis contribute to the objectives of 1) collecting new sea ice, lake ice and snow data in the Arctic and sub-Arctic and 2) providing validation data for airborne and satellite data over sea ice and lake ice, especially for CryoSat-2, the ESA polar radar altimetry mission. All of the work in this thesis is linked through various components of radar altimeter studies, generating validation data, developing novel applications and algorithms and validating and calibrating existing data for improved accuracy in future products. Chapter 5 presents a method to generate validation data from airborne altimeter data. Chapter 6 presents a novel application of CryoSat-2 data in order to improve our understanding of changes in lake ice thickness. Chapters 7 through 9 examine various aspects of SIRAL, the altimeter onboard CryoSat-2, over different snow and ice conditions in order to assess its accuracy and better understand the uncertainty sources and knowledge gaps. These chapters also provide comparisons with other measurement methods in order to determine the validity of CryoSat-2 data, weakness in our understanding and monitoring of sea ice and snow and to improve the CryoSat-2 freeboard and ice thickness retrieval products produced. Here I briefly explain motivation and the linkage between each of the following results chapters and publications.

Chapter 5 presents surface roughness estimates from a helicopter borne scanning laser altimeter without the use of inertial navigation data to correct for attitude. Normally such data would be discarded as sensor attitude information is important to identifying where on the surface each of the laser returns originates from. However, using the scanner data themselves we can estimate the most widely varying attitude parameter in the towed sensor, roll and retrieve surface roughness. The method could also be used to estimate sea ice freeboard as well as surface roughness and to produce statistical information about ridged ice. Airborne data such as those presented in Chapter 5 are critical validation data for satellite altimeters and to retrieving information about sea ice at high spatial resolution. Chapter 5 has been published as:

J. F. Beckers, A. H. H. Renner, G. Spreen, S. Gerland, and C. Haas. Sea-ice surface roughness estimates from airborne laser scanner and laser altimeter observations in Fram Strait and

north of Svalbard. *Annals of Glaciology*, **56(69)**, 235–244, 2015, doi: 10.3189/2015AoG69A717.

Several collaborations have come out of this publication (Appendix A). The airborne sea ice thickness measurements that I collected and processed coincidentally with the airborne laser scanner data during two research cruises with the Norwegian Polar Institute were used to examine the large-scale ice thickness distribution north of Svalbard by Renner et al. (2013b). These data were also combined with in-situ thickness measurements I helped perform during the cruises to provide evidence for Arctic sea ice thinning over decades of measurements in Fram Strait by Renner et al (2014). The thickness measurements were combined with aerial photographs taken from the survey helicopter for ice type classification to relate thickness and ice type north of Svalbard and in Fram Strait by Renner et al. (2013). Most recently, I processed airborne laser altimeter data collected by NPI in 2011 that were used to compare laser altimeter measured surface roughness to different parameterizations/measures of roughness in fully polarimetric C-Band Synthetic Aperture Radar imagery by Fors et al. (2016) which may aid in SAR image interpretation over sea ice.

With a method to collect new roughness, freeboard and thickness data from airborne laser altimeters/scanners developed I turned to examining CryoSat-2 data. An examination of CryoSat-2 surface height data over Arctic sea ice showed strong variations in waveforms and in surface height that suggested further study into the characterization of CryoSat-2 waveforms was necessary. As sea ice is a relatively rough and dynamic surface that undergoes deformation through compressive (shear, ridging and rafting) and divergent motion and has poorly measured and highly variable snow cover and physical properties, a study was then undertaken into lake ice as a potentially smooth homogenous target for CryoSat-2 waveform characterization and as a target to study the influence of some of the geophysical corrections. Because lake ice is not subjected to continuous drift, there is less dynamic ice growth and a generally smoother ice surface. However, variations in snow cover and some dynamic motion during early winter when the ice cover is thin and incomplete can lead to surface roughness features.

During the study, the waveforms of several CryoSat-2 orbits over Great Slave Lake showed strong double peaks separated by a distance comparable to a reasonable assumption for ice

thickness. Further processing and analysis of multiple years of data to confirm the results culminated in Chapter 6, the first retrievals of lake ice thickness with a satellite radar altimeter. Chapter 6 has been published as:

Beckers, J. F., J. Alec Casey and C. Haas. Retrievals of Lake Ice Thickness From Great Slave Lake and Great Bear Lake Using CryoSat-2. *IEEE Transactions on Geoscience and Remote Sensing*, **55(7)**, 3708-3720, July 2017, doi: 10.1109/TGRS.2017.2677583.

During the study of CryoSat-2 waveforms over lake ice, sea ice was also examined and the results presented in a IEEE International Geoscience and Remote Sensing Symposium conference proceedings. The paper demonstrates some issues with the early versions of the ESA CryoSat-2 sea ice retracking algorithm as the retracker used at the time retracked a point on the leading-edge slope of the maximum peak in returned power of the waveform rather than the first peak, making the surface height results very susceptible to across-track snagging. The study also presents a comparison between NASA OIB laser altimeter data and airborne electromagnetic induction measurements of total (snow plus ice) thickness to CryoSat-2 radar altimeter data from AWI in order to assess the effect of retracking the first peak in power and to examine the issues of incomplete snow penetration presented by others (e.g. Willatt et al. 2011, Hendricks et al. 2010). Chapter 7 was published as:

Beckers, J. F., J. A. Casey, S. Hendricks, R. Ricker, V. Helm and C. Haas. Characteristics of CryoSat-2 signals over multi-year and seasonal sea ice. *2013 IEEE International Geoscience and Remote Sensing Symposium - IGARSS*, Melbourne, VIC, 2013, pp. 220-223, doi: 10.1109/IGARSS.2013.6721131.

In the winter of 2011 and planning for my doctoral program I joined Dr. Haas and researchers from the University of Canterbury in New Zealand for Antarctic fieldwork in order to examine CryoSat-2 data over sea ice in McMurdo Sound in combination with in-situ and airborne electromagnetic induction measurements of thickness. Chapter 8 examines CryoSat-2 signals over landfast sea ice in McMurdo Sound for the retrieval of freeboard, the first CryoSat-2 freeboard retrievals over Antarctica. Furthermore, the study presents a detailed comparison of

the influence of snow depth and the influence of retracker selection through a comparison between areas of deep snow and thin snow and the retrackers utilized by ESA, AWI (Ricker et al. 2014) and NASA Goddard Space Flight Center (GSFC; Kurtz et al., 2014) and the latter two's respective freeboard products. The study highlights the challenges associated with radar altimeter freeboard retrieval and snow depth variability over sea ice and examines both supervised and automated freeboard retrievals. Chapter 8 has been published as:

D. Price, J. Beckers, R. Ricker, N. Kurtz, W. Rack, C. Haas, V. Helm, S. Hendricks, G. Leonard, and P. Langhorne. Evaluation of Cryosat-2 derived sea-ice freeboard over fast ice in McMurdo Sound, Antarctica. *Journal of Glaciology*, **61(226)**, 285–300, 2015, doi: 10.3189/2015JoG14J157.

I contributed analysis and code for the comparison of the ESA CryoSat-2 waveforms and retracking comparisons between the thick and thin snow regions along with the stacked averaging of waveform over these areas. Furthermore, I processed CryoSat-2 data to a state suitable for freeboard retrieval by Dr. Price. I also contributed to the direction and edits of the manuscript. The AWI retracker results were conducted by Dr. Ricker, and the NASA GSFC retracker results were provided by Dr. Kurtz. Dr. Price performed the freeboard calculation and analysis and wrote the bulk of the manuscript.

Finally, Chapter 9 presents analyses that I have performed under the ESA CryoSat Validation project where I have examined all available coincident airborne and CryoSat-2 data between 2010 and 2015 in order to examine the results of differences in the ESA and AWI CryoSat-2 processing schemes to understand the uncertainty and changes in results induced by e.g. lead identification, mean sea surface selection and filtering of erroneous data. The project also compares laser and radar altimeter freeboard results from multiple airborne laser and radar altimeters as well as electromagnetic induction measurements of sea ice thickness with estimates of thickness from CryoSat-2 and NASA laser altimetry. Chapter 9 will be submitted for peer review in the coming months as:

Beckers, J. F., C. Haas, S. Hendricks, R. Ricker, S. Baker, M. Davidson, S. Farrell, R. Forsberg, S. Gerland, S. M. Hvidegaard, J. King, H. Skourup, G. Spreen. Validation of CryoSat freeboard retrievals with coincident airborne measurements.

In addition to this study, the CryoSat Validation project has also resulted in a second publication examining the impact of geophysical corrections on sea-ice freeboard retrieved by CryoSat-2 by Ricker et al. (2016). Ricker et al. (2016) found that the spatial and temporal distribution of leads strongly influences the impact of geophysical corrections, especially ocean tide and the inverse barometer correction on sea ice freeboard and that regional impacts can influence both the thickest and thinnest ice regions even if the mean impact over the entire Arctic Ocean is minimal.

The data used in this paper were mainly collected as part of the European Space Agency CryoSat Validation Experiments in which I have participated since 2011. In addition to this study, additional studies of CryoSat-2 have resulted from data collected including King et al. (2015) who examined airborne and in situ snow depth measurements of snow depth to show that NASA's Operation IceBridge snow depth measurements underestimated in situ snow depth especially over MYI. King et al. (2015) also show that a significant amount of NASA OIB snow depth data is rejected over MYI.

5. Sea ice surface roughness estimates from airborne laser scanner and laser altimeter observations in Fram Strait and north of Svalbard

5.1. Abstract

We present sea ice surface roughness estimates, i.e. the standard deviation of relative surface elevation, in the Arctic regions of Fram Strait and the Nansen Basin north of Svalbard acquired by an airborne laser scanner and a single-beam laser altimeter in 2010. We compare the scanner to the altimeter and compare the differences between the two survey regions. We estimate and correct sensor roll from the scanner data using the hyperbolic response of the scanner over a flat surface. Measurement surveys had to be longer than 5 km north of Svalbard and longer than 15 km in Fram Strait before the statistical distribution in surface roughness from the scanner and altimeter became similar. The shape of the surface roughness probability distributions agrees with those of airborne electromagnetic induction measurements of ice thickness. The ice in Fram Strait had a greater mean surface roughness, 0.16 m vs. 0.09 m, and a wider distribution in roughness values than the ice in the Nansen Basin. An increase in surface roughness with increasing ice thickness was observed over fast ice found in Fram Strait near the coast of Greenland but not for the drift ice.

5.2. Introduction

During the past two decades, there have been rapid decreases in Arctic sea ice extent (Comiso et al. 2012), thickness (Haas et al., 2008; Kwok and Rothrock 2009; Hansen et al., 2013; Renner et al., 2014), and, as a result, volume (Schweiger et al., 2011 and Laxon et al., 2013). Passive microwave sensors and data from drifting buoys show that the Arctic sea-ice regime is becoming increasingly seasonal in nature, i.e. multi-year sea ice (MYI) is disappearing and being replaced with first-year sea ice (FYI; Rigor and Wallace, 2004; Maslanik et al., 2011). This regime shift has implications for the transfer of momentum and energy between the sea ice, the ocean, and the atmosphere. Sea-ice properties such as ice drift speed (Sprenn et al., 2011; Kwok et al., 2013), and deformation rate (Rampal et al., 2009) are changing as the ice thins and weakens. Enhanced deformation implies increased formation of open-water leads between floes and enhanced ridge formation, ice rafting and potentially rougher ice surfaces. Roughness both influences and is

influenced by the formation and development of melt ponds (Eicken et al., 2004). Enhanced roughness has important implications for maritime operations, remote sensing (Peterson et al., 2008), and modeling and measuring the interactions between sea ice, the atmosphere and the ocean; such as drag, drift, and the vertical transport of water (e.g. Rabe et al., 2011). The combination of increased drift speed and deformation could be an important mechanism contributing to the observed decline in sea ice extent. Enhanced surface roughness could result in an ice pack with a greater wind drag or water drag leading to increased ice drift speeds and decreased sea ice extent. By monitoring the temporal changes in surface roughness of sea ice in different regions and ice regimes, our understanding and quantification of these changes, and predictions of ice drift, volume, and area changes can be improved.

Fram Strait and the Nansen Basin region north of Svalbard are two important and dramatically different regions for the study of sea ice in the context of changing ice regimes. Fram Strait is the largest and deepest outflow region of the Arctic Ocean (Kwok et al., 2004; Serreze et al., 2006; Kwok, 2009). Ice drifting through Fram Strait integrates changes in the Arctic Ocean over a large area and over several years. The ice in Fram Strait is a mixture of FYI and MYI (e.g. Renner et al. 2013). In addition, Fram Strait often contains fast ice near the coast of Greenland, the Norske Øer Ice Barrier (Figure 5.1; Hughes et al. 2011)). The Norske Øer Ice Barrier is composed of icebergs and fast ice and extends out into the path of the Fram Strait drift ice. The mean and modal ice thickness and the fraction of ice more than 5 m thick have all decreased in Fram Strait over the past two decades (Hansen et al., 2013; Renner et al., 2014). Furthermore, changes in the drift speeds and deformation rates in Fram Strait have implications for ice export and volume loss for the entire Arctic Basin. In contrast, the ice in the Nansen Basin north of Svalbard is a seasonal ice regime at the margins of the Arctic ice pack (Renner et al. 2013b); however, we have limited knowledge of the changes in the sea ice thickness and roughness that are occurring in this region. The changes in ice properties occurring in these areas provide an important glimpse into potential future sea ice conditions over other regions of the Arctic Basin.

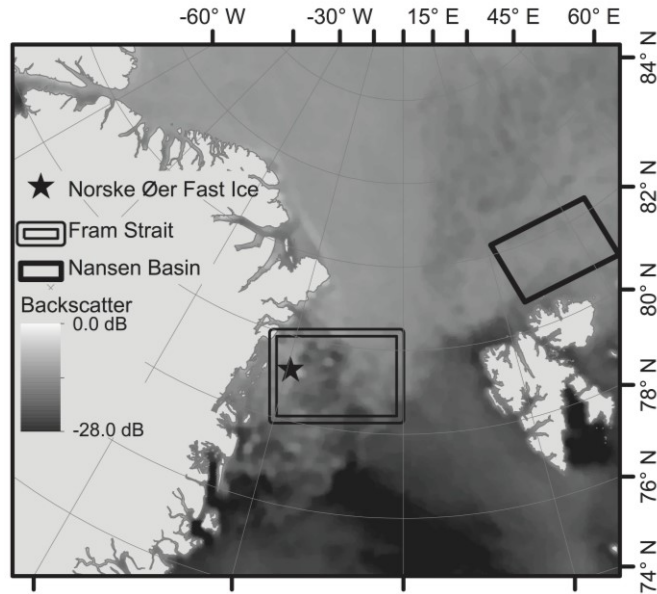


Figure 5.1: Map of study region overlain on ASCAT C-band scatterometer backscatter data from 6 September 2010. Backscatter variations over sea ice correspond to different ice concentration, ice type distribution and ice roughness. Over open water, backscatter varies with wind speed and direction.

The spatial distributions of sea-ice ridges, roughness, and floe size have traditionally been estimated from airborne laser altimeter measurements (Hibler, 1972; Hibler, 1972b; Dierking, 1995; von Saldern et al., 2006), aircraft mounted laser scanners (Kurtz et al., 2008; Doble et al., 2011), or upward-looking sonar sensors (Wadhams et al., 2008). In contrast to laser sensors, upward-looking sonar sensors measure the roughness of the underside of the ice. Single-beam laser altimeters have been included in airborne electromagnetic induction (AEM) sensors since 1999 and are used for the processing of the AEM data (Haas et al., 2009) and for investigating surface roughness and ridging properties (von Saldern et al. 2006, Tan et al. 2012). While sampling only in the direction of flight, one can use laser altimeter data in a similar fashion as laser scanner data, assuming that the distribution and orientation of leads, ridges, floe dimensions, rafted ice, hummocks and open water is random. However, this assumption is not valid for all sea-ice regions; e.g. where there are persistent ocean or atmospheric currents at the surface. Laser altimeters are used in AEM data processing to retrieve the distance between the sensor and the top of the ice surface while the AEM system measures the distance to the water below the sea ice. The sea-ice thickness retrieved for a three-dimensional (3D) AEM sensor

footprint is thus the difference between the laser altimeter measurement and the AEM system (Haas et al., 2009).

Table 5.1: Riegl LMS Q120 laser scanner characteristics. Data adapted from scanner settings used during study and the scanner specifications (Riegl, 2010).

Parameter (unit)	Value
Field of view (°)	80
Across-track angular spacing (°)	0.4
Laser beam divergence (rad)	2.7×10^{-3}
Pulse repetition frequency (Hz)	30 000
Measurement rate (Hz)	10 000
Scan-line rate (Hz)	50
Along-track spacing (m)	0.6 – 1.0
Accuracy (m)	0.025
Precision (m)	0.015

Airborne laser scanners provide two-dimensional (2-D) swaths of surface elevation measurements and related surface properties along extensive transects with the same high spatial resolution and accuracy as a one-dimensional (1-D) single-beam altimeter. To do so, accurate knowledge of the scanner viewing geometry is required; therefore, airborne laser scanners are normally operated in conjunction with an inertial navigation system (INS) or inertial measurement unit (IMU), and a differential, dual-frequency GPS system (DGPS). The processing and correction of the scanner attitude data using the INS/IMU and DGPS systems is non-trivial as each sensor has its own fixed orientation, timing offset, uncertainty, and drift relative to the other sensors. Laser scanner processing typically requires a survey over known, well-defined targets (e.g. buildings) to estimate sensor biases and uncertainties (e.g. possible laser squint angle).

From 20 to 29 August and 4 to 13 September 2010, AEM surveys were performed by helicopter in Fram Strait and over the Nansen Basin north of Svalbard (Figure 5.1; Renner et al., 2013; Renner et al., 2013b). During these surveys, a laser scanner system was installed in the AEM sensor for the first time; however, the system did not include an INS/IMU.

Here we present a method of retrieving a relative surface elevation and the sea ice surface roughness from the laser scanner without INS/IMU and DGPS sensors. The method does not require surveys over well-known targets but it only provides relative measurements of surface elevation with the level-ice surface as the reference datum. Using the standard deviation of the relative surface elevation as a proxy for roughness, we present a comparison of surface

roughness estimates from the traditionally-used single-beam laser altimeter and the laser scanner data in order to improve our understanding of the properties of the ice in these two regions. We contrast the results of the single-beam laser altimeter to the new laser scanner over various scales to examine their representativeness. Finally, we compare and contrast the two regions using the AEM ice thickness measurements and the new surface roughness estimates.

5.3. Measurements and Methods

A Riegl Laser Measurement Systems (Riegl LMS) Q120 laser scanner was mounted in the nose of the AEM sensor. Table 5.1 provides the important characteristics of the scanner and scanner settings adapted from Riegl LMS (2010). The scanner rotates a laser beam by a set angle across the 80° field of view resulting in a laser range measurement for each across-track angle. A scan line is all of the scanner measurements taken during one complete rotation across the field of view. The dataset collected in 2010 includes the laser scanner range (Figure 5.2d) and signal strength (Figure 5.2b), GPS position data, and the AEM measurements of the total snow plus ice thickness, referred to hereafter as total thickness (Renner et al., 2013b). Using the GPS timestamps and measurement ID numbers, the data streams from the different sensors were merged and coincident measurements were extracted. The system was flown 15 ± 5 m above the ice, at a speed of 40 ± 5 m s⁻¹. Data acquired when the AEM sensor was >30 m above the ice were removed from the analysis, and all data were resampled to 50Hz using linear interpolation.

An example of the laser scanner measurements (Figure 5.2b, d) and the processing methodology (Figure 5.2a, d-f) for a 40 m section of sea ice in the Nansen Basin is shown (Figure 5.2) omitting the true spacing of 0.7 m between successive line scans. The across-track spacing is much smaller, 0.1 m to 0.2 m for standard survey heights of 10 m - 15 m, respectively. The return strength of the laser scanner (Figure 5.2b) is sensitive to changes in the small-scale roughness properties, as illustrated by the lower return strength from the refrozen melt pond in

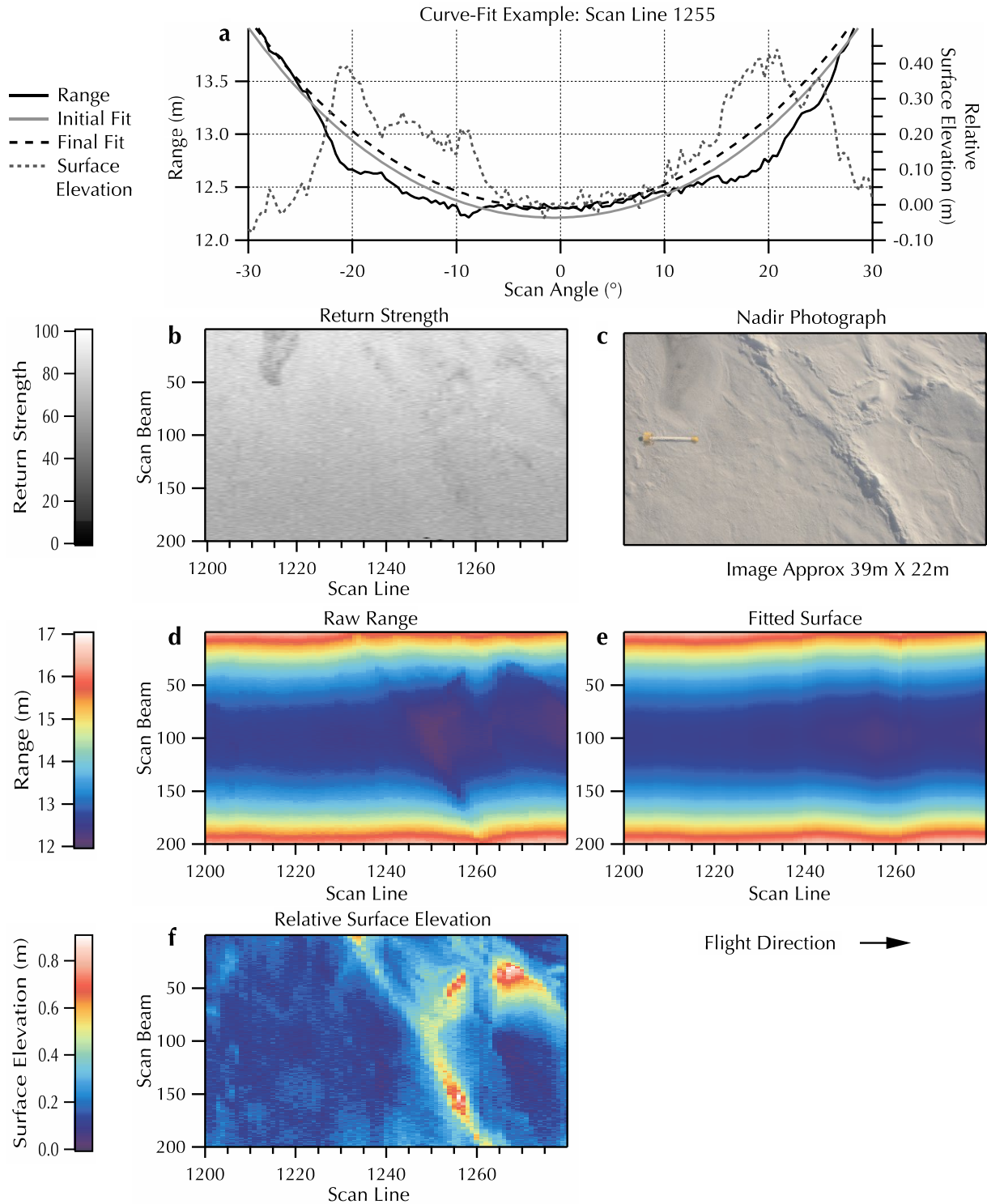


Figure 5.2: Laser-scanner results from example section of sea ice north of Svalbard. (a) Example curve-fit procedure for scanner line 1255; (b) laser return strength; (c) nadir photograph taken from helicopter; (d) raw laser scanner range measurements; (e) estimated flat surface; (f) relative elevation of measurements (d) to flat surface in (e).

the upper left corner of Figure 5.2b and Figure 5.2c. Smooth surfaces reflect the laser light away from the sensor in a specular manner while rough surfaces widen the angular distribution of scatterers reflecting the light in a diffuse manner, thereby increasing the power returned to the sensor. It may be possible to retrieve open water and melt pond information from the scanner return strength. In our data, many of the melt ponds are refrozen, or are drained and thus do not appear different from other ice surfaces. Figure 5.2d presents the range, the distance between the sensor and the surface, measured by the laser scanner. The main ridge visible in Figure 5.2c is also visible in Figure 5.2d as a shift in the range. Figure 5.2d is not corrected for sensor roll. Roll changes the reported range value by increasing the incidence angle of a scanner beam from its nominal value if the sensor had a roll angle of 0° , i.e. a roll angle of $+2^\circ$ means that the incidence angle for the 0° beam is changed from 0° to $+2^\circ$. Roll also changes the surface location that is sampled. The roll angle and range to the surface for the true nadir scanner-beam are retrieved using

$$y = \frac{A}{\cos(\theta - \beta)}, \quad \text{Eq. 5.1}$$

where y is the across-track range of an individual scanner beam, A is the range to the nadir scanner beam, θ is the across track angle of the scanner beam, and β is the roll of the scanner. Variables A and β are obtained by iterative curve-fitting using nonlinear least-squares optimization (WaveMetrics, 2014). Equation 5.1 is applied to the range data of each scan line (Figure 5.2a). After the curve fitting is performed, points where the range is less than the fitted curve are discarded and the curve fitting process is run again. This process is repeated once more (Figure 5.2a). By removing points with a range that is less than the fitted curve, the curve fit is adjusted to fit the points with a greater range, the lower level-ice surfaces (Figure 5.2a, e). The curve fitting was performed three times to strike a balance between the adjustment to the level-ice, and processing times. Sensor roll was nominally less than $\pm 10^\circ$, but occasionally more than $\pm 20^\circ$ when the helicopter was turning. After calculating the roll and distance to the true nadir location, the laser range is removed from the fitted range, resulting in a relative surface elevation for each laser scanner beam that is relative to the fitted surface representing the local level-ice surface (Figure 5.2f). As the fit is performed for each individual scan line, significant changes in the line-to-line surface elevation, or the absence of level-ice, can lead to incorrect relative surface

elevation retrievals. These problems are observable as across-track stripes in the relative surface elevation data (e.g. at scan line 1265 in Figure 5.2e). In the absence of a level-ice surface, the relative surface elevation will be overestimated because while the fit will trend towards the minimum surface (maximum range), this range will not be the level-ice surface. By adjusting the fit twice, we attempt to minimize the error for scan lines with low amounts of or no level-ice. For one flight, we extracted the roll-corrected nadir beam of the scanner and processed the data as a single-beam laser altimeter following the Hibler (1972) processing scheme, referred to hereafter as H72. This processing method is commonly used when examining relative surface elevation and surface roughness measurements from single-beam laser altimeters when INS and DGPS data are not available (e.g. von Saldern et al., 2006; Tan et al., 2012). However, the results did not show a conclusive improvement over the method presented above, so the H72 method was not applied.

When comparing laser scanner results to laser altimeter results, the roll-corrected nadir beam is extracted from the laser scanner line. Hereafter, when the terms altimeter or single-beam altimeter is used, it refers to the roll-corrected nadir beam of the scanner. Although the method corrects for sensor roll, changes in the yaw and pitch angles of the sensor are not corrected for.

5.4. Sources of Uncertainty

The major sources of uncertainty are the result of not correcting for the yaw and pitch angles, or the slant-range distortion. It was not possible to correct the sensor yaw, the rotation of the sensor around the vertical axis, from the available dataset. The AEM sensor was suspended from the helicopter by a 20 m long towline, so the AEM sensor experiences pendular motion. The yaw angle of the AEM sensor changes rapidly due to small changes in speed, direction of travel, and from the pendular motion. The GPS direction-of-travel information is provided at 1 Hz and thus can only be used to estimate low-frequency changes in yaw angle that result from the pendular motion of the sensor. IMU measurements from an AEM survey conducted in 2011 showed variations in yaw angle around the direction of travel of about $\pm 2^\circ$ (two standard deviations) (Haas et al., 2011, unpublished data) with both a low and high frequency component. At the maximum scan angle of $+40^\circ$ and assuming a range of 15 m and no roll or pitch, a yaw angle away from the direction of travel of $\pm 2^\circ$ results in sampling with a lateral offset of ~ 0.4 m ahead of

the nadir beam, or nearly the distance between successive scan lines. Yaw does not cause a geometric distortion, only a change in the surface sampling location by changing the orientation of the scan line over the surface.

IMU measurements from an AEM survey conducted in the Lincoln Sea in 2011 showed variations in pitch angle of about $\pm 2.4^\circ$ (two standard deviations) (Haas et al. 2011), unpublished data). When unaccounted for, the $\pm 2^\circ$ pitch angle also leads to an overestimation of the range to the surface of 0.01 m and a lateral offset of 0.53 m. The large circular drag-tail of the AEM sensor stabilizes the bird against yaw and pitch angle changes but because it is circular it does not reduce high-frequency roll. The drag skirt is able to reduce the low frequency roll caused by the aforementioned pendular motion of the bird below the helicopter.

Relief distortion, or slant-range distortion, i.e. the error caused by not measuring the height of a ridge normal to the surface but the distance along the scanner beam to the surface, also remains uncorrected. Relief distortion is greater for greater scan angles than for those close to nadir. While yaw and pitch errors were shown to be relatively small and affect the entire swath, the slant range distortions may partially explain some of the differences observed between the scanner and the altimeter. Furthermore, the slant-range distortion is greater for points further away from nadir and causes an increase in the apparent height of the surface since the measurement of height is made along the scanner laser beam.

5.5. Results

Firstly, we explore the relative surface elevation, and surface roughness for two small sections (37 m \times 20 m; 38 m \times 20 m) of flight FS20100906f1 (Figure 5.3). Here the surface roughness for the laser scanner is the standard deviation of the relative surface elevation estimates for each scan line, and the standard deviation of a five data-point moving window for the altimeter. The scanner standard deviation provides clear evidence of the off-nadir surface features such as the rafted blocks or ridges; these features are all missed by the laser altimeter (compare dashed (altimeter) to solid (scanner) line). At the scale of an individual floe, the laser altimeter may over-

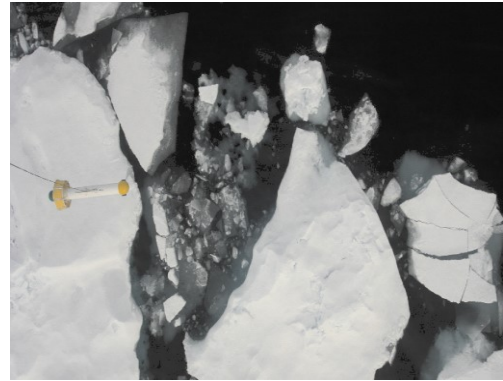
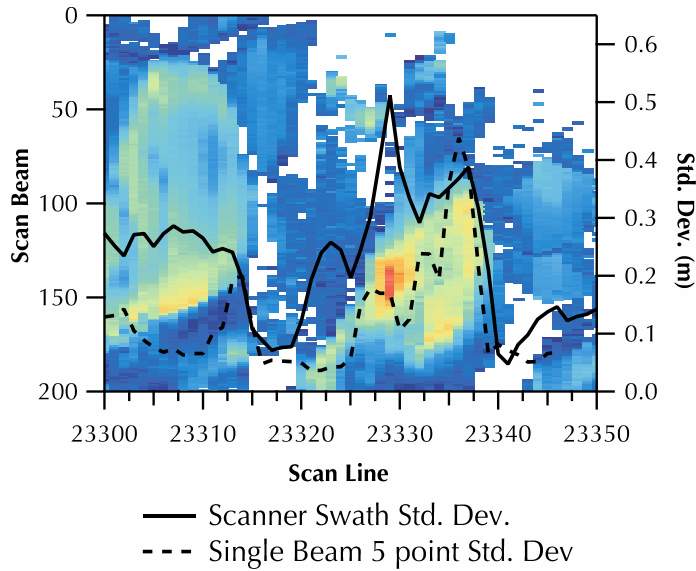


Image Approx: 37m X 20m

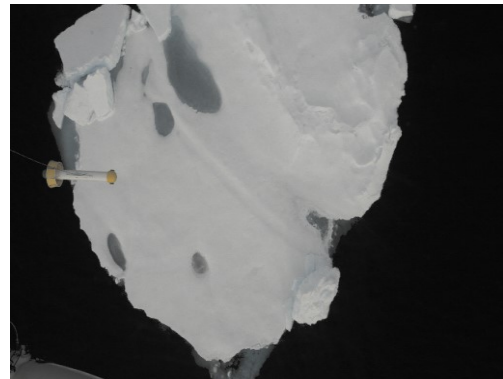
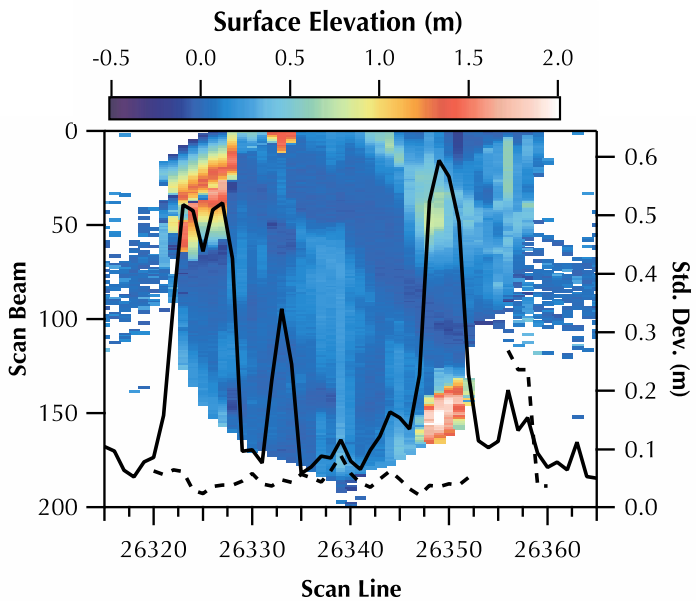


Image Approx: 38m X 20m

Figure 5.3: Comparison of standard deviation of relative surface elevation from the laser scanner and laser altimeter for two short sections of sea ice in Fram Strait from flight FS20100906f1. Adjacent photographs were taken from the helicopter and show the AEM sensor. The scanner standard deviation is the standard deviation of relative surface elevation of all beams in a single scan line. The laser altimeter standard deviation is computed using a running five-point along-track window.

or underestimate the roughness of the floe based on the random location of the surface roughness features with respect to the direction and location of the survey. The scanner is able to resolve small features such as a crack in a rafted piece of ice, narrow melt channels, small melt ponds, and small brash ice features (Figure 5.3). The minimum size of detectable features is

limited by the orientation of the feature and the along and across-track measurement spacing. Furthermore, the laser scanner provides more measurements over smooth open water where specular reflections result in missing data in the altimeter data record (e.g. right part of lower figure where dashed line is missing).

The scanner data have many potential uses including the examination of surface roughness and improving the sensor range measurement for an AEM footprint. The change in the distribution of surface roughness from the laser scanner for different moving-window sizes with which surface roughness was calculated for three flight sections, in the Nansen Basin, in Fram Strait, and the fast ice in Fram Strait (Figure 5.4a-c). Also shown is the change in the fractional proportion of ice with a relative surface elevation greater than 0.8 m (the High Elevation Fraction (HEF)), taken to be ridged or rafted ice, with increasing profile length as represented by the number of scan lines, for both the scanner and the altimeter (Figure 5.4d-f). Both the scanner and altimeter respond similarly for all flights. North of Svalbard, the two datasets converge while in Fram Strait the data diverge after a significant portion of the profile. In Fram Strait, it does not appear that a steady value is reached but both datasets exhibit the same changes over the length of the profile. Over the fast ice, the two datasets appear to reach a constant value.

Table 5.2 presents measurements of the ice properties including mean and modal thickness from the AEM sensor, mean and modal surface roughness, and the HEF for the ice north of Svalbard, in Fram Strait, and the fast ice in Fram Strait. The mean total thickness for the Fram Strait drift ice is greater than for the ice north of Svalbard although the modal thickness only differs by 0.1 m. The mean and modal thickness of the fast ice in Fram Strait was greater than that observed for the measurements over the drifting drift ice flowing through Fram Strait. The fast ice in Fram Strait has the greatest HEF, followed by the drift ice in Fram Strait, and finally the ice north of Svalbard.

Next, statistical distributions of total thickness, relative surface elevation, and surface roughness for the three ice regimes are investigated (Figure 5.5). The surface roughness is the standard deviation of the relative surface elevations within a 60 m along-track window, roughly corresponding to the footprint of the AEM sensor at typical flying heights. The ice north of Svalbard exhibits the narrowest distributions in all properties, followed by the Fram Strait drift

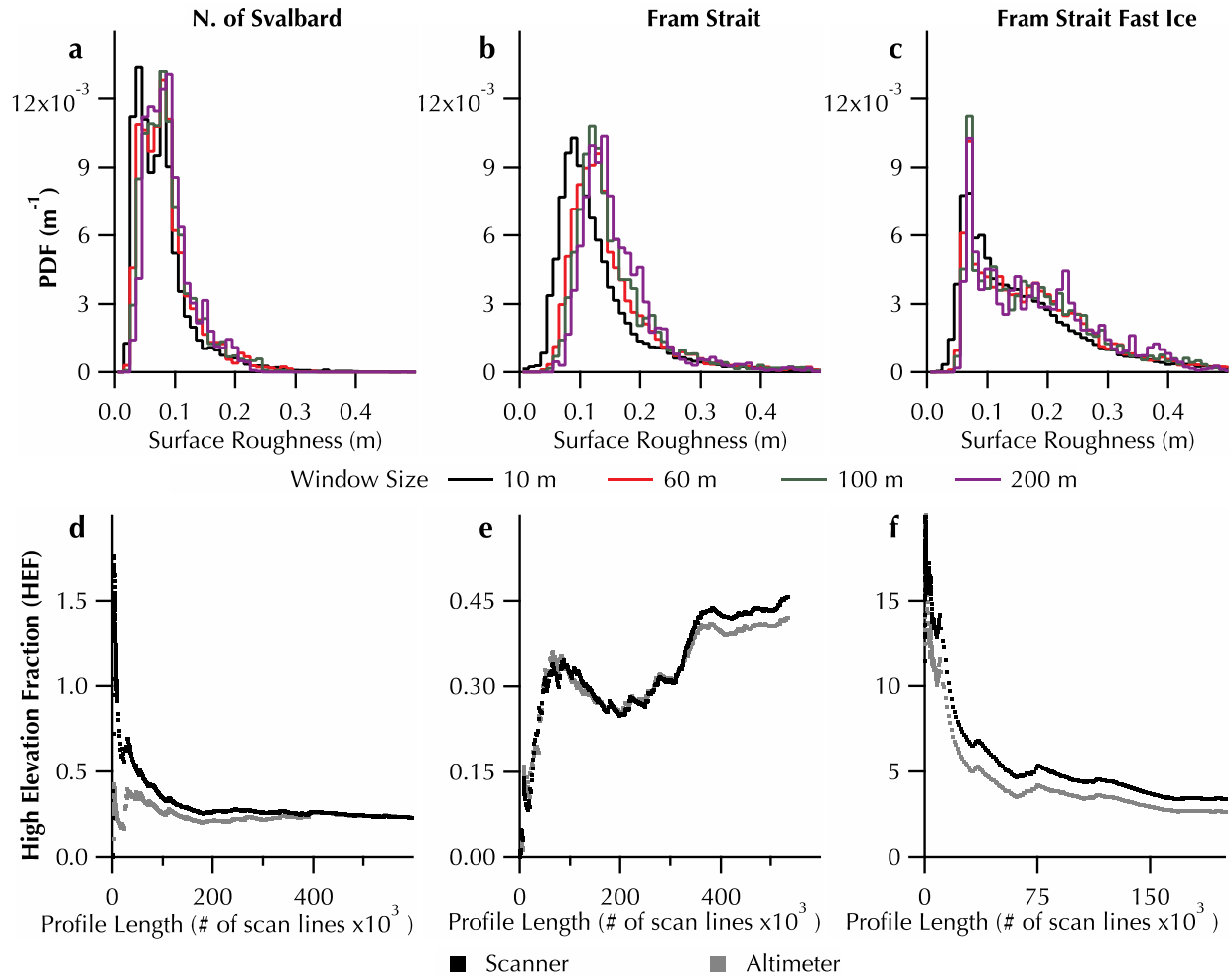


Figure 5.4: (a-c) Change in distribution of surface roughness for different window sizes (box-car filter length (m)) used to calculate the surface roughness. PDF: probability density function. The profiles represented are 38km, 40km and 45km long flight sections for the ice north of Svalbard, in Fram Strait and over the fast ice in Fram Strait, respectively. (d-f) High-elevation fraction (HEF) is the number of points higher than 0.8m divided by the total number of points in an increasing length of a profile, represented by the number of scan lines, for the altimeter for all measurements in each region.

ice and the Fram Strait fast ice. In shape, the statistical distributions of surface roughness (Figure 5.5a-c) matches those of the AEM thickness observations (Figure 5.5f); the surface roughness and thickness distributions for Fram Strait are broader than for the ice north of Svalbard. Over the Fram Strait fast ice, the surface roughness and thickness histograms show a multi-modal distribution. We examined the data for differences in surface roughness due to prevailing ice-drift conditions or orientation of surface roughness features using histograms of data collected within a 90° window around each of the four cardinal directions, north, south, east and west (e.g.

for north, GPS headings of 315° to 360° and 0° to 45° were used. In Fram Strait, the surface roughness for east to west (E-W) flight sections was slightly greater than observed for the north to south (N-S) flight sections (Figure 5.5e); no directional differences in roughness were observed for the ice north of Svalbard (Figure 5.5e). The survey over the Norske Øer fast ice was predominantly E-W; thus, not enough data were collected N-S to do a comparison for this region. An increase in surface roughness with increasing thickness is observed over the fast ice in Fram Strait (Figure 5.5i) but not for the drift ice in Fram Strait (Figure 5.5h) or the ice north of Svalbard (Figure 5.5g). Note that in Figure 5.5g-i, each data point is the average of a 1 km long section of the airborne survey.

Table 5.2: Total thickness and roughness data measured over the sea ice north of Svalbard, the drift ice in Fram Strait, and the fast ice in Fram Strait. AEM statistics calculated using data coincident with laser scanner observations.

Parameter	North of Svalbard	Fram Strait (excl. fast ice)	Fram Strait fast ice
Modal total thickness (m)	1.1	1.2	1.0
Secondary Modal total thickness (m)	N/A	N/A	3.0
Mean total thickness (m)	1.2	1.4	3.6
Modal surface roughness (m)	0.1	0.1	0.1
Secondary modal surface roughness (m)	N/A	N/A	0.2
Mean surface roughness (m)	0.09	0.16	0.21
Altimeter: % of points with relative surface elevation >0.8 m	0.23	0.42	2.6
Scanner: % of points with relative surface elevation >0.8 m	0.23	0.46	3.4
AEM sensor: % of points with thickness >5 m	0.06	0.19	17

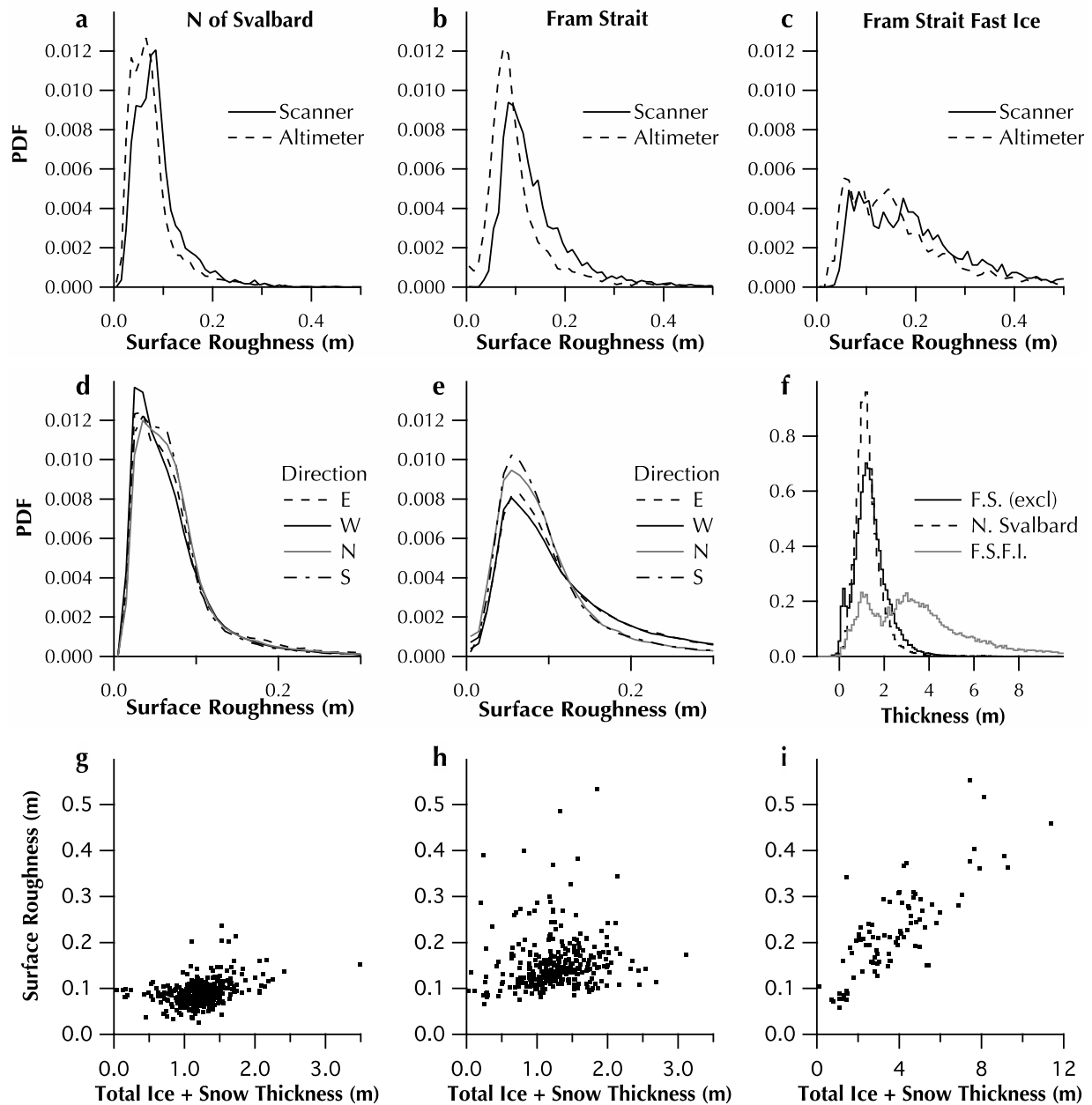


Figure 5.5: (a–c) Statistical distributions of surface roughness for all data collected over the three observed ice regimes, seasonal ice north of Svalbard, FYI/MYI mixture in Fram Strait, and fast ice in Fram Strait. (d, e) Distribution of surface roughness for data collected while flying in different cardinal directions (north, south, east and west). (f) Statistical distribution of total thickness measured by the AEM sensor for the three study regions. (g–i) Comparison of surface roughness and total thickness (snow plus ice thickness) for the three observed ice regimes using average values from successive 1 km sections of flight.

5.6. Discussion

5.6.1. Altimeter vs. Scanner

Ultimately, the scanner has been included into the AEM sensor to improve the processing of AEM data for retrievals of ice thickness; therefore, we have conducted a study into the capabilities and benefits of the scanner over the altimeter. The benefit of the across-track sampling of the scanner over the single beam of the altimeter was substantial but dependent on the purpose and the length scale examined. The scanner was able to identify small surface features, even off-nadir (Figure 5.2, Figure 5.3). It provided returns over smooth open water where the altimeter did not (Figure 5.3), likely because of the interaction of the beams with the surface at multiple angles. The identification of leads is a great benefit in processing AEM data as they are used to calibrate/validate the AEM thickness retrievals. AEM processing currently relies on the average of five laser altimeter measurements to each side of an EM point to determine the average distance between the sensor and the top of the ice (Haas et al., 2009). By utilizing the scanner instead of the altimeter, higher (lower) surfaces off-nadir would decrease (increase) the mean range to the surface over the measurement footprint, increasing the determined thickness of a footprint and vice versa. The scanner also provides a more realistic representation of the ice surface and aids in interpretation of the AEM thickness retrievals, especially in mixed footprint scenarios (e.g. brash ice or small floes off nadir with open water at nadir could be classified as open water by the altimeter even though significant ice exists within the AEM footprint).

To further the comparison of the scanner and altimeter, an examination of the representativeness of laser scanner and altimeter data to each other and of flight sub-sections to entire flights was made by extracting subsections of various lengths from the surface roughness and relative surface elevation data from each of the three regions. The surface roughness was calculated using a 60 m window, roughly the footprint of the AEM sensor at the typical survey height. For each subsection, the starting point was randomly selected and a continuous section extracted. The mean, standard deviation, kurtosis, and skewness of the subsections were compared to the values for the entire flight. Where all of the values from the subsection agreed to within $\pm 5\%$ of the flight values, the length of the subsection was retrieved. For each subsection length, up to 100 random samples were retrieved and tested. Kurtosis is a

measure of the peakiness of a distribution, the amplitude of the modal peak in relation to the strength and length of the tails of the distribution. Skewness is a measure of the asymmetry of a distribution using the relative length and strength of each tail of the distribution. Together, these statistical parameters can describe the shape of the statistical distribution of the dataset.

North of Svalbard, the statistical properties of the surface roughness data for survey subsections 5 km long matched those of the entire survey. The relative surface elevation distribution measured by the altimeter over 5 km long subsections also matched that measured by the scanner. The subsection lengths required to achieve representative statistics in Fram Strait were greater than 15 km. For some flights in Fram Strait, subsections of any length did not reproduce the statistics of the complete flight indicating strong heterogeneity in roughness. This also suggests that the altimeter provided representative measurements in comparison to the scanner in the Nansen Basin north of Svalbard but is less representative in Fram Strait where there is greater heterogeneity in floe size and surface properties. The HEF from the scanner and altimeter did not always agree or converge in Fram Strait (Figure 5.4). North of Svalbard and for the fast ice in Fram Strait it appears that a representative mean roughness value is reached after 1.5×10^5 scanner lines; this is $\sim 25\%$ of all the measurements acquired north of Svalbard and nearly 100% of the measurements over the fast ice. In Fram Strait, one cannot be sure that a representative mean value was observed. These results show that the statistical properties of the ice surface in these regions are non-stationary. Regional differences in the effect of window size on calculating surface roughness (Figure 5.4) reflect the homogeneity of the ice surface roughness. The effect of varying window size is greater for the heterogeneous ice in Fram Strait than for the ice observed North of Svalbard.

While the laser scanner offers numerous benefits over the laser altimeter, the field of view, across-track angle step, and scan-line rate of the scanner should be adjusted to suit the nominal survey height and speed; the current spacing along-track may result in missing small surface features and their dimensions (e.g. maximum ridge heights, small melt ponds, or melt channels). The swath-width of the scanner data at typical AEM survey altitudes varies between 16 and 40 m, narrower than the AEM footprint and most ice floes. Depending on the designated purpose of the laser scanner, the swath width could be increased either by moving the scanner into the

aircraft itself to increase the sampling height, or by conducting dedicated surveys of the sea-ice surface from higher altitudes. Placing the scanner in the AEM sensor provides a fixed, defined orientation for the scanner, altimeter, AEM sensor and DGPS. Because of the high cost of a scanner in comparison to an altimeter, its inclusion and placement is ultimately dependent on its purpose and its potential benefits.

5.6.2. Regional Comparison

Laser scanners can provide new insight into AEM thickness measurements by providing a 2-D look at the ice surface. The laser data reveal that the roughness of the ice in Fram Strait is greater than that north of Svalbard but also found that there was no correlation between thickness and roughness, revealing the importance of local deformation. Hughes et al. (2011) showed that much of the fast ice we observed in Fram Strait in September 2010 had formed in 2008, but their results also suggest that some ice formed in previous years survived the summer break up events; thus, part of the fast ice observed in this study may be more than three years old. AEM surveys over this fast ice revealed greater mean (3.6 m) and modal thicknesses (3.0 m), and mean surface roughness (0.21 m) than the surrounding drift ice (Table 5.2). Furthermore, the HEF was significantly higher for the fast ice than the drift ice in Fram Strait or north of Svalbard (Table 5.2), i.e. the fast ice was more heavily deformed. According to linear regression analysis the fast ice observed in Fram Strait had a strong gradient in the increase in surface roughness with increasing total thickness (0.04 m m^{-1} ; squared correlation coefficient (R^2) = 0.67); the gradients observed for the Fram Strait drift ice or the ice north of Svalbard were insignificant ($R^2 < 0.02$; Figure 5.5g-i). The thickness distribution over the fast ice was multimodal (Figure 5.5f), likely thin FYI attached to the older MYI of different ages. The surface roughness histogram exhibited a similar multimodal distribution (Figure 5.5c). The multimodal distributions and roughness trend with thickness suggest a progression in the development of the fast ice. Over longer length scales the ice surface becomes rougher each successive summer as melt ponds form in topographic lows, i.e. previous melt ponds. Furthermore, ridges form at the edges of the fast ice, especially on the northern side of the Belgica Bank where drifting ice exported through Fram Strait collides with the fast ice. The addition of ice on the margins of the fast ice can lead to ridging and rafting. The weak correlations between thickness and roughness observed here are in contrast to previous

findings for Antarctic FYI by Takenobu et al. (2011) who found high correlations between surface roughness and ice thickness. However, that study was conducted over FYI at the end of winter and in a different drift regime. Their measurements do not include melt-ponded ice, floe edges, or brash ice. Fram Strait is a region of strong deformation due to the convergence of outflow from the Arctic Basin and subsequent rapid outflow through the southern part of Fram Strait. Local deformation likely dominates over the deformation over the lifetime of a particular floe. The presence of melt ponds causes local isostatic imbalance, and early season snowfall may complicate the results from the AEM sensor, as it cannot distinguish between a snow-free and a snow-covered surface.

The observations of total thickness presented in Renner et al., 2013; Renner et al., 2013b; Hansen et al., 2013; and Renner et al., 2014 show the differences in the ice types found in Fram Strait and north of Svalbard; the scanner data provide additional confirmation of the differences observed. North of Svalbard, the ice floes were large and relatively thin; whereas in Fram Strait, the ice was a mixture of smaller FYI and MYI floes with brash ice and rubble. The modal thickness of the Fram Strait drift ice and the ice north of Svalbard differed by only 0.1 m, indicating a high fraction of thin ice in Fram Strait, likely FYI, brash ice, or deteriorated ice (Table 5.2). Similarly, the modal surface roughness for each region was also the same (0.1 m; Figure 5.5d and e, Table 5.2). The greater mean total thickness of 1.4 m observed in Fram Strait compared to north of Svalbard (1.1 m) is caused by the mixture of FYI and MYI in Fram Strait in contrast to mainly FYI north of Svalbard (Renner et al., 2013; Figure 5.5f, Table 5.2). The mean surface roughness is also higher in Fram Strait (0.21 m) than north of Svalbard (0.15 m). Hansen et al. (2013) suggest that in 2010, the dominant input of ice in Fram Strait originated in the Kara and Laptev seas, regions of generally thinner, younger ice in comparison to ice found in the East Siberian Sea, the Makarov Basin, or the Canada Basin. Hansen et al. (2013) also indicate a strong decline in the fraction of thick MYI flowing through Fram Strait over the past two decades. Using a threshold of 0.8 m relative surface elevation as a minimum height for ridged ice, Fram Strait showed twice as many ridges as the area north of Svalbard; less than 1% of the drift ice in Fram Strait and north of Svalbard was identified as ridged ice using the relative surface elevation data or the AEM ice thickness data (Table 5.2). The higher HEF in Fram Strait versus north of Svalbard provides further

evidence of the higher fraction of multiyear ice, of ice ridging and rafting and of the dynamic nature of the region.

5.7. Conclusions

We have presented a method to retrieve relative surface elevation to estimate sea-ice surface roughness from an airborne laser scanner using the scanner data itself to correct for sensor roll. The method does not rely on data from an INS/IMU or DGPS unit. The retrieved relative surface elevation is the difference between the data and a theoretical flat surface representing the local level-ice component of each scan-line. The method is suitable when absolute measurements of surface elevation are not required, such as when examining surface roughness, relative ridge heights, widths, and spatial distributions. The identification of the level ice surface on a scan-line by scan-line basis usually provided reasonable relative surface elevation results. However, some flight sections exhibited striping and variability where a level-ice surface was not present or present in low fractions, such as where ridges run mainly across-track. A potential solution for the line-to-line variability in these situations is to use the method described here to retrieve sensor roll and estimate the local ice surface, then adjust the ice surface elevation of the nadir beam using the H72 processing method. As the H72 method utilizes data over larger distances, the results can provide elevations that are relative to an approximated local water or local level-ice; however, the result is still relative surface elevation. The relative surface elevation retrieved by the H72 method is calculated over a longer distance and thus should provide better estimates of relative surface height where level ice is not present or present in low fractions, reducing line to line biases in the determination of the local level ice. The combination of the two methods would also allow for the estimation of the line-to-line bias in the estimation of the level ice surface.

As a laser scanner is generally more expensive than a laser altimeter, the improved usefulness of a scanner in comparison to an altimeter is dependent on the measurement platform, the survey objectives, and the surface being sampled. We present a comparison of the scanner swath data to a traditionally used single-beam altimeter for measurements collected in 2010 in Fram Strait and north of Svalbard. Furthermore, surface roughness is a highly scale-dependent variable

and can be defined for scales ranging from those of a specific surface feature, over a sea-ice floe or for a region, i.e. from centimeters to kilometers.

Over distances of more than ~ 5 km the laser altimeter provided representative measurements of relative surface elevation in comparison to the scanner for the more homogeneous ice found north of Svalbard. Longer sections of at least 15 km of altimeter data were needed to reproduce the statistical distribution of the scanner data in Fram Strait. In Fram Strait ice roughness was higher for east-west profiles, perpendicular to the main ice drift, than for north-south profiles showing the ice anisotropy in this region with a predominant ridge direction. No such anisotropy was observed north of Svalbard. The sea ice in Fram Strait showed greater thickness and roughness values and wider distributions in both parameters than the ice north of Svalbard. The HEF was twice as high for drift ice in Fram Strait as the ice north of Svalbard. Furthermore, the HEF converged with increasing flight length for the ice north of Svalbard but did not converge for the ice in Fram Strait. This indicates that an altimeter may not always provide a representative estimate of surface roughness or proper estimates of ridge density, etc. in comparison to a laser scanner. The fast ice of the Norske Øer Ice Barrier had a much greater fraction of ridged ice than the drift ice in Fram Strait and north of Svalbard. This fast ice exhibited a strong linear relationship between roughness and thickness that we believe is related to the seasonal changes experienced by the fast ice over multiple years.

Laser scanner measurements offer the potential for new insights into 2-D anisotropy of physical properties of the sea ice surface, improved AEM measurements, improved up-scaling of in-situ to satellite data, and better observations and understanding of the changes in surface roughness that may occur as the Arctic sea ice cover switches to a more seasonal regime. In future work, the method presented here will be refined by the application of the H72 method to the scanner data and by providing more robust information for ridge and melt pond detection, and spatial measurements of their dimensions and orientation.

5.8. Acknowledgements

ASCAT data for Figure 1 were obtained from the NASA sponsored Scatterometer Climate Record Pathfinder at Brigham Young University courtesy of David G. Long (Long et al., 2001). J. F. Beckers is grateful to the Research Council of Norway for funding through the I.S. Bilat. Leiv Eiriksson

Mobility Programme, project (ID #2246777). This study received financial support from the Norwegian Polar Institute's Centre for Ice, Climate and Ecosystems, the Research Council of Norway CORESAT project (ID #222681), and the project "Sea Ice in the Arctic Ocean, Technology and Systems of Agreements" ("Polhavet", subproject "CASPER") of the Fram Centre, Tromsø, Norway. Additional financial support was provided by the University of Alberta, the Canadian Circumpolar Institute, the Canadian Polar Commission, the National Sciences and Engineering Research Council of Canada, Alberta Innovates - Technology Futures, and the Canada Foundation for Innovation. We are thankful to the crew of R/V Lance and the helicopter crew for their tireless help during the campaigns. We thank Hiroyuki Enomoto, Petra Heil, and two anonymous reviewers for feedback that improved the manuscript.

5.9. References

- Comiso JC (2012) Large decadal decline of the Arctic multiyear ice cover. *J. Climate*, 25(4), 1176–1193 (doi: 10.1175/JCLI-D-11-00113.1)
- Dierking W (1995) Laser profiling of the ice surface topography during the Winter Weddell Gyre Study 1992. *J. Geophys. Res.*, 100(C3), 4807–4820 (doi: 10.1029/94JC01938)
- Doble MJ, Skouroup H, Wadhams P and Geiger CA (2011) The relation between Arctic sea ice surface elevation and draft: a case study using coincident AUV sonar and airborne scanning laser. *J. Geophys. Res.*, 116(C8), C00E03 (doi: 10.1029/2011JC007076)
- Eicken H, Grenfell TC, Perovich DK, Richter-Menge JA and Frey K (2004) Hydraulic controls of summer Arctic pack ice albedo. *J. Geophys. Res.*, 109(C8), C08007 (doi: 10.1029/2003JC001989)
- Haas C, Pfaffling A, Hendricks S, Rabenstein L, Etienne J-L and Rigor I (2008) Reduced ice thickness in Arctic Transpolar Drift favors rapid ice retreat. *Geophys. Res. Lett.*, 35(17), L17501 (doi: 10.1029/2008GL034457)
- Haas C, Lobach J, Hendricks S, Rabenstein L and Pfaffling A (2009) Helicopter-borne measurements of sea ice thickness, using a small and lightweight, digital EM system. *J. Appl. Geophys.*, 67(3), 234–241 (doi: 10.1016/j.jappgeo.2008.05.005)
- Hansen E and 7 others (2013) Thinning of Arctic sea ice observed in Fram Strait: 1990–2011. *J. Geophys. Res.*, 118(C10), 5202–5221 (doi: 10.1002/jgrc.20393)

- Hibler WD (1972) Removal of aircraft altitude variation from laser profiles of the Arctic ice pack. *J. Geophys. Res.*, 77(36), 7190–7195 (doi: 10.1029/JC077i036p07190)
- Hibler WD III, Weeks WF and Mock SJ (1972) Statistical aspects of sea-ice ridge distributions. *J. Geophys. Res.*, 77(30), 5954–5970 (doi: 10.1029/JC077i030p05954)
- Hughes NE, Wilkinson JP and Wadhams P (2011) Multi-satellite sensor analysis of fast-ice development in the Norske Øer Ice Barrier, northeast Greenland. *Ann. Glaciol.*, 52 (57 Pt 1), 151–160 (doi: 10.3189/172756411795931633)
- Kurtz NT, Markus T, Cavalieri DJ, Krabill W, Sonntag JG and Miller J (2008) Comparison of ICESat data with airborne laser altimeter measurements over Arctic sea ice. *IEEE Trans. Geosci. Remote Sens.*, 46(7), 1913–1924 (doi: 10.1109/TGRS.2008.916639)
- Kwok R (2009) Outflow of Arctic Ocean sea ice into the Greenland and Barents Seas: 1979–2007. *J. Climate*, 22(9), 2438–2457 (doi: 10.1175/2008JCLI2819.1)
- Kwok R and Rothrock DA (2009) Decline in Arctic sea ice thickness from submarine and ICESat records: 1958–2008. *Geophys. Res. Lett.*, 36(15), L15501 (doi: 10.1029/2009GL039035)
- Kwok R, Cunningham GF and Pang S (2004) Fram Strait sea ice outflow. *J. Geophys. Res.*, 109(C1), C01009 (doi: 10.1029/2003JC001785)
- Kwok R, Spreen G and Pang S (2013) Arctic sea ice circulation and drift speed: decadal trends and ocean currents. *J. Geophys. Res.*, 118(C5), 2408–2425 (doi: 10.1002/jgrc.20191)
- Laxon SW and 14 others (2013) CryoSat-2 estimates of Arctic sea ice thickness and volume. *Geophys. Res. Lett.*, 40(4), 732–737 (doi: 10.1002/grl.50193)
- Long DG, Drinkwater MR, Holt B, Saatchi S and Bertoia C (2001) Global ice and land climate studies using scatterometer image data. *Eos*, 82(43), 503 (doi: 10.1029/01EO00303)
- Maslanik J, Stroeve J, Fowler C and Emery W (2011) Distribution and trends in Arctic sea ice age through spring 2011. *Geophys. Res. Lett.*, 38(13), L13502 (doi: 10.1029/2011GL047735)
- Peterson IK, Prinsenberg SJ and Holladay JS (2008) Observations of sea ice thickness, surface roughness and ice motion in Amundsen Gulf. *J. Geophys. Res.*, 113(C6), C06016 (doi: 10.1029/2007JC004456)

- Rabe B and 8 others (2011) An assessment of Arctic Ocean freshwater content changes from the 1990s to the 2006–2008 period. *Deep Sea Res. I*, 58(2), 173–185 (doi: 10.1016/j.dsr.2010.12.002)
- Rampal P, Weiss J and Marsan D (2009) Positive trend in the mean speed and deformation rate of Arctic sea ice, 1979–2007. *J. Geophys. Res.*, 114(C5), C05013 (doi: 10.1029/2008JC005066)
- Renner AHH, Hendricks S, Gerland S, Beckers J, Haas C and Krumpen T (2013a) Large-scale ice thickness distribution of first-year sea ice in spring and summer north of Svalbard. *Ann. Glaciol.*, 54(62 Pt 1), 13–18 (doi: 10.3189/2013AoG62A146)
- Renner AHH, Dumont M, Beckers J, Gerland S and Haas C (2013b) Improved characterisation of sea ice using simultaneous aerial photography and sea ice thickness measurements. *Cold Reg. Sci. Technol.*, 92, 37–47 (doi: 10.1016/j.coldregions.2013.03.009)
- Renner AHH and 7 others (2014) Evidence of Arctic sea ice thinning from direct observations. *Geophys. Res. Lett.*, 41(14), 5029–5036 (doi: 10.1002/2014GL060369)
- Riegl Laser Measurement Systems (Riegl LMS) (2010) Industrial 2D laser scanner Q120ii datasheet. Riegl Laser Measurement Systems, Horn http://www.riegl.com/uploads/tx_pxpriegldownloads/10_DataSheet_LMS-Q120_20-04-2010.pdf
- Rigor IG and Wallace JM (2004) Variations in the age of Arctic sea-ice and summer sea-ice extent. *Geophys. Res. Lett.*, 31(9), L09401 (doi: 10.1029/2004GL019492)
- Schweiger A, Lindsay R, Zhang J, Steele M, Stern H and Kwok R (2011) Uncertainty in modeled Arctic sea ice volume. *J. Geophys. Res.*, 116(C8), C00D06 (doi: 10.1029/2011JC007084)
- Serreze MC and 9 others (2006) The large-scale freshwater cycle of the Arctic. *J. Geophys. Res.*, 111(C11), C11010 (doi: 10.1029/2005JC003424)
- Spreen G, Kwok R and Menemenlis D (2011) Trends in Arctic sea ice drift and role of wind forcing: 1992–2009. *Geophys. Res. Lett.*, 38(19), L19501 (doi: 10.1029/2011GL048970)
- Takenobu, T, Massom R, Tateyama K, Tamura T and Fraser A (2011) Properties of snow overlying the sea ice off East Antarctica in late winter, 2007. *Deep Sea Res. II*, 58(9–10), 1137–1148 (doi:10.1016/j.dsr2.2010.12.002)

- Tan B, Li Z, Lu P, Haas C and Nicolaus M (2012) Morphology of sea ice pressure ridges in the northwestern Weddell Sea in winter. *J. Geophys. Res.*, 117(C6), C06024 (doi: 10.1029/2011JC007800)
- Von Saldern C, Haas C and Dierking W (2006) Parameterisation of Arctic sea-ice surface roughness for application in ice type classification. *Ann. Glaciol.*, 44, 224–230 (doi: 10.3189/172756406781811411)
- Wadhams P and Doble MJ (2008) Digital terrain mapping of the underside of sea ice from a small AUV. *Geophys. Res. Lett.*, 35(1), L01501 (doi: 10.1029/2007GL031921)
- WaveMetrics (2014) Curve-fitting. In *IGOR Pro 6 manual: Vol. 3, User's guide, Part 2*. WaveMetrics Inc., Lake Oswego, OR, 158–234 <http://www.wavemetrics.net/doc/igorman/III-08%20Curve%20Fitting.pdf>

6. Retrievals of Lake Ice Thickness From Great Slave Lake and Great Bear Lake Using CryoSat-2

6.1. Abstract

Satellite observations have revealed decreases in the duration of the seasonal snow and ice coverage of Great Slave Lake (GSL) and Great Bear Lake (GBL), large freshwater lakes in Northern Canada. However, limited information is available about ice thickness changes. Here, we present and validate a method to retrieve lake ice thickness using the CryoSat-2 (CS2) radar altimeter. These are the first satellite altimeter retrievals of lake ice thickness. Under optimal conditions, the CS2 signal is scattered from both the snow–ice and the ice–water interfaces, with returns from each interface being of sufficient power to be identified in the radar waveform. The distance between the scattering horizons is used to determine the ice thickness, similar to traditional ground penetrating radar measurements. The seasonal evolution of ice thickness of GBL and GSL is compared with in situ measurements, modeled ice thicknesses, and previous studies. The impact of ice and snow properties on signal penetration and the thickness retrieval are examined with synthetic aperture radar imagery. The CS2 ice thickness retrievals are able to observe the seasonal thickening of the lake ice and closely match the in situ measurements over both lakes ($R > 0.65$, $RMSE < 0.33$ m). Thickness retrievals of thin ice are limited by a minimum waveform peak separation of 2 range bins, approximately 0.26 m in ice. Although not designed for lake ice studies, CS2 and future SAR satellite altimeter missions offer new possibilities to monitor the ice and water levels of climatically sensitive and influential lakes.

6.2. Introduction

Lakes in North America’s Arctic and sub-Arctic regions cover between 15% and 40% of the landscape and play an important role in the climate of the region [1]–[6]. Arctic and sub-Arctic lakes are important to local communities and their economies, for hydroelectric power generation, and as wildlife habitats [7]. The phenology of the ice, i.e., the timing of freeze-up and break-up of the ice and snow covers, has been extensively studied as an important indicator of climate variability and change [6], [8], [9]. Additionally, lake ice is extensively used as a platform for fishing, hunting, and travel; therefore, knowledge of its thickness is critical for safe usage.

Recent studies suggest that with continued warming, Arctic and sub-Arctic lakes will experience reductions in ice thickness and the number of days the lakes are ice covered. Reference [9] showed that the duration of the ice cover will be reduced by 15–30 days between the time periods of 1961–1990 and 2041–2070 using simulations from the Canadian Regional Climate Model and the Canadian Lake Ice Model (CLIMo); a corresponding decrease of 5–60 cm in the mean maximum ice thickness was also predicted. Most studies of Arctic and sub-Arctic lakes have observed spatial and temporal changes of areal ice coverage using satellite imagery from optical, synthetic aperture radar (SAR), and passive microwave sensors (see [1], [2], [8], [10], [11]) because these methods are able to observe large regions with high temporal resolution where extensive in situ measurements are not feasible. However, these sensors are unable to observe water levels or ice thickness, and therefore little information on these variables is available. Here we show that lake ice thickness can be measured by means of satellite radar altimetry.

Satellite radar altimetry has been used in many studies to monitor lake water levels and volume [12]–[14]. These studies observed large noise in the water-level retrievals in winter assumed to be caused by the penetration of the radar signals into the ice; however, they did not examine the potential of this behavior to retrieve ice thickness from radar reflections from the bottom of the ice. During winter, observations of radar altimeter backscatter σ° were used in [15] and [16] to determine whether or not the lake surface was ice covered. The large footprint and coarse spatial resolution of older pulse-limited radar altimeters has allowed only for observations of large lakes such as the “Great Lakes” in Canada.

In this paper, we will demonstrate that Ku-band radar altimeter measurements from the CryoSat-2 (CS2) satellite can be used to retrieve lake ice thickness by identifying radar reflections from the ice surface and ice bottom and subtracting the travel times of the radar signals between these two surfaces. This paper presents the first satellite altimeter retrievals of lake ice thickness. This paper is organized as follows. In Section 6.3, the variables and equations governing radar penetration into snow and lake ice are discussed. Section 6.4 describes the study sites and the data used to retrieve and validate ice thickness. Section 6.5 examines the phenology of CS2 waveforms over lake ice. Section 6.6 presents the CS2 thickness retrieval algorithm. Section 6.7

presents the influence of ice properties on the CS2 retrieval algorithm. Section 6.8 compares the seasonal evolution of ice thickness from Great Slave Lake (GSL) and Great Bear Lake (GBL) retrieved by CS2 with in situ observations and a simple freezing degree day (FDD) model. Finally, in Section 6.9, we discuss the potential of the method and the advantages offered by CS2 along with suggestions for future studies and improvements to the method and provide concluding remarks.

6.3. Radar Penetration Into Snow and Ice

As our method is dependent on the identification of radar reflections from the ice surface and bottom, we briefly highlight the properties that influence the penetration of radar signals through snow and ice. According to [17], the maximum depth of penetration δ_p of a radar signal into a medium can be approximated by

$$\delta_p = \frac{\lambda_0}{4\pi} \left\{ \frac{\epsilon'}{2} \left[\left(1 + \left(\frac{\epsilon''}{\epsilon'} \right)^2 \right)^{1/2} - 1 \right] \right\}^{-1/2} \quad \text{Eq. 6.1}$$

where δ_p is dependent on the wavelength of the radar wave in free space λ_0 and the real and imaginary parts of the complex dielectric constant of the medium, ϵ' and ϵ'' . The real part of the dielectric constant of ice, ϵ'_i , is largely independent of frequency between 10 MHz and 300 GHz and is only slightly influenced by the temperature (T_i) of ice [18], [19]

$$\epsilon'_i = \begin{cases} 3.1884 + (9.1 \cdot 10^{-4}) \cdot T_i, & -30^\circ\text{C} < T_i \leq 0^\circ\text{C} \\ 3.1, & T_i \leq -30^\circ\text{C} \end{cases} \quad \text{Eq. 6.2}$$

Losses due to scatter are ignored by (1), and therefore, (1) only places an upper limit on the maximum depth of penetration. ϵ''_i is determined using the equations of [20] as published in [19]. Using these equations and ignoring scattering losses, the maximum penetration depth of Ku-band radar waves with a frequency of 13.65 GHz in freshwater ice is between 4.9 and 8.4 m at temperatures between 273.16 and 243.16 K. However, the presence of wet snow with as little as 1% volumetric liquid water content limits the penetration of Ku-band waves to less than 0.2 m [21]. Furthermore, lake ice is primarily congelation ice that may or may not contain significant air bubbles [22]. References [25]–[27] have shown that surface scattering due to the roughness of the ice/water interface, not double bounce from air bubbles as suggested by past studies, is the primary scattering mechanism over lake ice; double bounce and volume scattering caused by air

bubbles can also contribute to the overall scattering of the radar wave. Finally, in shallow areas where the ice may freeze to the lake bed, the dielectric contrast between the lake bed and the ice (≈ 8) is much smaller than between the water and ice (≈ 80), limiting the scattering of the Ku-band waves back to the satellite sensor from the ice bottom interface [28].

In addition to scattering within the ice, [29]–[34] have shown that the snow pack and surface roughness can lead to scattering of Ku-band radar waves. Furthermore, surface roughness features such as ridges can increase backscatter and influence altimeter measurements of the ice surface height by increasing noise and backscatter in the vicinity of the level ice surface. Ice lenses, large depth hoar crystals, snow density changes, and snow wetness can lead to scattering radar waves from within the snow pack rather than just at the snow/ice interface. These snowpack features also influence the penetration depth, propagation velocity, and scatter of the radar waves.

The propagation velocity (3) and the wavelength of the radar waves traveling through the ice and snow (4) are also dependent on ϵ

$$c_m = \frac{c}{\sqrt{\epsilon_m}} = \frac{c}{n_m} \quad \text{Eq. 6.3}$$

$$\lambda = \frac{1}{\sqrt{\epsilon_m}} \cdot \frac{c}{f} \quad \text{Eq. 6.4}$$

where c_m is the speed of light in a medium, c is the speed of light in free space, $299792458 \text{ m}\cdot\text{s}^{-1}$, f is the radar frequency in hertz, n_m is the refractive index of the medium at a given wavelength or frequency, and ϵ_m is the dielectric constant of the medium. Values of n_m for freshwater ice are provided in [35], which updated the optical constants of ice at microwave frequencies using data from [19]. The refractive index of ice n_i is 1.7861 at Ku-band [35]. The wavelength of the CS2 signal in ice is nearly half of that in free space (Eq. 6.4).

6.4. Data and Methods

6.4.1. Study Area

GBL (66°N , 120.5°W) and GSL (61.75°N , 114°W) are the two largest lakes in sub-Arctic Canada, with the surface areas of $31.1 \times 10^3 \text{ km}^2$ and $28.6 \times 10^3 \text{ km}^2$ [8]. GBL and GSL are located within the Mackenzie River Basin in the Northwest Territories (NWT) (Figure 6.1). During the study period, air temperatures ranged from low temperatures of -43°C in the winter to $+31^\circ\text{C}$ in the

summer. Both lakes are seasonally covered with ice, GBL from late November to July and GSL from December to early June [8]. The maximum ice thicknesses of GSL and GBL are typically ~ 1.2 and ~ 1.5 m, respectively [10], [36].

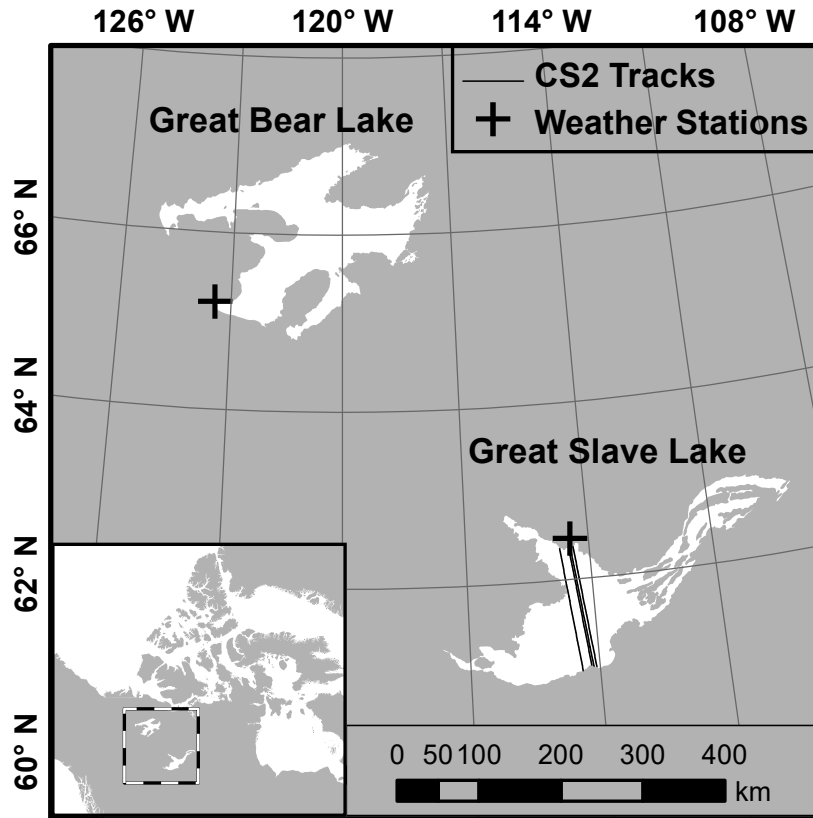


Figure 6.1: Map of GSL and GBL. The locations of weather stations used for FDD ice thickness modeling are shown by crosses. Tracks of four CS2 orbits plotted in Figure 6.2, Figure 6.3, and Figure 6.5 are shown by the black lines. Shoreline and islands data are from the GSHHG database v2.2 [37].

6.4.2. Data

6.4.2.1. CS2 Data

CS2 was launched by the European Space Agency (ESA) in 2010. CS2 carries the Synthetic Aperture Interferometric Radar Altimeter (SIRAL), a dual-antenna interferometric delay–Doppler radar altimeter system operating at 13.575 GHz (Ku-band) [38]. The SIRAL has three main operation modes: low-resolution mode (LRM), SAR mode, and SAR interferometric (SARIN) mode. In the LRM mode, operated over the open oceans, CS2 functions as a traditional pulse-limited radar altimeter [38], [39]. In the SAR mode, used over sea ice and the interior of the

continental ice sheets, bursts of coherently transmitted radar pulses are processed into narrow beams using SAR processing, resulting in a small beam-limited footprint ~ 300 m along track and ~ 1650 m across track [38], [40]. This is much smaller than the nominal footprint of ~ 2 to ~ 10 km of traditional pulse-limited radar altimeters such as those operated on ERS-1/2 and Envisat. In the SARIN mode, SAR processing is combined with measurements of the across-track phase angle made by the second antenna, allowing for the determination of the across-track position of the reflecting point of closest approach. Over GSL and GBL, CS2 collects data in the SARIN mode only.

CS2 SARIN mode Level 1B (L1B) Baseline B data were acquired from ESA for the period July 2010-June 2014. These data include waveform information, representing time-resolved measurements of the backscattered energy. These are provided at a sampling frequency of 20 Hz (~ 300 m) along track together with all geophysical and instrument corrections. A single SARIN L1B Baseline B waveform consists of 512 measurements of the return signal power over time, called range bins (see Figure 6.2). All instrument corrections have already been applied in the ESA L1B data set. Data over the lakes were extracted from each orbit passing over the lake. A 1-km buffer inside the shoreline and outside of islands identified in the Global Self-consistent, Hierarchical, High-resolution Geography (GSHHG) shoreline database [37] within GSL and GBL was applied to minimize the contribution of land and decrease off-nadir snagging [41]. Snagging occurs when across-track variations in surface properties and backscatter result in a peak in backscatter away from nadir [41], increasing the two-way travel time to the location of the backscatter peak.

6.4.2.2. *In Situ Ice Thickness Data*

Ice thickness and snow depth were measured weekly in drill holes on GSL near Yellowknife, NWT, between November and May since 1958 as part of the Canadian Ice Thickness Program (CITP) of the Canadian Ice Service [36]. There is no routine monitoring of ice thickness on GBL.

6.4.2.3. *Auxiliary*

As in situ validation data are extremely limited, a simple temperature-index-based FDD ice thickness model [42] was used to model ice thickness h_i using

$$h_i = \alpha \sqrt{\sum FDD} \quad \text{Eq. 6.5}$$

where α is usually calculated from the thermal conductivity of the ice κ_i , the density of the ice ρ_i , and the latent heat of ice λ_L

$$\alpha = \sqrt{\frac{2 \times \kappa_i}{\rho_i \cdot \lambda_L}}. \quad \text{Eq. 6.5}$$

Here we have used α as a calibration parameter rather than making assumptions about ice density and the thermal conductivity of the ice. The drill hole data and air temperature data from Yellowknife, NWT, were used to calibrate the FDD model using the Levenberg–Marquardt nonlinear least-squares fitting [43] to find the value of α . For the entire 2010 through 2014 time series of drill hole data, $\alpha = 1.8742$, which is within the range of typical values for snow-covered lakes reported in [42]. This α value was then used to calculate ice thickness for GSL and GBL using the air temperature data from Yellowknife, NWT, for GSL and Deline, NWT, for GBL. The weather station data were acquired from the Historical Climate Data Archive of Environment Canada [44].

Envisat ASAR wide swath mode images were acquired over the lakes between January and April 2012 to aid in interpretation of the waveforms and the thickness data. Although operating at a longer wavelength than CS2, the C-band backscatter data from Envisat ASAR are also impacted by ice roughness and air bubble content.

6.5. Phenology of Seasonal CS2 Waveform Shapes over Lakes

Figure 6.2 presents profiles of waveform data from four passes over GSL (shown on the map in Figure 6.1) on January 12, April 7, May 6, and July 28, 2013, representing early season ice, late season ice, early ice melt, and open water, respectively. Figure 6.2(a) clearly shows two peaks in power separated by a distance of approximately 1.5 m. Most likely, these peaks represent scattering from the ice surface and ice bottom early in the lake ice growth season. The same peaks can be seen in Figure 6.2(b), but they are ~ 3.0 m apart, interpreted as the same reflections as in Figure 6.2(a) but for thicker ice late in the growth season. However, the propagation velocity of light in ice is less than in a vacuum; thus, the true distances between the two peaks in Figure 6.2(a) and (b) are approximately 0.8 and ~ 1.6 m, respectively, well within the range of expected values for the thickness of the ice cover on GSL at the respective seasonal stages of growth. Under cold and thus dry conditions, we assume that the Ku-band signal typically penetrates the snow

and scatters from the snow/ice interface [29], [45]. Other studies of CS2 data over Arctic sea ice have suggested that signal penetration through snow can be incomplete and spatially and temporally variable [46]; thus, this assumption may not be valid for all waveforms.

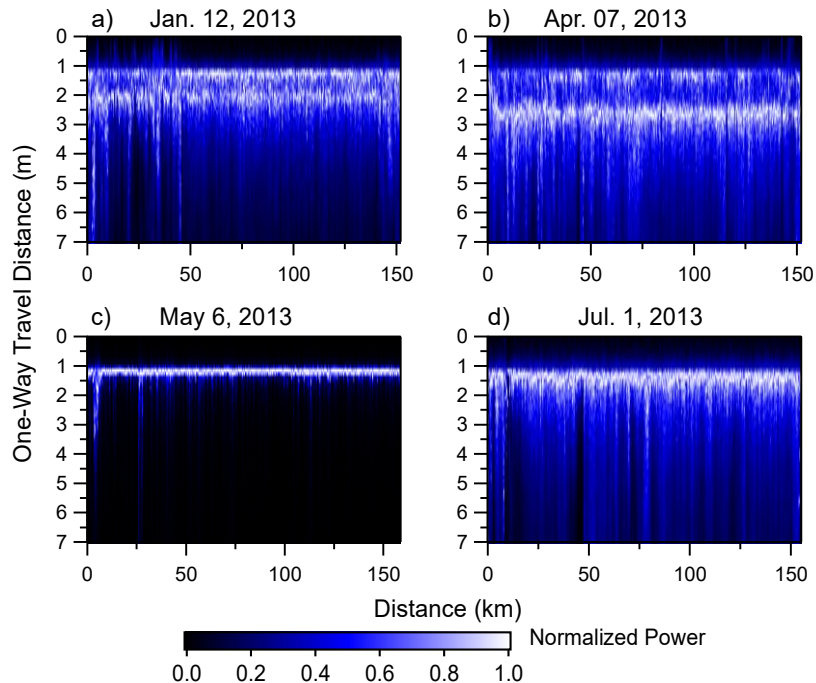


Figure 6.2: CS2 L1B waveform data from four orbits over GSL on (a) January 12, (b) April 7, (c) May 6, and (d) July 1, 2013, representing early season ice, late season ice, early snow/ice melt, and open water, respectively. The normalized power from 0.0 to 1.0 is displayed by the color scale with white representing 1.0. The one-way travel distance of the signal is displayed on the y-axis and the distance in kilometers along the track is displayed on the x-axis. The one-way travel distance is determined using the speed of light in free space and is calculated for range bins 140 (0 m) to 200 (14 m).

Some individual waveforms show modest power levels before the first peak, e.g., between 25 and 50 km in Figure 6.2(a). The increase in power before the first power peak arising from the ice surface may be the result of scattering within the snowpack or from surface roughness features in the CS2 footprint, or other noise. Variability in the location of the peaks depends on the dielectric properties of the snow and ice and other properties like surface roughness. Regions of rough ice can result from ice deformation early in the growth season. Large metamorphosed snow crystals, ice lenses, and strong changes in snow density/structure may lead to scattering of the radar signal from within the snow pack [23], [24], [26], [31], [32], [34], [46]. In addition, the variable presence, size, and density of air bubbles in the upper and lower layers of the ice can

lead to scattering from within the ice layer although the dominant source of scattering is a rough ice/water interface [26]. Transmitted energy penetrates through the snow and ice to the ice/water interface where the high dielectric contrast between ice and water causes scattering. Although the second peak is much noisier, a linear pattern parallel to the expected bottom of the ice is distinguishable along the orbit in both Figure 6.2(a) and (b). The noise in the location of the second peak is likely due to variations in thickness and from different scattering contributions.

Figure 6.2(c) shows data from just after the onset of snow melt when average daily air temperatures at Yellowknife had just become positive. The Landsat imagery from May 8 and May 13, 2013 (not shown) indicates that GSL was still ice covered but that snow and/or ice melt had begun. The single and high power peak, the low variability in the location of the peak, the sharp decline in power after the peak, and low power in the tail of the waveform all indicate that the scattering horizon originates from the snow or ice surface, and that there is little to no radar penetration through the ice or possibly no penetration through the snow pack due to the presence of liquid melt—water.

Figure 6.2(d) shows the response of the ice-free lake surface, with a strong peak but with considerable variability in the location of the peak. In this case, water waves create surface roughness, which increases the spread in the location of the peak and results in more diffuse waveforms with higher power in the tail of the waveform representing off-nadir reflections [39]. This waveform phenology is also observed over open ocean [39].

Figure 6.3 presents the maximum power in watts for a subset of the waveforms presented in Figure 6.1 and Figure 6.2. Waveforms from May 6, 2013, representative of wet snow conditions, have the highest maximum power and are clearly separated from the others. The high power supports the assertion that there was minimal signal penetration into the snow and ice and that therefore these waveforms are returned from the air/wet snow surface with its strong dielectric contrast. Variability in the maximum power for this date could be indicative of variable absorption within the snow pack due to variations in wetness or variability in the roughness of the air/snow interface. These waveforms have much higher maximum power than the others, which provides a potential method for the detection of snow melt. Waveforms from early in the

ice season (January 12, 2013) have the next highest maximum power and are substantially more powerful than those from the late season (April 7, 2013).

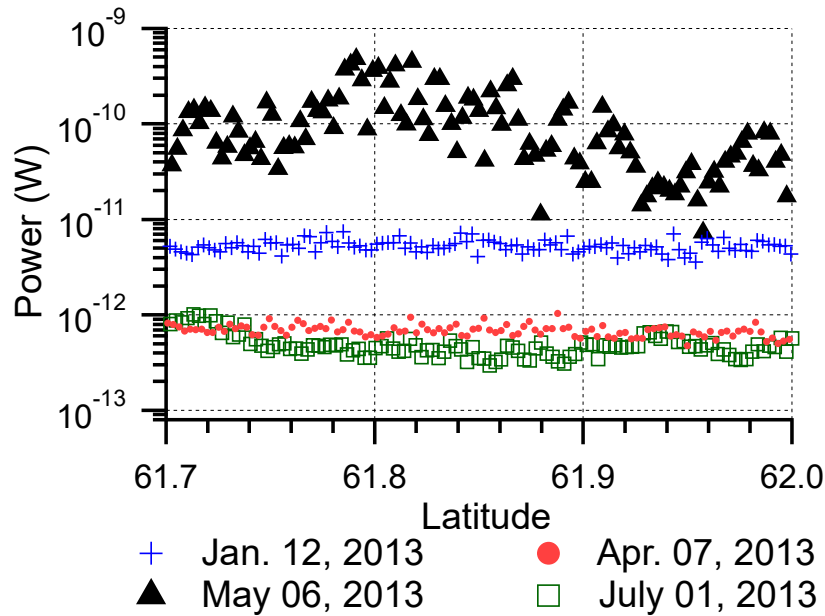


Figure 6.3: Maximum power (watts) of each waveform for the CS2 orbits shown in Figs. 1 and 2. Only a subset of the waveforms in each orbit is shown for clarity.

As the ice thickens, there is increased scattering and absorption loss as the Ku-band signal moves through more ice and potentially more air bubbles [24], [26]. While theoretically this suggests that it may be possible to retrieve ice thickness from the change in maximum power, the situation is complicated by variability in the air bubble density of the ice as well as minimal separation with the open water waveforms from July 1, 2013. An examination of calibrated radar backscatter, σ° , from the CS2 Level 2 products showed similar patterns in the separation of backscatter throughout the ice season. Finally, pulse peakiness (PP) [38], [46], a measure of the amount of power in the peak compared with the rest of the waveform, also showed similar patterns along the orbit

$$PP = \frac{\max(power)}{\sum_{j=1}^{j=512} power_j} \cdot 512.0 \quad \text{Eq. 6.7}$$

In agreement with maximum power (Figure 6.3), PP was highest on May 6, 2013 during snow melt ($20 \leq PP \leq 219$). The next highest PP values during the ice season ranged from 5 to 40 on January 12, 2013 and from 5 to 23 on April 7, 2013. As observed with the highest maximum power presented in Figure 6.3, there was very little separation between April 7, 2013 and July 1, 2013.

On July 1, 2013, when the lake was ice free, PP values ranged from 8 to 97. The PP values on July 1, 2013 vary widely and for some waveforms are higher than the values for April 7, 2013. The typical values of PP used to discriminate Arctic sea ice from open water leads are $PP \geq 40$ for leads and $PP \leq 10$ to discriminate open ocean [46]. PP has also been proposed as a metric for distinguishing multiyear sea ice from first-year sea ice [48]. Over the lakes PP may be useful for detecting snow melt, but not for distinguishing between open water and ice or for distinguishing between different ice thickness.

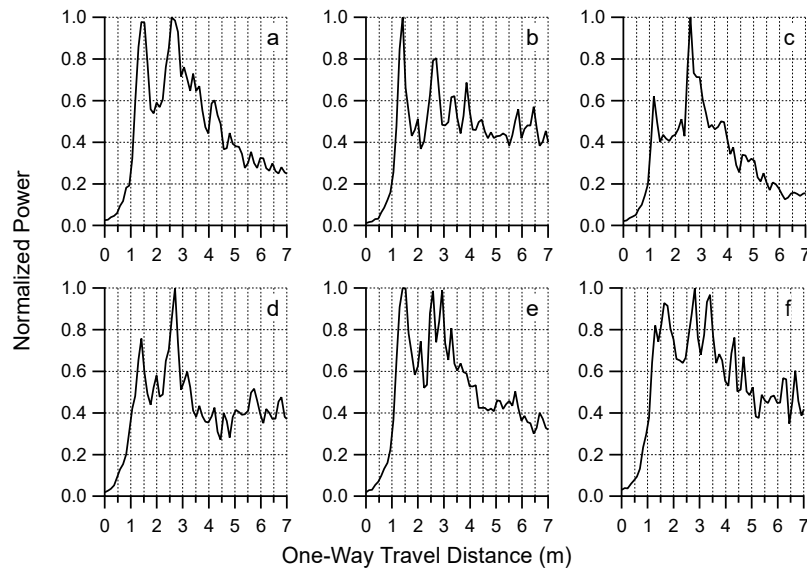


Figure 6.4: Six waveforms (a–f) from the CS2 L1B SARIN mode pass over GSL on April 7, 2013, illustrating the variability in relative power of the peaks, peak and signal noise, and the resulting challenges to retrieving the location of the power peaks originating from the ice surface and ice bottom. The normalized power is displayed on the y-axis and the one-way travel distance of the signal is displayed on the x-axis. The one-way travel distance is determined using the speed of light in free space and is calculated for range bins 140 (0 m) to 200 (14 m).

6.5.1. Characteristic CryoSat-2 Waveforms over Lake Ice

Identifying the power peaks associated with the snow/ice and ice/water interfaces in the CS2 waveforms is critical to the calculation of ice thickness and is complicated by the various scattering features and properties of the snow and ice. Figure 6.4(a)–(d) shows waveforms where it is rather straightforward to identify the returns from the top and bottom of the ice as there are two peaks that are much more pronounced than all the others. However, it is interesting to note that the relative strength of the first and second peaks is not constant, i.e., sometimes the first peak is more powerful than the second, and vice versa. The waveforms in Figure 6.4(e) and (f)

represent those where it is considerably more difficult to extract the peak power from the snow/ice and ice/water interfaces. In Figure 6.4(e), the snow/ice interface peak is clearly identifiable, but the ice/water interface is more difficult to detect as there are two peaks with the same high power separated by just 3 range bins. A priori information based on neighboring waveforms or preceding overpasses suggests that the peak at range bin 5.0 m is the ice bottom reflection. However, it is also possible that this peak results from air bubbles within the ice or near the ice bottom. Figure 6.4(f) presents an even more challenging waveform for peak extraction. The location of the first peak is now blurred and the two peaks at ~ 1.5 and 3.0 m may represent the snow and ice surfaces, respectively, based on their separation and the typical winter snow depths of 0.2 m to 0.3 m. Again, there are two peaks with high power values, at ~ 5.7 and 6.8 m, which possibly represent the ice/water interface.

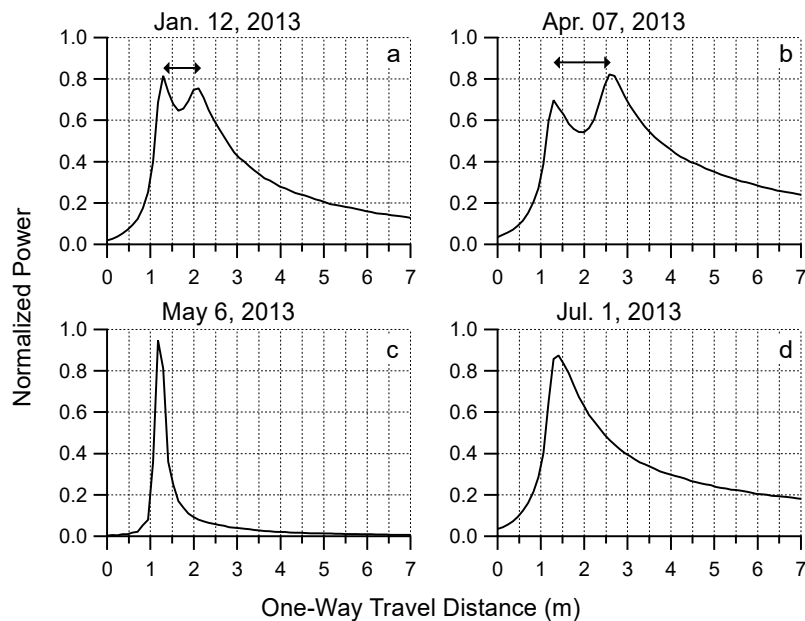


Figure 6.5: Mean waveforms from each of the four orbits over GSL presented in Figure 6.2, January 12, April 7, May 6, and July 1, 2013, representing (a) early season ice, (b) late season ice, (c) early ice melt, and (d) open water, respectively. The mean normalized power is displayed on the y-axis and the one-way travel distance of the signal is displayed on the x-axis. The one-way travel distance is determined using the speed of light in free space and is calculated for range bins 140 (0 m) to 200 (14 m). The horizontal lines in (a) and (b) indicate how ice thickness is calculated as the difference in the one way-travel distance of the peaks.

Given the multi-peaked character of these waveforms, the peak extraction algorithm needs to be robust but cautious. In addition to assessing multiple methods for selecting peaks (see

Section 6.6), we also implemented an along-track averaging approach. Successive waveforms (33 waveforms $\cong 10$ km) are averaged to provide an along-track averaged waveform. Although along-track averaging, similar to “stacking,” reduces the spatial resolution of the ice thickness estimates, it greatly reduces the uncertainty in the peak identification and thus in the ice thickness results (see Section 6.8). Along-track averaging smooths out less common peaks while enhancing the most common peaks, as can be seen by comparing the peaks from individual waveforms presented in Figure 6.4 and the orbit mean waveforms presented in Figure 6.5(a) and (b) and the 10-km along-track averaged waveforms in Figure 6.6.

Figure 6.5 shows the mean waveform calculated from all waveforms over GSL from each of the orbits shown in Figure 6.2. Figure 6.5(a) and (b) clearly shows the dual peaked nature of the mean waveforms over ice, with the distance between the peaks increasing through the winter as the ice thickens. Figure 6.5(c) presents the very narrow peaky return from a wet dielectrically lossy surface; very little energy is returned after the peak. Figure 6.5(d) illustrates a typical diffuse open water or Brownian waveform [39]. The mean waveforms provided in Figure 6.5(a) and (b) suggest that picking out the location of the two peaks is straightforward. However, roughness of the snow/ice and ice/water interfaces, snow moisture content, and scattering from the snow and air bubbles within the upper and lower layers of the ice introduces noise and complicates the ice thickness retrieval, especially from individual waveforms. The influence of air bubbles and surface roughness on the peak retrievals was exhibited in Figure 6.4, and is discussed again in Section 6.7.1 and Figure 6.6.

6.6. Ice Thickness Retrieval Algorithm

Whereas sea ice thickness retrievals are based on estimates of sea ice freeboard and conversion into ice thickness assuming isostatic balance, here we retrieve lake ice thickness from the radar travel time difference between the ice surface and bottom.

This is dependent on the correct identification of reflections from the ice surface and ice bottom in the CS2 L1B waveforms and application of the correct radar propagation speed through the ice. Reflections from these surfaces were identified by peaks in the waveforms. Peaks were defined as local maxima. We developed and tested numerous peak identification and filtering algorithms, which are briefly described here. We performed two types of analysis, full resolution

(waveform by waveform) and along-track averaging of waveforms. The methodology and results for each type are described separately.

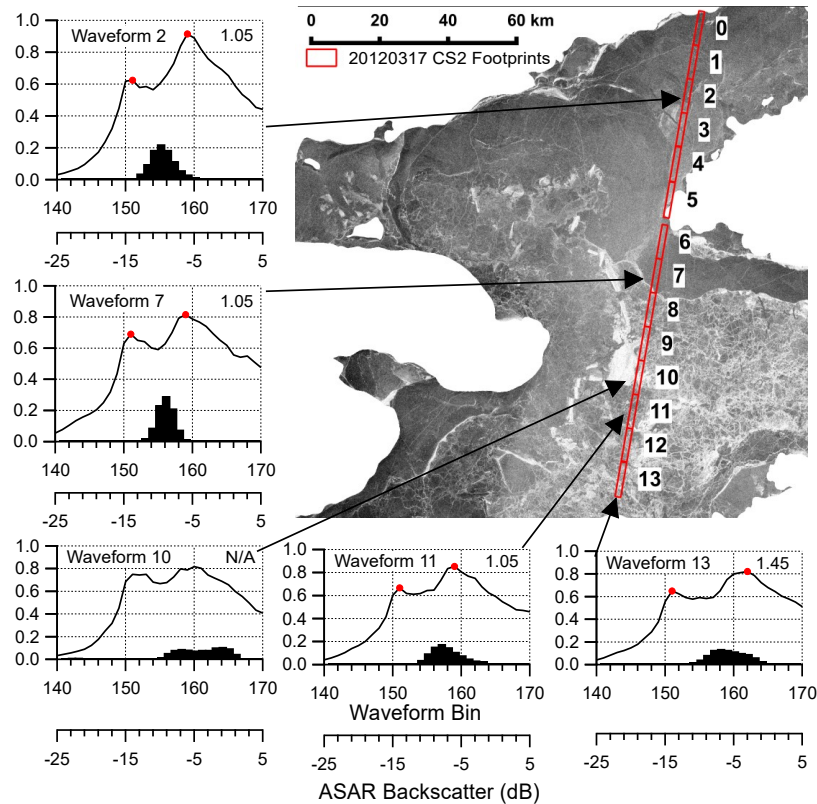


Figure 6.6: Envisat ASAR image of GBL acquired on March 15, 2012 overlain with the 10-km-long, 1.65-km-wide CS2 10 km mean waveform footprints from March 17, 2012. Subplots surrounding the map present the selected CS2 10-km mean normalized power waveforms and Envisat ASAR backscatter histograms for the pixels within the footprint of each CS2 10-km mean waveform. In the ASAR image, high backscatter is bright and low backscatter is dark. The circular markers in the normalized power waveform plots indicate the peaks in power used to calculate ice thickness. (Top right) Inset value within each histogram and waveform subplot is the retrieved ice thickness.

6.6.1. Full-Resolution Peak Selection

Waveforms were converted to normalized power and truncated to range bins 135 and 185 to limit the detection of false peaks. The truncation of the waveforms was performed after examining plots like those in Figure 6.2 that showed that the two strongest peaks fall well within this bin range. In accordance with classical thresholding approaches (see [46], [47]), we tested different peak power thresholds of 0.50 to 0.95 in 0.05 steps to identify true peaks from noise. Figure 6.4 and Figure 6.5 show that the relative power level of the two peaks representing the ice surface and ice bottom is not constant and that there can be more than two peaks. In order

to automatically select the two peaks associated with the ice surface and ice bottom, we tested several peak selection criteria including selecting the first peak and the most powerful peak ($P = F \&MPP$), the first two peaks ($P = FTP$), and the most powerful two peaks ($P = MPP$) in each waveform. For $P = F \&MPP$, if the first peak is also the most powerful peak in the waveform, the second most powerful peak is selected as the second peak. Next, in order to further reduce noise, we tested three different criteria for the number of peaks (N_{peaks}) detected in each waveform ($N_{peaks} = 2$, $N_{peaks} \geq 2$, and $2 \leq N_{peaks} \leq 3$). In addition, some local maxima are very small and located between the two powerful peaks associated with the ice surface and ice bottom, as can be seen in Figure 6.4(b), (d), and (e). Waveforms with peaks separated by a shallow trough, where the difference in normalized power of the two selected peaks and the minimum power in the range bins between them was less than 0.1, were rejected. For both lakes, selecting the first peak and the most powerful peak ($P = F \&MPP$) from waveforms with two or more peaks ($N_{peaks} \geq 2$) above a normalized power threshold of 0.5 resulted in strong correlations between the CS2 derived ice thickness estimated and the in situ ice thickness data and was the method selected for the full-resolution analysis presented in Section 6.8.1.

6.6.2. Along-Track Average Waveform Peak Selection

In addition to the full-resolution peak selection, we also performed along-track averaging (stacking) of the normalized power returns over 33 waveforms, spanning a distance of approximately 10 km along track. Along-track averaging reduces noise in the normalized power waveforms by smoothing out variations in power, as can be seen by visually comparing the individual waveforms from the same orbit in Figure 6.4 and the orbit mean waveform in Figure 6.5(b). We selected along-track averaged waveforms with two or more peaks ($N_{peaks} \geq 2$) and selected the two most powerful peaks ($P = MPP$) above a minimum normalized power of 0.5. For the averaged waveforms, $P = MPP$ provided stronger correlation coefficients with in situ thickness data than $P = F \&MPP$; in many cases, the two algorithms will identify the same peaks. Once peaks have been identified, the calculation of ice thickness was performed per the procedure outlined in Section 6.6.3.

6.6.3. Ice Thickness Calculation

Following the selection of peaks representing the ice surface and ice bottom in both the full-resolution and along-track averaged waveforms, the following filtering rules were applied to the data and ice thickness was calculated.

- 1) For the full-resolution waveforms, the local minimum or the position where the normalized power of successive range bins changed by less than 0.02 was identified to the left of both selected peaks. Waveforms where the difference in normalized power of each selected peak and the preceding trough was less than 0.05 were rejected. For the averaged waveforms, the local minimum was identified to the left of both selected peaks and waveforms where the difference in normalized power of each peak and the preceding trough was less than 0.05 were rejected.
- 2) For the full-resolution waveforms, the data were filtered to remove any waveforms where the one-way travel distance between the selected peaks was outside the range of the mean difference \pm the mean absolute deviation of the one-way travel distance for all peak pairs in the entire orbit, provided peaks were successfully identified for more than one waveform. Filtering of peak difference results was not performed for the along-track averaged waveforms as the number of points was reduced by the averaging process.
- 3) For the full-resolution waveforms, the differences of the one-way travel time of the first and second peaks were smoothed using an 11 point moving window average. Smoothing of peak difference results was not performed for the along-track averaged waveforms as the data has already been smoothed by the averaging process.
- 4) The one-way travel distance between two peaks, i.e., ice thickness, was calculated using the propagation velocity of light in ice using (Eq. 6.2) and (Eq. 6.3) and the air temperature from the weather station data [44]. We assume that the ice is isothermal and that the temperature of the ice is equal to the air temperature measured at the weather stations. Neither of these assumptions is true, but (Eq. 6.2) is so insensitive to temperature that the resulting error in ice thickness is negligible. Note that no retracking, i.e., interpolation or fitting of the waveform to provide for subrange bin

vertical resolution as is done in classical ice freeboard retrievals (see [31], [46], [47], [49]), was performed. The ice thickness h_i is calculated using

$$h_i = \Delta P \times c_i / (4 \times \beta) \quad \text{Eq. 6.8}$$

where P is the difference in the range bin location of the two peaks, c_i is the propagation velocity of light in ice, and β is the radar bandwidth of CS2, 320 MHz.

6.7. Algorithm Validation and Analysis

6.7.1. Impact of Ice Properties

Figure 6.4 and Figure 6.5 provided examples of noise complicating the identification of the peaks representing the ice surface and bottom reflections. Here, we use SAR imagery to qualitatively attribute this noise to variable surface roughness and air bubble content. Figure 6.6 shows radar backscatter observed by Envisat ASAR (C-band) over GBL in March 2012. C-band has a longer wavelength than Ku-band, 0.057 m versus 0.022 m, and is less sensitive to small- or fine-scale roughness features than Ku-band; therefore, areas with high variability in backscatter observed on the C-band SAR image would indicate that the selection of ice surface and bottom peaks from coincident CS2 waveforms is likely to be affected by noise. Radar backscatter over freshwater ice is primarily controlled by surface roughness, the dielectric contrast between the ice and underlying medium (be it liquid water or soil in the case of grounded ice), and the physical and dielectric properties of the ice and its snow cover. In Figure 6.6, five mean CS2 waveforms are shown along with the histogram of C-band backscatter over the 10 km along-track \times 1650 m across-track CS2 footprint. It should be noted that of the seventeen 10-km mean waveforms along this orbit, the algorithm successfully retrieved ice thickness for 13. Of the mean waveforms plotted in Figure 6.6, all but waveform 10 contained peaks that were identified by the algorithm. Peaks were identified in waveform 5 (not shown) but appeared to be contaminated by land despite the coastline buffer, likely due to across-track snagging. This resulted in a reported ice thickness for waveform 5 of 0.37 m. For the CS2 data coincident with the in situ measurements on GSL, an average of 36% of full-resolution waveforms provide thickness results; there is seasonal variation in this success rate, which ranges from just 10% to 30% in November through mid-December and 30% to 70% success through the rest of the winter. For the 10-km along-track averaged waveforms, the average success rate is 54%. The success rate is higher over GBL than

GSL, but the lack of extensive in situ data prevents a more detailed analysis of error. From Figure 6.6, it is clear that lake ice properties such as surface roughness, cracks and ridges, and bubble content can affect the shape of the 10-km mean waveform and therefore affect the retrieval of ice thickness. ASAR backscatter is high and varies widely in the region of waveform 10 and the CS2 waveform shows broad peaks in power with no clear maxima. Thus, the peak selection algorithm fails to identify suitable peaks. In contrast, waveforms 2, 7, and 11 show narrow ASAR backscatter distributions, low ASAR backscatter, and narrow peaks in the CS2 waveforms. Low ASAR backscatter is associated with smoother ice surface and ice bottom interfaces, reduced ice bubble content, and fewer cracks or ridges in the ice. A narrow ASAR backscatter distribution is indicative of reduced variability in these properties within the CS2 footprint. The wider and higher average ASAR backscatter distribution from the footprints of CS2 waveforms 10 and 13 indicate rougher ice interfaces [26] and potentially increased volume scattering from air bubbles in the ice. The influence of ice properties on C-band backscatter is also present in the CS2 waveforms with the wide peaks and high normalized power in waveforms 10 and 13 indicating that ice roughness, bubble content and shape, and snow volume scattering lead to significant backscatter and blurring of the response from the ice top and bottom.

6.8. Thickness Retrieval Results and Validation

After testing numerous methods for peak identification in the full-resolution data, $P = F$ &MPP, $N_{\text{peaks}} \geq 2$, and a normalized power threshold of 0.5 provided the best results (Section 6.6.1). These results along with the data from the 10- km along-track averaged waveform results (Section 6.6.2) were used to derive time series of ice growth on GSL and GBL for the winters of 2010/2011 to 2013/2014. In this section, we present a validation of the retrieved ice thicknesses by comparisons with the in situ measurements and the FDD model results. The weekly drill hole measurements from GSL were linearly interpolated to the CS2 dates and were also applied to GBL as no regular in situ monitoring data have been reported in the literature or elsewhere. We note that the in situ ice thickness measurements from GSL likely underestimate the ice thickness on GBL by up to ~ 0.3 m, as GBL is located further north than GSL, and previous work indicates that the end of winter maximum ice thickness for GBL is typically ~ 0.3 m thicker than for GSL

[51]. In all figures and statistics in Section 6.8, we have removed radar data from outside the period of the drill hole data in order to remove erroneous retrievals that occur during the early and late ice seasons. Possible explanations for the erroneous retrievals in the early and late ice seasons are discussed in the next section and in Section 6.9. The p-values for all correlations presented in Sections 6.8.1 and 6.8.2 are 0.001.

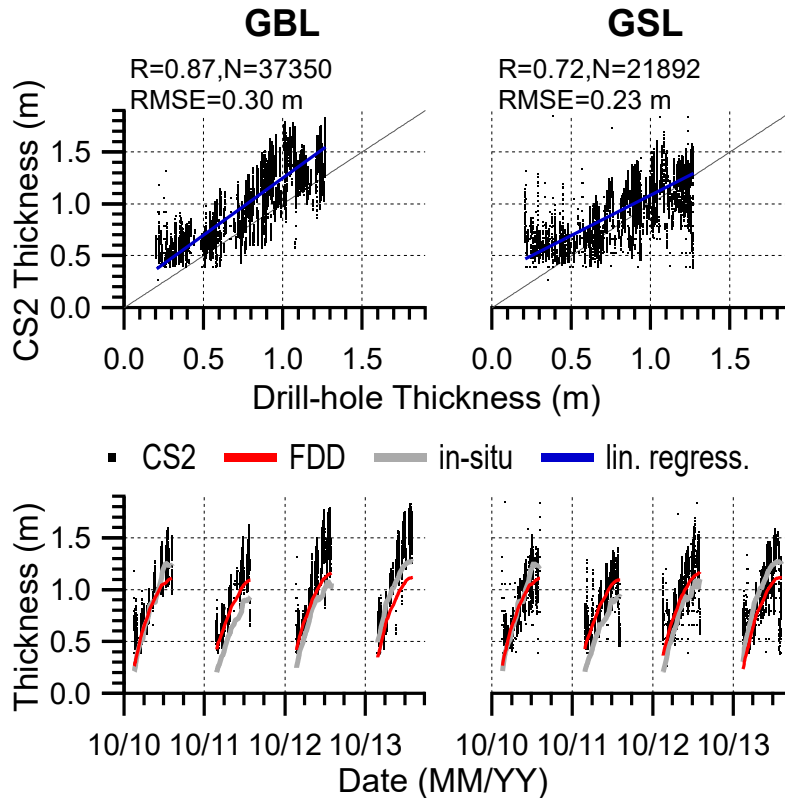


Figure 6.7: Validation results for ice thickness retrievals over GBL and GSL derived from the full-resolution CS2 data described in Section 6.6.1. (Top) Scatter plot of CS2 versus in situ ice thickness measurements. The blue line shows the linear regression with slope 1.10 ± 0.01 for GBL and 0.78 ± 0.01 for GSL. The black line is a one-to-one line. (Bottom) Comparison of time series of lake ice thickness from CS2, the FDD model, and in situ measurements.

6.8.1. Validation of Thickness Retrievals from Individual Waveforms

Using the $P = F \&MPP$, $N_{peaks} \geq 2$, peak selection criterion and a normalized power threshold of 0.5 (see Section 6.6.1), the correlations between all the thickness retrievals from the full-resolution waveforms and the drill hole data are 0.72 and 0.87 for GSL and GBL, respectively (Table 6.1 and Figure 6.7). The root-mean-square error (RMSE) values are near the vertical resolutions of CS2 and this method, which requires the separation of peaks in the range bins to

be greater than 2 bins, roughly 0.26 m. The correlations between in situ thickness and CS2 derived ice thickness of individual winters range from 0.93 to 0.94 for GBL and from 0.67 to 0.85 for GSL, stronger than that of the complete 2010/2011 through 2013/2014 data set (except for 2011/2012 over GSL; see Table 6.1). The reason for the poor performance of the algorithm in 2011/2012 over GSL eludes us. For both lakes, the correlations for individual winters are likely higher than the correlations for the complete (four winter) time series due to differences in the amount of overestimation/underestimation of thickness as a result of changes in the representativeness of the GSL in situ measurements to GBL and GSL in their entirety and variability in the properties of the snow and ice that affect the speed of light in ice, e.g., waveform shape, and the bubble content of the ice [23], [26], [32]–[34], [46].

Table 6.1: CORRELATION (R) AND RMSE OF THE INDIVIDUAL FULL-RESOLUTION CS2 ICE THICKNESS RETRIEVALS (SEE SECTION 6.6.1) AND THE FDD MODEL AND DRILL HOLE THICKNESS DATA OVER GSL AND GBL. TWO SETS OF STATISTICS ARE PROVIDED: ONE FOR THE FULLRESOLUTION INDIVIDUAL CS2 WAVEFORMS (SCALE = IND.) AND THE OTHER FOR THE ORBIT MEANS OF THOSE WAVEFORMS (SCALE = ORBIT). FOR THE ORBIT MEANS, IF AN ORBIT CONTAINED LESS THAN 33 WAVEFORMS (WHICH IS APPROXIMATELY ONE COMPLETE 10-km MEAN WAVEFORM), IT WAS NOT INCLUDED IN THE CALCULATED STATISTICS. RMSE IS IN METERS AND N IS THE NUMBER OF POINTS IN THE COMPARISON. THE 2010/2014 ENTRY COMBINES THE DATA FROM ALL STUDY YEARS

Year	GBL			GSL			Drill/ FDD	Scale (Individual or Orbit Mean)
	R	RMSE (m)	N	R	RMSE (m)	N		
2010/2011	0.93	0.162	8306	0.85	0.148	4745	Drill	Ind.
2010/2011	0.94	0.168	67	0.89	0.125	59	Drill	Orbit
2011/2012	0.94	0.327	7728	0.67	0.284	5065	Drill	Ind.
2011/2012	0.96	0.326	63	0.66	0.268	54	Drill	Orbit
2012/2013	0.93	0.372	11375	0.82	0.264	6060	Drill	Ind.
2012/2013	0.95	0.355	75	0.81	0.228	65	Drill	Orbit
2013/2014	0.94	0.254	9941	0.74	0.203	6022	Drill	Ind.
2013/2014	0.94	0.225	74	0.72	0.202	60	Drill	Orbit
2010/2014	0.87	0.296	37350	0.72	0.233	21892	Drill	Ind.
2010/2014	0.88	0.280	279	0.73	0.212	238	Drill	Orbit
2010/2011	0.92	0.211	8306	0.84	0.174	4745	FDD	Ind.
2010/2011	0.92	0.209	67	0.88	0.129	59	FDD	Orbit
2011/2012	0.94	0.224	7728	0.70	0.197	5065	FDD	Ind.
2011/2012	0.95	0.219	63	0.68	0.194	54	FDD	Orbit
2012/2013	0.94	0.307	11375	0.82	0.204	6060	FDD	Ind.
2012/2013	0.96	0.288	75	0.81	0.177	65	FDD	Orbit
2013/2014	0.94	0.362	9941	0.74	0.245	6022	FDD	Ind.
2013/2014	0.94	0.331	74	0.72	0.226	60	FDD	Orbit
2010/2014	0.90	0.290	37350	0.78	0.209	21892	FDD	Ind.
2010/2014	0.91	0.270	279	0.78	0.185	238	FDD	Orbit

Underestimation of ice thickness in the CS2 data seems to occur more often at higher thicknesses, near the end of the ice season when snow and ice melt may have already initiated. Warmer ice and wetter snow without a change in the thickness of the snow or ice could explain the decrease in thickness retrieved by CS2 by decreasing the penetration of the radar signal into the snow or ice.

The correlation between the orbit means of the full-resolution retrievals of thickness and the drill hole data is 0.88 for GBL and 0.73 for GSL (Table 6.1). These correlations are comparable to the results from the 10-km mean waveforms and the orbit means of the 10-km mean waveforms (Section 6.8.2 and Table 6.2). However, there is significantly more noise in the full-resolution results than in either of the aforementioned retrievals; the majority of the noise remains limited to the early and late ice season, but the full-resolution data also show larger variability throughout the winter, relative to the along-track averaged and orbit averaged data. The CS2 thickness retrievals from the individual waveforms presented errors at the beginning and end of the ice season where the peak selection criterion resulted in overestimation (early season) and underestimation (late season) of ice thicknesses.

The time series plot in Figure 6.7 confirms that underestimation of ice thickness by the CS2 algorithm occurs primarily at the end of the ice season. Over GSL, retrieved thicknesses decrease at the end of the season before the FDD or in situ data show a decline in ice thickness. This may, in part, be due to the presence of liquid water in the snow, which can limit or prevent penetration of the Ku-band signal into the ice. Underestimation of ice thickness by the CS2 algorithm occurs more frequently over GSL than GBL, likely because GBL CS2 data are limited to the temporal range of the GSL drill hole data and ice melt may not initiate over GBL for several additional weeks. Also, [10], [11], and [51] and the more northerly location of GBL indicate that ice thickness is typically higher over GBL, and as we are comparing it to in situ data from GSL, we expect overestimation of ice thickness on GBL by CS2. Both the time series and scatter plots in Figure 6.7 indicate that overestimation of ice thickness by the CS2 algorithm occurs most frequently and notably during the early part of the ice season.

Compared with the FDD model, CS2 also overestimates ice thickness on GBL; however, this may in part be due to the fact that the α coefficient (Eq. 6.6) in the FDD model (Eq. 6.5) was

derived using the drill hole and air temperature data from GSL, and thus the FDD model is expected to be less accurate over GBL than over GSL. As expected, the CS2 thickness data from GSL are closer to the one to one line and more closely match the FDD and the drill hole data. The FDD model results suggest that the assumption of linear ice growth between the weekly drill hole measurements is valid for most of the winter growth period. The correlation between the CS2 retrievals and FDD model results is higher than between the CS2 retrievals and the drill hole data. One potential explanation is that the drill hole measurements on GSL may not be representative of the entire GSL ice thickness, while the temperature at Yellowknife may be more representative of the mean temperatures over the lake region. Variability in the depth of snow across the lake, which leads to variation in ice thickness, may explain why the drill hole measurements on GSL may not be representative of thickness over the entire lake.

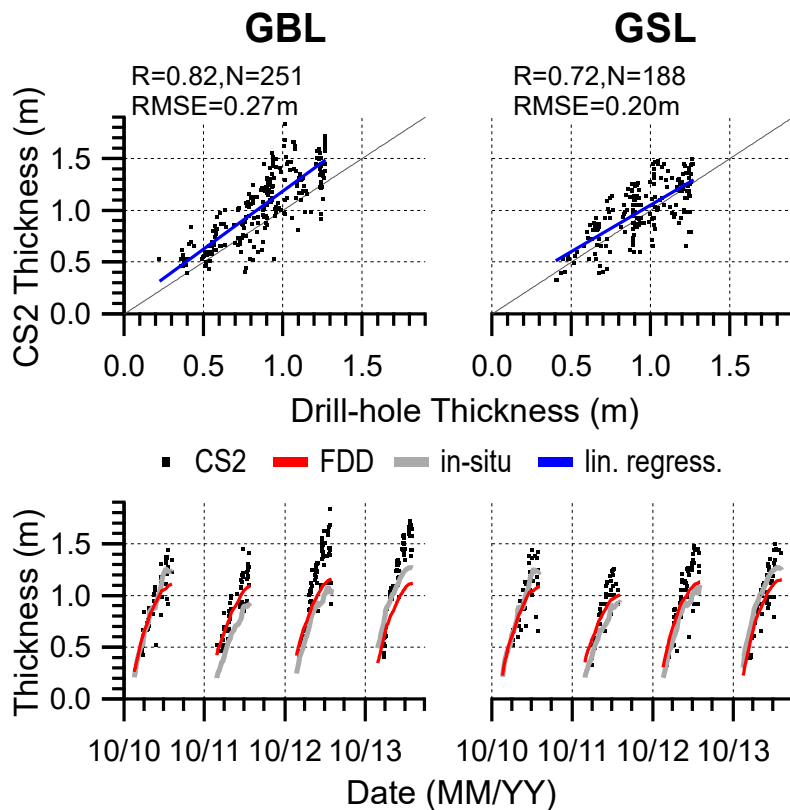


Figure 6.8: Validation results for ice thickness retrievals over GBL and GSL derived from the orbit means of the 10-km along-track averaged CS2 waveforms described in Section 6.6.2. (Top) Scatter plot of CS2 versus in situ ice thickness measurements. The blue line shows the linear regression with slope 1.12 ± 0.05 for GBL and 0.90 ± 0.06 for GSL. The black line shows a one-to-one line. (Bottom) Comparison of time series of lake ice thicknesses from CS2, the FDD model, and in situ measurements.

6.8.2. Validation of Thickness Retrievals from 10-km Mean Waveforms

Figure 6.8 shows a comparison between the 10-km mean waveform CS2 results averaged over each orbit and the in situ ice thickness measurements. The correlations between the CS2 thickness and the drill hole data were 0.82 and 0.72 for GBL and GSL from 2010/2011 to 2013/2014, respectively (Table 6.2). The RMSE between the CS2 and drill hole measurements is less than 0.27 m indicating close agreement considering that the vertical resolution [50] of CS2 in ice is ~ 0.26 m.

Table 6.2: CORRELATION (R) AND RMSE OF THE 10-km MEAN WAVEFORM CS2 ICE THICKNESS RETRIEVALS (SEE SECTION 6.6.2) AND THE FDD MODEL AND DRILL HOLE THICKNESS DATA OVER GSL AND GBL. TWO SETS OF STATISTICS ARE PROVIDED: THE RESULTS FOR THE INDIVIDUAL 10-km MEAN WAVEFORMS (SCALE = 10 km) AND ORBIT MEANS OF THOSE 10-km MEAN WAVEFORMS (SCALE = ORBIT) WHERE AN ORBIT CONTAINED MORE THAN ONE 10-km MEAN WAVEFORM. RMSE IS IN METERS AND N IS THE NUMBER OF POINTS IN THE COMPARISON. THE 2010/2014 ENTRY COMBINES THE DATA FROM ALL STUDY YEARS

Year	GBL			GSL			Drill/ FDD	Scale (10 km or Orbit Mean)
	R	RMSE (m)	N	R	RMSE (m)	N		
2010/2011	0.80	0.201	419	0.69	0.234	216	Drill	10 km
2010/2011	0.91	0.124	56	0.75	0.178	41	Drill	Orbit
2011/2012	0.78	0.328	379	0.77	0.271	235	Drill	10 km
2011/2012	0.90	0.269	58	0.85	0.210	40	Drill	Orbit
2012/2013	0.81	0.400	547	0.74	0.303	285	Drill	10 km
2012/2013	0.90	0.350	74	0.85	0.239	54	Drill	Orbit
2013/2014	0.87	0.301	451	0.76	0.213	281	Drill	10 km
2013/2014	0.96	0.241	63	0.84	0.174	53	Drill	Orbit
2010/2014	0.73	0.322	1796	0.65	0.258	1017	Drill	10 km
2010/2014	0.82	0.266	251	0.72	0.203	188	Drill	Orbit
2010/2011	0.80	0.225	419	0.69	0.254	216	FDD	10 km
2010/2011	0.90	0.158	56	0.76	0.193	41	FDD	Orbit
2011/2012	0.78	0.218	379	0.80	0.205	235	FDD	10 km
2011/2012	0.90	0.133	58	0.87	0.148	40	FDD	Orbit
2012/2013	0.82	0.326	547	0.74	0.250	285	FDD	10 km
2012/2013	0.91	0.275	74	0.85	0.198	54	FDD	Orbit
2013/2014	0.87	0.408	451	0.77	0.243	281	FDD	10 km
2013/2014	0.96	0.355	63	0.85	0.180	53	FDD	Orbit
2010/2014	0.80	0.310	1796	0.76	0.239	1017	FDD	10 km
2010/2014	0.89	0.252	251	0.84	0.182	188	FDD	Orbit

The correlations between the drill hole measurements on GSL and the CS2 retrievals on GBL are higher than between the GSL CS2 retrievals and in situ measurements on GSL (Table 6.2). It is possible that the GSL results are affected by the inclusion of orbits within the eastern arm of the lake that contain very few 10-km waveforms; removing orbits with just one 10-km mean

waveform increased the correlation coefficient. There are more valid 10-km mean waveforms and more orbits with more than one 10-km mean waveform over GBL than over GSL, again likely due to the narrowness of the channels in GSL's eastern arm (see Figure 6.1). Limiting the data to just the larger central portion of GSL and GBL increased the correlation between the drill hole data and the CS2 retrievals, but reduced the number of orbits, especially on GSL. It is also possible that some islands are not included in the GSHHG coastline data set used to mask the mainland and islands.

The correlations between in situ and CS2 ice thickness for individual winters range from 0.90 to 0.96 for GBL and from 0.75 to 0.87 for GSL, stronger than that of the complete 2010/2011 through 2013/2014 data set (Table 6.2). The correlations and RMSE between the CS2 thickness data and the FDD model results for individual winters are very similar to those of the CS2 and drill hole comparison for individual winters but are markedly better when calculated over the entire 2010–2014 study period. The correlation between CS2 thickness and the FDD modeled thickness over GSL is much higher than with the drill hole data, 0.84 versus 0.72, respectively (Table 6.2). This is likely due to the total data set containing a higher fraction of data points closer to the one-to-one line than the individual ice seasons.

The time-series plots of CS2 thickness estimates for GSL and GBL (Figure 6.8) indicate agreement with the time series of drill hole data from GSL and the FDD modeled thickness data. Over both lakes, the CS2 retrievals of thickness are greater than the in situ thicknesses, with the amount of overestimation increasing toward the end of the ice season. Furthermore, unlike the full-resolution data, there are few points that underestimate thickness right at the end of the ice season. We postulate that this occurs because along-track averaging limits the misclassification of air bubbles as the ice/water interface when liquid water in the snow and ice reduces penetration and the power returned by the ice/water interface. Retrievals during the early part of the ice season were also higher than the expected values from the FDD model and the drill hole data. However, there were only few such data points, nine of which are removed by limiting the CS2 data to the temporal extent of the drill hole measurements. The difference between the CS2 results and the in situ and FDD data appears greater over GBL than GSL (Figure 6.8). This is unsurprising considering that the drill-hole data were collected on GSL and that the FDD model

was calibrated using the GSL temperature and drill hole data. Scattering from the snow pack, superimposed ice and snow ice formation, and possible misidentification of the snow surface as the ice surface can explain only part of the difference as the maximum snow depth is typically less than 0.3 m [36]. We have no in situ ice structure information to identify the presence of snow ice or superimposed ice.

As postulated above, variations in snow cover, air bubble content in the ice, surface roughness, and the narrowness of the northern and eastern branches of GSL (see Figure 6.1) may be partly responsible for the larger variability in CS2 thickness data from GSL observed in Figure 6.7 and Figure 6.8. As the GBL ice season is longer than that of GSL, the maximum ice thickness is higher for GBL than GSL. Therefore, the CS2 retrievals for GBL lie above the one-to-one line with the GSL drill hole data. The maximum simulated ice thickness reported by [10] was between 1.4 and 1.6 m for GBL and 1.0 and 1.2 m for GSL for 2003/2004 and 2005/2006. Additional work using AMSR-E in [51] showed maximum simulated thicknesses for GBL and GSL from the CLIMo ranging from ~ 1.2 to ~ 1.6 m and ~ 1.0 to ~ 1.3 m, respectively. Furthermore, Kang et al. [10] report a maximum in situ measured ice thickness on GBL between ~ 1.5 and ~ 1.75 m during 2003/2004. This compares favorably with the CS2 retrievals over GBL, which indicate the annual maximum ice thicknesses between ~ 1.45 and ~ 1.9 m.

Comparing all of the GBL and GSL 10-km mean waveforms with the drill hole data without computing the orbit mean, the correlations decrease and the RMSE values increase (GBL: $R = 0.73$, $RMSE = 0.32$ m, $N = 1796$; GSL: $R = 0.65$, $RMSE = 0.26$ m, $N = 1017$) for the 2010/2011 through 2013/2014 time series, respectively (see Table 6.2).

6.9. Discussion and Conclusion

We have outlined a method to retrieve the thickness of freshwater lake ice from CS2 L1B waveform data based on the identification of peaks in the power echo that represent reflections of the radar wave at the snow/ice interface and the ice/water interface. The distance between the peaks is then used to determine ice thickness. To our knowledge, this is the first time lake ice thickness has been retrieved from satellite radar altimetry. We introduced various methods to determine the correct ice surface and ice bottom interfaces including along-track averaging and

a variety of peak selection criteria. We have shown that the algorithm works at a variety of spatial scales going from the waveform scale of 0.3 km along track to 10 km along track to the mean of the entire orbit over the lake surface (10 to 280 km). Although validation of the algorithm is limited by a lack of extensive in situ measurements, correlations with measurements conducted at a single location on GSL during the study period suggest that the CS2 ice thickness retrievals are valid. The CS2 retrievals appear to capture the seasonal evolution of ice thickness compared with the in situ measurements and to FDD model results. Spurious measurements primarily arising at the beginning and end of the ice season are believed to be caused by: 1) peak selection errors; 2) across-track snagging; and 3) the influence of ice surface roughness, melt, and ice air bubble content. Furthermore, over GBL, some of these differences arise from the use of the GSL in situ data to compare with the CS2 results, as there are no regular in situ measurements of ice thickness on GBL. It may be possible to improve the FDD model and ice thickness results using a distance weighted average of air temperatures from all Environment Canada weather stations around GBL and GSL to better constrain the number of FDDs and to improve our estimation of ϵ'_i (Eq. 6.2).

The results obtained in this paper agree well with previous estimates of ice thickness over GSL and GBL from AMSR-E brightness temperatures [10], [51]. The higher frequency of AMSR-E should be more sensitive to small variations in dielectric properties of the snow and ice and thus less sensitive to just ice thickness changes and thus may have higher noise. Model output results from CLIMo are also presented in [10] and indicate a maximum thickness of ~ 1.5 m over GBL. Results from [10] indicate a maximum thickness of ~ 1.2 m over GSL; the drill hole measurements from the CITP indicate a maximum thickness of < 1.3 m in all years since 2004. The thickness results for both lakes from [51] are similar to those from [10]. Furthermore, [23] recently presented lake ice thickness retrievals from a ground-based Ku-band scatterometer, demonstrating penetration to the ice–water interface and further supporting the applicability of CS2 data to freshwater ice thickness retrievals as is presented here.

Gridded AMSR-E brightness temperature data were utilized in [51] to map ice thickness distributions across GBL and GSL and found that the deeper central regions of both lakes are

covered by thinner ice that results from a delay in freeze-up in comparison with shallower regions. The results from [11] confirm that the ice season is longer on GBL than on GSL, with earlier freeze onset, longer freeze-up, later melt onset and longer melt duration. These factors all allow thicker ice to develop over GBL than GSL. Additionally, these factors explain why underestimation of ice thickness by CS2 at the end of the ice season did not occur over GBL as often as over GSL.

The method presented here to retrieve lake ice thickness is simpler than CS2 estimates of sea ice thickness, which assume hydrostatic equilibrium to convert measurements of ice freeboard into ice thickness. Sea ice thickness retrievals require retracking of the waveform data, use of a mean sea surface height product, open water discrimination, and assumptions about snow depth and the density of the ice, water and snow, all of which can contribute considerable errors to sea ice thickness retrievals. In contrast, the method presented in this paper is only dependent on the accurate identification of the lake ice surface and bottom interfaces in the waveform and on the application of the correct radar propagation speed in the ice. Throughout the winter, the water level in the lakes may change, but this does not affect the performance of the retrieval algorithm, as it is a relative measurement between the ice surface and ice bottom. The lakes become completely covered with ice and even when not, the waveforms from large and small patches of open water would not include a secondary peak with significant power. In fact, waveforms from small and large open water patches would appear similar to those in Figure 6.2(c) and (d), respectively.

Although we have chosen to study the two largest lakes in the region, the strong correlations between in situ data and the CS2 retrievals suggest that the method can be applied to many other smaller lakes across the sub-Arctic. We estimate that ice thickness could be retrieved from lakes as small as ~ 25 km in diameter, to allow for multiple waveforms and a shoreline buffer. However, we note that the orbit of CS2 was designed to provide maximum overlap over the high Arctic and thus will have limited or no coverage over smaller lakes at lower latitudes. The application of this method will be limited by the geometry of the lake and the CS2 orbits passing over it. There are numerous lakes in northern Canada, Russia, and Alaska where this method may be applicable.

For reference, there were 750 orbits over GBL and 802 orbits over GSL between July 2010 and June 2014.

The high correlation coefficients and low RMSE values, relative to the range resolution of CS2 in lake ice, suggest that the retrieval algorithm is robust and applicable at a variety of spatial scales. Although the noise of the full-resolution individual waveform results is high, the comparisons are limited by the single point location of the in situ validation data.

CS2 retrievals generally overestimated ice thickness over both lakes, though the results over GBL are not unexpected for the given application of in situ data from GSL. The largest uncertainties in CS2 thickness occur at the start and end of the ice season, when the ice thickness is near the resolution of CS2 in lake ice (~ 0.26 m) or when melt may reduce penetration into the ice. Overestimation occurs at the start of the season and underestimation is more common at the very end of the season. Although ice growth at the end of the ice season is very slow, ice growth is rapid during the early season freeze-up; uncertainty in the CS2 thickness retrievals at these times could also be argued to be of higher importance to stakeholders who are interested in determining if the ice has grown thick enough or has melted too much to be travelled on.

As discussed throughout Sections 6.3–6.8, the CS2 waveform data are influenced by the physical and dielectric properties of the various layers that make up the lake ice cover. The various forms of lake ice, e.g., congelation ice, snow–ice, superimposed ice, slush, and frazil [52], all have variations in dielectric and physical properties but only influence our results if they lead changes in the position of the peaks in power. For example, skim ice, slush, and frazil crystals in the open water column will influence backscatter from the lake but will not result in two separate and detectable peaks, as these layers are thin or have a high liquid water content. Snow ice or superimposed ice may be identified as the snow/ice interface, pushing the peak earlier in time; this would require the accumulation of ≥ 0.13 m of snow ice/superimposed ice. Air bubbles in the ice can cause volume scattering and may cause double bounce scattering, but primarily act as surface scatterers and enhance the radar roughness of the ice/water interface [25]–[27]. Increasing the roughness of the ice/water interface may bias the ice thickness retrieval. Snow on ice has been shown to be a significant source of CS2 waveform interpretation error and can introduce bias in freeboard retrievals [29]–[34]. The air/snow interface may be confused for the

snow/ice interface. Unfortunately, no studies have been published on the structure of the lake ice cover on GSL or GBL. The snow and ice properties will also vary within the CS2 footprint, further limiting our ability to assess the role of ice type or properties with certainty.

During the initial stages of ice growth, it is possible that the ice cover is discontinuous and may cause snagging [41]. Furthermore, the algorithm is dependent on the selection of two peaks, which requires at least 1 range bin between the two peaks to be the joint minimum for the peaks; therefore, the minimum peak separation is 2 bins, or roughly 0.26 m using the speed of light in ice. Due to these two factors, CS2 ice thickness retrievals are less reliable until the lake is close to completely covered with ice ≥ 0.26 m thick. The maximum ice thickness for which this method will work is unknown, as neither GSL nor GBL have ice thicknesses that approach the theoretical maximum penetration depth of 4.9–8.4 m for Ku-band radar waves in freshwater ice. The accuracy of the method is limited by the one-way travel distance of a range bin, 0.13 m. The method should work best over “black” ice with limited air bubbles and smooth interfaces as this ice type will have fewer potential scatterers other than the ice top and bottom interfaces relative to gray ice, white ice, or deformed ice.

In addition to monitoring ice thickness, the method also allows the retrieval of lake water level and volume throughout the winter. Winter lake water volume and levels are important for water supply for domestic, commercial, and industrial (e.g., power generation) use and as a habitat for fish. Although not performed here, one simply needs to keep track of the first peak associated with the snow/ice interface throughout the winter along with the range to this peak, in addition to the ice thickness. Retracking of the waveform data in order to retrieve accurate absolute ellipsoidal elevations would be required. The volume of water within the lake could then be determined using the first peak to determine the total lake ice and water volume and by removing the volume of lake ice.

Furthermore, changes in the waveform power values from CS2 may be useful for the identification of grounded ice, melt onset, and ice thickness change detection and warrant further study. An examination of CS2 waveform maximum power (Figure 6.3) indicated potential for the detection of snow melt, as the waveforms returned during melt had much higher maximum power than during the ice growth season or from open water. The increase in wetness

in the snow limits penetration through the snow and ice and causes scattering to mainly occur from the air/wet snow interface. A proper time-series analysis of snow melt timing and CS2 maximum waveform power will be needed to determine the ability of CS2 to detect snow melt. The maximum power of CS2 waveforms decreased with increasing ice thickness and may provide yet another way to estimate lake ice thickness.

The next step in calculating ice thickness of freshwater lakes using CS2 will be to improve the spatial resolution of the algorithm by improving the full-resolution individual waveform peak selection and filtering procedures and applying the method to more ice-covered lakes. Implementing waveform retracking to allow for subrange bin resolution may lead to improved thickness retrievals. Finally, including power thresholds instead of normalized power thresholds for the identification of valid waveforms may also improve the CS2 thickness retrievals by filtering out weak waveforms.

By improving the spatial resolution of ice thickness estimates, we will be able to study the seasonal cycles of ice thickness and volume and the interannual variability and changes in these parameters for the many smaller lakes in the sub-Arctic. Furthermore, additional studies into the accuracy of the method and more extensive validation should be performed not only for both GSL and GBL but also for other smaller and shallower lakes. The method should also be tested with other satellite altimeters such as AltiKa, Sentinel-3/-6, and Jason-3. We believe that the larger footprint of older pulse-limited sensors results in too much noise for ice thickness retrievals. Additionally, the larger footprint of pulse-limited radars precludes the application to small sub-Arctic lakes. Finally, examinations of changes in the maximum thickness, seasonal development, and ice onset/melt detection using CS2 should be performed over longer time periods for the many lakes in the sub-Arctic in order to develop a time series of lake ice changes.

6.10. Acknowledgement

The authors would like to thank the thorough and helpful reviews provided by two anonymous reviewers.

6.11. References

- [1] C. R. Duguay, G. M. Flato, M. O. Jeffries, P. Ménard, K. Morris, and W. R. Rouse, "Ice-cover variability on shallow lakes at high latitudes: Model simulations and observations," *Hydrol. Process.*, vol. 17, no. 17, pp. 3465–3483, 2003.
- [2] C. R. Duguay and P. M. Lafleur, "Determining depth and ice thickness of shallow sub-arctic lakes using space-borne optical and SAR data," *Int. J. Remote Sens.*, vol. 24, no. 3, pp. 475–489, 2003.
- [3] W. M. Schertzer, W. R. Rouse, P. D. Blanken, and A. E. Walker, "Overlake meteorology and estimated bulk heat exchange of Great Slave Lake in 1998 and 1999," *J. Hydrometeorol.*, vol. 4, no. 4, pp. 649–659, 2003.
- [4] W. R. Rouse, C. M. Oswald, J. Binyamin, P. D. Blanken, W. M. Schertzer, and C. Spence, "Interannual and seasonal variability of the surface energy balance and temperature of central Great Slave Lake," *J. Hydrometeorol.*, vol. 4, no. 4, pp. 720–730, 2003.
- [5] W. R. Rouse et al., "An investigation of the thermal and energy balance regimes of Great Slave and Great Bear Lakes," *J. Hydrometeorol.*, vol. 9, no. 6, pp. 1318–1333, 2008.
- [6] L. C. Brown and C. R. Duguay, "The response and role of ice cover in lake-climate interactions," *Progr. Phys. Geogr.*, vol. 34, no. 5, pp. 671–704, Oct. 2010.
- [7] T. D. Prowse, C. Furgal, R. Chouinard, H. Melling, D. Milburn, and S. L. Smith, "Implications of climate change for economic development in northern Canada: Energy, resource, and transportation sectors," *AMBIO, J. Human Environ.*, vol. 38, no. 5, pp. 272–281, 2009.
- [8] S. E. Howell, L. C. Brown, K.-K. Kang, and C. R. Duguay, "Variability in ice phenology on Great Bear Lake and Great Slave Lake, Northwest Territories, Canada, from SeaWinds/QuikSCAT: 2000–2006," *Remote Sens. Environ.*, vol. 113, no. 4, pp. 816–834, 2009.
- [9] L. C. Brown and C. R. Duguay, "The fate of lake ice in the North American Arctic," *Cryosphere*, vol. 5, no. 4, pp. 869–892, Oct. 2011.
- [10] K.-K. Kang, C. Duguay, S. E. L. Howell, C. Derksen, and R. Kelly, "Sensitivity of AMSR-E brightness temperatures to the seasonal evolution of lake ice thickness," *IEEE Geosci. Remote Sens. Lett.*, vol. 7, no. 4, pp. 751–755, Apr. 2010.

- [11] K.-K. Kang, C. R. Duguay, and S. E. L. Howell, "Estimating ice phenology on large northern lakes from AMSR-E: Algorithm development and application to Great Bear Lake and Great Slave Lake, Canada," *Cryosphere*, vol. 6, no. 2, pp. 235–254, 2012.
- [12] C. M. Birkett, "The contribution of TOPEX/POSEIDON to the global monitoring of climatically sensitive lakes," *J. Geophys. Res. Oceans*, vol. 100, no. C12, pp. 25179–25204, 1995.
- [13] J.-F. Crétaux and C. Birkett, "Lake studies from satellite radar altimetry," *Comp. Rendus Geosci.*, vol. 338, nos. 14–15, pp. 1098–1112, 2006.
- [14] S. Sarmiento and S. Khan, "Spatial and temporal variability of Great Slave Lake levels from satellite altimetry," *IEEE Geosci. Remote Sens. Lett.*, vol. 7, no. 3, pp. 426–429, Jul. 2010.
- [15] A. V. Kouraev, S. V. Semovski, M. N. Shimaraev, N. M. Mognard, B. Légresy, and F. Remy, "Observations of Lake Baikal ice from satellite altimetry and radiometry," *Remote Sens. Environ.*, vol. 108, no. 3, pp. 240–253, 2007.
- [16] A. V. Kouraev, S. V. Semovski, M. N. Shimaraev, N. M. Mognard, B. Légresy, and F. Remy, "The ice regime of Lake Baikal from historical and satellite data: Relationship to air temperature, dynamical, and other factors," *Limnol. Oceanogr.*, vol. 52, no. 3, pp. 1268–1286, 2007.
- [17] F. T. Ulaby, W. H. Stiles, and M. Abdelrazik, "Snowcover influence on backscattering from terrain," *IEEE Trans. Geosci. Remote Sens.*, vol. GE-22, no. 2, pp. 126–133, Mar. 1984.
- [18] C. Mätzler and U. Wegmuller, "Dielectric properties of freshwater ice at microwave frequencies," *J. Phys. D, Appl. Phys.*, vol. 20, no. 12, p. 1623, 1987.
- [19] C. Mätzler, "Microwave dielectric properties of ice," in *Thermal Microwave Radiation: Applications for Remote Sensing*, vol. 52, C. Mätzler, Ed. London, U.K.: Institution of Engineering and Technology, 2006, ch. 5.3, pp. 455–463.
- [20] G. Hufford, "A model for the complex permittivity of ice at frequencies below 1 THz," *Int. J. Infr. Millim. Waves*, vol. 12, no. 7, pp. 677–682, 1991.
- [21] S. E. L. Howell, J. J. Yackel, R. D. Abreu, T. Geldsetzer, and C. Breneman, "On the utility of SeaWinds/QuikSCAT data for the estimation of the thermodynamic state of first-year sea ice," *IEEE Trans. Geosci. Remote Sens.*, vol. 43, no. 6, pp. 1338–1350, Jun. 2005.

- [22] K. Morris, M. O. Jeffries, and W. F. Weeks, "Ice processes and growth history on Arctic and sub-Arctic lakes using ERS-1 SAR data," *Polar Rec.*, vol. 31, pp. 115–128, Apr. 1995.
- [23] G. E. Gunn, C. R. Duguay, L. C. Brown, J. King, D. Atwood, and A. Kasurak, "Freshwater lake ice thickness derived using surface-based X- and Ku-band FMCW scatterometers," *Cold Regions Sci. Technol.*, vol. 120, pp. 115–126, Sep. 2015.
- [24] G. E. Gunn, M. Brogioni, C. Duguay, G. Macelloni, A. Kasurak, and J. King, "Observation and modeling of X- and Ku-band backscatter of snow-covered freshwater lake ice," *IEEE J. Sel. Topics Appl. Earth Observ. Remote Sens.*, vol. 8, no. 7, pp. 3629–3642, Jul. 2015.
- [25] M. Engram, K. W. Anthony, F. J. Meyer, and G. Grosse, "Characterization of L-band synthetic aperture radar (SAR) backscatter from floating and grounded thermokarst lake ice in Arctic Alaska," *Cryosphere*, vol. 7, no. 6, pp. 1741–1752, Nov. 2013.
- [26] G. E. Gunn, "Re-evaluating scattering mechanisms in snow-covered freshwater lake ice containing bubbles using polarimetric ground-based and spaceborne radar data," Ph.D. dissertation, *Geogr. Environ. Manage.*, Univ. Waterloo, Waterloo, ON, Canada, Jul. 2015.
- [27] D. K. Atwood, G. E. Gunn, C. Roussi, J. Wu, C. Duguay, and K. Sarabandi, "Microwave backscatter from Arctic lake ice and polarimetric implications," *IEEE Trans. Geosci. Remote Sens.*, vol. 53, no. 11, pp. 5972–5982, Nov. 2015.
- [28] M. O. Jeffries, K. Morris, W. F. Weeks, and H. Wakabayashi, "Structural and stratigraphic features and ERS 1 synthetic aperture radar backscatter characteristics of ice growing on shallow lakes in NW Alaska, winter 1991–1992" *J. Geophys. Res. Oceans*, vol. 99, no. C11, pp. 22459–22471, 1994.
- [29] R. Willatt, K. Giles, S. Laxon, L. Stone-Drake, and A. Worby, "Field investigations of Ku-band radar penetration into snow cover on Antarctic sea ice," *IEEE Trans. Geosci. Remote Sens.*, vol. 48, no. 1, pp. 365–372, Jan. 2010.
- [30] R. Willatt, S. Laxon, K. Giles, R. Cullen, C. Haas, and V. Helm, "Ku-band radar penetration into snow cover on Arctic sea ice using airborne data," *Ann. Glaciol.*, vol. 52, no. 57, pp. 197–205, 2011.

- [31] N. T. Kurtz, N. Galin, and M. Studinger, "An improved CryoSat-2 sea ice freeboard retrieval algorithm through the use of waveform fitting," *Cryosphere*, vol. 8, no. 4, pp. 1217–1237, 2014.
- [32] R. Kwok, "Simulated effects of a snow layer on retrieval of CryoSat-2 sea ice freeboard," *Geophys. Res. Lett.*, vol. 41, no. 14, pp. 5014–5020, 2014, doi: 10.1002/2014GL060993.
- [33] R. Ricker, S. Hendricks, D. K. Perovich, V. Helm, and R. Gerdes, "Impact of snow accumulation on CryoSat-2 range retrievals over Arctic sea ice: An observational approach with buoy data," *Geophys. Res. Lett.*, vol. 42, no. 11, pp. 4447–4455, 2015, doi: 10.1002/2015GL064081.
- [34] D. Price et al., "Evaluation of CryoSat-2 derived sea-ice freeboard over fast ice in McMurdo Sound, Antarctica," *J. Glaciol.*, vol. 61, no. 226, pp. 285–300, 2015.
- [35] S. G. Warren and R. E. Brandt, "Optical constants of ice from the ultraviolet to the microwave: A revised compilation," *J. Geophys. Res. Atmos.*, vol. 113, no. D14, pp. 1–10, 2008.
- [36] E. Canada. (May 2013). Canadian Ice Thickness Program: Yellowknife, N. W. T. [Online]. Available: <http://www.ec.gc.ca/glacesice/default.asp?lang=En&n=E1B3129D-1>
- [37] P. Wessel and W. H. F. Smith, "A global, self-consistent, hierarchical, high-resolution shoreline database," *J. Geophys. Res. Solid Earth*, vol. 101, no. B4, pp. 8741–8743, 1996.
- [38] C. Bouzinac, *Cryosat Product Handbook*. Paris, France: European Space Agency, 2013.
- [39] G. S. Brown, "The average impulse response of a rough surface and its applications," *IEEE Trans. Antennas Propag.*, vol. 25, no. 1, pp. 67–74, Jan. 1977.
- [40] D. J. Wingham et al., "Cryosat: A mission to determine the fluctuations in Earth's land and marine ice fields," *Adv. Space Res.*, vol. 37, no. 4, pp. 841–871, 2006.
- [41] T. W. K. Armitage and M. W. J. Davidson, "Using the interferometric capabilities of the ESA CryoSat-2 mission to improve the accuracy of sea ice freeboard retrievals," *IEEE Trans. Geosci. Remote Sens.*, vol. 52, no. 1, pp. 529–536, Jan. 2014.
- [42] U. S. Army Corps Eng., Washington, DC, USA. (2002). Engineering and Design: Ice Engineering. [Online]. Available: http://www.publications.usace.army.mil/Portals/76/Publications/EngineerManuals/EM_1110-2-1612.pdf
- [43] Wavemetrics. (2014). Igor Pro User Manual: Curve-Fitting. [Online]. Available: <http://www.wavemetrics.net/doc/igorman/IgorMan.PDF>

- [44] Environ. Canada. (2014). Environment Canada Historical Climate Data Archive. [Online]. Available: http://climate.weather.gc.ca/index_e.html#access
- [45] S. G. Beaven et al., "Laboratory measurements of radar backscatter from bare and snow-covered saline ice sheets," *Int. J. Remote Sens.*, vol. 16, no. 5, pp. 851–876, 1995.
- [46] R. Ricker, S. Hendricks, V. Helm, H. Skourup, and M. Davidson, "Sensitivity of CryoSat-2 Arctic sea-ice freeboard and thickness on radar-waveform interpretation," *Cryosphere*, vol. 8, no. 4, pp. 1607–1622, 2014.
- [47] S. W. Laxon et al., "CryoSat-2 estimates of Arctic sea ice thickness and volume," *Geophys. Res. Lett.*, vol. 40, no. 4, pp. 732–737, 2013.
- [48] M. Zygmuntowska and K. Khvorostovsky, "Analysis of CryoSat's radar altimeter waveforms over different Arctic sea ice regimes," Ph.D. dissertation, Geophys. Inst., Univ. Bergen, Bergen, Norway, Jun. 2014. [Online]. Available: <http://hdl.handle.net/1956/9393>
- [49] R. L. Tilling, A. Ridout, A. Shepherd, and D. J. Wingham, "Increased Arctic sea ice volume after anomalously low melting in 2013," *Nature Geosci.*, vol. 8, no. 8, pp. 643–646, 2015.
- [50] H.-P. Marshall, M. Schneebeli, and G. Koh, "Snow stratigraphy measurements with high-frequency FMCW radar: Comparison with snow micro-penetrometer," *Cold Regions Sci. Technol.*, vol. 47, nos. 1–2, pp. 108–117, 2007.
- [51] K.-K. Kang, C. Duguay, J. Lemmetyinen, and Y. Gel, "Estimation of ice thickness on large northern lakes from AMSR-E brightness temperature measurements," *Remote Sens. Environ.*, vol. 150, pp. 1–19, Sep. 2014.
- [52] B. Michel and R. O. Ramseier, "Classification of river and lake ice," *Can. Geotech. J.*, vol. 8, pp. 36–45, Apr. 1971.

7. Characteristics of CryoSat-2 Signals Over Multi-Year and Seasonal Sea Ice

7.1. Abstract

CryoSat-2 Level 1B and Level 2 data are compared with coincident airborne laser scanner and airborne electromagnetic induction surveys conducted in the Baltic Sea in March 2011 and in the Lincoln Sea in March and April 2012. Across-track snagging caused range retrieval errors in all examined tracks. The L2 surface height profiles are very noisy due to poor retracker performance. Cryosat-2 L2 data are produced by tracking the strongest return in the Level 1B waveforms, not the first return. When a strong reflector is present off-nadir, the retracker incorrectly selects this surface as the surface location of the nadir point. The surface height profile is smoothed by tracking the first return point instead of the peak power return. Ice thickness data produced by retracking the CryoSat-2 L1B data showed good correlation with airborne electromagnetic induction measurements. CryoSat-2 and NASA Operation Ice Bridge data exhibited similar latitudinal freeboard gradients. Accurate measurements of sea ice freeboard or thickness changes can be achieved using appropriate spatial and temporal averaging.

7.2. Introduction

Sea ice strongly influences the exchange of energy between the atmosphere and oceans, is a leading indicator of climate change and a critical habitat for e.g. whales, polar bears and ice-associated fish, zoo- and phyto-plankton and bacteria. Sea ice poses a significant hazard to marine activity in the Canadian Arctic Archipelago, in the Arctic Ocean, and in the Baltic Sea.

Passive microwave observations of sea ice extent from 1979-2012 show a decrease in the maximum and minimum extent of $-2.6\%/decade$ and $-13\%/decade$, respectively [1]. The decrease in sea ice extent is greater than predicted by global climate models [2, 3]. Poor representation and parameterization of the distribution of sea ice thickness in the Arctic has been suggested as one reason current climate models fail to accurately estimate the decreasing sea ice extent [2].

While ice extent is readily monitored from space, measurements of ice thickness have been limited to: spatially and temporally sparse in-situ measurements; upwards looking sonar on

ocean moorings and submarines; airborne electromagnetic induction (AEM); airborne laser scanning/ altimetry; a short-lived spaceborne laser altimeter mission (ICESat); or coarse spatial resolution satellite radar altimeters with limited coverage over the Arctic Ocean [ERS & Envisat; 4–7]. All of the data show decreases in the thickness of the sea ice over the past half century.

Altimetric estimates of sea ice thickness rely on measuring the height of the ice or snow surface above the water, called freeboard. The thickness and density of the sea ice and snow, and the density of the seawater all influence the ice freeboard [7]. Additionally, the radar signal may not consistently penetrate to the snow-ice interface, causing further errors in the inversion of freeboard to sea ice thickness [8].

Launched in 2010, the European Space Agency's (ESA) CryoSat-2 satellite carries a new type of radar altimeter capable of synthetic aperture (SARM) and interferometric (SARInM) measurements to improve spatial resolution and tracking of the surface in the across track direction [9]. The orbit of CryoSat-2 provides coverage of the Arctic Ocean up to 88°N, 7.5° further north than previous satellite radar altimetry missions [9]. CryoSat-2 data require calibration and validation because of the aforementioned issues that affect sea ice freeboard and its measurement. Although CryoSat-2 has now reached the end of its planned mission duration, calibration and validation (cal-val) of CryoSat-2 remains limited and incomplete. Post-launch cal-val experiments over sea ice have been performed at several sites in the Arctic in April of 2011 and 2012. Recently, Laxon et al. [10] provided the first results of CryoSat-2 sea ice thickness in the Arctic Ocean. They observed good agreement between CryoSat-2 measurements and upward looking sonar measurements of draft, airborne electromagnetic induction, and NASA Operation IceBridge (OIB) ice thickness measurements. Nevertheless, questions regarding the performance of CryoSat-2 over the Arctic and other ice-covered regions such as the Southern Ocean and the Baltic Sea remain.

Here, CryoSat-2 data over regions of primarily multiyear and seasonal (first year) sea ice are examined. Sea ice freeboard and thickness from CryoSat-2 are compared to coincident airborne and ground-based validation studies from the Lincoln Sea north of Ellesmere Island in March and April 2012 and in the Baltic Sea in March of 2011.

7.3. Data and Methods

In March and April of 2012, the Alfred Wegener Institute (AWI) and NASA's OIB performed airborne electromagnetic induction (AEM) and airborne laser scanner (ALS) measurements coincidentally with CryoSat-2 acquisitions over the Lincoln Sea and in the Arctic Ocean. A coincident OIB flight was conducted on March 26 along a CryoSat-2 SARin mode pass in the experimental "Wingham Box" north of the Canadian Arctic Archipelago (Figure 7.1a).

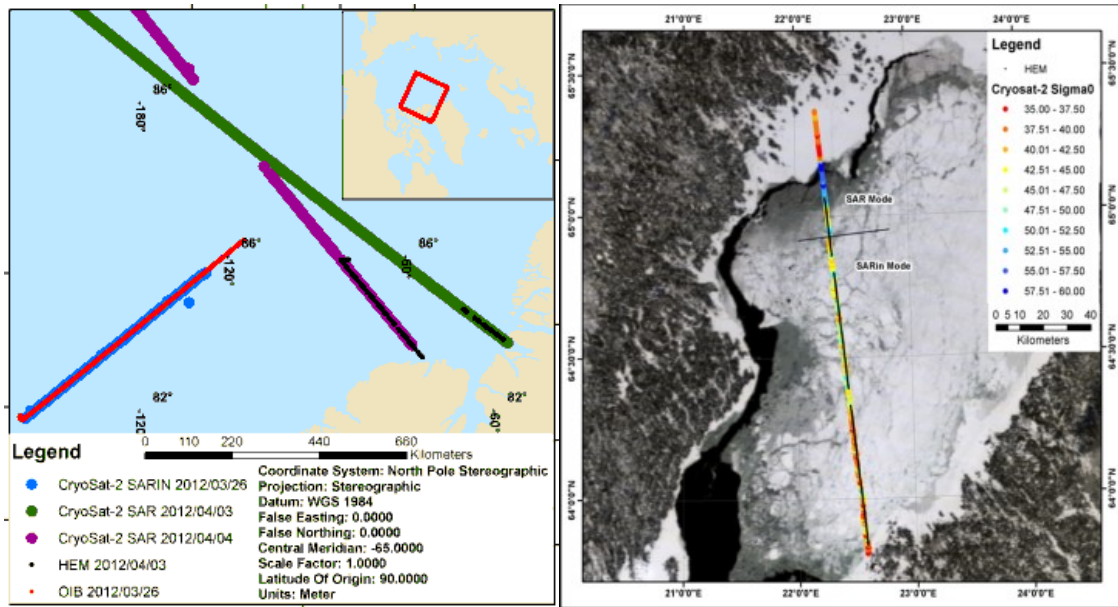


Figure 7.1: Maps showing examined Cryosat-2 tracks in the Arctic Ocean (a) and Baltic Sea (b). Thin lines represent airborne data.

In this study, we make use of the experimental OIB Sea Ice Freeboard, Snow Depth, and Thickness Quick Look product available via the National Snow and Ice Data Center (http://nsidc.org/data/docs/daac/icebridge/evaluation_products/sea-ice-freeboard-snowdepththickness-quicklook-index.html). The uncertainties of the product are still being assessed; however the product has been used by [11] to improve seasonal forecasts of sea ice extent. For details on the production of the quick look product, see [11, 12]. The archival OIB ice freeboard, snow depth and thickness for the 2012 OIB Arctic campaign has not yet been released.

On April 3 and 4, AWI performed AEM flights along CryoSat-2 SAR mode passes in the Lincoln Sea (Figure 7.1). Validation of the surface type and sea ice properties was done visually using Synthetic Aperture RADAR (SAR) imagery from Envisat ASAR and TerraSAR-X. CryoSat-2 data from the Arctic were processed by AWI to produce freeboard and ice thickness estimates. The AWI

processor retracks the CryoSat-2 L1B waveforms using a Threshold Spline Retracker Algorithm (TSRA) and uses the CryoSat-2 L1B peakiness, beam kurtosis, and beam standard deviation to identify thin ice/open water leads between the ice floes. Ice thickness is computed using the hydrostatic balance equation. For simplicity, the processor used here assumes either there is no penetration into the snow, or that a continuous 20 cm snow pack is present and penetrated by the radar.

On March 2, 2011, a helicopter-borne AEM survey was conducted along a CryoSat-2 SARIn and SAR mode track in the Baltic Sea (Figure 7.1b).

For comparison with the CryoSat-2 data, the average and standard deviation of the OIB quick look and the AWI AEM data were determined for each CryoSat-2 footprint; approximately 6 OIB and 57 AEM measurements were averaged for each CryoSat-2 footprint, respectively. Note that AEM measurements of ice thicknesses are actually the thickness of the ice plus the overlying snow cover. See [6] and references therein for details on the AEM system.

7.4. Results and Discussion

7.4.1. Baltic Sea

While CryoSat-2 was not designed for the retrieval of sea ice thickness in the Baltic Sea, the characteristics of Cryosat-2 data over the Baltic Sea may apply to other regions of seasonal ice cover such as the marginal ice zone. The analysis in the Baltic Sea focused on across-track snagging and retracking issues. An example of extreme across-track snagging from a CryoSat-2 SAR mode pass on March 4, 2012 is presented in Figure 7.2.

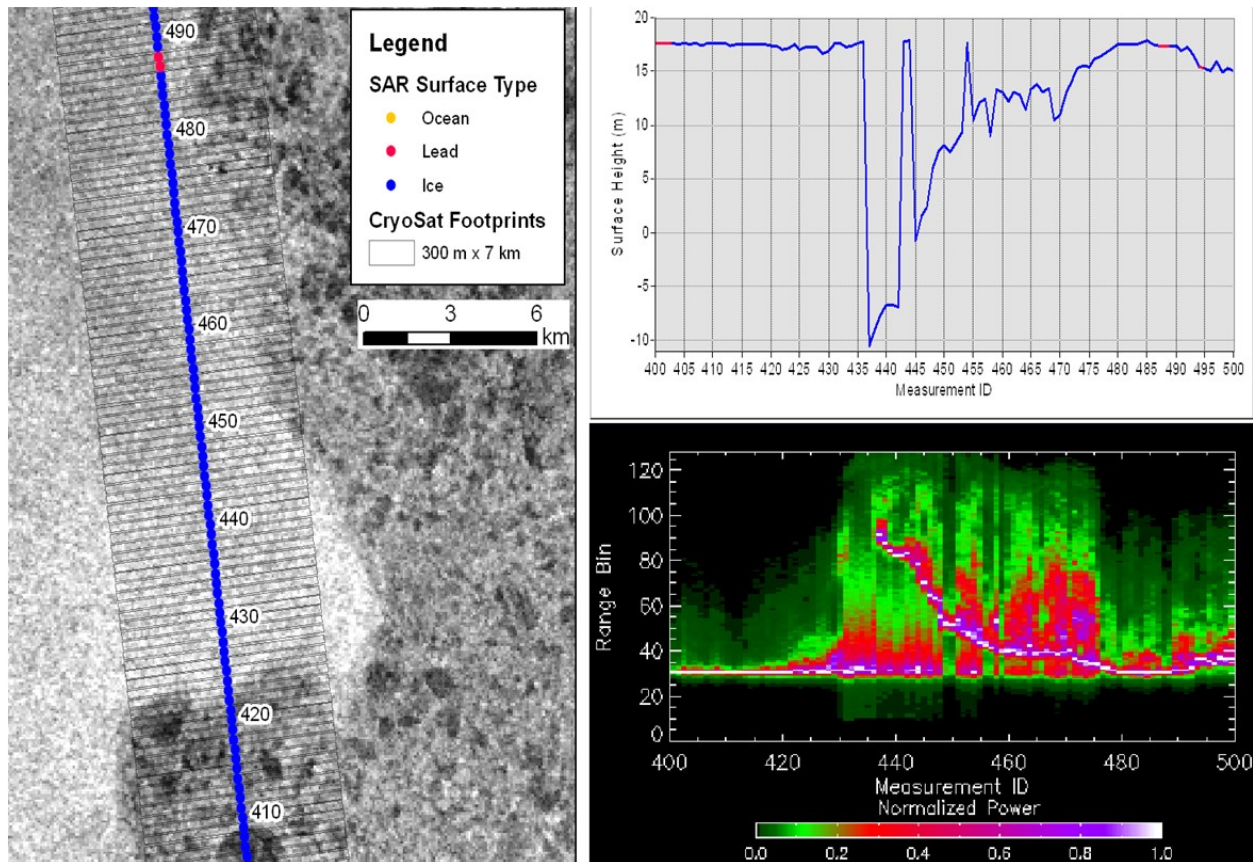


Figure 7.2: Examples of extreme across-track snagging in CryoSat-2 L2 SARM data (March 4, 11:55). The L2 surface height profile (top right) and waveforms (bottom right) are shown for measurements 400-500. The CryoSat-2 data are overlaid on an Envisat ASAR image (Mar 4, 09:16 UTC) (left). In the ASAR image, wind-roughened open water appears white, and the ice appears dark. 7 km wide footprints are drawn for distance reference purposes.

In this instance, the Cryosat-2 L2 retracker snags to specular reflections from the thin ice and open water leads more than 6 km to the east of the CryoSat-2 nadir position instead of the wind-roughened open water at nadir (Figure 7.1). In contrast to [13], who found that snagging occurred infrequently in ERS data over sea ice in the Arctic Ocean, snagging was found to be widespread in the CryoSat-2 data over the Baltic Sea. Furthermore, Figure 7.2 also illustrates misclassification of the surface type from the Cryosat-2 SAR surface discriminator flags as wind-roughened open water is identified as ice. The discriminator algorithm can be improved by the inclusion of additional waveform and radar backscatter parameters.

Figure 7.3 presents four waveforms just prior to and at the point of maximum across-track snagging in Figure 7.2. As can be seen in Figure 7.3c and Figure 7.3d, whether snagging occurs is dependent on the relative strength of the nadir and off-nadir returns. The waveform tracker used

by ESA to produce the L2 data tracks the peak power, not the first peak. Thus, when the off-nadir point return is stronger than that from the nadir point, snagging occurs. In Figure 7.3 below, the wind-roughened open water at nadir has a lower return than the ice edge off-nadir.

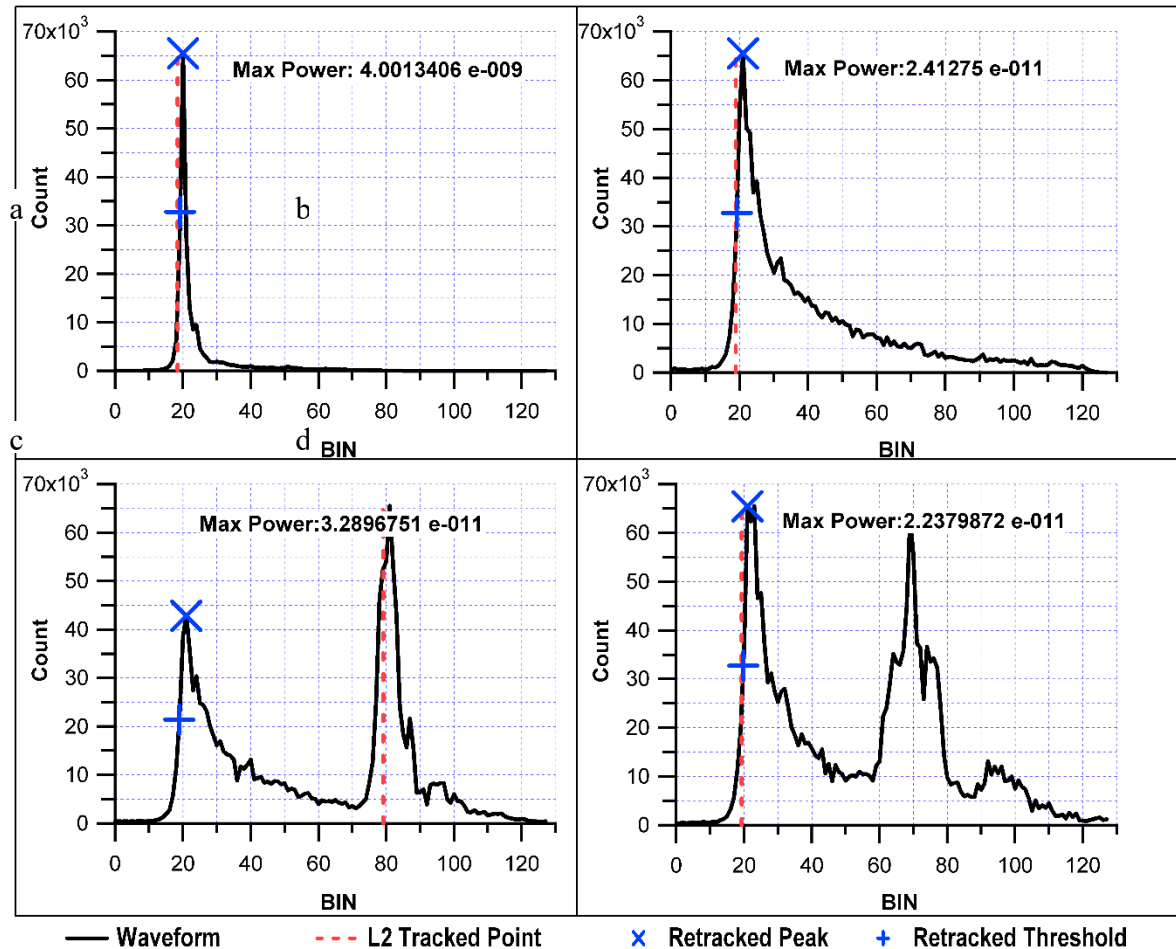


Figure 7.3: Normalized power waveforms from the extreme across-track snagging example in Figure 2 containing a) ice at nadir, b) open water at nadir, c) open water at nadir with a smooth reflector off-nadir (leading to snagging), and d) open water at nadir with a smooth reflector off-nadir (no snagging). The vertical dashed line indicates the position within the waveforms selected by the CryoSat-2 L2 retracker. X and + represent the location of the first peak and retracked power threshold value identified by a retracker under development at the University of Alberta.

7.4.2. Arctic

SARIn and SAR mode CryoSat-2 L2 data in the Arctic also exhibited across-track snagging and poorly retracked surface heights. The L2 surface height exhibited large waveform-to-waveform variations in surface height of over 8 m (Figure 7.4). Applying a simple retracking algorithm such

as the TSRA and tracking the first peak and not the peak of maximum power reduced these point-to-point variations dramatically.

The agreement between the AEM and CryoSat-2 thicknesses presented in Figure 7.5 is good. Although there is some disagreement in the latitudinal gradient, particularly for the data acquired on April 4, 2012, both datasets show good visual correlation in the location of peaks, troughs, and changes in thickness.

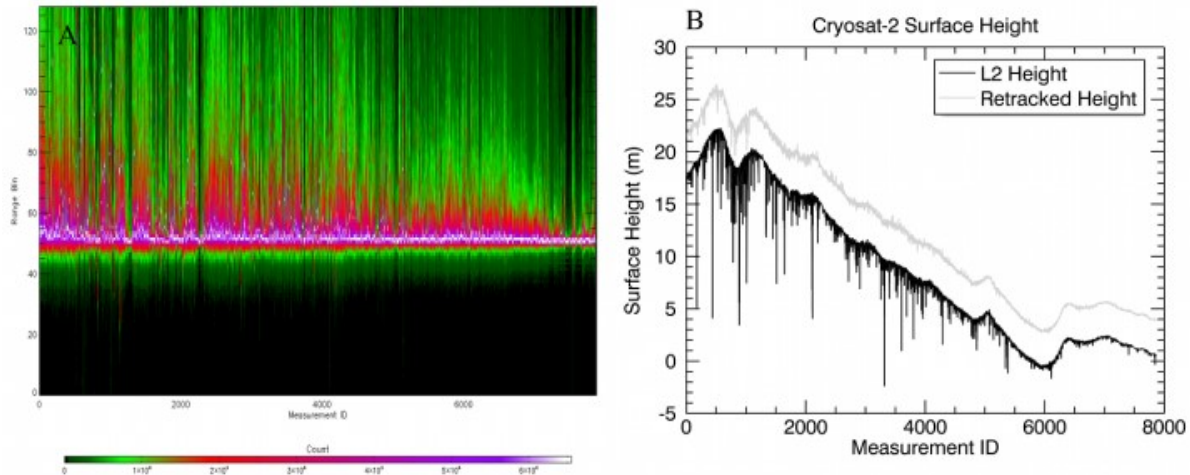


Figure 7.4: a) Normalized power waveforms from CryoSat-2 L1B data over the Lincoln Sea in the Arctic Ocean on April 3, 2012. b) Profile of the surface height from the L2 product (black) and after retracking the Level 1B waveforms (grey).

The CryoSat-2 thickness presented in Figure 7.5 assumes a continuous 20 cm snow cover. Uncertainties in the retrieved thicknesses are introduced by variations in the snow depth; differences in the depth of snow on multiyear and first year ice; unknown variability in the penetration depth of the radar signal in the snow; and the widely different scales of the airborne and satellite measurements all introduce uncertainty. AWI is currently developing a snow thickness field to improve the estimation of sea ice thickness from CryoSat-2. Furthermore, the AEM system measures the thickness of the snow + ice and is unable to determine the snow depth

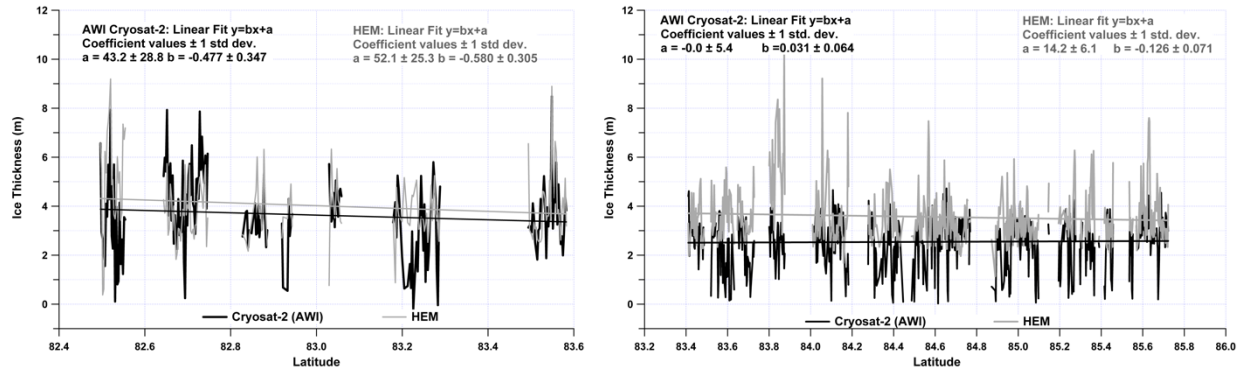


Figure 7.5: Comparison of the CryoSat-2 sea ice thickness estimates produced by AWI and AEM sea ice thickness measurements for CryoSat-2 SAR mode acquisitions from 2012/04/03 and 2012/04/04 over the Lincoln Sea.

The OIB flight on March 26, 2012 contains much more coincident data with Cryosat-2 than the AEM flights. A comparison of the CryoSat-2 freeboard produced by AWI and that measured by the OIB ATM system showed no difference in the modal freeboard value (Figure 7.6). The recorded OIB freeboard is the height of the snow surface above open water, termed the snow freeboard or total freeboard.

The agreement of the modal freeboards suggests that the Ku-band signal of Cryosat-2 may not completely penetrate the snow and may instead return from some point at or near the snow surface. Furthermore, the increased width of the CryoSat-2 freeboard histogram may indicate variability in the depth of penetration or the influence of other factors such as surface roughness or spatial sampling. Although large differences in the footprint size of Cryosat-2 and NASA OIB limits one-to-one comparisons, the latitudinal freeboard gradients from both systems are similar for this track (Figure 7.6).

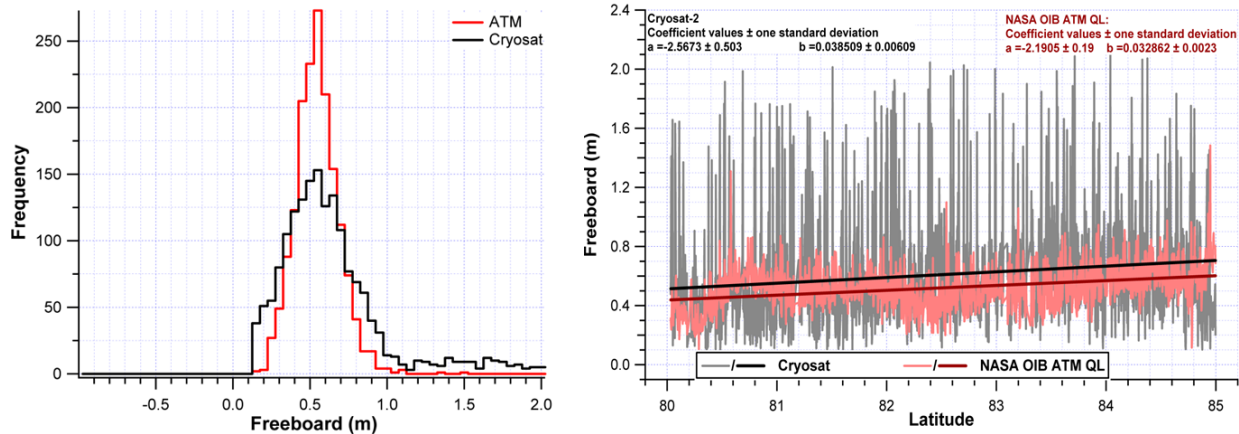


Figure 7.6: Comparison of CryoSat-2 freeboard produced by AWI and NASA OIB quick look freeboard for a CryoSat-2 SARIn mode pass from 2012/03/26 in the Arctic Ocean. OIB freeboard is the height of the snow surface above the water.

7.5. Conclusions and Recommendations

Issues such as across-track snagging and poor retracking quality were observed in all CryoSat-2 L2 data products examined in the Arctic and the Baltic Sea. Snagging was especially pronounced in the Baltic Sea. Re-tracking of waveforms to select the first return peak instead of the strongest return peak decreased the variability of the calculated surface heights suggesting that improvements to the Cryosat-2 Level 2 retracker operated by ESA are required. The AWI CryoSat-2 sea ice thickness estimates and the AEM measurements showed reasonable agreement in changes and trends. Modal freeboard measurements from a CryoSat-2 and a NASA OIB pass were indistinguishable suggesting that Cryosat-2 radar signal may not consistently penetrate through the snow to the snow/ice interface. Both datasets exhibited very similar latitudinal freeboard gradients.

Airborne validation datasets remain limited due to logistical difficulties and the need for open water leads for radar and laser altimetry measurements of freeboard. Long-distance regional surveys across thickness gradients and different ice regimes are needed for validation of CryoSat-2. Measuring gradients mitigates the issues related to the differences in spatial coverage and resolution of airborne and satellite sensors. Optimal regions for these types of measurement include the Lincoln Sea and other regions north of the Canadian Arctic Archipelago.

A dedicated and careful comparison of different retrackers, pre-processing methodology and output data is urgently required in order to provide the best quality product to the scientific

community and policy makers. A “standard” validation dataset should be selected and used to compare Cryosat-2 retracers, processors and products being produced by different research teams.

Although specified for Arctic sea ice, the possibility for the retrieval of sea ice freeboard in other regions such as the Baltic Sea and the Southern Ocean should be explored.

With the solution of the identified issues, and proper validation and calibration, CryoSat-2 offers the possibility of accurately monitoring the rapid changes in the sea ice thickness distribution of the Arctic Ocean.

7.6. References

- [1] D. K. Perovich, W. Meier, M. Tschudi, S. Gerland, and J. A. Richter-Menge, “Sea Ice,” in *Arctic Report Card 2012*, 2012.
- [2] J. Stroeve, M. M. Holland, W. Meier, T. Scambos, and M. Serreze, “Arctic sea ice decline: Faster than forecast,” *Geophysical Research Letters*, vol. 34, no. 9, p. L09501, May 2007.
- [3] J. C. Stroeve, V. Kattsov, A. Barrett, M. Serreze, T. Pavlova, M. Holland et al., “Trends in Arctic sea ice extent from CMIP5, CMIP3 and observations,” *Geophysical Research Letters*, vol. 39, no. 16, p. L16502, Aug. 2012.
- [4] R. Kwok and D. A. Rothrock, “Decline in Arctic sea ice thickness from submarine and ICESat records: 1958–2008,” *Geophysical Research Letters*, vol. 36, no. 15, p. L15501, Aug. 2009.
- [5] S. Laxon, N. Peacock, and D. Smith, “High interannual variability of sea ice thickness in the Arctic region,” *Nature*, vol. 425, pp. 947–950, 2003.
- [6] C. Haas, S. Hendricks, H. Eicken, and A. Herber, “Synoptic airborne thickness surveys reveal state of Arctic sea ice cover,” *Geophysical Research Letters*, vol. 37, no. 9, p. L09501, 2010.
- [7] K. A. Giles, S. W. Laxon, D. J. Wingham, D. W. Wallis, W. B. Krabill, C. J. Leuschen et al., “Combined airborne laser and radar altimeter measurements over the Fram Strait in May 2002,” *Remote Sensing of Environment*, vol. 111, no. 2–3, pp. 182–194, Nov. 2007.
- [8] R. Willatt, S. W. Laxon, K. A. Giles, R. Cullen, C. Haas, and V. Helm, “Ku-band radar penetration into snow cover Arctic sea ice using airborne data,” *Annals Of Glaciology*, vol. 52, no. 57, pp. 197–205, 2011.

- [9] D. J. Wingham, C. R. Francis, S. Baker, C. Bouzinac, D. Brockley, R. Cullen et al., "CryoSat: A mission to determine the fluctuations in Earth's land and marine ice fields," *Advances in Space Research*, vol. 37, no. 4, pp. 841–871, Jan. 2006.
- [10] S. W. Laxon, K. A. Giles, A. L. Ridout, D. J. Wingham, R. Willatt, R. Cullen et al., "CryoSat-2 estimates of Arctic sea ice thickness and volume," *Geophysical Research Letters*, vol. 40, no. 4, pp. 732–737, 2013.
- [11] R. Lindsay, C. Haas, S. Hendricks, P. Hunkeler, N. Kurtz, J. Paden et al., "Seasonal forecasts of Arctic sea ice initialized with observations of ice thickness," *Geophysical Research Letters*, vol. 39, no. 21, p. L21502, Nov. 2012.
- [12] N. Kurtz, M. Studinger, J. Harbeck, V. Onana, and S. Farrel, "Ice- Bridge sea ice freeboard, snow depth, and thickness." Digital Media, National Snow and Ice Data Center, Boulder, Colo., 2012.
- [13] N. R. Peacock and S. W. Laxon, "Sea surface height determination in the Arctic Ocean from ERS altimetry," *Journal of Geophysical Research*, vol. 109, no. C7, p. C07001, 2004.

8. Evaluation of CryoSat-2 derived sea-ice freeboard over fast ice in McMurdo Sound, Antarctica

8.1. Abstract

Using in situ data from 2011 and 2013, we evaluate the ability of CryoSat-2 (CS-2) to retrieve sea-ice freeboard over fast ice in McMurdo Sound. This provides the first systematic validation of CS-2 in the coastal Antarctic and offers insight into the assumptions currently used to process CS-2 data. European Space Agency Level 2 (ESAL2) data are compared with results of a Waveform Fitting (WfF) procedure and a Threshold-First-Maximum-Retracker-Algorithm employed at 40% (TFMRA40). A supervised freeboard retrieval procedure is used to reduce errors associated with sea surface height identification and radar velocity in snow. We find ESAL2 freeboards located between the ice and snow freeboard rather than the frequently assumed snow/ice interface. WfF is within 0.04m of the ice freeboard but is influenced by variable snow conditions causing increased radar backscatter from the air/snow interface. Given such snow conditions and additional uncertainties in sea surface height identification, a positive bias of 0.14 m away from the ice freeboard is observed. TFMRA40 freeboards are within 0.03 m of the snow freeboard. The separation of freeboard estimates is primarily driven by the different assumptions of each retracker, although waveform alteration by variations in snow properties and surface roughness is evident. Techniques are amended where necessary, and automatic freeboard retrieval procedures for ESAL2, WfF and TFMRA40 are presented. CS-2 detects annual fast-ice freeboard trends using all three automatic procedures that are in line with known sea-ice growth rates in the region.

8.2. Introduction

Although Antarctic sea-ice extent and concentration have been routinely monitored since 1979 (Parkinson and Cavalieri, 2012), the spatial and temporal distribution of sea-ice thickness remains one of the least understood physical components of the global cryosphere (Vaughan and others, 2013). Quantification of thickness is of crucial importance, since when combined with areal data it allows the computation of sea-ice volume. Sea-ice volume provides insight into the heat budget of the Antarctic sea-ice system and quantification of freshwater and saltwater fluxes

in the Southern Ocean. Due to the scarcity of in situ measurements of Antarctic sea-ice thickness, there is great demand for improved temporal and spatial thickness data through satellite altimeter observations (Zwally and others, 2008; Yi and others, 2011; Kurtz and Markus, 2012; Xie and others, 2013). Such observations support the capability to monitor trends and in turn provide data to model forecasts of future Antarctic sea-ice properties (Massonnet and others, 2013; Holland and others, 2014).

The use of satellite altimetry for sea-ice thickness estimation is entirely reliant upon the measurement of freeboard (Figure 8.1). Following this, thickness can be estimated based on the assumptions of hydrostatic equilibrium given input of values for the densities of snow, ice, water and snow thickness (Alexandrov and others, 2010). The ability to accurately measure freeboard and to include information on snow morphology is vital, as any errors in these input factors are greatly magnified in the eventual sea-ice thickness estimation. The European Space Agency's (ESA) Synthetic aperture radar Interferometric Radar ALtimeter system (SIRAL) on-board CryoSat-2 (CS-2) is the most advanced satellite radar altimeter instrument for sea-ice freeboard retrieval in operation to date (Drinkwater and others, 2004; Wingham and others, 2006), and at the time of writing is improving understanding of the Arctic sea-ice thickness distribution (Laxon and others, 2013; Kurtz and others, 2014; Ricker and others, 2014). Given the more heterogeneous and thinner state of Antarctic sea ice, primarily due to its exposed oceanic setting and its highly variable snow distribution and morphology (Massom and others, 2001; Ozsoy-Cicek and others, 2013), the uncertainty in resultant thickness estimates from CS-2 in the Southern Ocean is likely to be higher.

In this study, we validate freeboard measurements from CS-2 over fast ice in McMurdo Sound in 2011 and 2013. The fast ice in this area provides a safe platform for the collation of in situ data (Price and others, 2014), and the area has been well investigated (Jeffries and others, 1993; Gow and others, 1998; Leonard and others, 2006; Dempsey and others, 2010; Mahoney and others, 2011; Gough and others, 2012; Smith and others, 2012). The sea ice in McMurdo Sound is largely uniform and level, with smooth gradients in thickness. The complexity in view of satellite validation is significantly reduced in comparison to the more dynamic pack ice conditions.

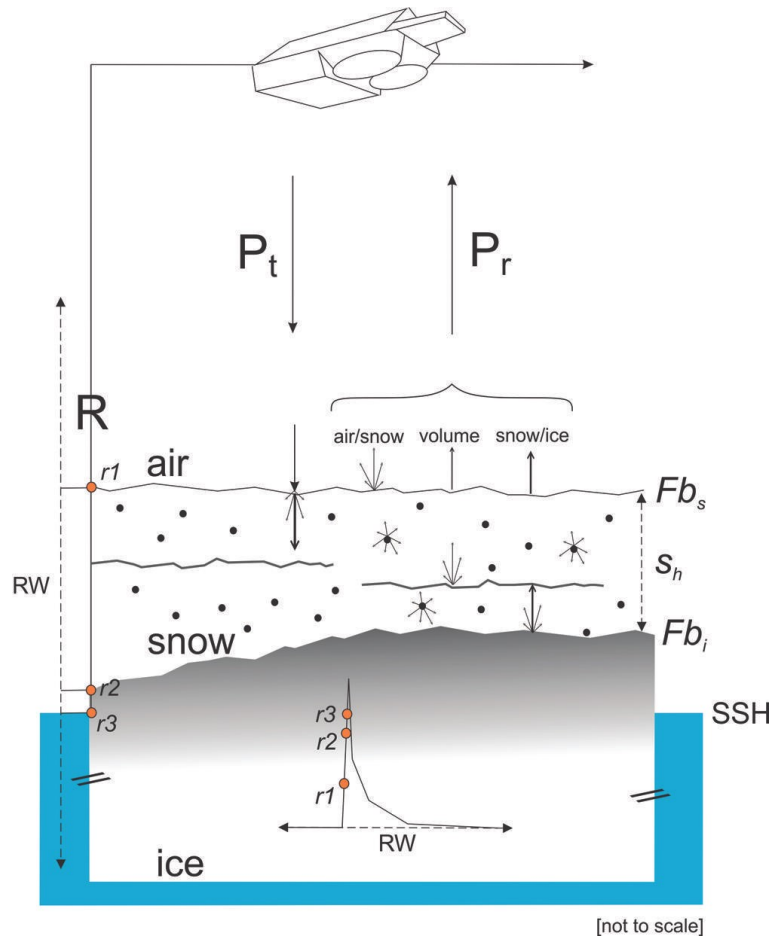


Figure 8.1: Components relating to the interpretation of CryoSat-2 freeboard data. The reception period is maintained by a range window (RW; 120m in SIN mode) which is constantly adjusted in the vertical dimension to receive echoes from the surface. The transmitted power (P_t) is subject to interaction at the surface from the air/snow interface, volume of the snow cover and snow/ice interface which all influence the power returned to the satellite (P_r). The dominant backscattering surface is variable and is displaced by varying snow depth (S_h), snow layering and snow and ice properties. The retracking procedure is completed, resulting in a range (R) between r_1 and r_2 over sea ice (r_3 over water) dependent upon the assumptions of the respective retracking technique. This range is subtracted from the satellite altitude above the ellipsoid to provide uncorrected height. After application of geophysical corrections, freeboard is obtained by discerning the difference between local sea surface height (SSH) and an interface in the range of the ice freeboard (Fb_i) and the snow freeboard (Fb_s) as measured by the satellite.

In common with many other coastal Antarctic regions (Fedotov and others, 1998; Fraser and others, 2011) McMurdo Sound harbors extensive areas of fast-ice neighboring coastal polynyas and ice shelves as regions of significant sea-ice production (Massom and others, 1998; Tamura and others, 2008). The performance of radar altimeters for freeboard retrieval in these regions

of highly variable ocean conditions is yet to be evaluated, specifically with regard to sea-ice/water discrimination over differing surface types (i.e. leads and polynyas of varying sizes).

Compared to ICESat (the Ice, Cloud and land Elevation Satellite; infrared laser shots with 70m footprints every 170m along track), the CS-2 radar signal penetrates cloud cover but produces a larger footprint of $\sim 380 \text{ m} \times 1650 \text{ m}$ dependent upon orbit parameters and surface geometry (Bouzinac, 2013). Freeboard retrieval using laser instrumentation is simplified by the fact that the main reflection from the snow surface is well defined. In Ku band (SIRAL center frequency 13.6 GHz) the backscattered radar energy is more susceptible to alteration from surface conditions, but the main reflection is assumed to originate primarily from the snow/ice interface (Laxon and others, 2013). A recent simulation suggests that the influence of snow on sea ice is not negligible as it can broaden the waveform of the returned signal, thus displacing the tracking point (corresponding to the retrieved surface height) toward the altimeter (Kwok, 2014). The influence of snow on the shape of the returned waveform depends on its dielectric properties which are dictated by salinity, liquid water content, density, grain size and temperature (Hallikainen and others, 1986; Ulaby and others, 1986; Barber and others, 1995).

Given the complex snow stratigraphy and snow microwave interaction, there is no consensus on a dominant backscattering surface. For example, no single dominant backscattering surface was found for stratified snow during in situ investigations using a 10–16 GHz band instrument, but returns from the snow/ice interface dominated when layering in the snow cover was absent (Willatt and others, 2010). Surface roughness also influences the freeboard retrieval as it directly affects the shape of the returning radar waveform (Drinkwater, 1991; Beaven and others, 1995; Hendricks and others, 2010). Surface roughness may be separated into radar and geometric roughness: the former is associated with small-scale features at length scales comparable to the radar wavelength (in this case 0.02 m), and the latter is concerned with large-scale surface undulations (e.g. ridging and cracks). The bandwidth of the compressed high-intensity radar pulse (chirp) of SIRAL (320 MHz) results in a range resolution of 0.47 m. This can resolve neither the air/snow nor the snow/ice interface, making the identification of surface height highly dependent on the slope of the leading edge of the returned waveform (Figure 8.2).

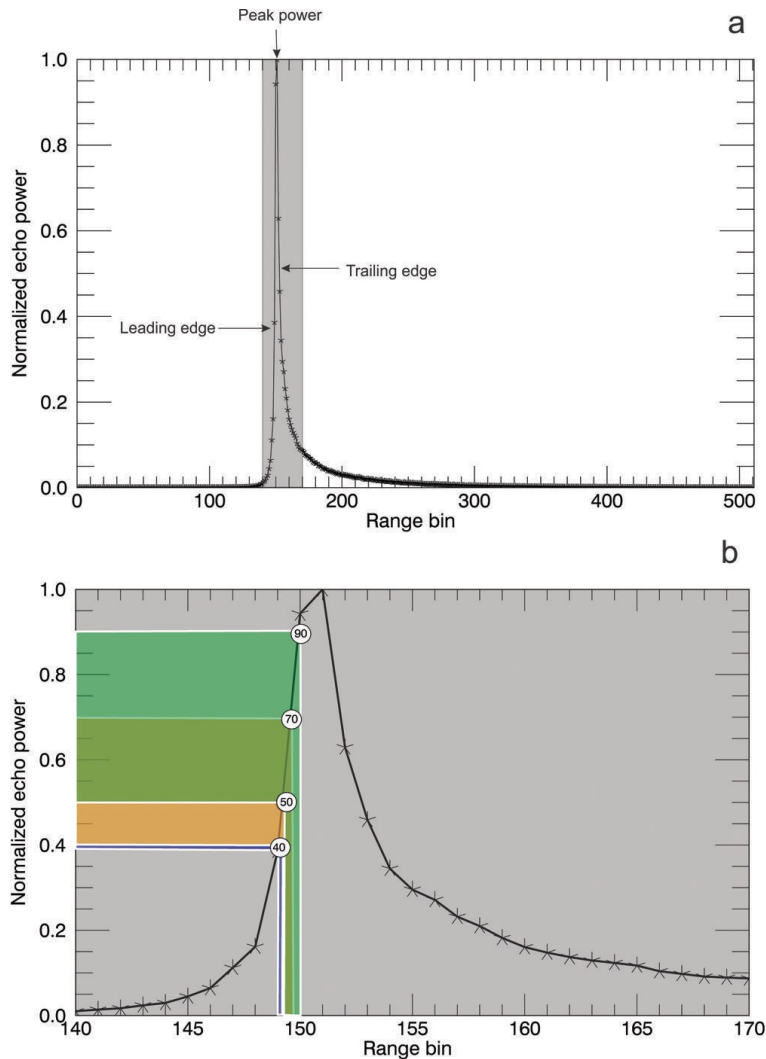


Figure 8.2: (a) Typical CryoSat-2 SIN mode waveform over snow-covered sea ice in McMurdo Sound with labelling of characteristics mentioned in the text. (b) An expanded view of the outlined grey area in (a) from range bins 140–170 (1 bin = 0.234 m) and the expected retracking points on the leading edge for the techniques described here: ESAL2 (40–70% orange), WfF (50–90% green) and TFMRA40 (40% blue).

The factors described above exacerbate the accurate localization of a dominant backscattering surface over sea ice, and, in turn, the retracking, a procedure which interprets the waveform to estimate the range to the surface, is complicated (Figure 8.1 and Figure 8.2). There are currently two separate approaches using waveform interpretations to establish retracking points: (1) a waveform-fitting approach that takes into account the shape of the returned waveform based on a physical model; and (2) an empirical approach that only considers the leading edge and estimates surface height at a given power threshold. Waveform fitting is the

basis for the ESA's Level 2 product (ESAL2) and the Waveform Fitting (WfF) procedure as described by Kurtz and others (2014). The Threshold-First-Maximum-Retracker-Algorithm employed at 40% (TFMRA40) is an empirical approach presented by Helm and others (2014) and applied over sea ice by Ricker and others (2014).

In this paper, we assess the assumptions behind the techniques referenced above with a detailed in situ investigation on fast ice in McMurdo Sound. With the addition of Moderate Resolution Imaging Spectroradiometer (MODIS) imagery we undertake a supervised freeboard retrieval procedure in which sea surface height is manually classified on a small number of selected CS-2 tracks. Using this optimal dataset, and additional CS-2 waveform information, we provide insight into the influence of differing surface conditions (snow properties and surface roughness) on the resultant freeboards from each technique: ESAL2, WfF and TFMRA40. This supervised analysis also provides information on the estimated accuracy of CS-2 freeboard retrievals over the fast ice in McMurdo Sound. With information gained in an initial evaluation, we subsequently develop three automatic freeboard retrieval procedures and assess the sea-ice regime in McMurdo Sound for the entirety of 2011 and 2013.

First, we describe the study area of McMurdo Sound and in situ information and provide an overview of CS-2 in Section 8.3. In Section 8.4, we describe and discuss the surface height retrieval procedure for CS-2 under each technique. In Section 8.5, we manually identify sea surface height and complete a supervised freeboard retrieval investigation providing freeboard estimates for each technique and report the findings of these results and their implications. Following this, in Section 8.6, we describe the three automatic algorithms used to assess the years 2011 and 2013 in a larger area of McMurdo Sound. Results from these automated procedures are then reported and discussed in the final sections.

8.3. CryoSat-2 Assessment in McMurdo Sound

This section describes the study area of McMurdo Sound, the in situ investigation and provides an overview of CS-2. The study area (Figure 8.3) is located in the southwestern Ross Sea and occupies an area of ~ 6400 km². McMurdo Sound's proximity to ice shelves and the outflow of cold ice-shelf water from the ice-shelf cavity contributes to sea-ice formation in this area (Purdie and others, 2006; Dempsey and others, 2010; Mahoney and others, 2011; Gough and

others, 2012; Price and others, 2014). This influence is hypothesized to be present in similar settings around the Antarctic with potential basin-wide implications (Hellmer, 2004; Bintanja and others, 2013). At the time of writing, McMurdo Sound harbors a first-year (FY) sea-ice regime with extensive areas of highly homogeneous fast ice in its southern and western extremities and the McMurdo Sound Polynya (MSP) at its center. The MSP undergoes complete freeze-up and breakout events throughout autumn and winter but is typically open water during spring and summer. This open-water area can become intermittently inundated with a cover of sea-ice floes that have drifted south from the Ross Sea.

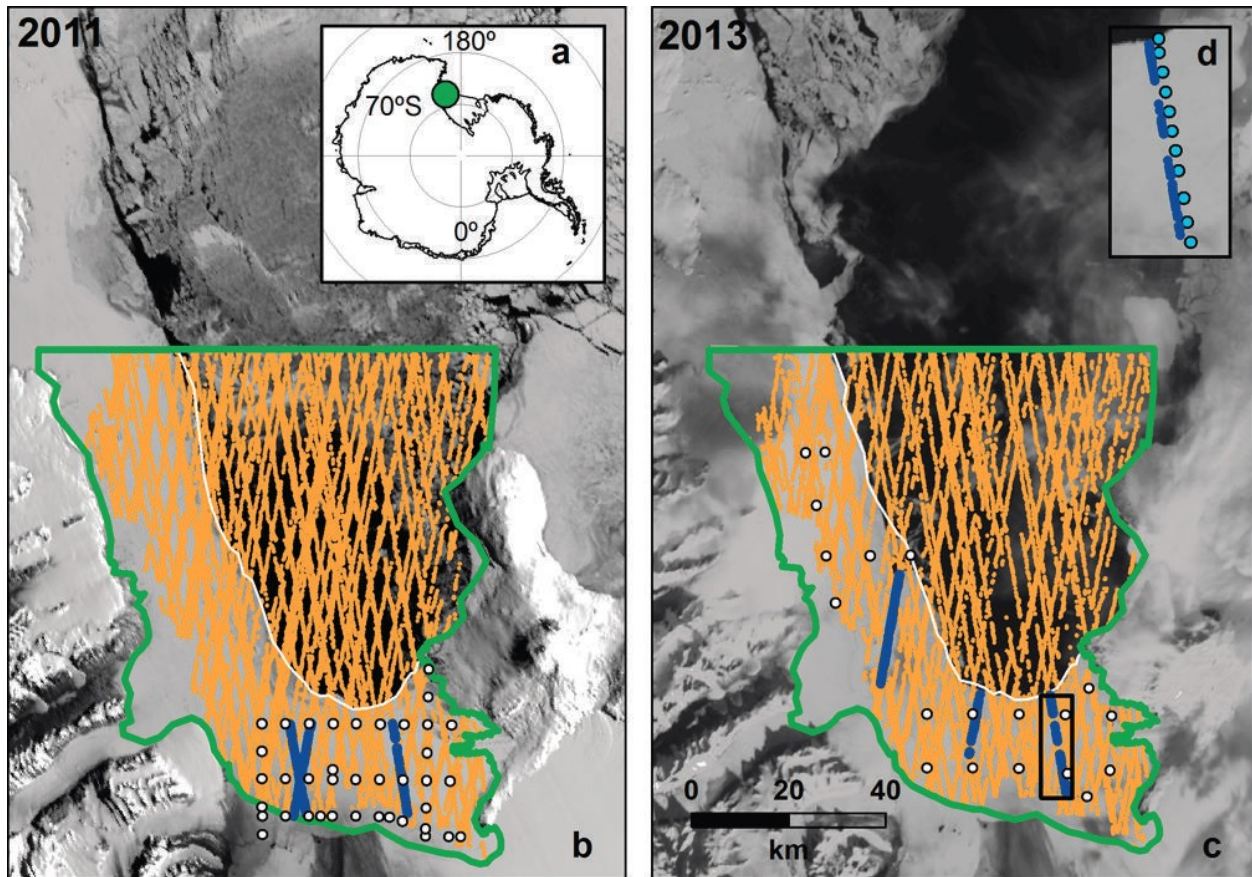


Figure 8.3: (a) Location of the study area within the Antarctic. (b, c) McMurdo Sound and the study area for 2011 (b) and 2013 (c), showing the distribution of CryoSat-2 tracks for those used in the supervised analysis (blue lines), the automatic study period (orange lines) and locations of in situ measurement sites (white dots). The November fast-ice edge is displayed for each year (white line). The full study area for each annual automatic analysis is outlined in green. The validation line in Figure 8.4 is highlighted by the black rectangle and expanded in (d) to show each in situ measurement point (light blue dots) along the CryoSat-2 track.

8.3.1. In situ investigations

During two in situ measurement campaigns in November and December 2011 and 2013, sea-ice freeboard, thickness and snow depth/density measurements were made for comparison with CS-2 freeboard retrievals. The locations of in situ measurements within McMurdo Sound are shown in Figure 8.3. The in situ measurement campaign in 2011 along with an overview of sea-ice conditions in McMurdo Sound is described in Price and others (2014), and these same measurement procedures were carried out in 2013. Even though the sea-ice conditions in 2013 were very similar to 2011, it is important to note that surface conditions were slightly different with regard to the snow cover and surface roughness. The first of the differences was related to sea-ice deformation. The sea-ice cover was more deformed in the west in 2013, resulting in higher geometric surface roughness. The second notable difference was in the snow cover. In 2011 the snow was characterized as wind-compacted, with a large variability in hardness, density and grain size. Grain size was generally large near the ice (~ 3 mm), and smaller in the upper layers, typically ~ 0.5 mm and smaller. Where snow was 0.20 m in thickness we found two to three layers, with densities varying between 330 and 450 kgm^{-3} with no significant correlation between depth and density. In 2013 a similar situation existed, but both thickness and layering were reduced, while radar roughness was likely higher given a less uniform snow surface at the centimeter scale. In both years the distribution was highly variable, with many different snow types present.

8.3.2. CryoSat-2

Launched in April 2010, CS-2 operates in a near-circular polar orbit with an inclination of 92° and has a repeat cycle of 369 days with a subcycle of 30 days. Its on-board altimeter, SIRAL, operates at a center frequency of 13.6GHz and is normal-incidence, with two receiver chains operating in two modes over sea-ice areas (Bouzinac, 2013). Its dedicated sea-ice mode uses synthetic aperture radar (SAR) processing for height retrievals along-track at an improved spatial resolution. In addition, being pulse-limited across track results in a footprint size of approximately $380\text{m} \times 1650$ m, with along-track sampling at $\sim 300\text{m}$ intervals permitting enhanced along-track ice/water discrimination and higher sampling (Bouzinac, 2013). In Antarctic coastal regions, SIRAL

switches to SAR interferometric (SIN) mode for ice-sheet margin investigation. Interferometric processing discerns the arrival angle of radar returns via phase comparison of the returning signal. This permits them to be correctly positioned on the Earth's surface, and off-nadir returns to be accurately ranged (Wingham and others, 2006; Bouzinac, 2013). This is a necessity in complex terrain, where off-nadir reflections can be received by the satellite prior to nadir reflections. The SIN mask extends out to a maximum distance of ~ 300 km from the Antarctic coastline and ice-shelf margins. Due to the study area's proximity to the Antarctic continental coast it falls within the SIN mask. To account for the increased range over which the surface may be encountered by the incident radar beam in complex terrain, a longer tracking window is permitted in SIN mode. At the same time the reduction in burst-repetition frequency decreases the number of resulting measurements by a factor of four compared to SAR mode (Wingham and others, 2006; Bouzinac, 2013). The measurement range window is segmented into 512 bins providing a range sampling of 1.563 ns (0.234 m in vacuo). A CS-2 SIN mode example waveform with labelling relevant to the text is shown in Figure 8.2. The surface is maintained in a range window along track, which constantly adjusts to keep the leading edge at a specific point near the center of the window (Bouzinac, 2013). Energy from the surface that is returned to the satellite builds above the noise level and increases along the leading edge to the peak power. This then decays (the trailing edge) to the end of the tracking window. The retracking procedure is then used to identify the point on the waveform that provides the range to the surface. Multiple methods exist to execute this procedure based on different assumptions about the interaction of radar energy and the surface.

8.4. Tracking Surface Height from CS-2 Waveforms

We begin our analysis with a description of the respective retracking procedures for each method. The retracking procedure aims to provide the best estimate of range between the satellite center of mass and the dominant backscattering horizon on the Earth's surface. This is achieved by interrogating ESA's baseline B Level 1B (SIR_SIN_L1) waveforms. It results in geolocated surface heights (h^*) which are referenced to the World Geodetic System 1984 (WGS84) ellipsoid after subtracting retracked range from the satellite's altitude.

8.4.1. European Space Agency Level 2 data product (ESAL2)

We utilize ESA baseline B Level 2 SIN mode (SIR_SIN_L2) data which have already undergone a retracking procedure (Bouzinac, 2013). Using SIR_SIN_L1 the ESA processor applies a model fit to determine heights from waveforms fitted to the model echo shape (Wingham and others, 2004, 2006). The ESA waveform retracker is described as a ‘customer furnished item’ in the CryoSat Product Handbook (Bouzinac, 2013), but no further information is provided by ESA at the time of this publication. Using SIR_SIN_L1 and SIR_SIN_L2 data in unison from CS-2 data within our study area, the retracking point is shown to vary on the leading edge over a range of 40–70% of peak power (Figure 8.2). Using phase information, a correction for off-nadir scattering is also applied in this product. With the available literature, we are unable to conclude with confidence which surface (air/ snow or snow/ice) is expected to dominate the backscatter, or what assumptions are made in the model.

8.4.2. Waveform Fitting procedure data product (WfF)

Kurtz and others (2014) provide an overview of this product. Surface height is estimated by fitting a physical model to the SIR_SIN_L1 waveforms. The model parameters include the surface roughness, which is assumed to be Gaussian, and the variation of the backscatter with incidence angle. Dependent upon the parameters described in Kurtz and others (2014), WfF establishes its retracking point at $\sim 50\text{--}90\%$ (Figure 8.2) of peak power on the leading edge for nonspecular returns and assumes that the dominant backscattering surface is the ice/snow interface. For specular returns, the model converges to the shape of the compressed transmit pulse and the retracking point is near the point of peak power, but can also be beyond the leading edge due to the finite sampling resolution of the waveform.

For the SIN mode data used in this product, the phase information is used to determine the angle to the point of closest arrival determined by the retracking point. A correction for the retracked height, due to off-nadir scattering, is determined and applied from the phase information using the procedure described by Armitage and Davidson (2014).

8.4.3. Threshold-First-Maximum-Retracker-Algorithm 40 (TFMRA40)

This product is based on SIR_SIN_L1 waveforms, but phase information from the returning echo is discarded. The range of the main scattering horizon is obtained by applying a Threshold-First-Maximum retracker to the waveforms; in this study, we use a threshold of 40%. The processing follows Ricker and others (2014) by:

1. Oversampling of the original waveform by a factor of 10 using linear interpolation.
2. Smoothing of the oversampled waveform by applying a running mean with a width of ten range bins to reduce noise.
3. Determination of the first maximum by the derivative of the interpolated curve.
4. Retrieval of the ellipsoidal elevations by tracking the leading edge of the first maximum at 40% of the peak power (as in Figure 8.2).

The main scattering horizon is assumed to be close to the surface, whether this is the air/snow interface or, in the absence of snow cover, the ice/air interface.

8.4.4. Tracking of sea surface height

The sea surface state at the time of the satellite overpass can alter the shape of the returning waveform. Over leads, given their small fetch, the surface is typically smooth. This provides a uniform surface with a characteristic specular waveform response, an ideal surface for both discrimination of water from sea ice and the use of consistent techniques for tracking the sea surface. However, as the size of the open-water area being referenced is increased so is its susceptibility to wind. This is clearly evident over the polynya area in McMurdo Sound, which does not exhibit the typical specular waveform expected from a lead. This is the first of three issues related to the identification of sea surface height (SSH) noted in this study and is described in more detail below. These areas were observed to hamper the identification of SSH in certain sea conditions. When the significant wave height (SWH) is increased by wind forcing, the slope of the leading edge of the radar waveform is flatter due to increasing off-nadir contributions. In the case of TFMRA40 this influence resulted in insufficient separation of fast-ice elevation retrievals from sea surface retrievals (i.e. SSH was too high relative to the sea-ice surface). Such an influence was not observed on the ESAL2 or WfF techniques that retrack 'higher' on the leading edge and attempt to account for physical differences in surface roughness and incidence

angle backscatter variations. This emphasizes the need for the inclusion of an additional surface type to the TFMRA40 procedure. The surface type polynya has been added to the original three, ocean, lead and sea ice (Ricker and others, 2014), to accurately record SSH for the open-water area in McMurdo Sound. Over surfaces flagged as polynya the surface is tracked at 60%, as opposed to 40% over leads and sea ice. This increase in the retracking threshold accommodates for the flatter leading edge forced by a higher SWH. This amendment improved agreement between TFRMA40 freeboard retrievals and in situ measured freeboard data.

Secondly, the occurrence of ‘mixed’ surface types within the CS-2 footprint produces noisy waveforms. Regions in which larger open-water areas are intertwined with sea-ice floes and smaller open-water areas, more representative of leads, caused complications with the retracking procedure. These conditions were more prevalent in 2011, when ice floe conditions were more variable in the regions classified as open-water areas. The WfF procedure was influenced by this, which led to SSH retrievals being too low. Slight amendments were applied to attempt to discard noisy waveforms that were causing a delay in range. These amendments, which attempted to remove noisy waveforms by assessing the occurrence of early peaks in power before maximum power, and altering the initial guess of the power to be retracked, resulted in negligible improvements. Further improvement of this procedure is a current research focus.

Thirdly, as the leading edge is not necessarily affected over its entire height in the same manner, this can result in the influence of sea conditions being variable between retrackers that are operating at different positions on the leading edge (Figure 8.2). This introduces an inter-retracker bias given the same sea surface conditions. The quantification of these errors is not within the scope of this study given our inability to confidently establish sea surface conditions at the time of data acquisition. Although we are not able to fully resolve all the issues discussed in this section we include them here to provide context for the discussions which follow.

8.5. Supervised Freeboard Retrieval

The retrieval of sea-ice freeboard from radar altimetry requires multiple processing steps. These steps remove spurious influences on the height profile, revealing desired variations driven by freeboard. At this stage, the main uncertainties in the CS-2 freeboard retrieval are driven by:

1. The ability of an algorithm to distinguish between water and sea ice and therefore accurately establish SSH.
2. The availability and accuracy of snow depth information.
3. The limited understanding of the reflected waveform as a function of surface and volume scattering.

Here we minimize the uncertainty under point 1 with the use of MODIS optical imagery by undertaking a supervised identification of the sea surface, establishing a more accurate SSH. We greatly reduce the uncertainty from point 2 with available in situ snow depth/density information. We use these additional data sources, and retrieve a supervised freeboard (Fb_{sup}) for six CS-2 tracks, three from each year 2011 and 2013, for the period mid-November to early December (Figure 8.3). This places the in situ measurements in near temporal coincidence with the CS-2 data which were acquired between 21 November and 4 December. The uncertainty introduced by point 3 is expanded upon in Section 8.7.

We begin our analysis using h^* estimated for each technique in Section 8.4, which is first corrected for varying influences on the transmitted radar wave as it propagates through the atmosphere (cr_i): dry tropospheric, wet tropospheric and ionospheric corrections (Bouzinac, 2013). The ellipsoidal height is then reduced to a quasi-orthometric height (h) after subtracting geoid height (N) provided by the Earth Gravitational Model 2008 (EGM2008). This approximates mean sea level (MSL). To construct a SSH from this, further information is needed to quantify the sea surface height anomaly, which is the sum of the varying influences of tides (t) and atmospheric pressure and wind (i). No corrections are applied for t at this stage, as the tidal gradient was found to be negligible over the spatial area in the supervised assessment. This was determined through the use of global navigation satellite systems (GNSS) stations deployed on fast ice in McMurdo Sound which showed no tidal gradient across the assessed distances (Price and others, 2014).

Table 8.1: Mean freeboard values, standard deviations and sample sizes (n) derived by each retracker by the supervised procedure in austral spring (November and December) 2011 and 2013 and comparison to interpolated in situ mean ice (F_i) and snow freeboards (F_s). The satellite tracks from which each $F_{b_{sup}}$ mean is derived are displayed in blue in Figure 8.3.

Retracker	Spring 2011 $F_{b_{sup}}$ n = 148 m	Spring 2013 $F_{b_{sup}}$ n = 163 m
F_{b_i}	0.22 ± 0.07	0.21 ± 0.04
F_{b_s}	0.33 ± 0.01	0.26 ± 0.04
ESAL2 $F_{b_{sup}}$	0.29 ± 0.14	0.24 ± 0.17
WfF $F_{b_{sup}}$	0.36 ± 0.13	0.17 ± 0.13
TFMRA40 $F_{b_{sup}}$	0.36 ± 0.15	0.29 ± 0.11

Given the ~ 50 km distance, we also expect the influence of i to be negligible. We therefore arrive at h with

$$h = (h^* + cr_t) - N \quad \text{Eq. 8.1}$$

Using MODIS imagery, we identify open-water areas along each CS-2 track and manually prescribe surface types of water or sea ice to each h value. The construction of SSH requires the removal of surface height outliers over the water surface type. The mean is largely biased by such outliers, so, in this case, where we are confident open water dominates, we use the median to establish the supervised SSH (SSH_{sup}). We sample ~ 25 km sections along track, which provides ~ 100 individual h values from which to construct SSH_{sup} . Radar freeboard ($F_{b_{radar}}$) is then derived by

$$F_{b_{radar}} = h - SSH_{sup} \quad \text{Eq. 8.2}$$

Given the assumptions about each retracker with regard to snow penetration, we follow Kurtz and others (2014) and freeboard is then derived with the addition of a correction for the speed of light in snow. This correction (h_c) over sea-ice areas is given by

$$h_c = s_h \left(1 - \frac{c_{snow}}{c} \right) \quad \text{Eq. 8.3}$$

where s_h is the snow depth, c the speed of light in a vacuum, and c_{snow} the speed of light in the snowpack following Tiuri and others (1984) parameterized as

$$c_{snow} = \frac{c}{\sqrt{1 + 1.7\rho_s + 0.7\rho_s^2}} \quad \text{Eq. 8.4}$$

where ρ_s is the snow density (g cm^{-3}) measured as 0.385 gcm^{-3} in McMurdo Sound (Price and others, 2014). This value was also measured as the mean snow density from in situ measurements in 2013. s_h is provided by the spatial interpolation of in situ snow depth measurements. With regard to snowpack penetration by the incident radar wave we assume full penetration for ESAL2 and WfF and no penetration for TFMRA40. The reduction of c in the snow cover results in an increased range estimate from satellite to surface. This will force a negative bias in the resultant freeboard if uncorrected; we therefore arrive at Fb_{sup} for each respective retracker under the manual assessment over fast ice with

$$Fb_{sup} = Fb_{radar} + h_c \quad \text{Eq. 8.5}$$

We treat Fb_{sup} outliers by removing any retrieval that deviates by >3 standard deviations from the mean over the sea-ice area. Finally, we ensure datasets are comparable with the manual removal of Fb_{sup} values that are not available for all three products.

8.5.1. Supervised freeboard retrieval results

In this subsection, we provide results from the supervised analysis of CS-2 derived freeboards from each retracker. We compare these results to in situ freeboard measurements and use this in combination with complementary field and satellite data to relate the effect of surface conditions on the resultant Fb_{sup} values. In situ ice freeboard (F_i) and snow freeboard (F_s) are provided from the interpolation of in situ measurements and extracted to be spatially coincident with each individual CS-2 Fb_{sup} retrieval (the tracks of which are shown in Figure 8.3). This step was undertaken to provide a better spatial comparison between in situ measurements and CS-2. The mean values of the interpolated points extracted at each Fb_{sup} retrieval agree to within 0.01m of the in situ mean values. The variability introduced by the interpolation is largest with regard to Fb_s driven by variations in s_h . Leave-one-out cross-validation indicates that a maximum deviation of 0.05 m can be expected (Price and others, 2014). Fb_{sup} which are the mean values of the three CS-2 tracks in each year are shown with in situ means in Table 8.1. The retracking techniques produce Fb_{sup} mean values ranging from 0.17 to 0.36 m, which are in line with the range of in situ measured freeboards in McMurdo Sound of 0.21 – 0.33 m. All retrackers provide higher Fb_{sup} estimates in 2011 than in 2013 when the snow was deeper. 2013 Fb_{sup} values for each technique are in agreement with what is expected given the assumptions of the described

retrackers (see Figure 8.2 and difference in range), WfF the lowest and TFMRA40 the highest. WfF shows closer agreement with F_i , while TFMRA40 freeboards are closer to F_s . ESAL2 Fb_{sup} is established between F_i and F_s . Therefore, the trivial relationship between differences in retracked range and resultant freeboard values is maintained in 2013. The comparison is complicated in 2011 with regard to WfF, as its Fb_{sup} value is 0.19 m higher than in 2013, with only a 0.01 m change in F_i recorded in situ. The cause of this discrepancy is unclear. It is likely that interference with SSH_{sup} establishment, as alluded to in Section 8.4.4, played a role in the high freeboard value for WfF, but we also need to consider the influence of the snow cover. The full snow-cover penetration assumption of the WfF method may not be fulfilled given a smooth snow cover can be an effective scatterer of the incident radar energy. When the echo power from the snow/ice interface and that from the air/snow interface have a similar magnitude, a positive freeboard bias may be introduced (Kurtz and others, 2014; Kwok, 2014). This bias is estimated to reach a maximum of 0.04 m for homogeneous snow conditions (Kurtz and others, 2014). It is likely to have played a more significant role here due to snow stratification and wind crusts at the surface. From the limited information about the retracking procedure for ESAL2 we would expect to see a similar relationship. Such a relationship is observed, with ESAL2 Fb_{sup} 0.05 m higher in 2011 than in 2013.

To provide further insight into the influence of snow cover and ice conditions on the radar signal, we show Fb_{sup} along a coincident in situ validation line on 27 November 2013 (Figure 8.4). The validation measurements along this line were temporally coincident to within 3 hours of the CS-2 overpass.

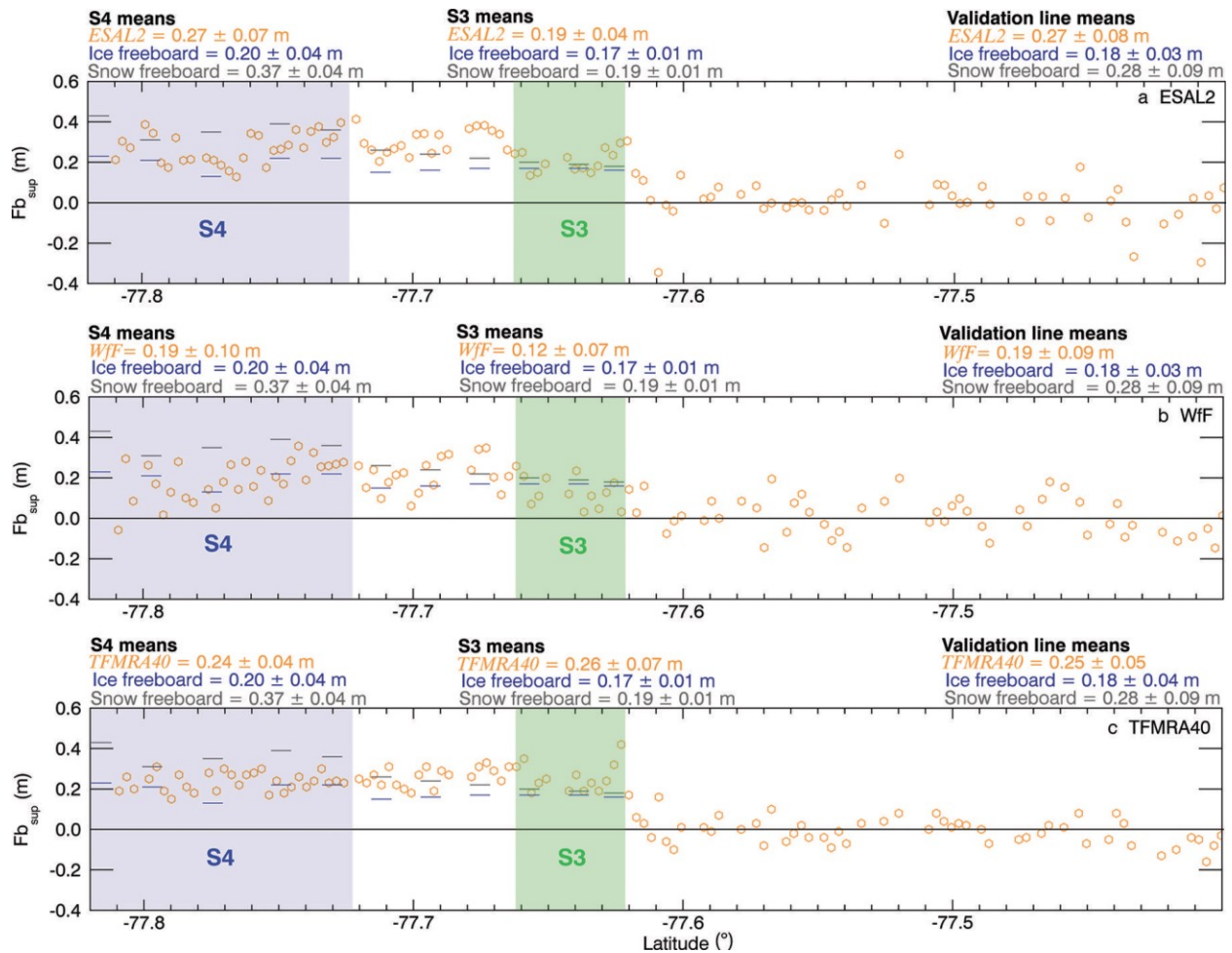


Figure 8.4: Comparison of each method along a validation line coincident with a CryoSat-2 overpass on 27 November 2013 for (a) ESAL2, (b) WfF and (c) TFMRA40. In situ measured ice and snow freeboards are shown as blue and grey horizontal lines respectively. Segments 3 (S3) and 4 (S4) in Figure 8.5 are also shown. Sea surface height was identified using the supervised procedure. The CryoSat-2 height profile begins in the north over open water and progresses south over the fast-ice edge at the beginning of segment 3. The freeboard retrievals for each respective retracker are displayed as orange circles, and the validation line statistics describe the sea-ice area only. S3 and S4 means are also displayed for each technique, along with the ice freeboard and snow freeboard measured in situ.

It should be noted that due to a satellite orbit maneuver the validation line was .1km east of the CS-2 ground track. Visually we observed no significant changes to the characterized sea-ice surface conditions or snow depth over this distance and therefore find the in situ and CS-2 datasets comparable. The surface conditions on the sea ice varied along the validation line from north to south. Clear differences in Fb_{sup} are displayed between the techniques. Mean Fb_{sup} for WfF shows good agreement with F_i . ESAL2 mean Fb_{sup} is in better agreement with F_s , but the

response of the height retrievals to surface conditions follows a similar pattern to that observed for WfF. TFMRA40 has a very consistent $F_{b_{sup}}$ profile which exhibits minimal response to changing surface conditions, producing values that closely agree with F_s across the whole profile. We are able to assess the response of each of the retracking techniques to the presence of a homogeneous section of dry snow in segment 4 (Figure 8.4). For all techniques, $F_{b_{sup}}$ appears to track an interface which is in good agreement with measured in situ F_i over segment 4. ESAL2 and WfF record the in situ measured decrease in F_{b_i} in the central part of the segment. Further in support of WfF assumptions, its mean $F_{b_{sup}}$ value agrees to within 0.01m of in situ measured F_i with no positive bias as CS-2 passes over this area of relatively homogeneous snow cover (segment 4: mean WfF $F_{b_{sup}} = 0.19$ m, in situ $F_i = 0.20$ m, in situ $F_s = 0.37$ m). However, for the 2011 WfF freeboard, measured when the snow cover was smoother and more layered in comparison to segment 4 in 2013, the mean WfF $F_{b_{sup}}$ value is 0.36 m, 0.14m higher than F_i (Table 8.1). Both ESAL2 and WfF clearly exhibit a large variability in freeboard retrievals over sea ice in response to either snow or ice conditions. We attempt to separate the influences of snow and sea-ice conditions using near-coincident TerraSAR-X (X-band) imagery, in situ measurements, and observations. We provide four segments in McMurdo Sound in 2013 over which sea-ice geometric roughness (GR) and radar roughness (RR) varied. Considering the similar wavelengths in X band (~ 0.03 m) and Ku band (~ 0.02 m), and also assuming the incidence angle dependence of backscattering properties is dominated by surface scattering, a near-inverse relationship between backscattered power between Terra- SAR-X (40° incidence angle) and CS-2 (normal incidence) can be expected (Ulaby and others, 1982).

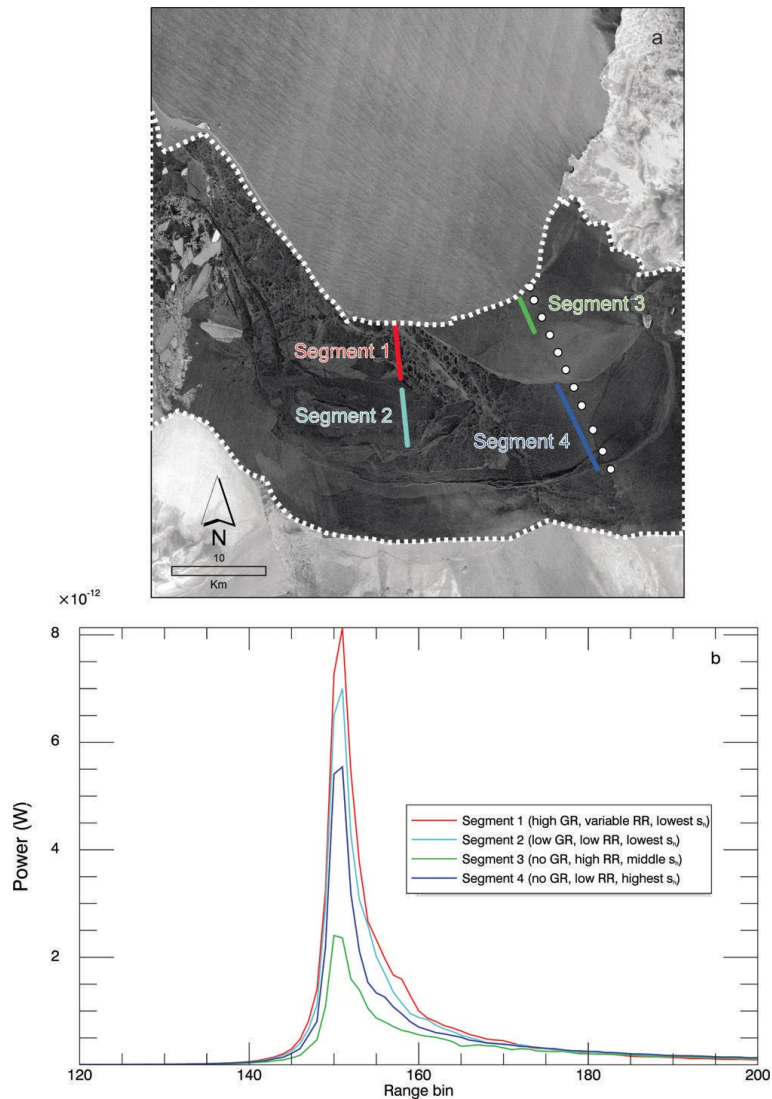


Figure 8.5: (a) Segments 1–4 over the first-year sea-ice area (bounded by white dotted line) overlaid upon a TerraSAR-X radar image from 28 November 2013. TerraSAR-X image (courtesy DLR (German Aerospace Center)). (b) Mean waveforms from these segments plotted as power for multiple sea-ice surface conditions with variable geometric roughness (GR), radar roughness (RR) and snow depth (s_h).

In the TerraSAR-X image the relatively bright areas on level sea ice (bounded by a white dotted line in Figure 8.5a) are rough with respect to the radar wavelength, and the dark areas are smooth. For the sea-ice area, we assess the differences in CS-2 waveforms that have been averaged and stacked to represent these different segments. The numbers of waveforms averaged to create each representative waveform were between 15 and 28. We identify an area of high GR (segment 1: FY ice that has likely been deformed by storm activity) and low GR

(segment 2: older FY ice which was less deformed) over the FY fast-ice area. These were established primarily from field observations, with the TerraSAR-X image as support. Segment 1 (high GR, variable RR, lowest s_h) causes the largest power return, closely followed by segment 2 (low GR, low RR, lowest s_h). It is clear that other variables also influence the signal return, which is evident from comparison of segments 3 and 4. Segment 3 has the lowest power return of the assessed waveforms and exhibits high radar backscatter in the TerraSAR-X image. This indicates that RR is high. These observations are supportive of the fact that RR is the dominant influence on the power returned to the satellite and that GR is playing a secondary role. It is difficult to attribute the influence of volume scattering from snow, as no areas with the same RR are available with large differences in snow depth.

In an attempt to assess the influence of snow depth, we look at two tracks in 2011 that exhibited a larger difference in snow depth for which we expect RR to be less variable. For these example tracks, the waveforms retrieved over snow (mean depth 0.20 m) and those retrieved over reduced snow (mean depth 0.07 m) are displayed in Figure 8.6 with the retracking points for each technique. These waveforms are the mean normalized echo power of ~ 50 waveforms and are aligned by peak power to achieve comparativeness between each technique. The mean retracking point for each waveform for each technique is also displayed. It should be noted here that comparison of their absolute range differences cannot be inferred from the available information, only the inter-example variation in the waveform shape. It is shown that in the presence of a snow cover of ~ 0.20 m the slope of the leading edge becomes shallower, and that the power of the trailing edge is increased along with the overall width of the waveform. This finding is comparable to results of simulations of CS-2 waveform responses to increasing snow cover provided by Kwok (2014).

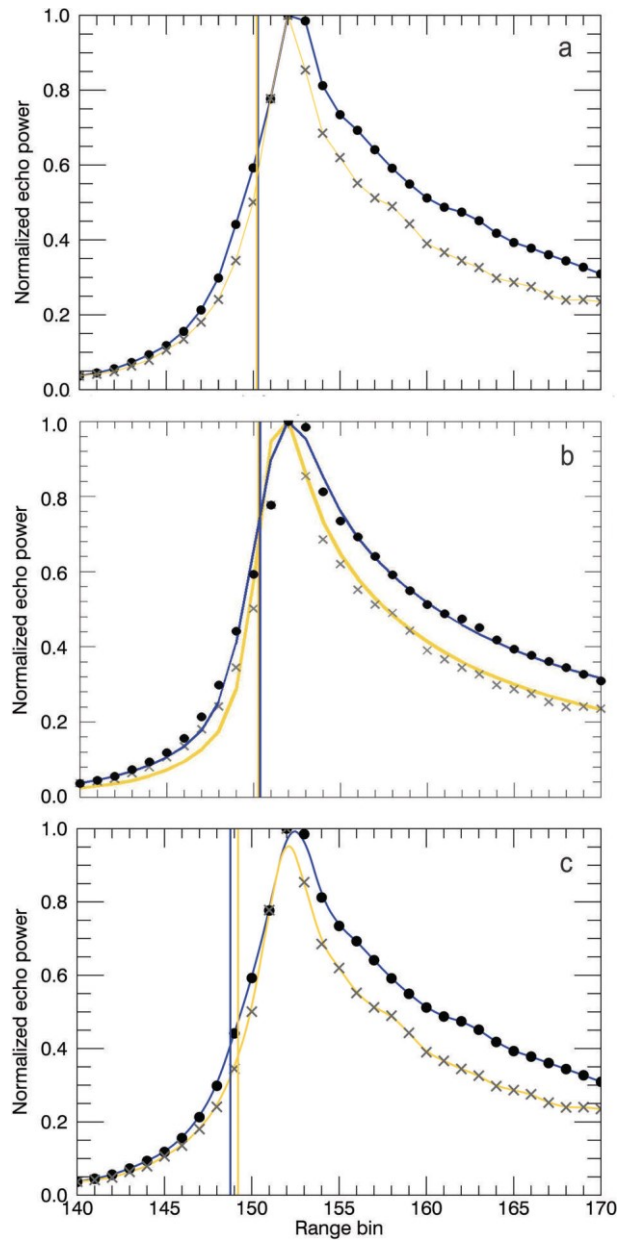


Figure 8.6: Mean waveform examples for sea ice in 2011 with significant snow cover (circles and blue fits) and minimal snow cover (crosses and orange fits). The area with significant snow cover had a mean snow depth of 0.20m with consistent coverage. Over the minimal area a mean snow depth of 0.07m was measured with a patchy distribution. (a) The retracking points for ESAL2 with linear fits between each bin; (b) the retracking points for WfF with respective model fits; and (c) the retracking points for TFMRA40 with interpolated curves.

8.6. Automatic Freeboard Retrieval Procedure

In this section, we develop automatic freeboard retrieval procedures without the prerequisite for coincident satellite imagery for the establishment of SSH. The automatic differentiation of sea ice and water is a fundamental requirement for large-scale altimetric sea-ice freeboard retrieval. Automated methods generally fall into two categories, the first relying on the use of information received in the returning signal from the surface and the second on mathematical generalizations that approximate expected surface conditions, or, a combination of the two. In the case of CS-2, methods currently presented in the literature (Laxon and others, 2013; Kurtz and others, 2014; Ricker and others, 2014) fall into the first category, following similar investigative procedures initially demonstrated by Peacock and Laxon (2004). These contemporary methods use the pulse peakiness and stack standard deviation, among other parameters, to differentiate between radar returns from small open-water leads in the sea-ice cover and sea-ice floes. In the second category, the expected amount of water along-track is given a value, and the heights of this lowest percentage are averaged for a certain segment of track, giving a sea surface height (Zwally and others, 2008; Price and others, 2013). This approach, commonly termed along-track filtering, is yet to be examined in the literature with respect to CS-2. The three automatic retrieval procedures used for each retracking method are described in the following subsections. Following from h established in Section 8.5, all data undergo the same additional corrections to produce comparable datasets. h is further corrected for t and i to give H :

$$H = h + t + i \quad \text{Eq. 8.6}$$

The influence of i is accounted for using a dynamic atmosphere correction and compensates for the influence of barometric pressure and winds on the sea surface. t is the sum of corrections for ocean tide, long-period equilibrium tide, ocean loading tide, solid earth tide and the geocentric pole tide. Further details on the corrections applied for t and i are given in Bouzinac (2013). These additional corrections accommodate for the larger geographical region under investigation in the automatic procedure (Figure 8.3) over which tidal and atmospheric effects will be influential on the ‘flattening’ of the height profile. Each method then produces its own automatic SSH (SSH_{auto}) to provide Fb_{auto} as

$$Fb_{auto} = H - SSH_{auto} \quad \text{Eq. 8.7}$$

No adequate snow depth information is available for the two annual periods assessed by the automatic procedure, so no correction is applied for h_c . The procedures for attaining SSH_{auto} for each technique and other relevant amendments are described in the following subsections.

8.6.1. ESAL2 automatic SSH identification

Measurement quality flags provided in the CS-2 Level 2 record structure were used to improve the quality of the dataset. H values are discarded if the following parameters in the product are flagged as poor: block degraded, orbit error, orbit discontinuity, height error, calibration caveat, backscatter error, peakiness error, SIN cross-track angle error, SIN receive channel 1 error, SIN receive channel 2 error, mispointing error and delta time error which are given in Bouzinac (2013). In SIN mode, the off-nadir location of the height retrieval can be determined from phase information of the dominant scattering in the power echo, which over sea-ice areas can be significantly off-nadir (Armitage and Davidson, 2014). This ability prevents underestimations of ocean elevation as a result of ‘snagging’ from leads located off-nadir, providing a reduction in noise over height profiles. According to the across-track offset computed from the phase difference, open water and level sea-ice areas also produce echoes geolocated off-nadir. From assessment of ~ 800 separate elevation retrievals over open water in McMurdo Sound from two tracks in 2013, identified by comparison with near-coincident MODIS imagery, the mean deviation from nadir was 270 ± 70 m. We apply a removal threshold of ± 750 m from nadir simply to limit information to the expected nadir footprint area, maintaining comparativeness to the TFMRA40 method and to in situ measurements.

To remove height outliers, we apply a vertical threshold of ± 2 standard deviations of the mean to each track. Heights outside this threshold are discarded.

We use the Level 2 parameter peakiness (P) to differentiate between three surface types: open water, leads and fast ice. P is suggestive of how sharply peaked the returning waveform is, and is defined as the ratio of the highest bin value to the mean of all bins above the retracking point (Bouzinac, 2013). P ranges between 0 and 120 in our investigation area (Figure 8.7). High P values are indicative of leads, which are geometrically of similar size to the radar footprint and typically have specular surfaces. Low P values are indicative of open-water areas that are geometrically larger than the radar footprint and are typically diffuse surfaces. Fast-ice P values

are between these two extremes but are affected by sea-ice surface conditions. We establish thresholds for these surface types after comparison of P values over certain surface types in the study region as indicated by MODIS and TerraSAR-X imagery and knowledge of the sea-ice regime. P has a large standard deviation even when a certain surface type is completely isolated, indicating it is highly sensitive to small changes in surface conditions.

First we assessed the P threshold for leads. It is very challenging to constrain such a value, due to the difficulty of achieving coincidence between CS-2 measurements and satellite imagery. Therefore, we investigated P values in March when sea ice in McMurdo Sound starts to freeze and the surface is dominated by developing ice floes. At this time, leads are abundant and we take the upper quartile of P values as representative of the leads surface type ($P > 90$) for both years.

The two remaining surface types require further scrutiny due to overlaps in their P distributions. McMurdo Sound was assessed in February 2013 when it was dominated by open water. In both 2011 and 2013 the majority (>95%) of P values were < 15 . However, in 2011 the surface types open water and fast ice overlapped, whereas in 2013 a clear separation is achievable (Figure 8.7). This is a result of fast-ice surface conditions differing in 2011 that lowered values in the P distribution. We are unable to fully establish the cause of this change. The pulse shape and, thus, P are largely determined by variation of backscatter with incidence angle (Wingham and others, 2006). This is related to RR, and, given the differing conditions over the fast ice between the two years, a change in RR at the dominant backscattering surface was likely the cause. In 2013 it is possible to clearly differentiate and establish open water as $P < 15$ and fast ice as $15 < P < 90$. In 2011 we lowered the threshold for open water to $P < 7.5$ to reduce the amount of fast ice potentially included in the expected open-water retrievals. 2011 fast ice is therefore given thresholds of $5 < P < 90$. We appreciate these thresholds for open water and fast ice overlap, but if a higher bound is taken for the lower limit of P for fast ice in 2011, $\sim 60\%$ of height retrievals identified as fast ice will be discarded. The fast-ice P distributions were established from assessment of the fast-ice area. The sea-ice growth season in McMurdo Sound begins in March, but fast ice does not become fully established for some time.

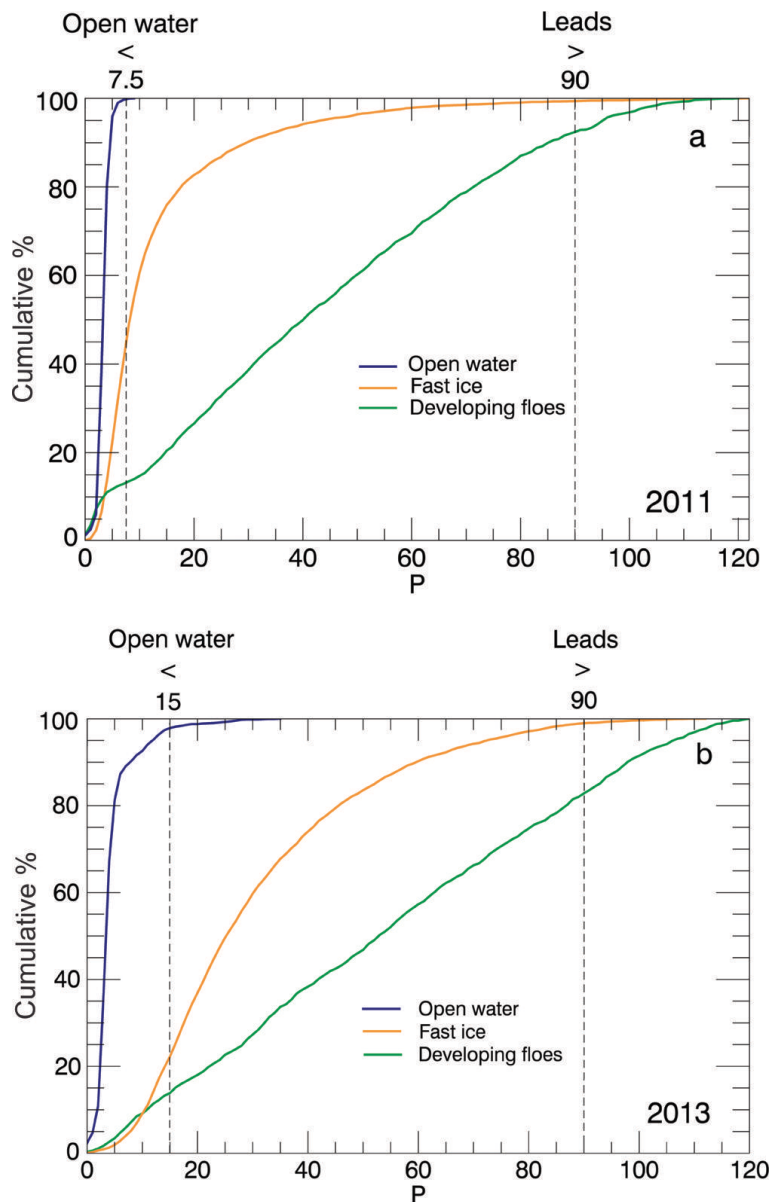


Figure 8.7: Surface type discrimination as indicated by Level 2 parameter peakiness (P) displayed as a cumulative percentage. Surface types, open water, fast ice and developing floes are displayed for 2011 (a) and 2013 (b). In 2011, surface conditions made the discrimination of open water and fast ice more difficult. This resulted in a change in the thresholds between the years. The expected inclusion of sea ice in the open-water surface type is indicated by the percentage overlaps.

We are confident that fast ice is fully established by August and derive a P value for this surface type by masking fast-ice area from August to December. We assume the fast-ice area is also representative of P values for ice floes in McMurdo Sound. Finally, due to the discussed overlaps of open water and fast ice (Figure 8.7), and potential inclusion of sea ice in expected

open-water retrievals, it is necessary to filter H values with regard to their heights. This approach is altered for each year to account for the expected inclusion of ice in the open-water retrievals (Figure 8.7; 40% in 2011 and 20% in 2013). We calculate the means of the lowest 60% of H values in 2011 and 80% in 2013 that meet the open-water and lead criteria and establish SSH_{auto} for each track from this.

8.6.2. WfF automatic SSH identification

We attain SSH_{auto} by using a similar parameter to ESA Level 2 P, the pulse peakiness (PP) as described by Armitage and Davidson (2014). The assigned values for the discrimination of each surface type were chosen after comparison of PP values over surface types in the study area using the same method as described for ESAL2 in Section 8.6.1. We flag leads as $PP > 0.30$ and open water as $PP < 0.05$. Sea ice is classified as $0.08 < PP < 0.30$. Overlaps of sea-ice and open-water surface types were noted as in Section 8.6.1. To remove this height bias from inclusion of sea ice, we establish SSH_{auto} from the mean of the lowest 60% and 80% of elevations flagged as leads of open water in 2011 and 2013 respectively. Phase information is also used in this product in the same manner as ESAL2. We again remove elevation outliers with application of a vertical threshold of ± 2 standard deviations of the mean to the track.

8.6.3. TFMRA40 automatic SSH identification

We use the algorithm described in Ricker and others (2014) but amend the procedure, as surface conditions differ in the investigation area from those for which the technique has previously been applied. As mentioned in Section 8.4.4 we maintain the inclusion of the additional surface type, polynya, and its amended 60% retracking threshold. The elevations retrieved for both leads and polynyas in close proximity should be of the same mean value to construct a consistent SSH_{auto} . We compared the elevations of detected leads that were in close proximity to the polynya surface type for several CS-2 tracks and found sufficient agreement using a 60% and 40% threshold for each surface type in conjunction. Track sections with a significantly inaccurate SSH_{auto} , as a consequence of sparse lead/open-water coverage, have been discarded.

8.6.4. Automatic results

The application of the three retracking techniques produced Fb_{auto} datasets for McMurdo Sound for 2011 and 2013 (Table 8.2). All techniques show a decrease in freeboard in McMurdo Sound from 2011 to 2013 over the study area as a whole, and the fast-ice area when assessed alone. The magnitude of this change varies between methods. ESAL2 and TFMRA40 both identify the fast-ice area as having a higher freeboard than the mean of the entire study area. WfF does not show such a relationship, with fast-ice mean Fb_{auto} being 0.01 m lower in 2011 and the same value in 2013. A lower mean freeboard is expected for the entire study area, as sea ice in the dynamic MSP area is included. Sea ice in this area is expected to be thinner than the fast ice that has undergone near-continuous and stable growth over winter. This discrepancy may be driven by the identified problems with surface type discrimination. Open-water areas may have been erroneously included as sea ice, lowering the Fb_{auto} averages. Clearly apparent are the large standard deviations of the CS-2 data (Table 8.2).

To investigate the ability of CS-2 further and to minimize the influence of the MSP sea-ice area, we assess the fast-ice area with regard to its seasonal development. The FY fast-ice regime in McMurdo Sound typically breaks out in February, and often in one of every two years (Heine, 1963) leaves McMurdo Sound nearly entirely ice-free.

Table 8.2: Mean automatic procedure freeboard values and standard deviations derived by each technique for each year for the entire study area and fast ice only (bold). The total number of measurements (n) for each year is also displayed. The spatial distribution of the satellite tracks from which the Fb_{auto} means are derived are shown in orange in Figure 8.3.

Retracker	2011 m	2013 m
ESAL2 Fb_{auto}	0.09 ± 0.25 0.11 ± 0.27 (n = 16 611)	0.08 ± 0.24 0.09 ± 0.26 (n = 12 884)
WfF Fb_{auto}	0.12 ± 0.24 0.11 ± 0.25 (n = 7094)	0.10 ± 0.23 0.10 ± 0.22 (n = 9439)
TFMRA40 Fb_{auto}	0.16 ± 0.35 0.23 ± 0.36 (n = 7532)	0.11 ± 0.38 0.15 ± 0.46 (n = 8244)

Sea ice begins to form in March when air temperatures are low enough to initiate freezing as indicated by field studies (Leonard and others, 2006; Purdie and others, 2006) and MODIS imagery. This was also the case in 2011 and 2013. The sea ice develops into a fast-ice cover in a coastal band (Figure 8.3) around McMurdo Sound, with fast-ice establishment intermittently interrupted by storm events (as indicated by optical and SAR imagery). Sea-ice growth continues until about mid-December (Jeffries and others, 1993). We use the region of McMurdo Sound that is covered by fast ice at the end of the growth season as a mask for the entire year. We expect to observe a signal in the recorded Fb_{auto} datasets indicative of increasing freeboard from March to December. Such findings are displayed in Figure 8.8, where we clearly see this development using all three retracking techniques. Fb_{auto} increases through autumn and winter toward Fb_i and Fb_s in situ measurements in spring. We apply a linear trend from the beginning of March to mid-December to capture the sea-ice growth measured by Fb_{auto} . Using this trend to compare Fb_{auto} results in mid-November (\sim day 260 in Figure 8.8) to the mean of all in situ measurements in each year, we find ESAL2 Fb_{auto} underestimates Fb_i in both years by 0.04 m. In 2011 WfF Fb_{auto} overestimates in situ measured sea-ice freeboard by 0.08m and in 2013 underestimates it by 0.02 m. TFMRA40 provides a mean Fb_{auto} value of 0.37 ± 0.22 m in 2011, 0.04 m lower than Fb_s . In 2013 TFMRA40 Fb_{auto} underestimates Fb_s by 0.01 m. All techniques also display a decrease in Fb_{auto} after reaching their respective maximums in line with the observed breakout of the fast-ice area in late February/early March of each year. Mean values and standard deviations for each month are displayed in Table 8.3.

We are able to evaluate the performance of the automatic procedures by comparison of the CS-2 mean Fb_{sup} over the validation line (Figure 8.4) against the Fb_{auto} mean over the same track. With the application of a correction for c in snow, Fb_{auto} overestimates Fb_{sup} by 0.07, 0.05 and 0.01m for ESAL2, WfF and TFMRA40 respectively. The overestimation of freeboard by Fb_{auto} for ESAL2 and WfF is driven by the applied along-track filtering of H . The filtering assumes a percentage inclusion (20% for 2013) of sea ice within the total sampled area over water along each track. In this case, the open-water area to the north has an ice concentration of zero and therefore SSH_{auto} is established too low, and subsequent Fb_{auto} is too high. This simple comparison

showcases the additional error which can be expected by applying fully automatic methods for the identification of SSH which only generalize expected open-water availability.

8.7. Discussion

We have evaluated the performance of two retracking techniques currently presented in the literature: WfF (Kurtz and others, 2014) and TFMRA40 (Ricker and others, 2014). The first assumes the surface is retracked at Fb_i and the second near Fb_s . We also use ESAL2, a product for which we have limited information about its retracking procedure and assumptions therein. Here we discuss the extent to which our in situ observations support the assumptions in view of the mean and standard errors of the measured Fb_{sup} and Fb_{auto} datasets and information provided by the waveform responses to surface conditions.

Table 8.3: Mean automatic procedure freeboard values (m), standard deviations and number of measurements (in parentheses) used to derive the statistics for each technique in each year over the fast-ice area. The data are binned into calendar months. The day corresponding approximately to the middle of each calendar month from the start of the analysis (day zero = 1 March) is also displayed.

Month (day) after 1 Mar	2011			2013		
	ESAL2	WfF	TFMRA40	ESAL2	WfF	TFMRA40
Mar (+15.2)	-0.04±0.16 (494)	0.00±0.35 (232)	0.05±0.29 (105)	-0.01±0.30 (394)	0.01±0.21 (260)	0.05±0.19 (271)
Apr (+45.6)	0.02±0.24 (560)	0.13±0.18 (400)	0.03±0.15 (317)	0.03±0.12 (480)	0.08±0.15 (488)	0.16±0.43 (362)
May (+76)	0.06±0.14 (537)	0.12±0.16 (296)	0.14±0.38 (526)	0.05±0.26 (623)	0.13±0.15 (508)	0.08±0.19 (238)
Jun (+106.4)	0.14±0.31 (400)	0.02±0.30 (246)	0.05±0.22 (204)	0.07±0.24 (543)	0.04±0.21 (409)	0.03±0.19 (267)
Jul (+136.8)	0.19±0.25 (859)	0.17±0.18 (395)	0.12±0.12 (221)	0.04±0.22 (732)	0.11±0.17 (531)	0.08±0.32 (266)
Aug (+167.2)	0.05±0.23 (838)	0.16±0.17 (165)	0.31±0.35 (443)	0.08±0.16 (604)	0.16±0.13 (486)	0.26±0.41 (588)
Sep (+197.6)	0.12±0.25 (952)	0.11±0.26 (199)	0.24±0.22 (703)	0.03±0.28 (647)	0.10±0.21 (499)	0.03±0.23 (241)
Oct (+228)	0.11±0.22 (786)	0.24±0.19 (102)	0.21±0.39 (341)	0.14±0.14 (208)	0.36±0.14 (159)	0.14±0.19 (199)
Nov (+258.4)	0.15±0.20 (725)	0.27±0.24 (121)	0.37±0.22 (196)	0.17±0.18 (602)	0.19±0.18 (286)	0.24±0.26 (255)
Dec (+288.8)	0.11±0.29 (847)	0.26±0.21 (136)	0.39±0.43 (527)	0.26±0.34 (910)	0.09±0.26 (705)	0.11±0.35 (453)
Jan (+319.2)	0.19±0.35 (643)	0.10±0.30 (161)	0.37±0.45 (407)	0.18±0.22 (313)	0.01±0.31 (228)	0.46±0.72 (516)
Feb (+349.6)	0.10±0.44 (340)	-0.10±0.18 (119)	0.33±0.70 (72)	0.00±0.34 (325)	-0.14±0.20 (216)	-0.11±0.62 (455)

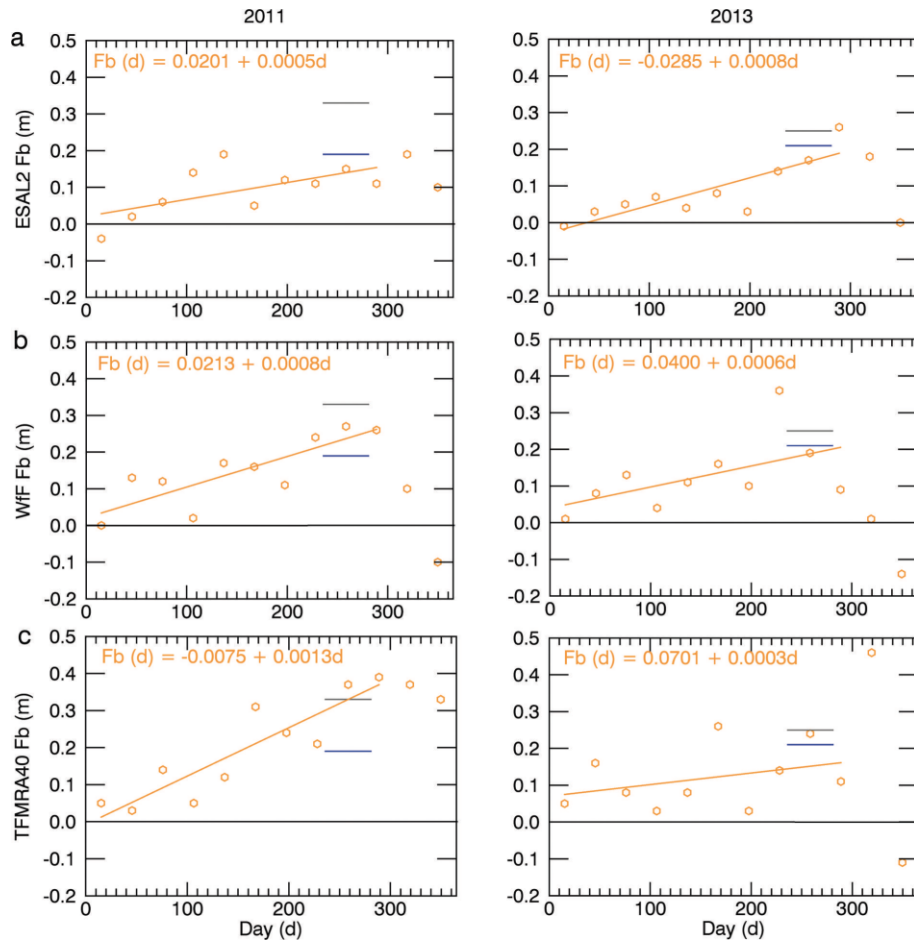


Figure 8.8: The development of the McMurdo Sound fast-ice cover from mean automatic procedure freeboard values for each month for 2011 and 2013 over the expected sea-ice growth period (day zero = 1 March) for ESAL2 (a), WfF (b) and TFMRA40 (c). A linear fit from the beginning of mid-March (\sim day 15) to mid-December (\sim day 290) defines the expected sea-ice growth period. Mean in situ measured ice and snow freeboards measured in November/December of each year are shown by the blue and grey lines respectively. The standard deviations for each mean value are provided in Table 8.3.

As expected, the best agreement is found between in situ measurements and CS-2 freeboard retrieval techniques for ESAL2, WfF and TFMRA40 using a supervised SSH identification with the exception of WfF in 2011. For the latter, we attribute the anomalously high freeboard to two sources. The first is a low SSH estimate due to the reduced ability of the technique to establish SSH in the presence of differing surface types over a small segment of the SSH reference area. Secondly the introduction of a positive freeboard bias is noted which is forced by a smoother, thicker and morphologically more complex snow cover in 2011. These findings are supportive of other studies (Kurtz and others, 2014; Kwok, 2014) which also show that snow can introduce a

positive elevation bias due to an increase in power returned from above the snow/ice interface. We also observe a higher Fb_{sup} for ESAL2 in 2011 when compared to 2013, and suggest a similar response to the change in snow properties has influenced the retrieval. Our observations show that the snow in the study area has higher mean densities and exhibits distinct layers with varying hardness, density and crystal size, as compared with the simplified assumptions in Kurtz and others (2014). It is speculated that in combination with the larger grain size and higher salinity near the snow/ ice interface, the effective point of scattering is shifted even further away from the ice surface. The only way to quantify what impact the snow cover had on the retrieved freeboards would be to know the backscatter coefficients of the snow and ice. Lacking this information, we are limited to more qualitative statements based on comparisons to in situ information. Our ability to convey qualitative information on the waveform interaction at the surface, as suggested in Section 8.5, is also restricted. In the presence of a snow cover that is fully transparent to the incident Ku-band radar energy, no bias is expected to be observed for retracking procedures. Attaining knowledge of the dominant backscattering surface is crucial to undertake any meaningful time-series assessment of sea-ice freeboard, permitting thickness estimation. Therefore, the role of the heterogeneity of the snow cover on CS-2 freeboard retrieval requires further observational study.

Although we observe the influence of the snow cover in the freeboard retrieval, we are unable to fully quantify the error in the SSH identification, even under the supervised assessment. Experiments in which the influence of SSH misidentification is isolated will need to be carried out to completely quantify the positive bias introduced by a snow cover using WfF. In addition, the use of automatic SSH identification procedures can be expected to increase freeboard errors. Direct comparisons between supervised and automatic procedures suggest differences in excess of 0.05 m.

It was not possible to determine the accuracy of the established SSH_{sup} , and we can only evaluate the resulting freeboards. The SSH_{sup} of all three data products was independently assessed without tuning to in situ measured freeboards. However, the characteristics of the study area made it necessary to modify the processing methods for sea surface identification currently used in the Arctic (Kurtz and others, 2014; Ricker and others, 2014). The surface type polynya

was added to the surface classification for TFMRA40 to improve ice–water discrimination. This surface type produces similar waveforms to sea ice, but more diffuse, with a leading edge that is typically flatter. The power threshold for retracking over this surface type was increased to 60%. The fact that larger open-water areas can result in significantly different SSH estimates may introduce a significant inter-retracker difference in SSH establishment due to the inconsistent change along the leading edge. Future improvement of the WfF technique over varying surface types in close proximity (i.e. leads, open water, sea-ice floes within a few hundred meters) is required. These conditions cause noisy waveforms, and improvement of our understanding of the influence of this noise on the retracking procedure is a current research focus. It seems that the more sophisticated approach of WfF is more sensitive to these conditions than TFMRA40, and a more stringent data discard procedure may need to be adopted to reject such waveforms. Further, using automatic surface discrimination algorithms resulted in insufficient separation of sea-ice and water surface types. It may be of benefit to adopt procedures that account for the seasonal change in sea-ice/snow surface conditions which force alteration of surface discriminatory parameters (e.g. P, PP, SSD). This may improve the separation of surface types and Fb_{auto} results, both in this investigation area and when larger regions are considered for assessment.

With the aid of information gained in the supervised freeboard retrieval procedure, we were able to place in context and develop automatic freeboard retrieval procedures for each technique. Our results have shown the ability of CS-2 to record the development of a fast-ice cover in the Antarctic. Although our supervised analysis provides insight into the surface that is tracked with respect to Fb_s and Fb_i we do not have the confidence to estimate sea-ice thickness with an acceptable error margin. However, we do find the growth rate as recorded by Fb_{auto} over both years for all techniques, of 0.7 mmd^{-1} (mean of all rates displayed in Figure 8.8), is in agreement with other studies of ice growth rates in McMurdo Sound (Purdie and others, 2006; Gough and others, 2012). By April, all retracking techniques identify positive freeboard values. Although we identify the onset and the trend in freeboard growth, we note that standard deviations of Fb_{auto} are typically twice that found over this area when it was assessed using ICESat from 2003 to 2009 (Price and others, 2013). There was an extensive multi-year sea-ice cover in

McMurdo Sound from 2003 to 2009. However, we are not aware of any changes to the FY sea-ice surface conditions between the two satellite observation periods that could be responsible for the observed differences in standard deviations, although the CS-2 assessment area is smaller. Therefore, it is appropriate to look to instrumental and methodological sources to explain the observed noise. Findings from CS-2 presented here were attained using SIN mode which acquires data at a reduced (by a factor of four) burst repetition interval compared to SAR mode which is used over the majority of the Antarctic sea-ice pack. The ability to average and reduce measurement noise in the SIN mask which occupies the entire coastal Antarctic, a key area of sea-ice production, is therefore reduced. Assuming normally distributed noise, the values for the standard deviations would reduce by a factor of two if data were acquired in SAR mode. Even with this restriction, there is no evidence that SIN mode is inadequate for sea-ice freeboard retrieval. Other studies (Armitage and Davidson, 2014) provide evidence in support of its usage, as SIN mode provides phase information which can be used to reduce the impact of snagging on height retrievals. This ability is beneficial, as a less stringent data discard is required to remove off-nadir range estimates which exhibit a positive range bias and subsequently height retrievals that are too low. The standard deviations of Fb_{auto} using TFMRA40 are higher than those from the other two procedures, perhaps an indication of the noise introduced from the range bias as a result of omitting phase information. An additional source of scatter and an increased standard deviation could be introduced to the TFMRA40 procedure, as the slope of the leading edge at the tracking point is typically shallower in comparison to higher thresholds. This could force a higher noise if waveforms change significantly from one measurement to the next. The noise in TFMRA40 heights could also indicate that undulations or roughness of the snow surface was often higher than the ice surface beneath. These factors do not seem to have been influential along the validation line (Figure 8.4), where TFMRA40 produced the least noisy Fb_{sup} dataset of the three techniques.

The surface height that is tracked is dependent upon where on the leading edge each processor establishes its retracking point, which is selected on the basis of the assumed dominant backscattering interface (e.g. retracking at 40%, 40 – 70% or 50 – 90%). This is a trivial consideration and, in the absence of any alteration of the waveform by surface conditions, these

simple differences in range would cause the resultant differences in measured freeboard. Our results show that in McMurdo Sound using the supervised analysis in an optimal scenario, when there is a thin and homogeneous snow cover (mean = 0.05 m), TFMRA40 approximates F_s well, WfF approximates F_i well, and ESAL2 identifies a horizon in between F_i and F_s . Although we have identified that GR, RR and snow are influential on the leading edge, we cannot separate their influence with any certainty. It is evident from interpretation of the leading edge alone that no separation of the air/snow interface and ice/snow interface is directly achievable, which is expected due to the range resolution of CS-2 (Wingham and others, 2006; Bouzinac, 2013; Kurtz and others, 2014; Kwok, 2014). However, using a comparison between a snow-covered sea-ice area and an area with significantly less snow, the gradient of the leading edge becomes shallower and the width of the entire waveform is extended in the presence of snow. Based on the model assumptions of WfF, very small changes in the leading edge are expected as a function of surface roughness, and insufficiencies in the fit of the leading edge as shown in Figure 8.6b indicate a higher than expected influence of roughness and snow cover on the leading edge. This will alter the retracking position on the leading edge for every retracker in a different way. It is therefore reasonable to conclude that not only the trivial relationship of different retracking points is responsible for the observed differences in freeboards between methods, but variations in surface properties were also influential. Further work is required to separate and quantify these influences.

Relating our findings to the development of larger-scale Antarctic assessments outside the coastal band is hindered by the nature of our study area compared to the majority of the Antarctic sea-ice pack. However, the dynamic sea-ice area in the MSP is more representative of the wider Antarctic sea-ice zone. Although this area was not the focus of our assessment, automatic freeboard retrieval procedures which included this area have produced freeboards that are considered reasonable for Antarctic pack ice, i.e. 0.08 – 0.16 m (Table 8.2). We have identified certain issues within our analysis which are applicable at the larger scale which must be addressed in order to develop techniques. Given the abundance of large open-water areas in the Antarctic sea-ice zone which do not exhibit the typical ‘peaky’ response from leads, it is necessary to characterize them. If they are large enough and their sea-ice concentration is low,

they can be masked using auxiliary satellite information. However, in regions of high ice concentration where leads are too large to be discernible from radar information, ice – water discrimination may be hindered. At what size a lead becomes too large to exhibit a typical waveform would need to be ascertained to conclude whether open-water areas may be an issue in the Antarctic sea-ice pack. The spatial and temporal heterogeneity of the snow cover, even in our small study area, highlights the challenge presented for freeboard retrieval algorithms to assess larger areas in the Antarctic. Further advances in retracking techniques guided by in situ validation will need to be made in order to attain freeboard measurements with improved accuracy. Further complications will be introduced by snow loading which typically suppresses sea-ice freeboard, resulting in a close to zero ice freeboard condition in the Antarctic sea-ice pack. This issue may be addressed using a combination of different retracking procedures that attempt to identify the air/snow interface as shown to be successful here. In any case, it is clear that data treatment may need to be altered for different regions, in particular retracker algorithms to cater for the variability of the Antarctic sea-ice regime.

8.8. Conclusion

Our in situ freeboard measurements reveal that retracking techniques based on the fitting of waveforms (ESAL2 and WfF) and a threshold retracker (TFMRA40) can be used to derive freeboard estimates over Antarctic fast ice from CS-2. Although we find that the retrievals capture freeboard heights, the variability is expected to be high as indicated by the large standard deviations of mean freeboard values. In the validation area of McMurdo Sound, which harbors homogeneous fast ice, the results of the three separate techniques used for freeboard retrieval fall within the margins of expected freeboards as indicated by in situ measurements in austral spring 2011 and 2013. Mean freeboard values from ESAL2 are representative of a horizon between the air/snow and snow/ice interface. A smooth snow cover with multiple layers causes a bias of +0.14 m away from the ice freeboard using WfF. It should be noted that we are unable to identify any contribution from an inaccurate sea surface height establishment upon this bias. In the absence of such a snow cover, WfF-derived freeboards are 0.04 m lower than in situ measured ice freeboard. TFMRA40 produces mean freeboards 0.03 m higher than in situ measured snow freeboard. We observe higher standard deviations in automatic retrieval

procedures, which could be reduced by spatial averaging if data at a higher sampling rate (e.g. in SAR mode) were available. Difficulties in the identification of sea surface height were noted for TFMRA40 over larger open-water areas and for WfF over areas inclusive of multiple surface types (e.g. leads, sea ice and open water) within the radar footprint. Automatic algorithms were tested through 2011 and 2013 and recorded the growth of the FY fast-ice cover in McMurdo Sound. The CS-2 trends recorded from each method of 0.7mm d^{-1} are in line with sea-ice growth rates measured in situ in the region. Automatic surface type discrimination procedures may benefit from adjustments to account for spatial and temporal variations in snow/ice surface conditions, which could improve ice–water discrimination. In situ validation in the Antarctic pack ice is a fundamental component for the development of CS-2 freeboard retrieval techniques. The uncertainty of CS-2 freeboard datasets is expected to be improved over larger spatial scales than assessed here. We see our results as encouraging in this context, as expansion of spatial scales and further development of retracking techniques will likely improve Antarctic CS-2 freeboard products.

8.9. Acknowledgements

We thank all participants in the 2011 and 2013 Antarctica New Zealand field event K063 as well as Scott Base staff for their support. CS-2 data were provided by the European Space Agency for project AOCRY2CAL-4512. The Terra- SAR-X image was provided through DLR (German Aerospace Center) project OCE1592. The work of V. Helm and S. Hendricks was funded by the German Ministry of Economics and Technology (grant 50EE1008). We appreciate the efforts of Alec Casey who provided technical assistance in data processing. A research stay for the first author at the University of Alberta was supported by Air New Zealand. Further research support was provided by the National Institute of Water and Atmospheric Research, New Zealand, under contract CO1X1226. We thank Trimble NZ for the use of GNSS equipment, and Wolfgang Dierking for fruitful discussions. We are very grateful for the contributions of Nick Key and Justin Harrison in the design and preparation of field equipment. The comments of two anonymous reviewers and the sea-ice editor contributed to the manuscript. This work was collated at Gateway Antarctica, University of Canterbury, New Zealand.

8.10. References

- Alexandrov V, Sandven S, Wahlin J and Johannessen OM (2010) The relation between sea ice thickness and freeboard in the Arctic. *Cryosphere*, 4, 373–380 (doi: 10.5194/tc-4-373-2010)
- Armitage TWK and Davidson MWJ (2014) Using the interferometric capabilities of the ESA CryoSat-2 Mission to improve the accuracy of sea ice freeboard retrievals. *IEEE Trans. Geosci. Remote Sens.*, 52, 529–536 (doi: 10.1109/TGRS.2013.2242082)
- Barber DG, Reddan SP and Ledrew EF (1995) Statistical characterization of the geophysical and electrical properties of snow on landfast first-year sea ice. *J. Geophys. Res.*, 100(C2), 2673–2686 (doi: 10.1029/94JC02200)
- Beaven SG and 8 others (1995) Laboratory measurements of radar backscatter from bare and snow-covered saline ice sheets. *Int. J. Remote Sensing*, 16, 851–876 (doi: 10.1080/01431169508954448)
- Bintanja R, Van Oldenborgh GJ, Drijfhout SS, Wouters B and Katsman CA (2013) Important role for ocean warming and increased ice-shelf melt in Antarctic sea-ice expansion. *Nature Geosci*, 6, 376–379 (doi: 10.1038/ngeo1767)
- Bouzinac C (2013) CryoSat product handbook. https://earth.esa.int/documents/10174/125272/CryoSat_Product_Handbook
- Dempsey DE, Langhorne PJ, Robinson NJ, Williams MJM, Haskell TG and Frew RD (2010) Observation and modelling of platelet ice fabric in McMurdo Sound, Antarctica. *J. Geophys. Res.*, 115(C1), C01007 (doi: 10.1029/2008JC005264)
- Drinkwater, M. (1991) Ku-band airborne radar altimeter observations of marginal sea ice during the 1984 Marginal Ice Zone Experiment. *J. Geophys. Res.*, 96(C3), 4555–4572
- Drinkwater MR, Francis R, Ratier G and Wingham DJ (2004). The European Space Agency's Earth Explorer Mission CryoSat: measuring variability in the cryosphere. *Ann. Glaciol.*, 39, 313–320 (doi: 10.3189/172756404781814663)
- Fedotov VI, Cherepanov NV and Tyshko KP (1998) Some features of the growth, structure and metamorphism of East Antarctic landfast sea ice. In Jeffries MO ed. *Antarctic sea ice: physical processes, interactions and variability*. (Antarctic Research Series 74) American Geophysical Union, Washington, DC (doi: 10.1029/AR074p0343)

- Fraser AD, Massom RA, Michael KJ, Galton-Fenzi BK and Lieser JL (2011) East Antarctic Landfast sea ice distribution and variability, 2000–08. *J. Climate*, 25, 1137–1156 (doi: 10.1175/JCLI-D-10-05032.1)
- Gough AJ, Mahoney AR, Langhorne PJ, Williams MJM, Robinson NJ and Haskell TG (2012) Signatures of supercooling: McMurdo Sound platelet ice. *J. Glaciol.*, 58(207), 38–50 (doi: 10.3189/2012JoG10J218)
- Gow AJ, Ackley SF, Govoni JW and Weeks WF (1998) Physical and structural properties of landfast sea ice in McMurdo Sound, Antarctica. In Jeffries MO ed. *Antarctic sea ice: physical processes, interactions and variability*. (Antarctic Research Series 74) American Geophysical Union, Washington, DC, 355–374
- Hallikainen MT, Ulaby F and Abdelrazik M (1986) Dielectric properties of snow in the 3 to 37 GHz range. *IEEE Trans. Antennas Propag.*, 34(11), 1329–1340
- Heine AJ (1963) Ice breakout around the southern end of Ross Island, Antarctica. *New Zeal. J. Geol. Geophys.*, 6(3), 395–401
- Hellmer HH (2004) Impact of Antarctic ice shelf basal melting on sea ice and deep ocean properties. *Geophys. Res. Lett.*, 31(10), L10307 (doi: 10.1029/2004GL019506)
- Helm V, Humbert A and Miller H (2014) Elevation and elevation change of Greenland and Antarctica derived from CryoSat-2. *Cryosphere*, 8, 1539–1559 (doi: 10.5194/tc-8-1539-2014)
- Hendricks S, Stenseng L, Helm V and Haas C (2010) Effects of surface roughness on sea ice freeboard retrieval with an Airborne Ku-Band SAR radar altimeter. In *International Geoscience and Remote Sensing Symposium (IGARSS 2010)*, 25–30 July 2010. Proceedings. Institute of Electrical and Electronics Engineers, Piscataway, NJ, 3126–3129
- Holland PR, Bruneau N, Enright C, Losch M, Kurtz NT and Kwok R (2014) Modelled trends in Antarctic sea ice thickness. *J. Climate*, 27, 3784–3801 (doi: 10.1175/JCLI-D-13-00301.1)
- Jeffries MO, Weeks WF, Shaw R and Morris K (1993) Structural characteristics of congelation and platelet ice and their role in the development of Antarctic land-fast sea ice. *J. Glaciol.*, 39(132), 223–238

- Kurtz NT and Markus T (2012) Satellite observations of Antarctic sea ice thickness and volume. *J. Geophys. Res.*, 117(C8), C08025 (doi: 10.1029/2012JC008141)
- Kurtz NT, Galin N and Studinger M (2014) An improved CryoSat-2 sea ice freeboard retrieval algorithm through the use of waveform fitting. *Cryosphere*, 8, 1217–1237 (doi: 10.5194/tc-8-1217-2014)
- Kwok R (2014). Simulated effects of a snow layer on retrieval of CryoSat-2 sea ice freeboard. *Geophys. Res. Lett.*, 41, 5014–5020 (doi: 10.1002/2014GL060993)
- Laxon SW and 14 others (2013) CryoSat-2 estimates of Arctic sea ice thickness and volume. *Geophys. Res. Lett.*, 40, 732–737 (doi: 10.1002/grl.50193)
- Leonard GH, Purdie CR, Langhorne PJ, Haskell TG, Williams MJM and Frew RD (2006) Observations of platelet ice growth and oceanographic conditions during the winter of 2003 in McMurdo Sound, Antarctica. *J. Geophys. Res.*, 111(C4), C04012 (doi: 10.1029/2005JC002952)
- Mahoney AR and 6 others (2011) The seasonal appearance of ice shelf water in coastal Antarctica and its effect on sea ice growth. *J. Geophys. Res.*, 116(C11), C11032 (doi: 10.1029/2011JC007060)
- Massom R, Harris P, Michael KJ and Potter M (1998) The distribution and formative processes of latent-heat polynyas in East Antarctica. *Ann. Glaciol.*, 27, 420–426
- Massom RA and 13 others (2001) Snow on Antarctic sea ice. *Rev. Geophys.*, 39, 413–445
- Massonnet F and 6 others (2013) A model reconstruction of the Antarctic sea ice thickness and volume changes over 1980–2008 using data assimilation. *Ocean Model.*, 64, 67–75 (doi: 10.1016/j.ocemod.2013.01.003)
- Ozsoy-Cicek B, Ackely S, Xie H, Yi D and Zwally J (2013) Sea ice thickness retrieval algorithms based on in situ surface elevation and thickness values for application to altimetry. *J. Geophys. Res.*, 118, 3807–3822 (doi: 10.1002/jgrc.20252)
- Parkinson CL and Cavalieri DJ (2012) Antarctic sea ice variability and trends, 1979–2010. *Cryosphere*, 6, 871–880 (doi: 10.5194/tc-6-871-2012)
- Peacock NR and Laxon S (2004) Sea surface height determination in the Arctic Ocean from ERS altimetry. *J. Geophys. Res.*, 109(C7), C07001 (doi: 10.1029/2001JC001026)

- Price D, Rack W, Haas C, Langhorne PJ and Marsh O (2013) Sea ice freeboard in McMurdo Sound, Antarctica, derived by surface-validated ICESat laser altimeter data. *J. Geophys. Res.*, 118(7), 3634–3650 (doi: 10.1002/jgrc.20266)
- Price D, Rack W, Langhorne PJ, Haas C, Leonard G and Barnsdale K (2014) The sub-ice platelet layer and its influence on freeboard to thickness conversion of Antarctic sea ice. *Cryosphere*, 8, 1031–1039 (doi: 10.5194/tc-8-1031-2014)
- Purdie CR, Langhorne PJ, Leonard GH and Haskell TG (2006) Growth of first-year landfast Antarctic sea ice determined from winter temperature measurements. *Ann. Glaciol.*, 44, 170–176 (doi: 10.3189/172756406781811853)
- Ricker R, Hendricks S, Helm V, Skourup H and Davidson M (2014) Sensitivity of CryoSat-2 Arctic sea-ice volume trends on radar-waveform interpretation. *Cryosphere Discuss.*, 8, 1831–1871 (doi: 10.5194/tcd-8-1831-2014)
- Smith IJ, Langhorne PJ, Frew RD, Vennell R and Haskell TG (2012) Sea ice growth rates near ice shelves. *Cold Reg. Sci. Technol.*, 83–84, 57–70 (doi: 10.1016/j.coldregions.2012.06.005)
- Tamura T, Ohshima KI and Nihashi S (2008) Mapping of sea ice production for Antarctic coastal polynyas. *Geophys. Res. Lett.*, 35(7), L07606 (doi: 10.1029/2007GL032903)
- Tiuri ME, Sihvola AH, Nyfors E and Hallikaiken M (1984) The complex dielectric constant of snow at microwave frequencies. *IEEE J. Ocean. Eng.*, 9, 377–382
- Ulaby FT, Moore RK and Fung AK (1982) Physical mechanisms and empirical models for scattering and emission. In *Microwave remote sensing: active and passive. Vol. II: Radar remote sensing and surface scattering and emission theory*. Addison-Wesley Publishing Co., Reading, MA
- Ulaby F, Moore RK and Fung AK (1986) *Microwave remote sensing: active and passive. Vol. III*. Artech House, Dedham, MA
- Vaughan DG and 13 others (2013) Observation: cryosphere. In Stocker TF and 9 others eds *Climate change 2013: the physical science basis. Contribution of Working Group I to the Fifth Assessment Report of the Intergovernmental Panel on Climate Change*. Cambridge University Press, Cambridge and New York

- Willatt RC, Giles KA, Laxon SW, Stone-Drake L and Worby AP (2010) Field investigations of Ku-band radar penetration into snow cover on Antarctic sea ice. *IEEE Trans. Geosci. Remote Sens.*, 48, 365–372
- Wingham DJ, Phalippou L, Mavrocordatos C and Wallis D (2004) The mean echo and echo cross product from a beamforming interferometric altimeter and their application to elevation measurement. *IEEE Trans. Geosci. Remote Sens.*, 42(10), 2305–2323 (doi: 10.1109/tGrs.2004.834352)
- Wingham DJ and 15 others (2006) CryoSat: a mission to determine the fluctuations in Earth's land and marine ice fields. *Adv. Space Res.*, 37, 841–871 (doi: 10.1016/j.asr.2005.07.027)
- Xie H, Tekeli AE, Ackley SF, Yi D and Zwally HJ (2013) Sea ice thickness estimations from ICESat altimetry over the Bellingshausen and Amundsen Seas, 2003–2009. *J. Geophys. Res.*, 118(5), 2438–2453 (doi: 10.1002/jgrc.20179)
- Yi D, Zwally HJ and Robbins JW (2011) ICESat observations of seasonal and interannual variations of sea-ice freeboard and estimated thickness in the Weddell Sea, Antarctica (2003–2009). *Ann. Glaciol.*, 52(57 Pt 1), 43–51 (doi: 10.3189/172756411795931480)
- Zwally HJ, Yi D, Kwok R and Zhao Y (2008) ICESat measurements of sea ice freeboard and estimates of sea ice thickness in the Weddell Sea. *J. Geophys. Res.*, 113(C2), C02S15 (doi: 10.1029/2007JC004284)

9. Validation of CryoSat freeboard retrievals with coincident airborne measurements

9.1. Abstract

In 2010 the European Space Agency (ESA) launched CryoSat, a new generation of radar altimeter mission, to measure changes in the freeboard of sea ice, and elevation changes of glaciers and ice sheets. We compare two CryoSat freeboard products along individual ground tracks with coincident airborne freeboard and thickness measurements obtained by laser and radar altimetry and electromagnetic (EM) thickness sounding during ESA's CryoSat Validation Experiment (CryoVEx) campaigns and by NASA's Operation Ice Bridge (OIB). The airborne data were collected between September 2010 and April 2014 and are resampled to the approximate CryoSat-2 beam-sharpened footprint of ~ 1.65 km across track and ~ 0.3 km along track. Along-track averages of 3, 10, 25, and 50 km of the footprint data were also examined and comparisons between ice types and modal versus mean data were also performed. Correlations between mean airborne freeboard and CryoSat freeboard increased with increased along-track averaging distance, e.g. from 0.2 to 0.6 for Operation IceBridge (OIB). Root mean squared differences (RMSD) decreased with increasing averaging distance, e.g. 0.07 m for OIB but mean differences were largely scale-invariant. Examinations of footprint mode data showed slightly higher correlations ($\Delta = <0.1$), slightly lower RMSDs ($\Delta = <0.1$ m) and much smaller mean differences ($\Delta = -50\%$) than the footprint average. Airborne data have primarily been collected over multi-year ice; our examination of ice type differences while inconclusive suggests stronger correlations over multiyear ice than first-year ice but larger mean differences and RMSDs; in agreement with the rougher ice surface and large snow depths observed over multiyear ice. OIB snow freeboard showed the highest correlation with CryoSat radar and radar-derived freeboard, followed by other laser altimeter snow freeboard data. ASIRAS radar freeboard had lower correlations with CryoSat than the laser altimeters but also had the smallest mean difference.

9.2. Introduction

Sea ice is an important component of the Earth system, and sea ice changes will affect global climate, the ecosystem, and humans (e.g. Meier et al., 2014). Over the past decades, passive microwave satellite observations have shown that the area of Arctic sea ice has strongly decreased, while Antarctic sea ice cover has slightly expanded. To better understand these changes and to distinguish between thermodynamic and dynamic causes (e.g. Haas, 2003), concurrent ice thickness measurements are required. In response to this need, the European Space Agency (ESA) launched CryoSat, the first satellite mission dedicated to the observation of Arctic and Antarctic sea and glacial ice thickness (Wingham et al., 2006). After the original satellite was lost in a launch failure in October 2005, a new satellite, CryoSat-2, was immediately built and launched in April 2010. CryoSat reaches latitudes up to 88° North and South, and therefore covers larger regions of the Arctic than previous ESA missions or NASA's ICESat satellite.

CryoSat measures the thickness of sea ice by means of radar altimetry. It carries a novel, Ku-Band (13.6 GHz) Synthetic-Aperture Interferometric Radar Altimeter (SIRAL) which has a smaller footprint and higher spatial along-track resolution than conventional satellite radar altimeters (Wingham et al., 2006). SIRAL's across track, pulse-limited footprint is approximately 1.65 km, and its sharpened pulse-Doppler-limited along-track footprint is only 0.31 km. The high along-track resolution allows for better discrimination of ice floes and open water leads which is needed for accurate freeboard and thickness retrievals (e.g. Peacock and Laxon, 2004).

Ice thickness products have been generated by various groups in the UK (e.g. Laxon et al., 2013; Tilling et al., 2015), the US (e.g. Kurtz et al., 2014; Kwok and Cunningham, 2015), and in Germany (e.g. Ricker et al., 2014), and experiences from these are continuously utilized by ESA to improve their own operational products.

Ice thickness cannot be obtained directly from radar altimetry, but requires numerous processing steps and the use of auxiliary data. The primary observable of radar altimetry is surface height. In the case of a sea ice cover, the surface is composed of ice floes and open water leads. The sea surface height (SSH) of leads can be taken as a reference for the elevation of ice floes above the local water level. This elevation is called ice freeboard (see Table 9.2). Ice thickness can be calculated from ice freeboard using Archimedes' Principle when the densities of

water, ice, and snow as well as snow thickness are known. Uncertainties in these parameters, particularly snow thickness, can lead to errors of more than 30% when deriving ice thickness (e.g. Giles et al., 2008; Kwok and Cunningham, 2008; Alexandrov et al., 2010; Forsström et al., 2011).

But freeboard retrievals themselves can have high uncertainties too, for at least four main reasons (Wingham et al., 2001): First, accurate height retrievals are only obtained by “retracking” of the time-resolved radar return (the “radar waveform”). This retracking adjusts the time delay of the radar’s receive window to the actual distance to the Earth surface, accurate within centimeters. However, different empirical or theoretical methods can be used for retracking causing freeboard biases of up to 0.12 m (Kurtz et al., 2014; Ricker et al., 2014). Second, the shape of each individual waveform is subject to instrument noise and radar speckle, such that retracking results in variable range retrievals even over flat surfaces. This speckle noise can be as large as ± 0.14 m (e.g. Wingham et al., 2006). Third, unresolved geoid undulations and variable dynamic sea surface topography affect the actual SSH but remain undetected where no leads are nearby, or when leads are misidentified. Finally, it is unclear if the radar scattering horizon, i.e. the height within the snow from where the main radar energy is scattered back to the satellite, always coincides with the ice surface as is commonly assumed (e.g. Willatt et al., 2011; Ricker et al., 2014; Ricker et al., 2015). Insufficient penetration of the radar signals to the snow/ice-interface will cause overestimations of freeboard. Validation of CryoSat freeboard and thickness retrievals is therefore crucial to assessing these uncertainties

In recognition of the need for validation, most CryoSat thickness products have been compared with independent ice thickness data from upward looking sonars, airborne laser altimetry, and airborne electromagnetic sounding (Laxon et al., 2013; Kurtz et al., 2014; Kwok and Cunningham, 2015; Tilling et al., 2015). To account for the lack of truly spatially and temporally coincident validation data, and for the fact that the statistical accuracy of CryoSat retrievals improves with increased spatial and temporal averaging, these comparisons were typically carried out with monthly averaged CryoSat data on a 25 x 25 km² grid. Table 9.1 summarizes some typical results thus obtained, here comparing CryoSat thickness retrievals with those from NASA’s Operation IceBridge (OIB; Kurtz et al., 2013; see below). In those studies, correlation coefficients between CryoSat and OIB ranged between 0.53 and 0.67, and mean

differences between -0.16 m and 0.11 m were obtained. RMS differences ranged between 0.66 m and 0.87 m. The relatively small mean differences indicate that average CryoSat thickness retrievals can be quite accurate, and variations between the different studies are likely due to the different retracker used, different assumptions about snow penetration, and different freeboard to thickness conversion. Note that retracker settings and assumed snow properties can also be tuned to minimize mean differences (e.g. Kurtz et al., 2014). The much larger RMS differences show that uncertainties are larger on smaller, grid-size scales due to the impact of factors mentioned above. Note also that the CryoSat data represent monthly grid averages while the OIB data are ice thickness snapshots along the aircraft flight tracks which may be limited in their representation of grid-scale thickness variability, and of ice growth, advection, and deformation during the rest of the month of each flight.

Table 9.1: Previous CryoSat ice thickness validation results using NASA Operation IceBridge (OIB) ice thickness retrievals resampled onto monthly 25 x25 km² grids. Table shows correlation coefficients (r), mean differences (MD), and RMS differences (RMSD) between CryoSat and OIB data.

	r	MD (m)	RMSD (m)
Laxon et al. (2013)	0.61	0.05	0.72
Kurtz et al. (2014)*	0.57	0.11	0.69
Kwok and Cunningham (2015)	0.53	-0.16	0.87
Tilling et al. (2015)	0.67	0.00	0.66

*Best results from March 2013.

Here we chose a different approach for the validation of CryoSat data to gain more insights into the character of uncertainties of CryoSat ice thickness retrievals. Rather than using gridded products as reviewed in Table 9.1, we compare CryoSat along individual ground tracks with coincident airborne freeboard and thickness measurements. These were obtained by laser and radar altimetry and electromagnetic (EM) thickness sounding. These dedicated measurements were carried out during ESA supported CryoSat Validation Experiment (CryoVEx) campaigns (Haas, 2002), and were also coordinated with OIB. In addition, rather than comparing CryoSat ice thickness retrievals, we focus on CryoSat freeboard retrievals. Freeboard is the primary CryoSat sea ice observable and can be more directly compared with freeboard retrievals from airborne laser and radar altimetry surveys. By using freeboard retrievals, we also avoid further complications and blurring due to the added uncertainties resulting from assumptions about

snow and ice properties, which affect freeboard to thickness conversion and the results reviewed in Table 9.1.

When considering freeboard, the underlying variable for ice thickness retrieval, it is important to be aware of the different definitions of freeboard, and that different sensors and methods yield different freeboard estimates which can be converted into each other when snow thickness, density, and/or radar penetration are known (Table 9.2). While laser altimetry provides estimates of snow freeboard, radar altimetry yields estimates of radar freeboard, which coincides with ice freeboard if the snow cover is completely penetrated by the radar signals and if the radar propagation speed in snow is known.

The paper is organized as follows. In Section 9.2.1 the origin and processing of airborne and CryoSat data are described. In Section 9.3 we first illustrate the comparison of airborne and CryoSat freeboard data along one typical orbit, which demonstrates that better results are obtained for longer averaging distances (Section 9.3.1). Then we present results for all coincident data, accounting for the effects of along-track averaging (Section 9.3.2). In Section 9.3.3 we distinguish between results over first- and multiyear ice. In Section 9.3.4 we compare mean and modal airborne freeboard with CryoSat freeboard. In Sections 9.3.5 and 9.3.6 we extend the freeboard analysis to ice thickness retrievals, and compare airborne EM and OIB thickness retrievals with CryoSat thickness estimates, respectively. The paper concludes with a discussion of the results (9.4).

Table 9.2: Different definitions of freeboard required for discussion of comparison of altimeter freeboard retrievals and conversion to ice thickness.

Parameter	Definition
Ice freeboard	Height of the ice surface above local sea level.
Snow freeboard	Height of the snow surface above local sea level. Snow freeboard = Ice freeboard plus snow thickness.
Radar freeboard	Height of the radar scattering horizon above local sea level. Radar freeboard is the difference of retracked range and local sea surface height, before radar propagation speed correction in snow is applied (e.g. Kurtz et al., 2014; Ricker et al., 2014).
Radar-derived freeboard	Radar freeboard range-corrected for slower radar wave propagation speed in snow. Correction magnitude is between 20 to 30% of snow depth, depending on snow density. Radar derived freeboard coincides with ice freeboard in the case of negligible influence by snow backscatter and accurate snow depth/density information and complete penetration of the radar signal through the snow to the snow/ice interface.
Altimeter freeboard	Freeboard sensed by the corresponding sensor type without any geophysical corrections. Altimeter freeboard equals radar freeboard for radar altimeters, and snow freeboard for laser altimeters.

9.2.1. Methods and measurements

In this study, we use data collected during ESA’s CryoVEx and NASA OIB campaigns since 2011. All campaigns were performed during the months of March to May, i.e. in late winter when snow and ice were still cold and when CryoSat freeboard retrievals are possible. During CryoVEx, airborne measurements of sea ice freeboard and thickness were conducted along CryoSat ground tracks by the German Alfred Wegener Institute (AWI), Danish University of Technology (DTU), Norwegian Polar Institute (NPI), York University (YU), and NASA OIB (Figure 9.1, Appendix A1). The dataset includes data from airborne laser scanning (ALS), radar altimetry with ESA’s Airborne Synthetic-Aperture, Interferometric Radar Altimeter System (ASIRAS, or ASR), and airborne EM sounding (AEM). We compare the airborne data with two CryoSat freeboard products: the ESA CryoSat-2 Baseline-C freeboard data and the AWI CryoSat sea ice freeboard and thickness product (Ricker et al. 2014, Ricker et al. 2015, Hendricks et al. 2015). Below we briefly review each of the methods and products and then present the resampling method used to account for different footprint sizes.

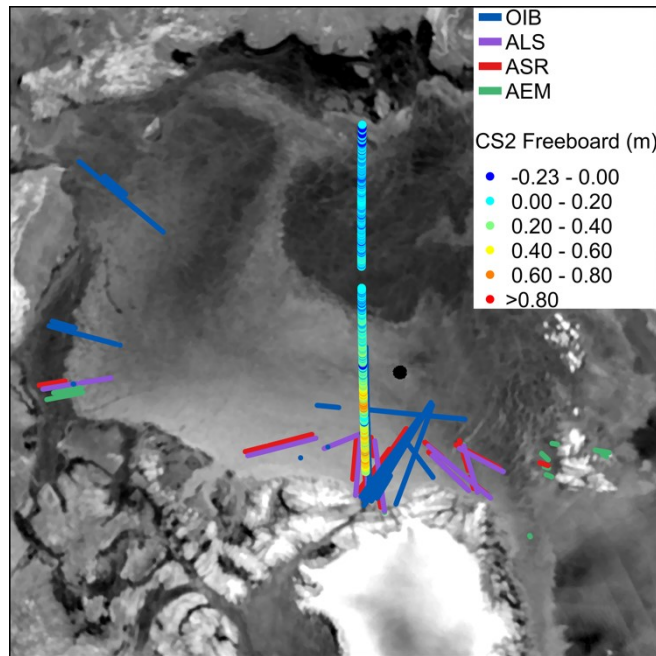


Figure 9.1: Map of all coincident laser (OIB and ALS), radar (ASR), and AEM flights used in this study (see flight list in Appendix 9.1). Note that flight tracks overlap and therefore not all sensor's tracks are visible on the map. Freeboard retrievals along one coincident CryoSat ground track between Canada and Siberia (orbit 021011 on March 26, 2014) are also shown as example. Background shows radar backscatter on March 26, 2014 (from ASCAT; Long et al., 2001) chosen to represent typical ice conditions during CryoVEx campaigns, with first-year ice indicated by low (darker) and multiyear ice by high backscatter (bright).

9.2.2. Airborne measurements

9.2.2.1. OIB

Since 2009, the NASA Operation Ice Bridge (OIB) mission has conducted large-scale airborne surveys of the Arctic Ocean every year in March/April using long-range aircraft (Koenig et al., 2010). The primary OIB measurement is based on Airborne Laser Scanning (ALS) with the Airborne Terrain Mapper (ATM, Krabill et al., 2002). OIB surveys are performed at a nominal survey height of 460 m, resulting in an ATM swath approximately 240 m wide. Freeboard retrieval from the ATM data and subsequent conversion to ice thickness utilizes several additional instruments operated on the same aircraft, such as high-resolution cameras and altimetric and snow-penetrating radars (Kurtz et al., 2013). Once processed, these data are made freely available to the public via the National Snow and Ice Data Center (NSIDC). In this study, all OIB data from 2011-2013 are the IDCSI4 version 1 (Kurtz et al. 2015), and all the data from 2014 are

from the NASA OIB 'quick-look' product as a final product was not yet available (Kurtz, 2015). The OIB freeboard product, and additional ice and snow thickness information are averaged to an along-track resolution of 40 m centered on the snow radar footprint (Kurtz et al., 2013). The uncertainties associated with the OIB freeboard and ice and snow thickness estimates are included in the data product files.

The OIB freeboard data are dependent on the identification of open water leads to identify and remove the instantaneous sea surface height from the measurements of the snow surface height. The OIB IDS14 version 1 product used the DTU10 Mean Sea Surface height (MSS) product to remove the main geoid undulations from the ATM data; the EGM2008 geoid is used in the OIB quick-look data product. The OIB IDS14 version 1 and the OIB quick-look data both use an automatic algorithm that uses the ATM and aerial photos to identify leads as described in Kurtz et al. (2013). Note that OIB freeboard represents snow freeboard (Table 9.2). It is adjusted to account for the amount of open water, thin ice, and grey ice detected in each 40 m average. The uncertainty of the OIB snow freeboard ranges from 0.01 m to 0.20 m (Kurtz et al. 2013).

9.2.2.2. *ALS*

During CryoVEx campaigns, ALS measurements were also performed by DTU and AWI using Twin Otter and DC3-T aircraft (e.g. Hvidegaard and Forsberg, 2002; Forsberg and Skourup, 2005; Ricker et al., 2014). These ALS measurements used Riegl instruments operated at altitudes of 100 m (DC3-T) or 300 m (Twin Otter), resulting in swath widths of ~100 to ~200 m.

The ALS freeboard data are dependent on the identification of open water leads to remove the instantaneous sea surface height. Leads are flagged manually along track and the DTU13 MSS product is used to subtract the main geoid undulations from the ALS data. No other geophysical corrections are applied to the data and a freeboard value is provided for each laser scanner point with no averaging. Like with OIB, ALS freeboard represents snow freeboard (Table 9.2). The ALS snow freeboard measurements have a typical uncertainty of 0.13 m (Hvidegaard and Forsberg, 2002).

9.2.2.3. *ASIRAS*

The Airborne Synthetic-Aperture, Interferometric Radar Altimeter System (ASIRAS, or ASR) was designed as an airborne CryoSat simulator (Mavrocordatos et al., 2004). The antenna is

mounted at the bottom of a fixed wing aircraft, usually a Twin Otter, and is typically operated at an altitude of 300 m over sea ice. With the Doppler beam sharpening, ASIRAS measurements have a footprint of about 3 m along-track. The across track footprint depends on the altitude of the antenna; with the given opening angle of 2.2°, and a normal survey altitude of 300 m, the across track footprint is roughly 12 m. The ASIRAS data were processed by AWI and the waveforms were retracked with a threshold spline retracker algorithm (TSRA, Ferraro and Swift, 1995, Ricker et al. 2014). The retracked point is obtained by a half power threshold that is applied to the leading edge of the first maximum of the waveform smoothed with a cubic spline.

As with OIB and ALS, the ASIRAS freeboard data are dependent on the identification of open water leads to remove the instantaneous sea surface height. Leads are manually identified from the ASIRAS waveform data and interpolated with a cubic spline. The DTU13 MSS product is used to subtract the main geoid undulations. ASIRAS freeboard represents radar freeboard (Table 9.2).

The radar freeboard retrievals have not been further modified or corrected in this study. Note that retrieved radar freeboard not only depends on snow properties, but also on the used retracker. The estimated uncertainty in the ASIRAS radar freeboard is unknown.

9.2.2.4. AEM

With airborne electromagnetic (AEM) sounding the height of the EM instrument above the ice/water-interface is measured by means of EM induction, and the height above the snow surface is measured with a laser altimeter. The difference between both height measurements corresponds to the total ice + snow thickness; AEM sounding cannot distinguish between snow and ice (Haas et al. 2009). CryoVEx AEM surveys were performed with towed sensors below helicopters by NPI (e.g. Renner et al., 2014), and below DC3-T airplanes by AWI and YU (Haas et al., 2010). The accuracy of EM thickness retrievals is approximately ± 0.1 m over level sea ice (e.g. Pfaffling et al., 2007). However, as the footprint of the EM method is 3 to 4 times the flying altitude of the EM Bird of 15 to 20 m, the maximum thickness of pressure ridges can be underestimated by as much as 50 to 60 percent, depending on the geometry and porosity of ridge keels (e.g. Haas and Jochmann, 2003). The AEM thickness retrievals are independent of the identification of open water leads as leads are only used to confirm that the thickness at these locations is 0 m.

9.2.3. CryoSat data products

9.2.3.1. AWI product

The primary CryoSat ice thickness product used in this study is the AWI freeboard and thickness product available at meereisportal.de and extensively described by Ricker et al. (2014; 2015). However, instead of the original ESA Baseline-B product used in Ricker et al. (2014), here we used the ESA MSSL pre-release candidate Baseline-C data. Freeboard is derived with a 50 % Threshold-First-Maximum retracker (e.g. Ricker et al., 2014).

The CryoSat freeboard retrievals require the identification of open water leads to remove the instantaneous sea surface height. Leads are identified from surface type discrimination using thresholds of waveform parameters like pulse peakiness (PP), stack kurtosis (K), standard deviation (SSD), and others (Ricker et al., 2014; Table 9.3). For PP, values to the left (PP_l) and right of the power maximum (PP_r) are distinguished, minimizing the effect of off-nadir leads but at the cost of discarding up to 60% of the detected leads (Ricker et al., 2014; Wernecke and Kaleschke, 2015). K and SSD are provided in the ESA CryoSat-2 L1B data product and are based on the OCOG Width (Wingham et al., 1986). The ice concentration used by AWI is obtained from the Ocean and Sea Ice Satellite Application Facility (OSI SAF).

After subtraction of DTU13 MSS geoid undulations lead elevations are linearly interpolated between lead locations. The AWI CryoSat freeboard data represents radar-derived freeboard and includes estimates of freeboard uncertainty. The AWI product distinguishes between first-year ice and multi-year ice using the OSI SAF ice type product and uses the modified Warren et al. (1999) climatological snow depth and density as in Ricker et al (2014) to account for the reduced wave speed velocity in snow; the correction term applied to freeboard is 22% of the snow depth. Ice density is also dependent on ice type and the AWI product uses 882 kg m^{-3} for multi-year ice and 916.7 kg m^{-3} for first-year ice. The OSI SAF ice type grid data is weighted by the OSI SAF ice type product confidence flag data and interpolated for each footprint and is used to weigh the ice density.

Table 9.3: Waveform parameters and ice concentration thresholds used in the AWI and ESA CryoSat-2 processing algorithms to discriminate between the surface types: “ocean”, “lead” and “sea ice”: pulse peakiness (PP), stack kurtosis (K), standard deviation (SSD), peakiness left of the power maximum (PP_l), peakiness right of the power maximum (PP_r), sea-ice concentration (IC) and the width of the OCOG box (OCO_g WIDTH).

		Waveform Parameter							
	Type	PP	K	SSD	PP _l	PP _r	IC (%)	OCO _g WIDTH	Stack Width
AWI	Ocean	0 ≤ PP ≤ 10		≥ 18.5			≤ 5	≥ 38	
	Lead	≥ 40	≥ 40	≤ 4	≥ 40	≥ 30	≥ 70		
	Sea Ice		≤ 8			≤ 15	≥ 70		
ESA	Ocean	0 ≤ PP ≤ 16					≤ 10		≥ 400
	Lead	≥ 31							≤ 400
	Ice	0 ≤ PP ≤ 16					≥ 75		≥ 400

9.2.3.2. ESA product

The ESA CryoSat Baseline C product used in this study was a pre-release version of Baseline C with minor differences from the final release product. These differences include the orbit information used to calculate the position of CryoSat-2. Radar freeboard is obtained in a similar manner as the AWI product, using the UCL13 MSS. The major differences between the two are a different retracker, a different MSS product, and different waveform shape parameters used for lead detection (Table 9.3). The ESA product uses ice concentration information produced by MSSL from the National Snow and Ice Data Center (NSIDC) SSMI Near-Real-Time (NRT) data. The pulse peakiness used by the ESA product is calculated differently than in the AWI product.

The ESA CS2 freeboard represents radar freeboard; it has not been corrected for the influence of snow properties or the retracker. Estimates of uncertainty of the ESA CS2 radar freeboard product are not yet included in the product.

9.2.4. Resampling airborne data to CryoSat footprints

To compare airborne and CryoSat data, the high-resolution airborne data were resampled to the CryoSat footprints. For each specific orbit, the geographic coordinates of the nadir point of the satellites were extracted from the CryoSat-2 L1B files. For each nadir point, a geographic box was constructed with an across track width of 1650 m (approximate beam limited footprint width of CryoSat-2) and an along track width half way between the surrounding nadir points,

approximately 300 m and just smaller than the actual along track footprint to avoid overlap (Figure 9.2). Next, a point-in-polygon search was performed to identify all airborne points within each CryoSat footprint. The number of airborne measurements within a CryoSat footprint varies greatly with each sensor, depending on their sampling characteristics. Therefore, every footprint nominally included seven 40 m OIB data, 30000 ALS data, 120 ASIRAS data and 50 AEM measurements.

To account for the freeboard and thickness variability in each CryoSat footprint, not only the mean airborne freeboard or thickness and standard deviation were calculated from the points within each footprint (Figure 9.2) but also the frequency distribution of all ALS, ASIRAS, and AEM measurements was stored from which we used modal values in this study. As there were only few OIB data in each footprint, their probability distribution and mode may not be representative and were therefore not included.

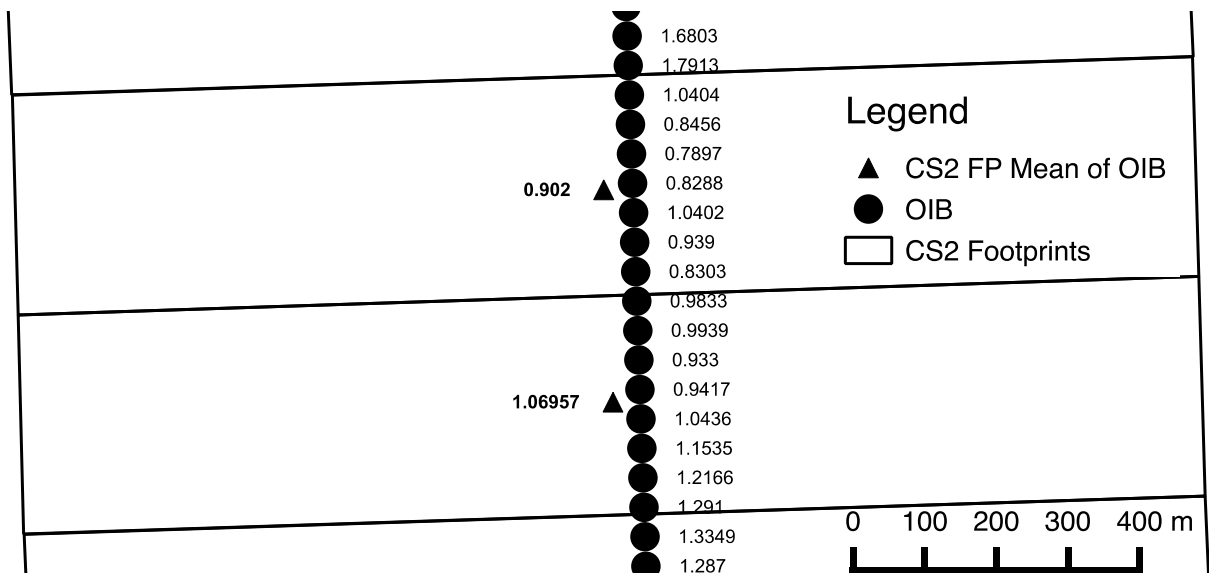


Figure 9.2: Example for the averaging of OIB freeboard data to the beam-sharpened CryoSat footprints (large rectangles). Black circles are 40 m in diameter and show the OIB freeboard retrieval locations and the values for each measurement. Triangles and left labels show the averaged OIB freeboard data in each footprint.

The collection of coincident airborne and CryoSat data is very difficult due to large differences in spatial coverage, ground velocity, weather and logistical constraints, and data processing

methodologies. The nominal survey velocity of the airborne sensors is 40 to 100 m s⁻¹ while CryoSat travels nearly 7 km s⁻¹. The spatial footprint of CryoSat is also much larger than the airborne sensor footprints. Given the slower survey velocity and more limited spatial coverage of the airborne sensors in comparison to CryoSat, ice drift may result in different ice being sampled during hours-long surveys even for airborne flights that are initially coincident with CryoSat. In addition, the airborne data have been collected in the western Arctic and just hundreds of kilometers from the coast. As many of the surveys have been performed in the Lincoln Sea and Beaufort Sea, most of the data are over MYI. Finally, the operation of the airborne sensors and the freeboard and thickness retrieval methods can result in data gaps that limit the amount of coincident data even if raw data were successfully collected. Data gaps can result when there are insufficient numbers of leads identified along the flight tracks, or from operational requirements such as in-flight sensor calibration. The coordination of multiple survey aircraft with different survey altitudes, velocities, and operational limitations is nontrivial and challenging but can provide for rich and unique datasets such as was collected during CryoVEx campaigns.

Our dataset of coincident airborne and CryoSat data includes 36 CryoSat orbits. Some 220,000 OIB measurements, 872 million ALS measurements, 1.76 million ASIRAS and 580,000 AEM measurements were collected coincidentally within CryoSat footprints. Most of the flights were collected within +1.5 and -6 hours of a CryoSat-2 overpass, with OIB showing the smallest range in offsets and centered around -0.4 hours. Mean flight distances of CryoSat overlap ranged from 204 km for AEM to 420 km for OIB. OIB data were collected along 19 of the CryoSat orbits, with 15, 16, and 18 surveys performed by the ALS, ASIRAS and AEM sensors, respectively. While 15 of the CryoSat orbits were flown by one sensor, 12 were surveyed by three or more sensors; unfortunately, just four orbits were surveyed by all four sensors and only two of those surveys had data returned from all airborne sensors.

9.3. Results

9.3.1. Illustration of detailed analysis of data along one orbit

One of the most extensive, complete data sets was collected along orbit 021011 on March 26, 2014 over MYI north of Ellesmere Island (Figure 9.1), including OIB, ALS, ASIRAS (ASR), and AEM surveys. Figure 9.3 shows typical full-resolution airborne freeboard measurements and the

same data resampled to the CryoSat footprints over a 10 km long section of the CryoSat orbit. Both figures include the AWI radar-derived and ESA radar freeboard CryoSat data; unfortunately, ESA freeboard is zero throughout this section. The OIB ALS, and ASIRAS data generally show the same ridge features, some of which are also observed in the AWI CryoSat freeboard. As expected, local airborne freeboard variance increases with increasing spatial resolution of the used products, e.g. between OIB and ALS. The CryoSat footprint averaged ALS and OIB snow freeboard data are highly correlated ($r = 0.89$) over this subset of the flight (Figure 9.3b). The correlation between OIB and ASIRAS freeboard measurements ($r = 0.70$) and ALS and ASIRAS radar freeboard ($r = 0.58$) is lower, likely due to variable snow penetration, ice surface roughness, and the comparatively limited footprint of the ASIRAS data.

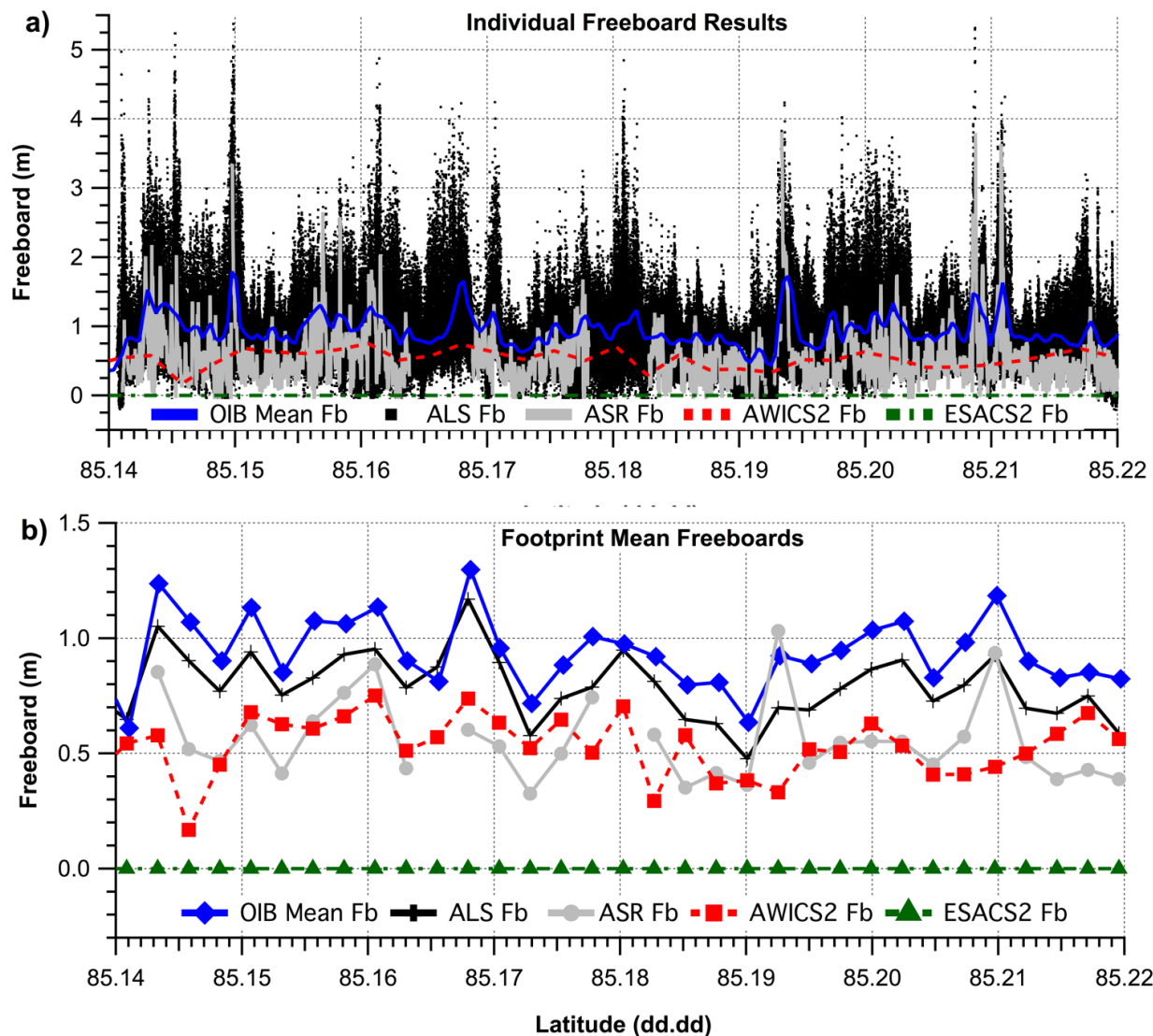


Figure 9.3: a) Typical 10 km section of the full resolution airborne data collected along CryoSat Orbit 21011 on March 26, 2014, showing OIB and ALS snow freeboard, ASIRAS (ASR) radar freeboard, and AWI and ESA CryoSat freeboard. b) Airborne data resampled to the CryoSat footprints.

Over the complete orbit (Figure 9.4), the correlations between the airborne and CryoSat data are lower than over the 10 km short, good example from Figure 9.3. Although there is good agreement between the two CryoSat freeboard products ($r = 0.77$, mean difference = 0.06 m), the correlations between the airborne freeboards and the CryoSat freeboards range between 0.14 and 0.22, and there are large RMS differences (RMSD) of 0.23 m to 0.40 m. In contrast, the correlation between the footprint-averaged airborne data remains high (ALS and ASIRAS = 0.71; ALS and OIB = 0.59; ASRIAS and OIB = 0.60). Even correlations between ALS, ASR and OIB

freeboard and AEM thickness are above 0.7. Sea ice drift, noise in the CryoSat data due to instrument and speckle noise, geophysical errors, MSS errors and insufficient spatial footprint coverage by the airborne data all contribute to the low correlations and large RMSDs, and will be discussed in more detail in Section 9.3.2. Results are also worse than those shown for gridded thickness data.

To extend our study to similar spatial scales as those shown in Table 9.1 we calculated along-track averages of the footprint resolution data over lengths of 3, 10, 25, and 50 kilometers. As an example, the 50 km averaged data are presented in the right column of Figure 9.4. Results show stronger correlations (0.16 to 0.57), smaller RMSDs (0.10 m to 0.33 m), and smaller mean differences (0.08 m to 0.29 m) than for the comparison of individual footprints shown in the left column of Figure 9.4. Furthermore, both the OIB and ALS snow freeboards lie above the one-to-one line while the ASIRAS (ASR) radar freeboard data are very close to the AWI radar-derived freeboard one-to-one line, i.e. snow freeboard estimates are clearly larger than radar retrieved freeboards, with airborne and satellite radar freeboard retrievals being very similar. The AWI radar-derived and ESA radar freeboard data also show high correlations, low mean differences and low RMSDs and thus fall close to the one-to-one line. Higher correlations between the OIB and ALS snow freeboard and the AWI radar-derived freeboard result may partially from their larger freeboard range compared with the ASIRAS freeboard range. In the next section, we examine the complete dataset of the individual footprint and 50 km averaged results from all CryoVEx flights.

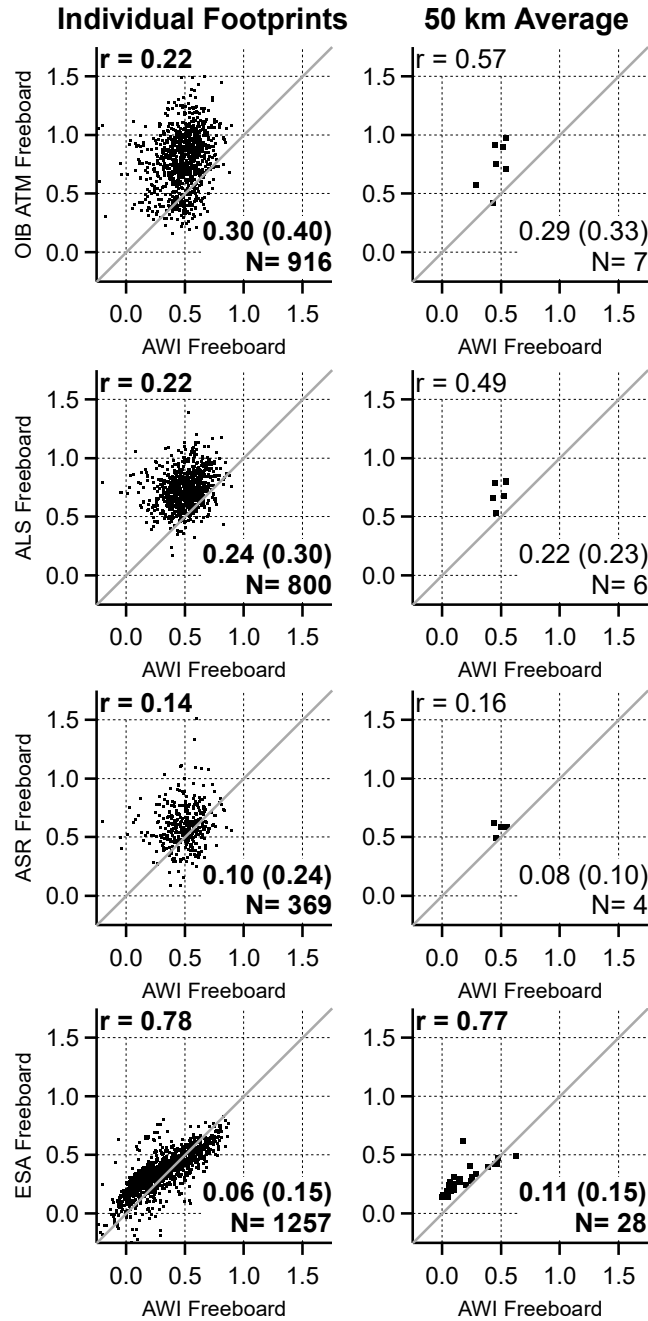


Figure 9.4: Example of the comparison between airborne and CryoSat freeboard retrievals along complete flight tracks for orbit 021011 on March 26, 2014 (see Figure 9.1). Left column shows comparisons between mean airborne data in individual CryoSat footprints. Right column shows data averaged along-track over 50 km. The scatter plots show the correlation coefficient r , Mean Difference and RMS Difference (RMSD, in parentheses) in the bottom right. N is the number of CryoSat footprints with coincident measurements (left column), or of coincident 50 km sections (right column). Bold correlations have a p -value less than 0.01 (statistically significant) and r is significantly different from 0.

9.3.2. Analysis of complete freeboard dataset and improvement by along-track averaging

The comparisons between CryoSat and airborne data illustrated in Section 9.3.1 were carried out with all available coincident data between March 2011 and the end of March 2014, excluding late summer data and a survey completed in the Baltic Sea. Results showed similarly large scatter, low correlation coefficients, and large RMSDs as with the example in Figure 9.1. A summary of all results is shown in Figure 9.5, where the distribution of all correlation coefficients, mean differences, and RMSDs are shown as box and whisker plots. Overall, there is much less agreement between our footprint-scale airborne data (black symbols in Figure 9.5) and CryoSat data than was observed for grid-scales by previous studies summarized in Table 9.1. For example, mean correlation coefficients of our analysis are less than 0.3 (Figure 9.5a), compared to the lowest correlation coefficient of 0.53 found by Kwok and Cunningham (2015). Our mean freeboard RMSDs are larger than 0.2 m, which would correspond to thickness RMSDs of more than 2 m or so. Laser and CryoSat mean freeboard differences are around 0.25 to 0.35 m, which is much larger than the mean differences of the grid-scale thickness comparisons in Table 9.1 but is comparable to mean snow depth in the Arctic over MYI (e.g. Warren et al. 1999). However, this also partially results from comparing snow freeboard with radar freeboard, and is not directly comparable with the approach that led to results in Table 9.1 (see Discussion below).

As in the example in Section 9.3.1, we have tried to improve the agreement between airborne and CryoSat data by averaging the footprint data over longer ground-track sections. Figure 9.5a shows that mean and median correlation coefficients increase with increasing averaging lengths of 3, 10, 25, and 50 km. With 50 km averaging, best results are obtained for OIB, with a median correlation coefficient between OIB and AWI CryoSat freeboard of 0.61. This is comparable to the correlation found by Kwok and Cunningham (2015; Table 9.1). For 50 km averaging length, ALS and ASIRAS also correlate better with the AWI CryoSat product with median values of $r = 0.46$ and $r = 0.45$, respectively, while correlations with the ESA product remain less than 0.23. Correlation coefficients between the AWI and ESA CryoSat data change little with increasing averaging length, and remain above 0.8.

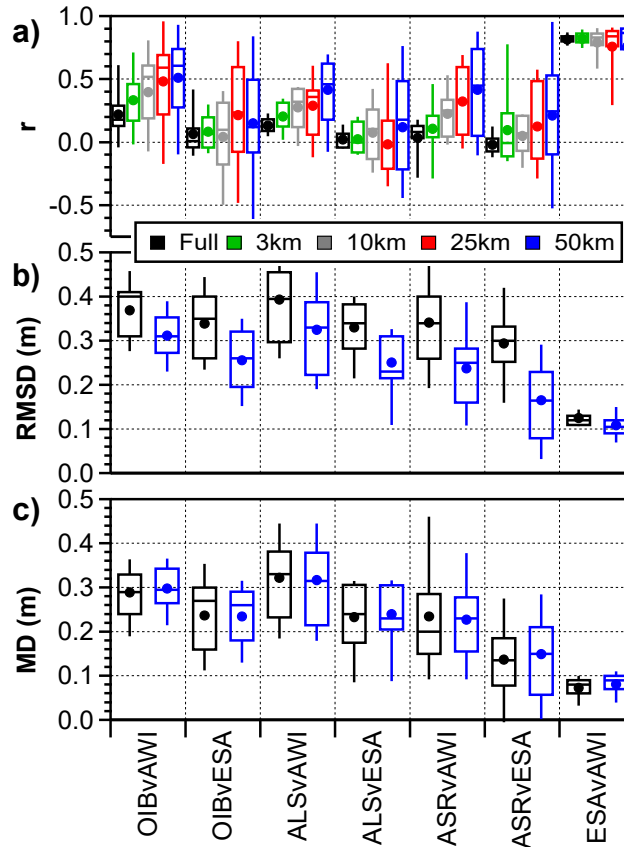


Figure 9.5: Summary of results of the comparison of airborne and CryoSat freeboard over different along-track averaging distances. Percentile analysis of a) correlation coefficient r , b) RMSD, and c) the mean difference (MD) between the resampled airborne data and the CryoSat freeboard data. Full denotes the footprint averaged results and 50 km is the 50 km along track average of the footprint resampled results. The boxes present the 25th and 75th percentiles, the horizontal line within the box is the median (50th percentile) and the whiskers end at the 10th and 90th percentiles. Circles show mean value.

Figure 9.5b shows the results for RMSDs between all airborne and CryoSat data for the footprint-scale comparison and 50 km averages. The RMSDs decreased with increased along-track averaging. The median RMSDs of the 50 km averaged data have decreased to less 0.35 m for all data. The RMSDs between the airborne data and the AWI CryoSat data are slightly smaller than those between the airborne data and ESA CryoSat data. The median RMSD between ASIRAS and CryoSat freeboards is slightly smaller than between laser data and CryoSat.

Finally, Figure 9.5c shows mean differences between the airborne and CryoSat data, both for the footprint-scale comparisons and 50 km along-track averages. Mean differences are calculated as the first listed data set minus the second listed dataset within each category, e.g. ESA CryoSat

freeboard – AWI CryoSat freeboard in the category ESAvAWI. In contrast to correlation coefficients and RMSD, mean differences between the airborne and CryoSat data vary little with increasing along-track averaging indicating systematic differences between airborne and CryoSat data products. As will be discussed later, we attribute these systematic differences to the different snow penetration and different treatment of snow of the different sensors and processing methods. Mean differences between OIB and ALS snow freeboard and CryoSat radar freeboard remain between 0.28 and 0.32 m independent of averaging length. Mean differences between ASIRAS and CryoSat radar freeboards are slightly smaller than for laser-derived snow freeboard, between 0.20 and 0.23 m. The ESA CryoSat radar freeboards are generally 0.07 to 0.11 m larger than the AWI CryoSat radar-derived freeboards, leading to smaller mean differences between the airborne data and the ESA CryoSat data than the airborne data to AWI CryoSat data.

Due to the improved results obtained for 50 km averaged data, the following analyses are all carried out with this averaging length. In addition, as there is generally better agreement between airborne data and the AWI CryoSat retrievals (Figure 9.5), we limit the analysis to the AWI freeboard and thickness products.

9.3.3. Differences over first- and multiyear ice

Figure 9.6 compares the correlations, RMSDs, and mean differences between the mean airborne data and AWI CryoSat radar-derived freeboard data for first-year ice (FYI) and multi-year ice (MYI) using the 50 km along-track averaged data. Ice types were distinguished from a flag in the AWI CryoSat product which is available for each measurement and is based on the OSI SAF ice type product. For the along-track averages, only 50 km sections in which there was exclusively FYI or MYI have been used.

Unfortunately, very few 50 km flight segments were found to be FYI; therefore, the FYI results are likely not representative. There is only one FYI flight with just three 50 km segments over FYI for ASIRAS and ALS. For OIB there are just three orbits with FYI segments. That said, Figure 9.6a shows that the correlations between OIB and ALS and CryoSat over MYI are higher than over FYI. Furthermore, the correlations between AWI and ESA CryoSat freeboards are also higher for MYI than for FYI. It should be noted that the freeboard range over FYI is much smaller than over MYI.

The correlations between both ASIRAS and CryoSat show the opposite but are based only on a single flight over FYI.

Figure 9.6b reveals that the RMSDs have a larger range, from 0 m to 0.17 m, and are larger over MYI than over FYI for which RMSDs range from 0 m to 0.08 m. This could be due to the higher surface roughness of MYI than FYI. The agreement between the two CryoSat products is very good over both FYI and MYI with RMSDs generally less than 0.05 m.

Mean differences between the airborne and AWI CryoSat data and between the ESA and AWI CryoSat data are rather similar (Figure 9.6c) except for the ALS data, which are based on only one data point. For both ice types, the mean differences between OIB and CryoSat range between 0.25 and 0.3 m, and are around 0.15 m between ASIRAS and CryoSat. The mean difference between the ESA and AWI CryoSat freeboards is greater over FYI (0.13 m) than over MYI (0.09 m).

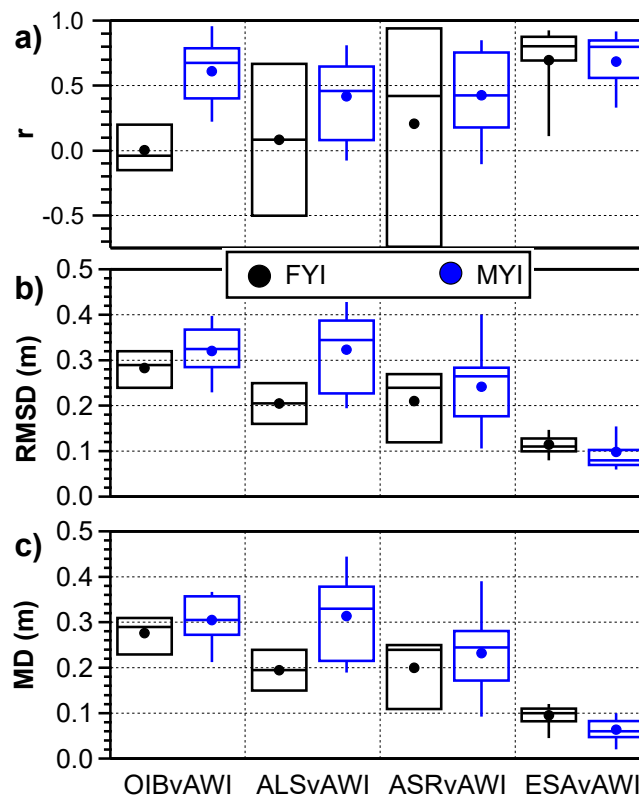


Figure 9.6: Summary of results of the comparison of airborne and CryoSat freeboard over FYI and MYI. Shown are results for 50 km along-track mean data. Percentile analysis of a) correlation coefficient r , b) RMSD, and c) the mean difference (MD) between the airborne and CryoSat freeboard data. The boxes present the 25th and 75th percentiles, the horizontal line within the box is the median (50th percentile) and the whiskers end at the 10th and 90th percentiles. Circles show mean value.

9.3.4. Differences between mean and modal freeboard

As explained in Section 9.2.4, we computed both mean and modal freeboard of the ALS and ASIRAS data within each CryoSat footprint. Here we examine if the CryoSat retrievals are in better agreement with the mean airborne freeboard fb_{mean} or with the modal airborne freeboard fb_{mode} in each footprint, noting that modal freeboard represents the freeboard of level ice within each footprint while mean freeboard includes the height of ridges.

Figure 9.7 presents a comparison of the 50 km along-track mean fb_{mean} ($\overline{fb_{mean}}$) and mean fb_{mode} ($\overline{fb_{mode}}$) ALS and ASIRAS freeboard with the 50 km along-track mean freeboard of both CryoSat products. OIB data are excluded because modal values were not computed for OIB as nominally only 7 OIB data points are found in each footprint. The median and mean correlation coefficients between the airborne $\overline{fb_{mode}}$ data and CryoSat are slightly higher than for $\overline{fb_{mean}}$ (Figure 9.7a). The improvement is largest with the ASIRAS data, where the median correlation coefficient between $\overline{fb_{mode}}$ and CryoSat is 0.2 larger than between $\overline{fb_{mean}}$ and CryoSat.

Median and mean RMSDs between $\overline{fb_{mean}}$ and CryoSat freeboard, and between $\overline{fb_{mode}}$ and CryoSat freeboard are nearly the same as for the mean airborne data but there is a slight reduction in the range of RMSD values (Figure 9.7b). However, mean differences between $\overline{fb_{mode}}$ and CryoSat freeboard are nearly half those of $\overline{fb_{mean}}$ and CryoSat freeboard (Figure 9.7c). The mean differences between ALS $\overline{fb_{mode}}$ and CryoSat are only 0.15 m, 0.1 to 0.15 m less than mean difference between ALS $\overline{fb_{mean}}$ and CryoSat. Similarly, small mean differences are observed between ASIRAS $\overline{fb_{mode}}$ and CryoSat freeboards.

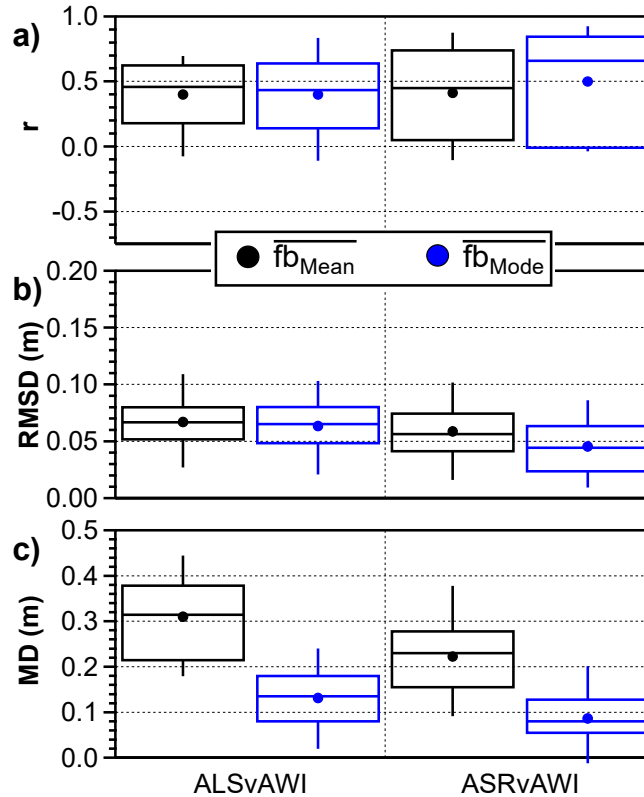


Figure 9.7: Comparison of airborne ALS and ASIRAS (ASR) $\overline{fb_{mean}}$ and $\overline{fb_{mode}}$ (see text) with 50 km along-track mean CryoSat freeboard. Percentile analysis of a) correlation coefficient r , b) RMSD, and c) the mean difference (MD) between the resampled airborne data and the CryoSat freeboard data. The boxes present the 25th and 75th percentiles, the horizontal line within the box is the median (50th percentile) and the whiskers end at the 10th and 90th percentiles. Circles show mean value.

9.3.5. Comparison of AEM ice thickness with CryoSat ice thickness

In addition to the freeboard data collected by NASA OIB and the ALS and ASIRAS systems, extensive airborne electromagnetic induction sounding (AEM) measurements of sea ice thickness have been performed coincidentally with CryoSat. Figure 9.8 compares the correlation, RMSD, and mean difference between the AEM total ice + snow thickness and the AWI CryoSat ice thickness. The AWI CryoSat ice thickness uses snow density and thickness from the Warren et al. (1999) snow climatology (Ricker et al. 2014 and Section 9.2.3). Besides the vastly different footprints and ice drift, the AEM ice thickness includes snow depth while the AWI thickness does not.

Figure 9.8a shows that correlations between the AEM and CryoSat thickness are low but do increase with increasing spatial averaging, from 0.1 up to 0.4 for the 50 km long segments. However, some orbits show strong negative correlations between thickness; this is interpreted

as either erroneous freeboard retrievals or resulting mainly from ice drift occurring between the airborne measurements and the CryoSat-2 measurements. Other factors such as poor SSH determinations and differences between the used and actual geophysical snow depth, snow density and ice density may also cause negative correlations. The correlation between AEM total thickness and AWI CryoSat ice thickness is also greater over MYI than FYI; further interpretation is limited by the paucity of observations over FYI. The 50 km averages of the footprint AEM modal thickness showed stronger correlations with CryoSat than the footprint AEM mean thickness and provides further support to the idea that CryoSat may be more representative of the modal ice within the footprint than the mean.

The RMSD (Figure 9.8b) is strongly reduced with increased spatial averaging, dropping from 1.3 m at the footprint scale to less than 0.4 m for the 50 km averaged data. The RMSD is greater over MYI than FYI, 0.35 m vs 0.16 m, respectively. There is only a slight reduction in the RMSD when using modal AEM data than when using the footprint mean, like the results for the airborne and CryoSat freeboard comparisons presented in Figure 9.7b. As was observed with the freeboard data, the RMSD values are lower when using the 50 km average of the mode of the AEM data within a CryoSat footprint.

The mean difference (Figure 9.8c) increases slightly with averaging distance and the negative mean differences observed at full resolution are not observed in the 50 km averaged data. The mean difference of FYI and MYI are similar with overlapping ranges but with a much narrower distribution, and small sample size, for FYI. The mean difference between the 50 km average of the footprint AEM modal thickness is much smaller than for the 50 km mean of the footprint mean thickness, shrinking from 0.68 m to 0.21 m. The improved correlation and reduced RMSD and mean difference for the modal results provide further support that CryoSat may be more representative of the modal ice within the footprint than the mean. Overall, the AEM thickness results provide evidence of how comparisons of thickness are complicated by the myriad of assumptions and additional processing steps required in comparison to freeboard.

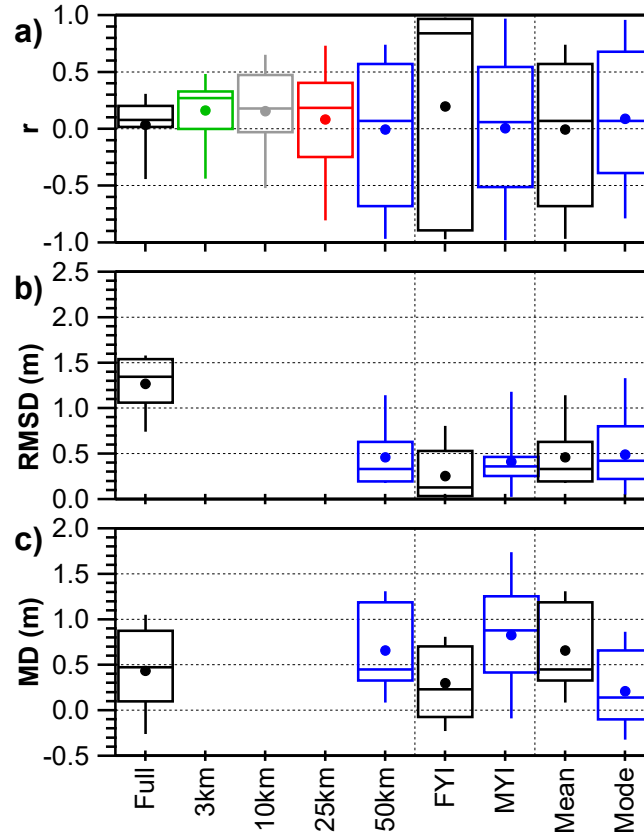


Figure 9.8: Comparison of the AEM and AWI CryoSat thickness, showing the effect of along-track averaging distance (left column), differences over different ice types (center column), and differences between the modal and mean thickness (right column; cf. Figure 9.5, Figure 9.6, Figure 9.7 for freeboard). The figure shows percentile analysis of a) correlation coefficient r , b) RMSD, and c) the mean difference (MD) between the resampled AEM thickness and CryoSat thickness. The boxes present the 25th and 75th percentiles, the horizontal line within the box is the median (50th percentile) and the whiskers end at the 10th and 90th percentiles. Circles show mean value.

9.3.6. Comparison of OIB with CryoSat Ice Thickness

As the NASA OIB data product also includes ice thickness, we compare these data to the AWI CryoSat Thickness (Figure 9.9). The OIB thickness data are based on the OIB freeboard and snow depth measurements and assume 320 kg m^{-3} snow density, 1024 kg m^{-3} water density and uses only a single ice density, 915 kg m^{-3} (Kurtz et al. 2013). As footprint scale modal values were not calculated for OIB (Section 9.2.4), only the comparisons of the different along-track averages and FYI vs MYI are presented.

The correlation between OIB thickness and AWI CryoSat thickness increases with increased along-track averaging distance as observed in all other airborne to CryoSat comparisons with the

median correlation rising from 0.13 to 0.54. These results are comparable to those observed in previous grid-based studies (see Table 9.1). These correlations are also higher than observed between the AEM thickness and CryoSat. Using the 50km averaged data, correlations were stronger over MYI ($r=0.63$) and negative over FYI (-0.34) but the FYI results are again limited to just three orbits. Over FYI the correlation between OIB thickness and CryoSat was more negative, likely for the same reasons as discussed in Section 9.3.5.

A similar large reduction of over 1.25 m in the RMSD was seen with increased along-track averaging. The mean RMSD of FYI and MYI are both around 0.5m but the median over FYI is 0.54 m compared to 0.32 over MYI; however, FYI observations are limited. The RMSD between AEM and CryoSat thickness is smaller at both averaging distances and smaller for both FYI and MYI than observed here for OIB.

The mean difference between OIB thickness and CryoSat thickness remains scale invariant and shows only minor differences between FYI and MYI. The range in mean differences is smaller over MYI than FYI but is based on a much larger sample size than the FYI. The mean difference is 0.56 m over FYI and 0.71 m over MYI. Again, the mean differences between AEM thickness and CryoSat thickness were smaller than are observed between OIB and CryoSat.

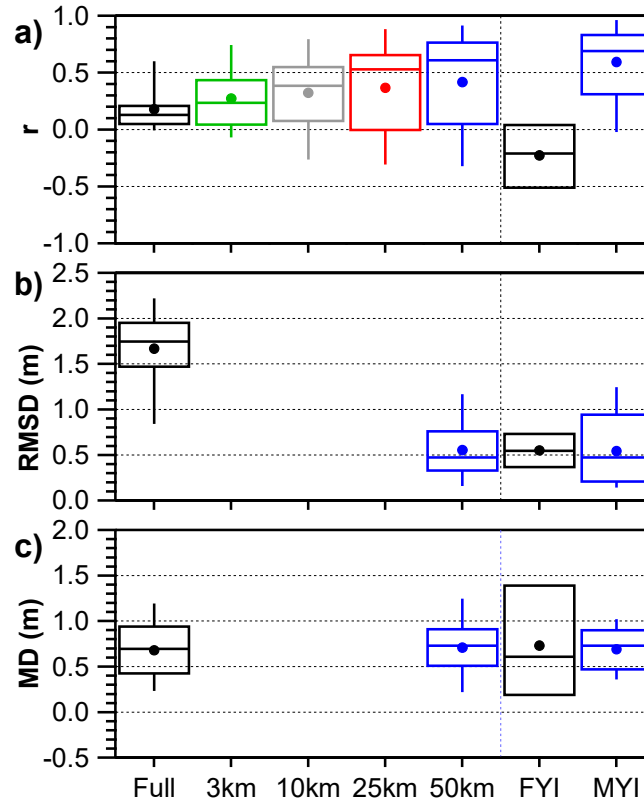


Figure 9.9: Comparison of the OIB and AWI CryoSat thickness, showing the effect of along-track averaging distance (left column) and differences over different ice types (right column; cf. Figure 9.5, Figure 9.6). The figure shows percentile analysis of a) correlation coefficient r , b) RMSD, and c) the mean difference (MD) between the resampled OIB thickness and the CryoSat thickness. The boxes present the 25th and 75th percentiles, the horizontal line within the box is the median (50th percentile) and the whiskers end at the 10th and 90th percentiles. Circles show mean value.

9.4. Discussion

In contrast to previous studies that used 25 km or larger grids and monthly averages, we have compared coincident CryoSat and airborne data at the footprint scale and for along-track spatial averages. Our results showed strong correlations between AWI CryoSat radar-derived freeboard ($r > 0.75$) and ESA CryoSat radar freeboard at all scales. Spatial averaging resulted in only small changes in the correlations, the RMSD and the mean difference between the two CryoSat products. The mean AWI CryoSat freeboards were generally 0.11 m smaller than the ESA CryoSat freeboards and the RMSD between the two products was less than 0.06 m. The RMSD and mean difference between the two CryoSat products result from the different algorithms used in each product.

Unlike the AWI CryoSat product, the ESA product does not include ice type, uses radar freeboard, and uses a different retracker for the sea ice and the open water leads. Furthermore, the ESA algorithm uses a different retracker than the AWI product, uses a different MSS product to remove the mean geoid undulations and uses a different algorithm for detecting leads. The AWI product applies ice type dependent ice density and snow depth corrections to the freeboard to determine radar-derived freeboard while the ESA product reports the radar freeboard. In addition, the AWI CryoSat product also contained 1.71 ± 0.52 times the number of valid freeboard measurements in the ESA CryoSat product. While the exact cause for this difference has not been identified, it is likely the result of the different quality control flags and lead identification thresholds being applied to the two CryoSat products. These data should be examined in detail and compared to the airborne data to determine the possible reasons for rejection in the ESA product and inclusion in the AWI product and to determine an optimum set of lead detection and data rejection criteria. These differences in the two CryoSat products lead to the different results observed when compared to the airborne data.

Comparisons between the airborne altimeter data at the footprint scale showed high correlations ($r > 0.55$) and give confidence in the airborne data. However, the individual footprint analysis showed low correlations and large RMSDs between the airborne data and both CryoSat products. While the results between airborne data and the AWI CryoSat radar-derived freeboard were more positive than with the ESA CryoSat, the individual footprint results indicated several challenges with conducting footprint scaled comparisons related to the spatial scale of the measurements. First, all the various airborne sensors have significantly smaller footprints than CryoSat. The ALS and OIB ATM sensors have the largest footprints with their wide measurements swaths of a 100 to 200 m, and ASIRAS has the smallest at roughly 12 m across-track; this is even smaller than the AEM footprint of approximately 60 m. As we are using the OIB thickness product, the actual footprint of the OIB ATM data used is much smaller at 40 x 40 m. Second, while the airborne systems can cover significantly long sections of the CryoSat orbit, the difference in ground velocity between the satellite and airborne systems results in increasing temporal offsets between the CryoSat and airborne data and allows for ice drift. Over landfast sea ice, this issue is reduced to changes in the physical properties of the ice that may occur between the CryoSat

orbit and the airborne overpass, but where the ice drifts, the airborne sensor may measure different ice than was observed by CryoSat. Ice drift between the CryoSat overpass and the airborne data can also result in different locations and distributions of the open water leads in the CryoSat, OIB, ALS, and ASIRAS data, affecting the quality of interpolation of the instantaneous sea surface height needed to retrieve freeboard. Over large areal averages the effects of these differences may be smoothed out as the general ice distribution of a region may vary less than at the smaller-scale of individual footprints.

Much better results were obtained with along-track averaging, namely higher correlations and lower RMS differences. The along-track averaged results agreed well with previous monthly grid based studies presented in Kwok and Cunningham (2015), Kurtz et al., (2014) and Tilling et al. (2015) and provides support for the assertion that much of the error in the CryoSat-2 freeboard/thickness data is random error that decreases with increased averaging of results. The agreement between the airborne data and the AWI CryoSat radar-derived freeboard data was generally stronger than between the airborne data and the ESA radar freeboard data, e.g. generally higher correlations and lower RMSDs. The OIB and ALS snow freeboards showed the highest correlations to the CryoSat radar freeboard. We suspect that this is due to the larger range in freeboard values, larger spatial footprints of these sensors in comparison to all the other airborne sensors. Furthermore, there were many more CryoSat footprints with valid OIB (~21500) and ALS (~17500) freeboard data than ASIRAS data (~11500) or AEM data (~9500). Mean differences between ASIRAS radar freeboard and both CryoSat freeboard products were lower than the laser snow freeboard measurements. However, the median and mean values of the mean difference were greater than 0.12 m and 0.21 m between ASIRAS and the ESA and AWI CryoSat freeboards, respectively. As the ASIRAS freeboards are greater than the CryoSat freeboards, the differences may be indicative of penetration bias and may provide an estimate of the effect of the different CryoSat freeboard processing algorithms as AWI provides a snow-depth corrected radar-derived freeboard and the ESA product does not.

The mean difference exhibited minimal variation with spatial scale, remaining between 0.2 m and 0.3 m for all freeboard comparisons. The mean difference between ASIRAS and CryoSat was smaller than between either OIB and ALS and CryoSat and could be indicative of the bias between

airborne laser and radar altimeters and CryoSat freeboard related to snow penetration. That the mean difference between the ASIRAS radar freeboard and ESA CryoSat radar freeboard and AWI CryoSat radar-derived freeboard is smaller than the ALS and OIB snow freeboard is expected as both the ASIRAS and CryoSat signals are radar altimeter freeboard and should be closer to the ice freeboard than the snow freeboard measurements provided by the OIB and ALS. Further, the mean difference between ASIRAS radar freeboard and the ESA CryoSat radar freeboard was smaller than when compared to the AWI radar-derived freeboard, though the correlations were smaller.

Modal freeboards showed slightly stronger correlations and smaller RMSDs and mean differences than the mean freeboard. Mean differences for airborne modal freeboard and CryoSat freeboard were significantly smaller than between airborne mean freeboards and CryoSat. The positive mean differences suggest that differences in snow penetration between airborne laser and radar freeboard and CryoSat freeboard could explain some of the remaining bias. Furthermore, the fact that the mean differences between modes are smaller than with means supports the idea that CryoSat is more sensitive to modal freeboard than to mean freeboard. This interpretation considers that due to the log - normal sea ice freeboard distribution mean freeboard is generally larger than modal freeboard. Therefore, the mean differences with CryoSat are smaller when comparing the modal than when using mean freeboards. Mean differences were also larger over MYI than over FYI, in agreement with climatological snow distributions such as Warren et al. (1999).

Unfortunately, our analysis over FYI is limited to just a few flights and a few data points. Furthermore, given that the ice type product is based on the much coarser OSI SAF sea ice type, it may not accurately capture the true ice type of a footprint or even for the 50km averages. Temporal offsets between OIB and other sensors also preclude the use of the OIB ice type for classification of the footprint. The lower correlations between airborne data and CryoSat over FYI compared to MYI may also be impacted by the relatively low range of FYI freeboard and thickness values observed at the end of the ice growth season most commonly sampled by the CryoVEx and OIB campaigns.

Comparisons of sea ice thickness are complicated by the assumptions required for the conversion of freeboard to thickness, especially snow depth and density. The comparison between the AEM total snow + sea ice thickness and the AWI CryoSat sea ice thickness revealed weak correlations. The mean differences between airborne and CryoSat thickness retrievals range from 0.38 m to 0.68 m, with the mean value increasing for longer averaging intervals; the median mean difference changed by less than 0.1m. The smaller mean differences for smaller averaging intervals result from negative mean differences observed for some of the flights. RMSD decreased with increasing averaging lengths, from 1.28 m at footprint scale to 0.42 m for 50 km averaging intervals. Adding the snow depth to the AWI CryoSat sea ice thickness decreased the mean difference with the AEM total ice and snow thickness; the RMSD and correlations changed only very slightly as the snow depth in the AWI product is a climatological dataset. Similar results were observed in the comparisons of OIB thickness with the AWI CryoSat thickness data though the correlations, RMSDs and mean differences in these comparisons were larger. The OIB thickness comparison also agreed with previous studies Laxon et al. (2013), Kurtz et al. (2014), Kwok and Cunningham (2015) and Tilling et al. (2015). In comparison to the AEM and AWI CryoSat thickness, the OIB ice thickness uses measured snow depth rather than total ice + snow thickness (AEM) or a snow depth climatology (AWI). The OIB thickness to CryoSat thickness comparison showed weaker correlations and larger RMSDs and mean differences than the OIB freeboard to CryoSat freeboard comparison. Given the number of assumptions needed to retrieve thickness (ice, snow, and water density), and the use of climatological snow depth data (Warren et al., 1999) for CryoSat thickness retrievals this is not surprising. Furthermore, several recent studies by King et al. (2015), Kwok et al. (2017), and Kwok and Haas (2015) raise questions about the accuracy of the OIB snow depth data, especially over MYI, adding more uncertainty to the thickness results.

In addition to differences in snow thickness between the climatology and OIB data and the influence that snow thickness has on the ice thickness retrievals from CryoSat, factors such as lead distribution and identification, geophysical corrections, and the mean sea surface height used to produce the interpolated instantaneous sea surface height also affect the differences between the airborne and CryoSat freeboards.

The distribution of leads was found to be extremely important for the retrieval of the instantaneous sea surface height and for the impact of geophysical corrections by Ricker et al. (2016) and thus for freeboard. Regions such as the Laptev Sea at the end of winter and the northern coast of the Canadian Arctic Archipelago can contain few leads to constrain the sea surface height interpolation. Although sea ice freeboard is a relative measurement of ice surface elevation minus the instantaneous sea surface height and the geophysical corrections applied are the same for both sets, because the sea surface height is interpolated between leads the impact of the correction is not the same for leads and the ice between the leads. While Ricker et al. (2016) concluded that the impact of the geophysical corrections uncertainty is likely less significant than the uncertainty in the CryoSat freeboard due to sea surface height interpolation, lead detection, and scattering from the snowpack, it can still affect the quality of freeboard retrievals from CryoSat in regions with few leads. Ricker et al. (2016) showed that nearly 7% of all gridded freeboard retrievals had a change in freeboard greater than 1cm due to application of the ocean tide corrections and that the mean change in freeboard for the impacted grid cells was nearly 0.05m. The results of Ricker et al. (2016) were reinforced by a study of the influence of different mean sea surface height products applied to CryoSat data for freeboard retrievals by Skourup et al. (2017). Skourup et al. (2017) showed that the detection of leads is critical to accurate freeboard retrievals especially where marine gravity features are not resolved in the MSS model as without leads, the change in sea surface height due to the gravity feature will map directly into freeboard. They also found that the choice of MSS influences freeboard results by 0.03 to 0.06m (standard deviation) and found that 60-80% of the grid cells were impacted by more than 0.01m. Their results also suggest that some geoid models (e.g. EGM2008, ArcGP) and MSS (DTU13, and DTU13) models that have been widely applied in the past should not be employed and that reprocessing using the current generation of MSS models (UCL13 and DTU15) should be performed to produce the most accurate long-term altimeter record of sea ice freeboard, thickness or volume change.

There are several additional studies that should be performed to assess and improve CryoSat freeboard retrievals. First, a detailed and extensive lead detection validation study should be performed using a combination of airborne optical imagery from CryoVEx aircraft and satellite

imagery. Next all available CryoVEx airborne and CryoSat-2 data should be processed to freeboard and thickness using the same input and auxiliary data. However, this will also require additional coincident multi-aircraft/sensor surveys along CryoSat-2 orbits as the amount of data is really still quite sparse. Additional coordinated surveys should be performed in new regions besides the Beaufort Sea and the Lincoln Sea. Ideally, surveys from the Russian Arctic or into the eastern Arctic should be performed and combined with other regions such as north of the CAA, Svalbard and north-eastern Greenland. An analysis on the impact of different freeboard retracers on the long-term trends in freeboard may also shed light on optimal and improved retracking methods.

This study suggests that much of the noise in CryoSat-2 freeboard measurements is random, in agreement with previous airborne and CryoSat-2 comparisons performed using monthly-average gridded data. Our work also suggests that CryoSat-2 freeboard data may be indicative of modal freeboard, the thermodynamically-grown ice within a footprint, rather than the mean freeboard which is biased by deformation processes. Furthermore, our results reiterate the importance of accurate snow and ice property information for the conversion of freeboard into thickness and volume.

Since 2010, ESA's CryoVEx and NASA's Operation IceBridge have shown that collaborative, coincident multi-mission campaigns are possible and extremely beneficial to validation and calibration efforts and datasets such as the dataset presented here. This dataset will become publicly available in the near future and can serve as a template to other calibration and validation missions and for additional sea ice and CryoSat studies.

9.5. Acknowledgements

The data and results presented in this paper are the result of the careful coordinated effort of teams from ESA, NASA, the Alfred Wegener Institute for Polar and Marine Science, DTU Space, the Norwegian Polar Institute, the University of Alberta, York University, the University of College London and the Mullard Space Sciences Laboratory and the other personnel that make up the NASA Operation IceBridge, ESA CryoVEx and CryoVal teams. The authors are thankful to the aforementioned Institutions and personnel as well as to the crews of the numerous aircraft (DTU/Norland Air Twin Otter, AWI Polar 5, NASA OIB P3, and Kenn Borek Twin Otter and DC3),

research and military stations, (Station Nord, Canadian Forces Station Alert, USAB Thule), and research vessels (RV Lance and RV Polarstern).

9.6. References

- Alexandrov, V., Sandven, S., Wahlin, J. & Johannessen, O. M. (2010), 'The relation between sea ice thickness and freeboard in the Arctic', *The Cryosphere*, **4 (3)**, 373 – 380, doi: 10.5194/tc-4-373-2010.
- Ferraro, E. J. & Swift, C. T. (1995), 'Comparison of retracking algorithms using airborne radar and laser altimeter measurements of the Greenland ice sheet', *IEEE Transactions on Geoscience and Remote Sensing*, **33 (3)**, 700 – 707, doi: 10.1109/36.387585.
- Forsberg, R. & Skourup H. (2005). 'Arctic Ocean Gravity, Geoid and Sea-ice Freeboard Heights from ICESat and GRACE'. *Geophysical Research Letters*, **32**, L21502, doi: 10.1029/2005GL023711.
- Forsström, S., Gerland, S. & Pedersen, C. A. (2011), 'Thickness and density of snow-covered sea ice and hydrostatic equilibrium assumption from in situ measurements in Fram Strait, the Barents Sea and the Svalbard coast', *Annals of Glaciology*, **52 (57)**, 261 – 270, doi: 10.3189/172756411795931598.
- Giles, K. A., Laxon, S. W. & Ridout, A. L. (2008), 'Circumpolar thinning of Arctic sea ice following the 2007 record ice extent minimum', *Geophysical Research Letters*, **35 (22)**, L22502, doi: 10.1029/2008GL035710.
- Haas, C. (2002), Validation of CryoSat sea-ice products: instruments and methods, in 'IGARRS 2002. 2002 *IEEE International Geoscience and Remote Sensing Symposium*', **3**, 1753 – 1755, doi: 10.1109/IGARSS.2002.1026243.
- Haas, C. (2003), Dynamics versus Thermodynamics: The Sea Ice Thickness Distribution, in D. N. Thomas & G. S. Dieckmann, eds, 'Sea Ice: An Introduction to its Physics, Chemistry, Biology and Geology', Blackwell Scientific.
- Haas, C., Hendricks, S., Eicken, H. & Herber, A. (2010), 'Synoptic airborne thickness surveys reveal state of Arctic sea ice cover', *Geophysical Research Letters*, **37 (9)**, L09501, doi: 10.1029/2010GL042652.

- Haas, C., Jochmann, P., Loset, S., Bonnemaire, B., Bjerkas, M. & Hamburg Ship Model Basin, F. R. o. G. (2003), Continuous EM and ULS thickness profiling in support of ice force measurements., in S. Loeset, B. Bonnemaire & M. Bjerkas, eds, 'Proceedings of the 17th International Conference on Port and Ocean Engineering under Arctic Conditions', pp. 849 – 856.
- Haas, C., Lobach, J., Hendricks, S., Rabenstein, L. & Pfaffling, A. (2009), 'Helicopter-borne measurements of sea ice thickness, using a small and lightweight, digital EM system', *Journal of Applied Geophysics*, **67 (3)**, 234 – 241, doi: 10.1016/j.jappgeo.2008.05.005.
- Hendricks, S., Ricker, R. & Helm, V. (2015), 'AWI CryoSat-2 Sea Ice Thickness Data Product (v1.1)', Alfred Wegener Institute for Polar and Marine Research. http://data.seaiceportal.de/data/cryosat2/doc/AWI_CryoSat2_Documentation_current
- Hvidegaard, H. & Forsberg, R. (2002), 'Sea-ice thickness from airborne laser altimetry over the Arctic Ocean North of Greenland', *Geophysical Research Letters*, **29 (20)**, 1952, doi: 10.1029/2001GL014474.
- King, J., Howell, S., Derksen, C., Rutter, N., Toose, P., Beckers, J. F., Haas, C., Kurtz, N., and Richter-Menge, J. (2015), 'Evaluation of Operation IceBridge quick-look snow depth estimates on sea ice', *Geophysical Research Letters*, **42**, 9302–9310, doi: 10.1002/2015GL066389.
- Koenig, L., Martin, S., Studinger, M. & Sonntag, J. (2010), 'Polar Airborne Observations Fill Gap in Satellite Data', *Eos, Transactions American Geophysical Union*, **91 (38)**, 333 – 334, doi: 10.1029/2010EO380002.
- Krabill, WB, Abdalati W, Frederick EB, Manizade SS, Martin CF, Sonntag JG, Swift RN, Thomas RH and Yungel JG (2002). 'Aircraft laser altimetry measurement of elevation changes of the Greenland ice sheet: Technique and accuracy assessment'. *Journal of Geodynamics*, **34 (3/4)**, 357–376, doi: 10.1016/S0264-3707(02)00040-6.
- Kurtz, N. (2015), 'Icebridge quick look sea ice freeboard, snow depth, and thickness product manual for 2014', National Snow and Ice Data Center. ftp://n5eil01u.ecs.nsidc.org/SAN2/ICEBRIDGE_FTP/

Evaluation_Products/IceBridge_Sea_Ice_Freeboard_SnowDepth_and_Thickness_QuickLook/Documentation/icebridge_ql_products_2014.pdf

- Kurtz, N., Studinger, M. S., Harbeck, J., Onana, V. & Yi, D. (2015), 'IceBridgeL4 Sea Ice Freeboard, Snow Depth, and Thickness', Version 1, Technical report, National Snow and Ice Data Center, doi: 10.5067/G519SHCKWQV6.
- Kurtz, N. T., Farrell, S. L., Studinger, M., Galin, N., Harbeck, J. P., Lindsay, R., Onana, V. D., Panzer, B. & Sonntag, J. G. (2013), 'Sea ice thickness, freeboard, and snow depth products from Operation IceBridge airborne data', *The Cryosphere*, **7 (4)**, 1035 – 1056, doi: 10.5194/tc-7-1035-2013.
- Kurtz, N. T., Galin, N. & Studinger, M. (2014), 'An improved CryoSat-2 sea ice freeboard retrieval algorithm through the use of waveform fitting', *The Cryosphere*, **8 (4)**, 1217 – 1237, doi: 10.5194/tc-8-1217-2014.
- Kwok, R. (2014), 'Simulated effects of a snow layer on retrieval of CryoSat-2 sea ice freeboard', *Geophysical Research Letters*, **41 (14)**, 5014 – 5020, doi: 10.1002/2014GL060993.
- Kwok, R. & Cunningham, G. F. (2008), 'Icesat over Arctic sea ice: Estimation of snow depth and ice thickness', *Journal of Geophysical Research: Oceans*, **113 (C8)**, C08010, doi: 10.1029/2008JC004753.
- Kwok, R. & Cunningham, G. F. (2015), 'Variability of Arctic sea ice thickness and volume from CryoSat-2', *Philosophical Transactions of the Royal Society of London A: Mathematical, Physical and Engineering Sciences*, **373 (2045)**, doi: 10.1098/rsta.2014.0157.
- Kwok, R. & Haas, C. (2015), 'Effects of radar side-lobes on snow depth retrievals from Operation IceBridge', *Journal of Glaciology*, **61 (227)**, doi: 10.3189/2015JoG14J229.
- Kwok, R., Kurtz, N.T., Brucker, L., Ivanoff, I., Newman, T., Farrell, S. L., King, J., Howell, S., Webster, M. A., Paden, J., Leuschen, C., Macgregor, J. A., Richter-Menge, J., Harbeck, J., and Tschudi, M. Inter- comparison of snow depth retrievals over Arctic sea ice from radar data acquired by Operation IceBridge. *The Cryosphere Discussions*, 2017:1–37, 2017.
- Laxon, S. W., Giles, K. A., Ridout, A. L., Wingham, D. J., Willatt, R., Cullen, R., Kwok, R., Schweiger, A., Zhang, J., Haas, C., Hendricks, S., Krisheld, R., Kurtz, N., Farrell, S. & Davidson, M. (2013),

- `CryoSat-2 estimates of Arctic sea ice thickness and volume', *Geophysical Research Letters*, **40 (4)**, 732 – 737, doi: 10.1002/grl.50193.
- Long, D. G., M. R. Drinkwater, B. Holt, S. Saatchi, and C. Bertoia (2001), 'Global ice and land climate studies using scatterometer image data', *Eos, Transactions American Geophysical Union*, **82(43)**, 503 – 503, doi: 10.1029/01EO00303.
- Mavrocordatos, C., Attema, E., Davidson, M., Lentz, H. & Nixdorf, U. (2004), Development of ASIRAS (Airborne SAR/Interferometric Altimeter System), in 'IGARSS 2004. 2004 IEEE International Geoscience and Remote Sensing Symposium', **4**, 2465 – 2467, doi: 10.1109/IGARSS.2004.1369792.
- Meier, W. N., Hovelsrud, G. K., van Oort, B. E., Key, J. R., Kovacs, K. M., Michel, C., Haas, C., Granskog, M. A., Gerland, S., Perovich, D. K., Makshtas, A. & Reist, J. D. (2014), 'Arctic sea ice in transformation: A review of recent observed changes and impacts on biology and human activity', *Reviews of Geophysics*, **52 (3)**, 185 – 217, doi: 10.1002/2013RG000431.
- Peacock, N. R. & Laxon, S. W. (2004), 'Sea surface height determination in the Arctic Ocean from ERS altimetry', *Journal of Geophysical Research: Oceans*, **109 (C7)**, C07001, doi: 10.1029/2001JC001026.
- Willatt R., Laxon, S. W., Giles, K., Cullen, R., Haas, C. & Helm, V. (2011), 'Ku-band radar penetration into snow cover on Arctic sea ice using airborne data', *Annals of Glaciology*, **52 (57)**, 197 – 205, doi: 10.3189/172756411795931589.
- Ricker, R., Hendricks, S., Helm, V., Skourup, H. & Davidson, M. (2014), 'Sensitivity of CryoSat-2 Arctic sea-ice freeboard and thickness on radar-waveform interpretation', *The Cryosphere*, **8 (4)**, 1607 – 1622, doi: 10.5194/tc-8-1607-2014.
- Ricker, R., Hendricks, S., Perovich, D. K., Helm, V. & Gerdes, R. (2015), 'Impact of snow accumulation on CryoSat-2 range retrievals over Arctic sea ice: An observational approach with buoy data', *Geophysical Research Letters*, 2015GL064081, doi: 10.1002/2015GL064081.
- Ricker, R.; Hendricks, S.; Beckers, J.F. (2016), 'The Impact of Geophysical Corrections on Sea-Ice Freeboard Retrieved from Satellite Altimetry'. *Remote Sensing*, **8**, 317, doi: 10.3390/rs8040317.

- Skourup, H., Farrell, S., Hendricks, S., Ricker, R., Armitage, T. W. K., Ridout, A., Andersen, O. B., Haas, C., Baker, S. (2017). An assessment of state-of-the-art mean sea surface and geoid models of the Arctic Ocean: Implications for sea ice freeboard retrieval. *Journal of Geophysical Research: Oceans*, **122**, 8593 – 8613, doi: 10.1002/2017JC013176
- Tilling, R. L., Ridout, A., Shepherd, A. & Wingham, D. J. (2015), 'Increased Arctic sea ice volume after anomalously low melting in 2013', *Nature Geoscience*, **8 (8)**, 643 – 646, doi: 10.1038/ngeo2489.
- Warren, S.G., Rigor, I. G., Untersteiner, N., Radionov, V. F., Bryazgin, N. N. & Aleksandrov, Y. I. (1999), 'Snow depth on arctic sea ice'. *Journal of Climate*, **12**, 1814 – 1829, doi: 10.1175/1520-0442.
- Wernecke, A. and Kaleschke, L. (2015), 'Lead detection in Arctic sea ice from CryoSat-2: quality assessment, lead area fraction and width distribution', *The Cryosphere*, **9**, 1955 - 1968, doi: 10.5194/tc-9-1955-2015.
- Wingham, D., Rapley, C., and Griffiths, H. (1986), New techniques in satellite altimeter tracking systems, in: 'ESA Proceedings of the 1986 International Geoscience and Remote Sensing Symposium (IGARSS '86) on Remote Sensing: Today's Solutions for Tomorrow's Information Needs', 8–11 September 1986, Zurich, Switzerland, 3, 1339–1344.
- Wingham, D., Francis, C., Baker, S., Bouzinac, C., Brockley, D., Cullen, R., de Chateau-Thierry, P., Laxon, S., Mallow, U., Mavrocordatos, C., Phalippou, L., Ratier, G., Rey, L., Rostan, F., Vial, P. & Wallis, D. (2006), 'CryoSat: A mission to determine the fluctuations in Earth's land and marine ice fields', *Advances in Space Research*, **37 (4)**, 841 – 871, doi: 10.1016/j.asr.2005.07.027.
- Wingham, D. J., Forsberg, R., Laxon, S. W., Lemke, P., Miller, H., Raney, K., Sandven, S., Scharoo, R., Vincent, P. & Rebhan, H. (2001), 'CryoSat Calibration and Validation Concept', CS-PL-UCL-SY-0004, E.S.A. and C.P.O.M.,
http://esamultimedia.esa.int/docs/Cryosat/CVC_14Nov01.pdf

9.7. Appendix: Overview of Golden Days

Summary of all coincident measurements used in this study, with CryoSat orbit numbers, acquisition date, region, and airborne measurements. N is the number of coincident, valid fb and AWI freeboard measurements. dT is the mean time difference between CryoSat overpass and airborne data acquisition in seconds (CryoSat-airborne). Empty cells indicate that no coincident measurements are available.

Orbit	Date	Region	OIB		ALS		ASIRAS		AEM	
			N	dT	N	dT	N	dT	N	dT
4759	2011/3/2	BalticSea							34	-2409
4979	2011/3/17	LincolnSea	1962	2713						
5266	2011/4/6	Svalbard							20	-998
5309	2011/4/9	Svalbard							5	-210
5399	2011/4/15	LincolnSea	0	-839	543	-6177	671	-6924	434	-6249
5428	2011/4/17	LincolnSea			793	-2703	459	-4057	488	-3189
5599	2011/4/29	Svalbard					7	-101488	0	-34162
5694	2011/5/5	Svalbard							34	-4965
10262	2012/3/15	BeaufortSea		-24852						
10263	2012/3/15	BeaufortSea	1817	-4424						
10291	2012/3/17	BeaufortSea	0	-22821						
10292	2012/3/17	BeaufortSea	497	-4549						
10346	2012/3/21	LincolnSea	1625	-5794						
10421	2012/3/26	LincolnSea	373	4082						
10450	2012/3/28	LincolnSea	1332	3032						
10462	2012/3/29	LincolnSea	1021	-4535	1343	-14681	1154	-7232		
10520	2012/4/2	LincolnSea	1508	-5618	1179	-6761	707	-5781		
10540	2012/4/3	LincolnSea			1064	17366	561	16840	184	20176
10555	2012/4/4	LincolnSea			872	15317	799	15110	653	15480
10565	2012/4/5	LincolnSea			1128	-16464	1053	-16353	731	-15682
10885	2012/4/27	LincolnSea								-15682
10915	2012/4/29	FramStrait			491	-2278	422	-2304		
15632	2013/3/20	LincolnSea	267	7031						
16139	2013/4/24	LincolnSea	1442	-1463						
20884	2014/3/18	BeaufortSea							280	-184756
20913	2014/3/19	BeaufortSea							237	-16208
20921	2014/3/20	Svalbard							27	-20321
20929	2014/3/20	Svalbard								8489
20942	2014/3/21	BeaufortSea	0	14333	715	-4737	268	-3048	389	-3844
21011	2014/3/26	LincolnSea	916	-14204	800	-24346	369	-24804	236	-22869
21021	2014/3/27	LincolnSea	11	40573	863	30444	16	32225	822	-30916
21067	2014/3/30	FramStrait			1152	-29398	598	-29485		
21081	2014/3/31	FramStrait			550	-48047	420	-47952	273	-48068
21082	2014/3/31	FramStrait	587	-30815						
21090	2014/3/31	FramStrait			603	325	422	498	241	441
21092	2014/3/31	LincolnSea	1247	25648						
Total			15923		12096		7926		5088	

10. Summary and Conclusions

10.1. Summary

The objectives of this research were to 1) advance our knowledge of sea and lake ice and its snow cover and 2) to examine CryoSat-2 data over these surfaces to assess their accuracy and develop novel retrievals of snow and ice properties. This thesis addresses these objectives by presenting two new algorithms, one primarily for the retrieval of sea ice freeboard or surface roughness using airborne laser scanners, and another for lake ice thickness retrievals using CryoSat-2 data. Furthermore, three separate studies into the accuracy of CryoSat-2 data and their application to sea ice were presented. Two of these studies examined regions with different snow conditions, i.e. Arctic and Antarctic, and the influence of these snow properties on the CryoSat-2 waveforms and freeboard results.

Chapter 5 presented a simple way to rapidly process raw laser scanner data from height measurements into relative surface elevation without using inertial navigation data or GPS data which add additional complexity and additional surveying and processing requirements, including significant post-processing; the method detailed in Chapter 5 could be implemented in near-real time. The theoretical flat surface hyperbola is fit to the laser scanner range measurements to estimate sensor roll and to retrieve surface elevation by removing the flat surface response. Iterations of the fitting procedure were performed to reference the theoretical response to the level flat ice, rather than the high points of the surface. Chapter 5 compared surface roughness of sea ice from different regimes, iceberg-fast MYI, MYI and FYI being exported out of Fram Strait, and predominantly FYI north of Svalbard as a case study. Surface roughness and the percentage of deformed ice were observed to be greatest over iceberg-fast MYI (0.21 m and 3.4%), followed by drift ice in Fram Strait (0.16 m and 0.46% and Svalbard (0.09 m and 0.23%). Comparisons between the laser scanner roughness and altimeter based roughness also highlighted benefits of across-track information for detecting ridges and cracks, for detecting ice within an AEM footprints and examining spatial patterns in roughness and its statistical distribution. The method presented in Chapter 5 allows for the retrieval of surface roughness, freeboard and other surface parameters which are of wider research interest for e.g. atmospheric drag of sea ice and deformation studies and for validation data.

In Chapter 6 we presented the first retrievals of lake ice thickness using satellite radar altimetry. In a method similar to ground penetrating radar sounding of freshwater ice, the top and bottom surfaces are identified by peaks in time-resolved backscatter waveforms and adjusted for the propagation velocity within the ice. The method was tested over Great Slave and Great Bear lakes in northern Canada using a combination of in-situ data and modelled ice thickness for validation. Between 2010 and spring of 2014, CryoSat-2 retrieved ice thickness closely matched the seasonal evolution of ice thickness from drill-hole data and modelled using Freezing Degree Days with correlations between the satellite and validation data always higher than 0.67 and usually greater than 0.8. The minimum detectable thickness ($\sim 0.26\text{m}$) is limited by the method as it requires two unique peaks in the CryoSat-2 backscatter waveforms; the peaks must be separated by a trough. The maximum detectable thickness depends on the maximum penetration depth of the radar signal; the maximum ice thickness on the lake was around 1.7m during the study period, below the theoretical penetration limit for CryoSat-2. Results showed that the method is sensitive to the roughness of both the ice top and bottom surfaces, to bubble content, and likely to variations in snow properties such as depth and grain size or layering; further investigation is required to determine the dominant property influencing accuracy of the thickness retrievals and to provide more validation data as these remain scarce.

Moving away from algorithm development and into investigations of CryoSat-2 data quality and accuracy, Chapter 7 presented some early investigations of CryoSat-2 data over sea ice. The first versions of the CryoSat-2 data were shown to have errors that required significant reprocessing, effectively rendering the L2, scientific end user product of little value (at the time). One specific issue, investigated and highlighted in Chapter 7 related to the retracking of CryoSat-2 radar waveforms over sea ice, was that the retracker was being applied to the most powerful peak in a waveform, even if this peak was arising from off-nadir leads, a process known as snagging. Chapter 7 showed that simply retracking the first peak above a certain threshold vastly improved the surface height results and eliminated most cases of snagging. Furthermore, Chapter 7 provided a comparison between Operation Ice Bridge snow freeboard, AEM measurements of ice thickness and CryoSat-2 freeboard and thickness retrievals from AWI. It was shown that while the meridional gradients in thickness were very similar, AEM thicknesses were

generally higher. Thickness comparisons are complicated by the influence that estimating snow, ice and water density as well as snow depth has on converting CryoSat-2 freeboard retrievals to thickness. Furthermore, the AEM sensor measures the total snow plus ice thickness. Comparisons between OIB and CryoSat-2 for a single orbit north of the Canadian Arctic Archipelago on March 26, 2012 showed that the modal OIB laser and CryoSat-2 radar freeboards were the same, 0.55m. As the OIB laser measures snow freeboard and CryoSat-2 is assumed to measure the ice freeboard, these results indicated that snow penetration was limited or that retracking thresholds of the CryoSat-2 data were retracking closer to the air/snow interface, rather than the snow/ice interface as often assumed. Similar observations had been made previously using ground based and airborne radar altimeters by Hendricks et al. (2010) and Willatt et al. (2010, 2011).

Arising from fieldwork conducted in McMurdo Sound in 2011, Chapter 8 presented an investigation of CryoSat-2 over Antarctic landfast sea ice and the influence of snow on retracking of CryoSat-2 waveforms. The paper presents what we believe to be the first retrievals of sea ice freeboard in Antarctica using CryoSat-2 but more importantly illustrates the influence of scattering from within the snowpack volume on retracking using three published retrackers/CryoSat-2 freeboard products. Regions of thin and thick snow and varying surface roughness were compared and shown to bias the freeboard retrievals up to 0.14 m by affecting the slope of the leading edge, i.e. reducing the slope in deep snow/rough areas. The paper also highlights the critical role of an accurate sea surface height retrieval which can be challenging when and where large areas of wind-roughened open water are found as waveforms from these areas are very different in appearance to small leads in the ice. Although conducted on fast-ice within McMurdo Sound, the methods and results presented in Chapter 8 should prove informative for sea ice retrievals in other parts of the Southern Ocean and seas around Antarctica using CryoSat-2.

Finally, Chapter 9 presented an analysis of all coincident airborne and CryoSat-2 validation data collected between 2010 and 2014 by NASA OIB, by AEM sensors from the University of Alberta, York University, AWI and NPI, and the ASIRAS data collected by ESA/DTU. The project examined CryoSat-2 freeboard provided in the newest version of the ESA CryoSat-2 dataset and the

freeboard and thickness calculated by AWI. While previous studies have made use of some of the airborne data for validation purposes, they had also done so by averaging over large (>25km by 25km) grid cells. The results presented in Chapter 9 examined CryoSat-2 and airborne data at the scale and resolution of individual CryoSat-2 footprints and using along-track averages. As one might expect from radar speckle noise, footprint-scale comparisons with airborne data showed very low correlations ($r < 0.3$) and significant scatter. With increasing along track averaging from 3 km to 50 km, the correlations improved significantly (up to $r = 0.6$). Interestingly, the RMSEs decreased slightly with increasing averaging distance but the mean differences stayed essentially the same. Modal airborne freeboards within a CryoSat-2 footprint were shown to be more strongly correlated with CryoSat-2 freeboard than the mean of the airborne data, possibly indicating that CryoSat-2 is more sensitive to the modal, level ice than the mean ice thickness which is skewed high by deformation. The results of Chapter 9 also reaffirm the importance of carefully managing uncertainty sources during freeboard processing, the importance of leads, mean sea surface retrieval and waveform classification as discussed in Chapter 3.

This thesis aimed to answer three questions; first, can new insight into the properties of snow depth, ice thickness and surface roughness be achieved with additional ground, satellite and airborne altimetry measurements? The results chapters of this thesis and the collaborative works listed in Appendix A and briefly discussed in Chapter 4, and the data sets collected for these publications, have provided new measurements of snow and ice properties including snow depth, ice thickness and surface roughness and have provided algorithms to collect such data using readily available sensors and datasets.

The second question that this thesis aimed to address was: Can Cryosat-2 provide measurements of lake ice thickness? Chapter 6 provides the first retrievals of lake ice thickness using a radar altimeter validated against limited in-situ measurements. The results presented in Chapter 6 show that there are likely improvements to be made but that drastic improvements to our understanding of lake ice thickness and changes to it can be measured using SAR altimeters like CryoSat-2.

The final question addressed by this thesis was: Are CryoSat-2 measurements of Arctic sea ice freeboard and thickness valid? Chapters 7, 8, and 9 examined CryoSat-2 measurements of

Arctic sea ice freeboard and thickness to assess their validity. Although Chapter 8 investigates Antarctic landfast ice, it showed that the seasonal evolution of CryoSat-2 freeboard matched ice thickness growth rates in the region. Furthermore, the differences in retracker performance over difference sea ice types and snow thickness regimes is applicable to the wider-Antarctic and Arctic sea ice pack. The results of Chapters 7 and 9 and other studies suggest that CryoSat-2 is able to reproduce the thickness gradient and distribution of large regions with sufficient spatial and temporal averaging, 10s of kilometers and/or monthly averages. However, the results of Chapter 7 and 9 also suggest that the amount of noise and uncertainty in individual CryoSat-2 freeboard observations can be as large or larger than the freeboard measurement.

10.2. Limitations

Regarding the study of CryoSat-2 over sea ice, the primary limitation of the work presented here is the lack of hard numbers on the uncertainty in CryoSat-2 freeboard and thickness results. This results from the spatial and temporal variability in the variables needed to compute freeboard and thickness and from the difficulty of collecting validation data. While the theoretical random uncertainty components have been assessed by two studies of CryoSat-2 freeboard and volume by Ricker et al. (2014) and Tilling et al. (2015), the uncertainties of some parameters are either assumed to be constant or negligible. Regional and temporal variability in properties such as water, ice, and snow density are not widely considered, nor is misclassification of surface or ice type considered. Biases due to errors in the sea surface height resulting from unresolved subsea features in the mean sea surface product also exist and are related to proper surface type classification and are also affected by the geophysical corrections applied to the data, for example ocean tide corrections (Ricker et al. 2016).

Another limitation of validating satellite measurements is the different spatial scale of measurement between airborne and satellite data, as well as temporal offsets between the two. As Chapter 9 discusses, collecting coincident airborne and satellite data is extremely difficult, even with dedicated efforts and campaigns. None of the measurement systems discussed in Chapters 7 – 9 cover the same spatial footprint as the CryoSat-2 data or travel at the same velocity, or cover complete orbits. Some airborne data, such as those collected by laser scanners, are capable of covering the complete spatial footprint at reduced spatial resolution or data

density and lower accuracy. Temporal offsets and the incomplete spatial coverage mean that it is difficult to assess the accuracy of CryoSat-2 data as features outside the airborne swath will affect the satellite measurement. Temporal offsets between CryoSat-2 and the airborne sensors can also mean that different ice or leads are measured. The different spatial footprints between airborne and CryoSat-2 data make assessing other issues such as signal penetration difficult to assess.

Assessment of CryoSat-2 signal penetration into the snow is still lacking clarity. Different retracers show different sensitivities to the width of the leading edge of the waveform. Furthermore, in some CryoSat-2 freeboard products, different retracers are applied to different surfaces, e.g. to ice and leads. Furthermore, penetration appears to be temporally and spatially variable and dependent on the microstructure of the snow and the seasonal evolution of the snow pack including wind redistribution, early fall/winter melt events and more. Chapter 8 and 9 assessed multiple retracers and different snow conditions in Antarctica and the Arctic, but separating out the influence of snow from other factors remains a challenge, especially as snow information from airborne platforms remains of limited accuracy and are limited to just measurements of snow depth, not density or grain size.

The limitations of the study of CryoSat-2 for lake ice thickness retrievals are mainly the scarcity of in-situ validation data and the application of the method to just two large lakes. The lack of data means that strong conclusions about the uncertainty of the method could not be made and it was not possible to rigorously assess the influence of snow on the ice thickness retrieval. Additional validation efforts over multiple lakes, using airborne grid surveys or on-ice autonomous systems and ground-penetrating-radar surveys, and using thermodynamic models such as the Canadian Lake Ice Model (CLiMo) are needed to provide a thorough assessment of the uncertainty in lake ice thickness retrievals from CryoSat-2.

10.3. Future Work

While pan-Arctic estimates of freeboard and thickness are useful for climatological studies of sea ice and energy balances, model validation, and computation of Arctic sea ice volume change, regional solutions will likely offer the most accurate freeboard/thickness retrievals for use in short-term seasonal forecasts, hazard assessment and estimates of freeboard, volume or energy

distribution changes. Regional studies may be able to utilize other geophysical parameters such as tide models or sea surface height models that are not pan-Arctic. While the results between regions may not be comparable, changes within a region will be relevant and may be more accurate.

Due to the importance of leads in the processing of CryoSat-2 freeboard and thickness, a detailed analysis of CryoSat-2 lead detections should be performed. The analysis should consider different lead detection algorithms and flags and compare available airborne and satellite data including airborne laser and radar altimeter data, airborne images, and satellite optical and radar imagery. This work has been begun as part of the CryoVal-SI project but requires very large amounts of data over multiple regions in order to provide meaningful conclusions. Several studies of lead detections have shown that the choice of waveform parameters to separate ice from leads and open water and to reduce or minimize across-track snagging provides critically different results (Zygmuntowska et al. 2013, Ricker et al. 2014). In addition to lead detection analysis, a comparison of ice and surface type classification from CryoSat-2 waveform parameters and the OSI-SAF ice type product using the satellite optical and radar imagery and airborne imagery and data is urgently needed to assess the accuracy of CryoSat-1 ice type classification from OSI-SAF as it pertains to the snow depth and ice density applied to CryoSat-2 freeboard retrievals in order for the calculation of ice thickness and volume.

Additional work from the CryoVal-SI project discussed in Chapter 9 is coming out over the next months. These studies, along the CryoVal-SI dataset will provide additional insight into CryoSat-2 lead detection, the effect of different retrackers and penetration, the influence of different mean sea surface height models, the role of surface roughness and more. These types of analysis will lead to improved CryoSat-2 freeboard products (regional or pan-Arctic) and ultimately more accurate thickness and volume estimates and a better understanding of changes in the Arctic Ocean's ice cover. Furthermore, as SAR altimetry is already being implemented for current and future radar altimeters, progress made using CryoSat-2 will benefit future missions e.g. Sentinel 3 and 6, the IceSat-2 laser altimeter, and ultimately the multi-mission time series needed for climate studies.

Future work with the CryoVal-SI database should include a detailed analysis of all of the airborne data collected. Thousands of kilometers of airborne laser scanner and airborne radar altimeter data are available through the database and may lead to new insight into radar penetration through comparisons between the two, lead detections from each sensor type, surface roughness and other associated parameters. Data from the airborne CryoSat-2 simulator, ASIRAS, is especially under-utilized.

Finally, additional examinations of lake ice thickness using radar altimeters should be expanded through several avenues of research to improve the accuracy at the beginning and end of the ice season, and to increase the spatial coverage and temporal resolution. As lake ice is used for travel and recreational use, providing ice thickness results in a routine manner would require additional information such as on-ice measurements from autonomous stations, and additional validation efforts and algorithm improvements to ensure highly accurate information throughout the ice season in order to keep users safe. These additional examinations should include: studying additional lakes and additional sensors including altimeters such as AltiKa and Sentinel-3 and IceSat-2, NASA's next satellite laser altimeter. IceSat-2 data could provide information about snow depth when combined with the radar altimeter data and possibly provide information on surface roughness. A multi-sensor approach to improve the thickness results by utilizing the strengths of different sensors and a minimizing their weaknesses, such as the different sensitivities to thick and thin ice or snow, temporal resolution and spatial coverage should be attempted using e.g. MODIS (Kheyrollah Pour et al., 2017) and AMSR-E (Kang et al. 2010) and the altimeter data. Another avenue to explore in order to improve thickness retrievals is the relationship between maximum power in the altimeter waveform data and seasonal growth observed in Chapter 9 as it may provide for improved thickness retrievals, either as a way to filter out poor retrievals due to roughness, or to provide a blended algorithm.

This thesis has provided new measurements of sea ice, lake ice and snow and examined CryoSat-2 data over these surfaces using coincident airborne data. Our understanding of CryoSat-2 data; the role of snow, lead detections, and sea surface height on altimeter retrievals; and the importance of minimizing uncertainty and errors throughout the processing chain have greatly

improved through the work conducted in this thesis and through collaborative works I have contributed to throughout my PhD program.

References

- Aagaard, K. and Carmack, E. C. (1989). The role of sea ice and other fresh water in the Arctic circulation. *Journal of Geophysical Research: Oceans*, **94(C10)**, 14485-14498, doi: 10.1029/JC094iC10p14485.
- Abdalati, W., Zwally, H. J., Bindshadler, R., Csatho, B., Farrell, S. L., Fricker, H. A., Harding, D., Kwok, R., Lefsky, M., Markus, T., Marshak, A., Neumann, T., Palm, S., Schutz, B., Smith, B., Spinhirne, J., and Webb, C. (2010). The ICESat-2 Laser Altimetry Mission. *Proceedings of the IEEE*, **98(5)**, 735-751, doi: 10.1109/JPROC.2009.2034765.
- Aksenov, Y., Popova, E. E., Yool, A., Nurser, A. J. G., Williams, T. D., Bertino, L., and Bergh, J. (2017). On the future navigability of Arctic sea routes: High-resolution projections of the Arctic Ocean and sea ice. *Marine Policy*, **75**, 300-317, doi: 10.1016/j.marpol.2015.12.027.
- Alexandrov, V., Sandven, S., Wahlin, J., and Johannessen, O. M. (2010). The relation between sea ice thickness and freeboard in the Arctic. *The Cryosphere*, **4(3)**, 373-380, doi: 10.5194/tc-4-373-2010.
- Alexeev, V. A., Arp, C. D., Jones, B. M., and Cai, L. (2016). Arctic sea ice decline contributes to thinning lake ice trend in northern Alaska. *Environmental Research Letters*, **11(7)**, 074022, doi: 10.1088/1748-9326/11/7/074022.
- Armitage, T. W. K. and Ridout, A. L. (2015). Arctic sea ice freeboard from AltiKa and comparison with CryoSat-2 and Operation IceBridge. *Geophysical Research Letters*, **42(16)**, 6724-6731, doi: 10.1002/2015GL064823.
- Armitage, T. W. K. and Davidson, M. W. J. (2014). Using the interferometric capabilities of the ESA CryoSat-2 mission to improve the accuracy of sea ice freeboard retrievals. *IEEE Transactions on Geoscience and Remote Sensing*, **52(1)**, 529-536, doi: 10.1109/TGRS.2013.2242082.
- Arndt, S. and Nicolaus, M. (2014). Seasonal cycle and long-term trend of solar energy fluxes through Arctic sea ice. *The Cryosphere*, **8(6)**, 2219-2233, doi: 10.5194/tc-8-2219-2014.

- Arrigo, K. R., van Dijken, G. L., Castelao, R. M., Luo, H., Rennermalm, Å. K., Tedesco, M., Mote, T. L., Oliver, H., and Yager, P. L. (2017). Melting glaciers stimulate large summer phytoplankton blooms in southwest Greenland waters. *Geophysical Research Letters*, **44(12)**, 6278-6285, doi: 10.1002/2017GL073583.
- Arrigo, K. R., Perovich, D. K., Pickart, R. S., Brown, Z. W., van Dijken, G. L., Lowry, K. E., Mills, M. M., Palmer, M. A., Balch, W. M., Bahr, F., Bates, N. R., Benitez-Nelson, C., Bowler, B., Brownlee, E., Ehn, J. K., Frey, K. E., Garley, R., Laney, S. R., Lubelczyk, L., Mathis, J., Matsuoka, A., Mitchell, B. G., Moore, G. W. K., Ortega-Retuerta, E., Pal, S., Polashenski, C. M., Reynolds, R. A., Schieber, B., Sosik, H. M., Stephens, M., and Swift, J. H. (2012). Massive Phytoplankton Blooms Under Arctic Sea Ice. *Science*, **336(6087)**, 1408-1408, doi: 10.1126/science.1215065.
- Assmy, P., Fernandez-Mendez, M., Duarte, P., Meyer, A., Randelhoff, A., Mundy, C. J., Olsen, L. M., Kauko, H. M., Bailey, A., Chierici, M., Cohen, L., Doulgeris, A. P., Ehn, J. K., Fransson, A., Gerland, S., Hop, H., Hudson, S. R., Hughes, N., Itkin, P., Johnsen, G., King, J. A., Koch, B. P., Koenig, Z., Kwasniewski, S., Laney, S. R., Nicolaus, M., Pavlov, A. K., Polashenski, C. M., Provost, C., Rosel, A., Sandbu, M., Spreen, G., Smedsrud, L. H., Sundfjord, A., Taskjelle, T., Tatarek, A., Wiktor, J., Wagner, P. M., Wold, A., Steen, H., and Granskog, M. A. (2017). Leads in Arctic pack ice enable early phytoplankton blooms below snow-covered sea ice. *Scientific Reports*, **7**, doi: 10.1038/srep40850.
- Atwood, D. K., Gunn, G. E., Roussi, C., Wu, J., Duguay, C., and Sarabandi, K. (2015). Microwave backscatter from Arctic lake ice and polarimetric implications. *IEEE Transactions on Geoscience and Remote Sensing*, **53(11)**, 5972-5982, doi: 10.1109/TGRS.2015.2429917.
- Barber, D. G., Reddan, S. P., and LeDrew, E. F. (1995). Statistical characterization of the geophysical and electrical properties of snow on Landfast first-year sea ice. *Journal of Geophysical Research: Oceans*, **100(C2)**, 2673-2686, doi: 10.1029/94JC02200.
- Beaven, S. G., Lockhart, G. L., Gogineni, S. P., Hossetnmostafa, A. R., Jezek, K., Gow, A. J., Perovich, D. K., Fung, A. K., and Tjuatja, S. (1995). Laboratory measurements of radar backscatter from bare and snow-covered saline ice sheets. *International Journal of Remote Sensing*, **16(5)**, 851-876, doi: 10.1080/01431169508954448.

- Beckers, J. F., Casey, J. A., and Haas, C. (2017). Retrievals of lake ice thickness from Great Slave and Great Bear Lakes using CryoSat-2. *IEEE Transactions on Geoscience and Remote Sensing*, **55(7)**, 3708-3720, doi: 10.1109/TGRS.2017.2677583.
- Beckers, J. F., Renner, A. H. H., Spreen, G., Gerland, S., and Haas, C. (2015). Sea-ice surface roughness estimates from airborne laser scanner and laser altimeter observations in Fram Strait and north of Svalbard. *Annals of Glaciology*, **56(69)**, 235-244, doi: 10.3189/2015AoG69A717.
- Bintanja, R., van Oldenborgh, G. J., Drijfhout, S. S., Wouters, B., and Katsman, C. A. (2013). Important role for ocean warming and increased ice-shelf melt in Antarctic sea-ice expansion. *Nature Geoscience*, **6(5)**, 376-379, doi: 10.1038/ngeo1767.
- Birkett, C. M. (1995). The contribution of TOPEX/POSEIDON to the global monitoring of climatically sensitive lakes. *Journal of Geophysical Research: Oceans*, **100(C12)**, 25179-25204, doi: 10.1029/95JC02125.
- Bokhorst, S., Pedersen, S. H., Brucker, L., Anisimov, O., Bjerke, J. W., Brown, R. D., Ehrich, D., Essery, R. L. H., Heilig, A., Ingvander, S., Johansson, C., Johansson, M., Jónsdóttir, I. S., Inga, N., Luojus, K., Macelloni, G., Mariash, H., McLennan, D., Rosqvist, G. N., Sato, A., Savela, H., Schneebeli, M., Sokolov, A., Sokratov, S. A., Terzago, S., Vikhamar-Schuler, D., Williamson, S., Qiu, Y., and Callaghan, T. V. (2016). Changing Arctic snow cover: A review of recent developments and assessment of future needs for observations, modelling, and impacts. *Ambio*, **45(5)**, 516-537, doi: 10.1007/s13280-016-0770-0.
- Bouzinac, C. (2013). Cryosat Product Handbook. European Space Agency.
- Brown, G. S. (1977). The average impulse response of a rough surface and its applications. *IEEE Transactions on Antennas and Propagation*, **25(1)**, 67-74, doi: 10.1109/TAP.1977.1141536.
- Brown, L. C. and Duguay, C. R. (2011). The fate of lake ice in the North American Arctic. *The Cryosphere*, **5(4)**, 869-892, doi: 10.5194/tc-5-869-2011.
- Brown, L. C. and Duguay, C. R. (2010). The response and role of ice cover in lake-climate interactions. *Progress in Physical Geography*, **34(5)**, 671-704, doi: 10.1177/0309133310375653.

- Brutel-Vuilmet, C., Menegoz, M., and Krinner, G. (2013). An analysis of present and future seasonal Northern Hemisphere land snow cover simulated by CMIP5 coupled climate models. *The Cryosphere*, **7(1)**, 67-80, doi: 10.5194/tc-7-67-2013.
- Budikova, D., Ford, T. W., and Ballinger, T. J. (2017). Connections between north-central United States summer hydroclimatology and Arctic sea ice variability. *International Journal of Climatology*, doi: 10.1002/joc.5097.
- Canada, E. (2014). Environment Canada Historical Climate Data Archive. Accessed at: http://climate.weather.gc.ca/index_e.html#access.
- Canada, E. (2013). Canadian Ice Thickness Program: Yellowknife, N. W. T. Accessed at: <http://www.ec.gc.ca/glaces-ice/default.asp?lang=En&n=E1B3129D-1>.
- Casey, J. A., Beckers, J., Busche, T., and Haas, C. (2014). Towards the retrieval of multi-year sea ice thickness and deformation state from polarimetric C- and X-band SAR observations. IEEE International Geoscience and Remote Sensing Symposium, IGARSS 2014, 1190-1193, doi: 10.1109/IGARSS.2014.6946644.
- Castro de la Guardia, L., Derocher, A. E., Myers, P. G., Terwisscha van Scheltinga, A. D., and Lunn, N. J. (2013). Future sea ice conditions in Western Hudson Bay and consequences for polar bears in the 21st century. *Global Change Biology*, **19(9)**, 2675-2687, doi: 10.1111/gcb.12272.
- Cavalieri, D. J. and Parkinson, C. L. (2012). Arctic sea ice variability and trends, 1979-2010. *The Cryosphere*, **6(4)**, 881-889, doi: 10.5194/tc-6-881-2012.
- Chase, J. R. and Holyer, R. J. (1990). Estimation of sea ice type and concentration by linear unmixing of Geosat altimeter waveforms. *Journal of Geophysical Research: Oceans*, **95(C10)**, 18015-18025, doi: 10.1029/JC095iC10p18015.
- Comiso, J. C. (2012). Large Decadal Decline of the Arctic Multiyear Ice Cover. *Journal of Climate*, **25(4)**, 1176-1193, doi: 10.1175/JCLI-D-11-00113.1.
- Comiso, J. C., Cavalieri, D. J., and Markus, T. (2003). Sea ice concentration, ice temperature, and snow depth using AMSR-E data. *IEEE Transactions on Geoscience and Remote Sensing*, **41(2)**, 243-252, doi: 10.1109/TGRS.2002.808317.

- Crétaux, J.-F. and Birkett, C. (2006). Lake studies from satellite radar altimetry. *Comptes Rendus Geoscience*, **338(14-15)**, 1098 - 1112, doi: 10.1016/j.crte.2006.08.002.
- Dempsey, D. E., Langhorne, P. J., Robinson, N. J., Williams, M. J. M., Haskell, T. G., and Frew, R. D. (2010). Observation and modeling of platelet ice fabric in McMurdo Sound, Antarctica. *Journal of Geophysical Research: Oceans*, **115(C1)**, doi: 10.1029/2008JC005264.
- Derksen, C., Brown, R., Mudryk, L., and Luoju, K. (2015). Arctic: Terrestrial Snow. In: Blunden, J. and Arndt, D. S. editor. *State of the Climate in 2014*, 33-135. Bulletin of the American Meteorological Society, doi: 10.1175/2015BAMSStateoftheClimate.1.
- Dierking, W. (1995). Laser profiling of the ice surface topography during the Winter Weddell Gyre Study 1992. *Journal of Geophysical Research: Oceans*, **100(C3)**, 4807-4820, doi: 10.1029/94JC01938.
- Doble, M. J., Skourup, H., Wadhams, P., and Geiger, C. A. (2011). The relation between Arctic sea ice surface elevation and draft: A case study using coincident AUV sonar and airborne scanning laser. *Journal of Geophysical Research: Oceans*, **116(C8)**, doi: 10.1029/2011JC007076.
- Drinkwater, M. R. (1991). Ku band airborne radar altimeter observations of marginal sea ice during the 1984 Marginal Ice Zone Experiment. *Journal of Geophysical Research: Oceans*, **96(C3)**, 4555-4572, doi: 10.1029/90JC01954.
- Drinkwater, M. R., Ratier, R. F. G., and Wingham, D. J. (2004). The European Space Agency's Earth Explorer Mission CryoSat: measuring variability in the cryosphere. *Annals of Glaciology*, **39**, 313-320, doi: 10.3189/172756404781814663.
- Du, J., Kimball, J. S., Duguay, C., Kim, Y., and Watts, J. D. (2017). Satellite microwave assessment of Northern Hemisphere lake ice phenology from 2002 to 2015. *The Cryosphere*, **11(1)**, 47-63, doi: 10.5194/tc-11-47-2017.
- Duguay, C. R., Bernier, M., Gauthier, Y., and Kouraev, A. V. (2015). Remote sensing of lake and river ice. In: Tedesco, M. editor. *Remote Sensing of the Cryosphere*, 273-306. John Wiley Sons, Ltd., doi: 10.1002/9781118368909.ch12.

- Duguay, C. R., Prowse, T. D., Bonsal, B. R., Brown, R. D., Lacroix, M. P., and Ménard, P. (2006). Recent trends in Canadian lake ice cover. *Hydrological Processes*, **20(4)**, 781-801, doi: 10.1002/hyp.6131.
- Duguay, C. R. and Lafleur, P. M. (2003). Determining depth and ice thickness of shallow sub-Arctic lakes using space-borne optical and SAR data. *International Journal of Remote Sensing*, **24(3)**, 475-489, doi: 10.1080/01431160304992.
- Duguay, C. R., Flato, G. M., Jeffries, M. O., Ménard, P., Morris, K., and Rouse, W. R. (2003). Ice-cover variability on shallow lakes at high latitudes: model simulations and observations. *Hydrological Processes*, **17(17)**, 3465-3483, doi: 10.1002/hyp.1394.
- Dwyer, R. E. and Godin, R. H. (1980). Determining sea-ice boundaries and ice roughness using GEOS-3 altimeter data. NASA-CR-156862, National Aeronautics and Space Administration.
- Egido, A. and Smith, W. H. F. (2017). Fully Focused SAR Altimetry: Theory and Applications. *IEEE Transactions on Geoscience and Remote Sensing*, **55(1)**, 392-406, doi: 10.1109/TGRS.2016.2607122.
- Eicken, H., Gradinger, R., Salganek, M., Shirasawa, K., Perovich, D., and Lepparanta, M. (2009). Field Techniques for Sea Ice Research. UA Press.
- Eicken, H., Grenfell, T. C., Perovich, D. K., Richter-Menge, J. A., and Frey, K. (2004). Hydraulic controls of summer Arctic pack ice albedo. *Journal of Geophysical Research: Oceans*, **109(C8)**, doi: 10.1029/2003JC001989.
- Engram, M., Anthony, K. W., Meyer, F. J., and Grosse, G. (2013). Characterization of L-band synthetic aperture radar (SAR) backscatter from floating and grounded thermokarst lake ice in Arctic Alaska. *The Cryosphere*, **7(6)**, 1741-1752, doi: 10.5194/tc-7-1741-2013.
- Farrell, S., Brunt, K. M., Ruth, J. M., Kuhn, J. M., Connor, L. N., and Walsh, K. M. (2015). Sea-ice freeboard retrieval using digital photon-counting laser altimetry. *Annals of Glaciology*, **56(69)**, 167-174, doi: 10.3189/2015AoG69A686.
- Farrell, S. L., Kurtz, N., Connor, L. N., Elder, B. C., Leuschen, C., Markus, T., McAdoo, D. C., Panzer, B., Richter-Menge, J., and Sonntag, J. G. (2012). A First Assessment of IceBridge Snow and Ice Thickness Data Over Arctic Sea Ice. *IEEE Transactions on Geoscience and Remote Sensing*, **50(6)**, 2098-2111, doi: 10.1109/TGRS.2011.2170843.

- Fedotov, V. I., Cherepanov, N. V., and Tyshko, K. P. (2013). Some Features of the Growth, Structure and Metamorphism of East Antarctic Landfast Sea Ice. In. Jeffries, M. O. editor. *Antarctic Sea Ice: Physical Processes, Interactions and Variability*, 343-354. American Geophysical Union, doi: 10.1029/AR074p0343.
- Ferraro, E. J. and Swift, C. T. (1995). Comparison of retracking algorithms using airborne radar and laser altimeter measurements of the Greenland ice sheet. *IEEE Transactions on Geoscience and Remote Sensing*, **33(3)**, 700-707, doi: 10.1109/36.387585.
- Fletcher, C. G., Thackeray, C. W., and Burgers, T. M. (2015). Evaluating biases in simulated snow albedo feedback in two generations of climate models. *Journal of Geophysical Research: Atmospheres*, **120(1)**, 12-26, doi: 10.1002/2014JD022546.
- Fors, A. S., Brekke, C., Gerland, S., Doulgeris, A. P., and Beckers, J. F. (2016). Late Summer Arctic Sea Ice Surface Roughness Signatures in C-Band SAR Data. *IEEE Journal of Selected Topics in Applied Earth Observations and Remote Sensing*, **9(3)**, 1199-1215, doi: 10.1109/JSTARS.2015.2504384.
- Forsberg, R. and Skourup, H. (2005). Arctic Ocean Gravity, Geoid and Sea-ice Freeboard Heights from ICESat and GRACE. *Geophysical Research Letters*, **32(L21502)**, doi: 10.1029/2005GL023711.
- Forsberg, R., Keller, K., and Jacobsen, S. M. (2001). Laser monitoring of ice elevations and sea-ice thickness in Greenland. *International Archives of the Photogrammetry, Remote Sensing and Spatial Information Sciences*, **34(3-W4)**, 163-168.
- Forsström, S., Gerland, S., and Pedersen, C. A. (2011). Thickness and density of snow-covered sea ice and hydrostatic equilibrium assumption from in situ measurements in Fram Strait, the Barents Sea and the Svalbard coast. *Annals of Glaciology*, **52(57)**, 261-270, doi: 10.3189/172756411795931598.
- Francis, J. and Skific, N. (2015). Evidence linking rapid Arctic warming to mid-latitude weather patterns. *Philosophical Transactions of the Royal Society of London A: Mathematical, Physical and Engineering Sciences*, **373(2045)**, doi: 10.1098/rsta.2014.0170.

- Fraser, A. D., Massom, R. A., Michael, K. J., Galton-Fenzi, B. K., and Lieser, J. L. (2012). East Antarctic Landfast Sea Ice Distribution and Variability, 2000-08. *Journal of Climate*, **25(4)**, 1137-1156, doi: 10.1175/JCLI-D-10-05032.1.
- Gerland, S., Renner, A. H. H., Spreen, G., Wang, C., Beckers, J. F., Dumont, M., Granskog, M. A., Haapala, J., Haas, C., Helm, V., Hudson, S. R., Lensu, M., Ricker, R., Sandven, S., Skourup, H., and Zygmuntowska, M. (2013). In-situ calibration and validation of Cryosat-2 observations over Arctic sea ice north of Svalbard. Proceedings of the CryoSat Third User Workshop CryoSat Third User Workshop, ESA SP-717, ESA.
- Gerland, S., Brandt, O., Hansen, E., Renner, A. H. H., Granskog, M. A., Forsström, S., Eltoft, T., Schwenke, F. A., Moen, M. A., Doulgeris, A. P., Haas, C., Beckers, J. F., and Hughes, N. (2011). Satellite calibration and validation experiments over Arctic sea ice in the vicinity of Svalbard. Proceedings of the CryoSat Second User Workshop/Validation Workshop, ESA SP-693, ESA.
- Giles, K. A., Laxon, S. W., and Ridout, A. L. (2008). Circumpolar thinning of Arctic sea ice following the 2007 record ice extent minimum. *Geophysical Research Letters*, **35(22)**, doi: 10.1029/2008GL035710.
- Giles, K. A., Laxon, S. W., Wingham, D. J., Wallis, D. W., Krabill, W. B., Leuschen, C. J., McAdoo, D., Manizade, S. S., and Raney, R. K. (2007). Combined airborne laser and radar altimeter measurements over the Fram Strait in May 2002. *Remote Sensing of Environment*, **111(2-3)**, 182-194, doi: 10.1016/j.rse.2007.02.037.
- Girard, L., Weiss, J., Molines, J. M., Barnier, B., and Bouillon, S. (2009). Evaluation of high-resolution sea ice models on the basis of statistical and scaling properties of Arctic sea ice drift and deformation. *Journal of Geophysical Research: Oceans*, **114(C8)**, doi: 10.1029/2008JC005182.
- Gough, A., Mahoney, A., Langhorne, P., Williams, M., Robinson, N., and Haskell, T. (2012). Signatures of supercooling: McMurdo Sound platelet ice. *Journal of Glaciology*, **58**, 38-50, doi: 10.3189/2012JoG10J218.

- Gow, A. J., Ackley, S. F., Govoni, J. W., and Weeks, W. F. (2013). Physical and Structural Properties of Land-Fast Sea Ice in McMurdo Sound, Antarctica. In. Jeffries, M. O. editor. *Antarctic Sea Ice: Physical Processes, Interactions and Variability*, 355-374. American Geophysical Union, doi: 10.1029/AR074p0355.
- Guerreiro, K., Fleury, S., Zakharova, E., Remy, F., and Kouraev, A. (2016). Potential for estimation of snow depth on Arctic sea ice from CryoSat-2 and SARAL/AltiKa missions. *Remote Sensing of Environment*, **186**, 339 - 349, doi: 10.1016/j.rse.2016.07.013.
- Gunn, G. E. (2015). Re-evaluating Scattering Mechanisms in Snow-Covered Freshwater Lake Ice Containing Bubbles Using Polarimetric Ground-based and Spaceborne Radar Data. University of Waterloo.
- Gunn, G. E., Brogioni, M., Duguay, C., Macelloni, G., Kasurak, A., and King, J. (2015). Observation and modeling of X- and Ku-Band backscatter of snow-covered freshwater lake ice. *IEEE Journal of Selected Topics in Applied Earth Observations and Remote Sensing*, **8(7)**, 3629-3642, doi: 10.1109/JSTARS.2015.2420411.
- Gunn, G. E., Duguay, C. R., Brown, L. C., King, J., Atwood, D., and Kasurak, A. (2015). Freshwater lake ice thickness derived using surface-based X- and Ku-band FMCW scatterometers. *Cold Regions Science and Technology*, **120**, 115 - 126, doi: 10.1016/j.coldregions.2015.09.012.
- Haas, C. (2003). Dynamics versus Thermodynamics: The Sea Ice Thickness Distribution. In. Thomas, D. N. and Dieckmann, G. S. editor. *Sea Ice: An Introduction to its Physics, Chemistry, Biology and Geology*, Blackwell Scientific, doi: 10.1002/9780470757161.ch3.
- Haas, C. (2002). Validation of CryoSat sea-ice products: instruments and methods. IEEE International Geoscience and Remote Sensing Symposium, IGARSS 2002, 3, 1753-1755 vol.3. IEEE.
- Haas, C. and Beckers, J. F. (2017). Sea Ice and Lake Ice Thickness Observations with CryoSat. *CMOS BULLETIN*, **45(1)**, 11-15.
- Haas, C. and Beckers, J. F. (2014). CryoVEx 2014 Final Report. ESA contract 4000110552/14/MP/vb, York University.
- Haas, C., Beckers, J., and Casey, J. A. (2011). Airborne sea ice thickness and laser scanner observations in the Lincoln Sea. Unpublished.

- Haas, C., Hendricks, S., Eicken, H., and Herber, A. (2010). Synoptic airborne thickness surveys reveal state of Arctic sea ice cover. *Geophysical Research Letters*, **37(9)**, doi: 10.1029/2010GL042652.
- Haas, C., Lobach, J., Hendricks, S., Rabenstein, L., and Pfaffling, A. (2009). Helicopter-borne measurements of sea ice thickness, using a small and lightweight, digital EM system. *Journal of Applied Geophysics*, **67(3)**, 234 - 241, doi: 10.1016/j.jappgeo.2008.05.005.
- Haas, C., Pfaffling, A., Hendricks, S., Rabenstein, L., Etienne, J.-L., and Rigor, I. (2008). Reduced ice thickness in Arctic Transpolar Drift favors rapid ice retreat. *Geophysical Research Letters*, **35(17)**, doi: 10.1029/2008GL034457.
- Haas, C., Jochmann, P., Loset, S., Bonnemaire, B., Bjerkas, M., and Hamburg Ship Model Basin, F. R. o. G. (2003). Continuous EM and ULS thickness profiling in support of ice force measurements. In: Loeset, S., Bonnemaire, B., and Bjerkas, M. editor. *Proceedings of the 17th International Conference on Port and Ocean Engineering under Arctic Conditions*, 849 - 856. POAC.
- Hallikainen, M. and Winebrenner, D. P. (1992). The Physical Basis for Sea Ice Remote Sensing. In: Carsey, F. D. editor. *Microwave Remote Sensing of Sea Ice*, 29-46. American Geophysical Union, doi: 10.1029/GM068p0029.
- Hallikainen, M., Ulaby, F., and Abdelrazik, M. (1986). Dielectric properties of snow in the 3 to 37 GHz range. *IEEE Transactions on Antennas and Propagation*, **34(11)**, 1329-1340, doi: 10.1109/TAP.1986.1143757.
- Hamilton, S. G., Castro de la Guardia, L., Derocher, A. E., Sahanatien, V., Tremblay, B., and Huard, D. (2014). Projected Polar Bear Sea Ice Habitat in the Canadian Arctic Archipelago. *PLoS ONE*, **9(11)**, e113746, doi: 10.1371/journal.pone.0113746.
- Hansen, E., Gerland, S., Granskog, M. A., Pavlova, O., Renner, A. H. H., Haapala, J., Løyning, T. B., and Tschudi, M. (2013). Thinning of Arctic sea ice observed in Fram Strait: 1990-2011. *Journal of Geophysical Research: Oceans*, **118(10)**, 5202-5221, doi: 10.1002/jgrc.20393.
- Hatam, I., Lange, B., Beckers, J. F., Haas, C., and Lanoil, B. (2016). Bacterial communities from Arctic seasonal sea ice are more compositionally variable than those from multi-year sea ice. *ISME J*, **10**, 2543-2552, doi: 10.1038/ismej.2016.4.

- Hatam, I., Charchuk, R., Lange, B., Beckers, J., Haas, C., and Lanoil, B. (2014). Distinct bacterial assemblages reside at different depths in Arctic multiyear sea ice. *FEMS Microbiology Ecology*, **90(1)**, 115, doi: 10.1111/1574-6941.12377.
- Heine, A. J. (1963). Ice breakout around the Southern end of Ross Island, Antarctica. *New Zealand Journal of Geology and Geophysics*, **6(3)**, 395-401, doi: 10.1080/00288306.1963.10422071.
- Hellmer, H. H. (2004). Impact of Antarctic ice shelf basal melting on sea ice and deep ocean properties. *Geophysical Research Letters*, **31(10)**, doi: 10.1029/2004GL019506.
- Helm, V., Humbert, A., and Miller, H. (2014). Elevation and elevation change of Greenland and Antarctica derived from CryoSat-2. *The Cryosphere*, **8(4)**, 1539-1559, doi: 10.5194/tc-8-1539-2014.
- Hendricks, S., Ricker, R., and Helm, V. (2015). AWI CryoSat-2 Sea Ice Thickness Data Product (v1.1). Alfred Wegener Institute for Polar and Marine Research. Accessed online at: http://data.seaiceportal.de/data/cryosat2/doc/AWI_CryoSat2_Documentation_current
- Hendricks, S., Stenseng, L., Helm, V., and Haas, C. (2010). Effects of surface roughness on sea ice freeboard retrieval with an Airborne Ku-Band SAR radar altimeter. IEEE International Geoscience and Remote Sensing Symposium, IGARSS 2010, 3126-3129. IEEE.
- Hibler, W. D. (1972). Removal of aircraft altitude variation from laser profiles of the Arctic ice pack. *Journal of Geophysical Research*, **77(36)**, 7190-719, doi: 10.1029/JC077i036p07190.
- Hibler, W.D., I. and LeSchack, L. A. (1972). Power spectrum analysis of undersea and surface sea-ice profiles. *Journal of Glaciology*, **11(63)**, 345 – 356, doi: 10.1017/S0022143000022322.
- Hibler, W. D., I., Weeks, W. F., and Mock, S. J. (1972). Statistical Aspects of Sea-Ice Ridge Distributions. *Journal of Geophysical Research*, **77(30)**, 5954 – 5970, doi: 10.1029/JC077i030p05954.
- Holland, P. R., Bruneau, N., Enright, C., Losch, M., Kurtz, N. T., and Kwok, R. (2014). Modeled Trends in Antarctic Sea Ice Thickness. *Journal of Climate*, **27(10)**, 3784-3801, doi: 10.1175/JCLI-D-13-00301.1.
- Hollowed, A. B., Planque, B., and Loeng, H. (2013). Potential movement of fish and shellfish stocks from the sub-Arctic to the Arctic Ocean. *Fisheries Oceanography*, **22(5)**, 355-370, doi: 10.1111/fog.12027.

- Howell, S. E. L., Duguay, C. R., and Markus, T. (2009). Sea ice conditions and melt season duration variability within the Canadian Arctic Archipelago: 1979-2008. *Geophysical Research Letters*, **36(10)**, doi: 10.1029/2009GL037681.
- Howell, S. E. L., Yackel, J. J., De Abreu, R., Geldsetzer, T., and Breneman, C. (2005). On the utility of SeaWinds/QuikSCAT data for the estimation of the thermodynamic state of first-year sea ice. *Geoscience and Remote Sensing, IEEE Transactions on*, **43(6)**, 1338-1350, doi: 10.1109/TGRS.2005.846153.
- Hu, X. and Myers, P. G. (2014). Changes to the Canadian Arctic Archipelago Sea Ice and Freshwater Fluxes in the Twenty-First Century under the Intergovernmental Panel on Climate Change A1B Climate Scenario. *Atmosphere-Ocean*, **52(4)**, 331-350, doi: 10.1080/07055900.2014.942592.
- Hufford, G. (1991). A model for the complex permittivity of ice at frequencies below 1 THz. *International Journal of Infrared and Millimeter Waves*, **12(7)**, 677-682, doi: 10.1007/BF01008898.
- Hughes, N. E., Wilkinson, J. P., and Wadhams, P. (2011). Multi-satellite sensor analysis of fast-ice development in the Norske Øer Ice Barrier, northeast Greenland. *Annals of Glaciology*, **52(57)**, 151-160, doi: 10.3189/172756411795931633.
- Hunke, E. C. (2014). Sea ice volume and age: Sensitivity to physical parameterizations and thickness resolution in the {CICE} sea ice model. *Ocean Modelling*, **82(0)**, 45 - 59, doi: 10.1016/j.ocemod.2014.08.001.
- Hutchings, J. K., Heil, P., Lecomte, O., Stevens, R., Steer, A., and Lieser, J. L. (2015). Comparing methods of measuring sea-ice density in the East Antarctic. *Annals of Glaciology*, **56(69)**, 77-82, doi: 10.3189/2015AoG69A814.
- Jackson, K., Wilkinson, J., Maksym, T., Meldrum, D., Beckers, J. F., Haas, C., and Mackenzie, D. (2013). A Novel and Low-Cost Sea Ice Mass Balance Buoy. *Journal of Atmospheric and Oceanic Technology*, **30(11)**, 2676-2688, doi: 10.1175/JTECH-D-13-00058.1.

- Jahn, A., Sterling, K., Holland, M. M., Kay, J. E., Maslanik, J. A., Bitz, C. M., Bailey, D. A., Stroeve, J., Hunke, E. C., Lipscomb, W. H., and Pollak, D. A. (2011). Late-Twentieth-Century Simulation of Arctic Sea Ice and Ocean Properties in the CCSM4. *Journal of Climate*, **25(5)**, 1431-1452, doi: 10.1175/JCLI-D-11-00201.1.
- Jeffries, M. O. and Morris, K. (2006). Instantaneous daytime conductive heat flow through snow on lake ice in Alaska. *Hydrological Processes*, **20(4)**, 803-815, doi: 10.1002/hyp.6116.
- Jeffries, M. O., Morris, K., Weeks, W. F., and Wakabayashi, H. (1994). Structural and stratigraphic features and ERS 1 synthetic aperture radar backscatter characteristics of ice growing on shallow lakes in NW Alaska, winter 1991-1992. *Journal of Geophysical Research: Oceans*, **99(C11)**, 22459-22471, doi: 10.1029/94JC01479.
- Jeffries, M. O., Weeks, W. F., Shaw, R., and Morris, K. (1993). Structural characteristics of congelation and platelet ice and their role in the development of Antarctic land-fast sea ice. *Journal of Glaciology*, **39**, 223-238, doi: 10.1017/S0022143000015884.
- Kaleschke, L., Tian-Kunze, X., Maas, N., Makynen, M., and Drusch, M. (2012). Sea ice thickness retrieval from SMOS brightness temperatures during the Arctic freeze-up period. *Geophysical Research Letters*, **39(5)**, doi: 10.1029/2012GL050916.
- Kang, K.-K., Duguay, C. R., Lemmetyinen, J., and Gel, Y. (2014). Estimation of ice thickness on large northern lakes from AMSR-E brightness temperature measurements. *Remote Sensing of Environment*, **150**, 1 - 19, doi: 10.1016/j.rse.2014.04.016.
- Kang, K.-K., Duguay, C. R., and Howell, S. E. L. (2012). Estimating ice phenology on large northern lakes from AMSR-E: algorithm development and application to Great Bear Lake and Great Slave Lake, Canada. *The Cryosphere*, **6(2)**, 235-254, doi: 10.5194/tc-6-235-2012.
- Kang, K.-K., Duguay, C. R., Howell, S. E. L., Derksen, C. P., and Kelly, R. E. J. (2010). Sensitivity of AMSR-E Brightness Temperatures to the Seasonal Evolution of Lake Ice Thickness. *Geoscience and Remote Sensing Letters, IEEE*, **7(4)**, 751-755, doi: 10.1109/LGRS.2010.2044742.
- Ketchum, R. D. (1971). Airborne laser profiling of the arctic pack ice. *Remote Sensing of Environment*, **2**, 41 - 52, doi: 10.1016/0034-4257(71)90076-9.

- Kheyrollah Pour, H., Duguay, C. R., Scott, K. A., and Kang, K. K. (2017). Improvement of Lake Ice Thickness Retrieval From MODIS Satellite Data Using a Thermodynamic Model. *IEEE Transactions on Geoscience and Remote Sensing*, **99**, 1-10, doi: 10.1109/TGRS.2017.2718533.
- Khvorostovsky, K. and Rampal, P. (2016). On retrieving sea ice freeboard from ICESat laser altimeter. *The Cryosphere*, **10(5)**, 2329-2346, doi: 10.5194/tc-10-2329-2016.
- King, J., Howell, S., Derksen, C., Rutter, N., Toose, P., Beckers, J. F., Haas, C., Kurtz, N., and Richter-Menge, J. (2015). Evaluation of Operation IceBridge quick-look snow depth estimates on sea ice. *Geophysical Research Letters*, **42(21)**, 9302-9310, doi: 10.1002/2015GL066389.
- Koenig, L., Martin, S., Studinger, M., and Sonntag, J. (2010). Polar Airborne Observations Fill Gap in Satellite Data. *Eos, Transactions American Geophysical Union*, **91(38)**, 333-334, doi: 10.1029/2010EO380002.
- Kouraev, A. V., Semovski, S. V., Shimaraev, M. N., Mognard, N. M., Légresy, B., and Remy, F. (2007). Observations of Lake Baikal ice from satellite altimetry and radiometry. *Remote Sensing of Environment*, **108(3)**, 240 - 253, doi: 10.1016/j.rse.2006.11.010.
- Kouraev, A. V., Semovski, S. V., Shimaraev, M. N., Mognard, N. M., Légresy, B., and Remy, F. (2007). The ice regime of Lake Baikal from historical and satellite data: Relationship to air temperature, dynamical, and other factors. *Limnology and Oceanography*, **52(3)**, 1268-1286, doi: 10.4319/io.2007.52.3.1268.
- Krabill, W. B., Abdalati, W., Frederick, E. B., Manizade, S. S., Martin, C. F., Sonntag, J. G., Swift, R. N., Thomas, R. H., and Yungel, J. G. (2002). Aircraft laser altimetry measurement of elevation changes of the Greenland ice sheet: technique and accuracy assessment. *Journal of Geodynamics*, **34(3)**, 357 - 376, doi: 10.1016/S0264-3707(02)00040-6.
- Krabill, W., Thomas, R., Jezek, K., Kuivinen, K., and Manizade, S. (1995). Greenland Ice Sheet thickness changes measured by laser altimetry. *Geophysical Research Letters*, **22(17)**, 2341-2344, doi: 10.1029/95GL02069.
- Kruppen, T., Janout, M., Hodges, K. I., Gerdes, R., Girard-Arduin, F., Holemann, J. A., and Willmes, S. (2013). Variability and trends in Laptev Sea ice outflow between 1992-2011. *The Cryosphere*, **7(1)**, 349-363, doi: 10.5194/tc-7-349-2013.

- Kubat, I. and Timco, G. (2003). Vessel Damage in the Canadian Arctic. Proceedings 17th International Conference on Port and Ocean Engineering Under Arctic Conditions, 1, 203 - 212. POAC.
- Kurtz, N., Studinger, M. S., Harbeck, J., Onana, V., and Yi, D. (2015). IceBridge L4 Sea Ice Freeboard, Snow Depth, and Thickness, Version 1. National Snow and Ice Data Center, doi: 10.5067/G519SHCKWQV6.
- Kurtz, N. (2015). IceBridge quick look sea ice freeboard, snow depth, and thickness product manual for 2014. National Snow and Ice Data Center. Accessed online at: ftp://n5eil01u.ecs.nsidc.org/SAN2/ICEBRIDGE_FTP/Evaluation_Products/IceBridge_Sea_Ice_Freeboard_SnowDepth_and_Thickness_QuickLook/Documentation/icebridge_ql_products_2014.pdf.
- Kurtz, N. T., Galin, N., and Studinger, M. (2014). An improved CryoSat-2 sea ice freeboard retrieval algorithm through the use of waveform fitting. *The Cryosphere*, **8(4)**, 1217-1237, doi: 10.5194/tc-8-1217-2014.
- Kurtz, N., Studinger, M., Harbeck, J., Onana, V., and S. Farrell (2012). Ice-Bridge sea ice freeboard, snow depth, and thickness. National Snow and Ice Data Center, doi: 10.5067/7XJ9HRV50O57.
- Kurtz, N. T. and Markus, T. (2012). Satellite observations of Antarctic sea ice thickness and volume. *Journal of Geophysical Research: Oceans*, **117(C8)**, doi: 10.1029/2012JC008141.
- Kurtz, N. T., Markus, T., Farrell, S. L., Worthen, D. L., and Boisvert, L. N. (2011). Observations of recent Arctic sea ice volume loss and its impact on ocean-atmosphere energy exchange and ice production. *Journal of Geophysical Research: Oceans*, **116(C4)**, doi: 10.1029/2010JC006235.
- Kurtz, N. T., Markus, T., Cavalieri, D. J., Krabill, W., Sonntag, J. G., and Miller, J. (2008). Comparison of ICESat Data With Airborne Laser Altimeter Measurements Over Arctic Sea Ice. *Geoscience and Remote Sensing, IEEE Transactions on*, **46(7)**, 1913-1924, doi: 10.1109/TGRS.2008.916639.
- Kwok, R. (2014). Simulated effects of a snow layer on retrieval of CryoSat-2 sea ice freeboard. *Geophysical Research Letters*, **41(14)**, 5014-5020, doi: 10.1002/2014GL060993.

- Kwok, R. (2009). Outflow of Arctic Ocean Sea Ice into the Greenland and Barents Seas: 1979-2007. *Journal of Climate*, **22(9)**, 2438-2457, doi: 10.1175/2008JCLI2819.1.
- Kwok, R., Kurtz, N. T., Brucker, L., Ivanoff, A., Newman, T., Farrell, S. L., King, J., Howell, S., Webster, M. A., Paden, J., Leuschen, C., Macgregor, J. A., Richter-Menge, J., Harbeck, J., and Tschudi, M. (2017). Inter-comparison of snow depth retrievals over Arctic sea ice from radar data acquired by Operation IceBridge. *The Cryosphere Discussions*, **2017**, 1-37, doi: 10.5194/tc-2017-103.
- Kwok, R. and Morison, J. (2016). Sea surface height and dynamic topography of the ice-covered oceans from CryoSat-2: 2011-2014. *Journal of Geophysical Research: Oceans*, **121(1)**, 674-692, doi: 10.1002/2015JC011357.
- Kwok, R. and Haas, C. (2015). Effects of radar side-lobes on snow depth retrievals from Operation IceBridge. *Journal of Glaciology*, **61(227)**, 576-584, doi: 10.3189/2015JoG14J229.
- Kwok, R. and Cunningham, G. F. (2015). Variability of Arctic sea ice thickness and volume from CryoSat-2. *Philosophical Transactions of the Royal Society of London A: Mathematical, Physical and Engineering Sciences*, **373(2045)**, doi: 10.1098/rsta.2014.0157.
- Kwok, R., Spreen, G., and Pang, S. (2013). Arctic sea ice circulation and drift speed: Decadal trends and ocean currents. *Journal of Geophysical Research: Oceans*, **118(5)**, 2408-2425, doi: 10.1002/jgrc.20191.
- Kwok, R., Cunningham, G. F., Manizade, S. S., and Krabill, W. B. (2012). Arctic sea ice freeboard from IceBridge acquisitions in 2009: Estimates and comparisons with ICESat. *Journal of Geophysical Research: Oceans*, **117(C2)**, doi: 10.1029/2011JC007654.
- Kwok, R., Cunningham, G. F., Wensnahan, M., Rigor, I., Zwally, H. J., and Yi, D. (2009). Thinning and volume loss of the Arctic Ocean sea ice cover: 2003-2008. *Journal of Geophysical Research: Oceans*, **114(C7)**, doi: 10.1029/2009JC005312.
- Kwok, R. and Rothrock, D. A. (2009). Decline in Arctic sea ice thickness from submarine and ICESat records: 1958-2008. *Geophysical Research Letters*, **36(15)**, doi: 10.1029/2009GL039035.
- Kwok, R. and Cunningham, G. F. (2008). ICESat over Arctic sea ice: Estimation of snow depth and ice thickness. *Journal of Geophysical Research: Oceans*, **113(C8)**, doi: 10.1029/2008JC004753.

- Kwok, R., Cunningham, G. F., Zwally, H. J., and Yi, D. (2006). ICESat over Arctic sea ice: Interpretation of altimetric and reflectivity profiles. *Journal of Geophysical Research: Oceans*, **111(C6)**, doi: 10.1029/2005JC003175.
- Kwok, R., Cunningham, G. F., and Pang, S. S. (2004). Fram Strait sea ice outflow. *Journal of Geophysical Research: Oceans*, **109(C1)**, doi: 10.1029/2003JC001785.
- Kwok, R., Zwally, H. J., and Yi, D. (2004). ICESat observations of Arctic sea ice: A first look. *Geophysical Research Letters*, **31(16)**, doi: 10.1029/2004GL020309.
- Lange, B. A., Flores, H., Michel, C., Beckers, J. F., Bublitz, A., Casey, J. A., Castellani, G., Hatam, I., Reppchen, A., Rudolph, S. A., and Haas, C. (2017). Pan-Arctic sea ice-algal chl a biomass and suitable habitat are largely underestimated for multiyear ice. *Global Change Biology*, doi: 10.1111/gcb.13742.
- Lange, B. A., Michel, C., Beckers, J. F., Casey, J. A., Flores, H., Hatam, I., Meisterhans, G., Niemi, A., and Haas, C. (2015). Comparing Springtime Ice-Algal Chlorophyll a and Physical Properties of Multi-Year and First-Year Sea Ice from the Lincoln Sea. *PLOS ONE*, **10(4)**, 1-26, doi: 10.1371/journal.pone.0122418.
- Laxon, S. (1990). Seasonal and inter-annual variations in Antarctic sea ice extent as mapped by radar altimetry. *Geophysical Research Letters*, **17(10)**, 1553-1556, doi: 10.1029/GL017i010p01553.
- Laxon, S. W., Giles, K. A., Ridout, A. L., Wingham, D. J., Willatt, R., Cullen, R., Kwok, R., Schweiger, A., Zhang, J., Haas, C., Hendricks, S., Krishfield, R., Kurtz, N., Farrell, S., and Davidson, M. (2013). CryoSat-2 estimates of Arctic sea ice thickness and volume. *Geophysical Research Letters*, **40(4)**, 732-737, doi: 10.1002/grl.50193.
- Laxon, S. W., Peacock, N., and Smith, D. (2003). High interannual variability of sea ice thickness in the Arctic region. *Nature*, **425(6961)**, 947-950, doi: 10.1038/nature02050.
- Lee, S., Im, J., Kim, J., Kim, M., Shin, M., Kim, H.-c., and Quackenbush, L. J. (2016). Arctic Sea Ice Thickness Estimation from CryoSat-2 Satellite Data Using Machine Learning-Based Lead Detection. *Remote Sensing*, **8(9)**, doi: 10.3390/rs8090698.

- Leonard, G. H., Purdie, C. R., Langhorne, P. J., Haskell, T. G., Williams, M. J. M., and Frew, R. D. (2006). Observations of platelet ice growth and oceanographic conditions during the winter of 2003 in McMurdo Sound, Antarctica. *Journal of Geophysical Research: Oceans*, **111(C4)**, doi: 10.1029/2005JC002952.
- Lindsay, R., Haas, C., Hendricks, S., Hunkeler, P., Kurtz, N., Paden, J., Panzer, B., Sonntag, J., Yungel, J., and Zhang, J. (2012). Seasonal forecasts of Arctic sea ice initialized with observations of ice thickness. *Geophysical Research Letters*, **39(21)**, doi: 10.1029/2012GL053576.
- Long, D. G., Drinkwater, M. R., Holt, B., Saatchi, S., and Bertoia, C. (2001). Global Ice and Land Climate Studies Using Scatterometer Image Data. *EOS, Transaction of the American Geophysical Union*, **82(43)**, 503, doi: 10.1029/01EO00303.
- Lowry, R. T. and Wadhams, P. (1979). On the statistical distribution of pressure ridges in sea ice. *Journal of Geophysical Research: Oceans*, **84(C5)**, 2487-2494, doi: 10.1029/JC084iC05p02487.
- Maas, N., Kaleschke, L., Tian-Kunze, X., and Drusch, M. (2013). Snow thickness retrieval over thick Arctic sea ice using SMOS satellite data. *The Cryosphere*, **7(6)**, 1971-1989, doi: 10.5194/tc-7-1971-2013.
- Maheshwari, M., Mahesh, C., Rajkumar, K. S., Pallipad, J., Rajak, D. R., Oza, S. R., Kumar, R., and Sharma, R. (2015). Estimation of Sea Ice Freeboard from SARAL/AltiKa Data. *Marine Geodesy*, **38(1)**, 487-496, doi: 10.1080/01490419.2015.1005782.
- Mahoney, A. R., Gough, A. J., Langhorne, P. J., Robinson, N. J., Stevens, C. L., Williams, M. M. J., and Haskell, T. G. (2011). The seasonal appearance of ice shelf water in coastal Antarctica and its effect on sea ice growth. *Journal of Geophysical Research: Oceans*, **116(C11)**, doi: 10.1029/2011JC007060.
- Markus, T. and Cavalieri, D. J. (2013). Snow depth distribution over sea ice in the Southern Ocean from satellite passive microwave data. In Jeffries, M. O. editor. *Antarctic Sea Ice: Physical Processes, Interactions and Variability*, 19-39. American Geophysical Union, doi: 10.1029/AR074p0019.

- Marshall, H.-P., Schneebeli, M., and Koh, G. (2007). Snow stratigraphy measurements with high-frequency FMCW radar: Comparison with snow micro-penetrator. *Cold Regions Science and Technology*, **47(1-2)**, 108 - 117, doi: 10.1016/j.coldregions.2006.08.008.
- Martin, C. F., Krabill, W. B., Maizade, S. S., Russell, R. L., Sonntag, J. G., Swift, R. N., and Yungel, J. K. (2012). Airborne Topographic Mapper Calibration Procedures and Accuracy Assessment. NASA/TM-2012-215891, National Aeronautics and Space Administration.
- Maslanik, J., Stroeve, J., Fowler, C., and Emery, W. (2011). Distribution and trends in Arctic sea ice age through spring 2011. *Geophysical Research Letters*, **38(13)**, doi: 10.1029/2011GL047735.
- Massom, R. A., Eicken, H., Hass, C., Jeffries, M. O., Drinkwater, M. R., Sturm, M., Worby, A. P., Wu, X., Lytle, V. I., Ushio, S., Morris, K., Reid, P. A., Warren, S. G., and Allison, I. (2001). Snow on Antarctic sea ice. *Reviews of Geophysics*, **39(3)**, 413-445, doi: 10.1029/2000RG000085.
- Massom, R. A., Harris, P. T., Michael, K. J., and Potter, M. J. (1998). The distribution and formative processes of latent-heat polynyas in East Antarctica. *Annals of Glaciology*, **27**, 420-426.
- Massonnet, F., Mathiot, P., Fichet, T., Goosse, H., Beatty, C. K., Vancoppenolle, M., and Lavergne, T. (2013). A model reconstruction of the Antarctic sea ice thickness and volume changes over 1980-2008 using data assimilation. *Ocean Modelling*, **64**, 67 - 75, doi: 10.1016/j.ocemod.2013.01.003.
- Mätzler, C. (2006). Microwave dielectric properties of ice. In: Mätzler, C. editor. *Thermal Microwave Radiation: Applications for Remote Sensing*, 455-463. Institution of Engineering and Technology, doi: 10.1049/PBEW052E_ch5.
- Mätzler, C. and Wegmuller, U. (1987). Dielectric properties of freshwater ice at microwave frequencies. *Journal of Physics D: Applied Physics*, **20(12)**, 1623, doi: 10.1088/0022-3727/20/12/013.
- Mavrocordatos, C., Attema, E., Davidson, M., Lentz, H., and Nixdorf, U. (2004). Development of ASIRAS (Airborne SAR/Interferometric Altimeter System). IGARSS 2004. 2004 IEEE International Geoscience and Remote Sensing Symposium, IGARSS 2004, **4**, 2465-2467, IEEE, doi: 10.1109/IGARSS.2004.1369792.

- Meier, W. N., Hovelsrud, G. K., van Oort, B. E. H., Key, J. R., Kovacs, K. M., Michel, C., Haas, C., Granskog, M. A., Gerland, S., Perovich, D. K., Makshtas, A., and Reist, J. D. (2014). Arctic sea ice in transformation: A review of recent observed changes and impacts on biology and human activity. *Reviews of Geophysics*, **52(3)**, 185-217, doi: 10.1002/2013RG000431.
- Michel, B. and Ramseier, R. O. (1971). Classification of river and lake ice. *Canadian Geotechnical Journal*, **8**, 36 – 45, doi: 10.1139/t71-004.
- Morison, J., Kwok, R., Peralta-Ferriz, C., Alkire, M., Rigor, I., Andersen, R., and Steele, M. (2012). Changing Arctic Ocean freshwater pathways. *Nature*, **481(7379)**, 66-70, doi: 10.1038/nature10705
- Morris, K., Jeffries, M. O., and Weeks, W. F. (1995). Ice processes and growth history on Arctic and sub-Arctic lakes using ERS-1 SAR data. *Polar Record*, **31**, 115-128, doi: 10.1017/S0032247400013619.
- Mussells, O., Dawson, J., and Howell, S. (2017). Navigating pressured ice: Risks and hazards for winter resource-based shipping in the Canadian Arctic. *Ocean & Coastal Management*, **137**, 57 - 67, doi: 10.1016/j.ocecoaman.2016.12.010.
- NSIDC: National Snow and Ice Data Center (2017). Arctic Sea Ice News and Analysis: Another record, but a somewhat cooler Arctic Ocean. Accessed online at: <https://nsidc.org/arcticseaicenews/2017/04/>.
- Ozsoy-Cicek, B., Ackley, S., Xie, H., Yi, D., and Zwally, J. (2013). Sea ice thickness retrieval algorithms based on in situ surface elevation and thickness values for application to altimetry. *Journal of Geophysical Research: Oceans*, **118(8)**, 3807-3822, doi: 10.1002/jgrc.20252.
- Parkinson, C. L. and Cavalieri, D. J. (2012). Antarctic sea ice variability and trends, 1979-2010. *The Cryosphere*, **6(4)**, 871-880, doi: 10.5194/tc-6-871-2012.
- Peacock, N. R. and Laxon, S. W. (2004). Sea surface height determination in the Arctic Ocean from ERS altimetry. *Journal of Geophysical Research: Oceans*, **109(C7)**, doi: 10.1029/2001JC001026.

- Perovich, D. K. and Richter-Menge, J. A. (2015). Regional variability in sea ice melt in a changing Arctic. *Philosophical Transactions of the Royal Society of London A: Mathematical, Physical and Engineering Sciences*, **373(2045)**, doi: 10.1098/rsta.2014.0165.
- Perovich, D. K., Meier, W., Tschudi, M., Gerland, S., and Richter-Menge, J. A. (2012). Sea Ice. In Jeffries, M. O., Richter-Menge, J. A., and Overland, J. E. editor. *Arctic Report Card 2012*, NOAA.
- Perovich, D. K., Jones, K. F., Light, B., Eicken, H., Markus, T., Stroeve, J., and Lindsay, R. (2011). Solar partitioning in a changing Arctic sea-ice cover. *Annals of Glaciology*, **52(57)**, 192 -196, doi: 10.3189/172756411795931543.
- Perovich, D. K., Richter-Menge, J. A., Jones, K. F., and Light, B. (2008). Sunlight, water, and ice: Extreme Arctic sea ice melt during the summer of 2007. *Geophysical Research Letters*, **35(11)**, doi: 10.1029/2008GL034007.
- Peterson, I. K., Prinsenber, S. J., and Holladay, J. S. (2008). Observations of sea ice thickness, surface roughness and ice motion in Amundsen Gulf. *Journal of Geophysical Research: Oceans*, **113(C6)**, doi: 10.1029/2007JC004456.
- Petrich, C. and Eicken, H. (2010). Growth, Structure and Properties of Sea Ice. In Thomas, D. N. and Dieckmann, G. editor. *Sea Ice*, 23-77. Wiley-Blackwell, doi: 10.1002/9781444317145.ch2.
- Petty, A. A., Tsamados, M. C., and Kurtz, N. T. (2017). Atmospheric form drag coefficients over Arctic sea ice using remotely sensed ice topography data, spring 2009-2015. *Journal of Geophysical Research: Earth Surface*, doi: 10.1002/2017JF004209.
- Petty, A. A., Tsamados, M. C., Kurtz, N. T., Farrell, S. L., Newman, T., Harbeck, J. P., Feltham, D. L., and Richter-Menge, J. A. (2016). Characterizing Arctic sea ice topography using high-resolution IceBridge data. *The Cryosphere*, **10(3)**, 1161-1179, doi: 10.5194/tc-10-1161-2016.
- Pizzolato, L., Howell, S. L., Derksen, C., Dawson, J., and Copland, L. (2014). Changing sea ice conditions and marine transportation activity in Canadian Arctic waters between 1990 and 2012. *Climatic Change*, **123(2)**, 161-173, doi: 10.1007/s10584-013-1038-3.

- Pizzolato, L., Howell, S. E. L., Dawson, J., Laliberté, F., and Copland, L. (2016). The influence of declining sea ice on shipping activity in the Canadian Arctic. *Geophysical Research Letters*, **43(23)**, 12,146-12,154, doi: 10.1002/2016GL071489.
- Polyakov, I. V., Pnyushkov, A. V., Alkire, M. B., Ashik, I. M., Baumann, T. M., Carmack, E. C., Goszczko, I., Guthrie, J., Ivanov, V. V., Kanzow, T., Krishfield, R., Kwok, R., Sundfjord, A., Morison, J., Rember, R., and Yulin, A. (2017). Greater role for Atlantic inflows on sea-ice loss in the Eurasian Basin of the Arctic Ocean. *Science*, **356(6335)**, 285-291, doi: 10.1126/science.aai8204.
- Price, D., Beckers, J., Ricker, R., Kurtz, N., Rack, W., Haas, C., Helm, V., Hendricks, S., Leonard, G., and Langhorne, P. J. (2015). Evaluation of CryoSat-2 derived sea-ice freeboard over fast ice in McMurdo Sound, Antarctica. *Journal of Glaciology*, **61(226)**, 285-300, doi: 10.3189/2015JoG14J157.
- Price, D., Rack, W., Langhorne, P. J., Haas, C., Leonard, G., and Barnsdale, K. (2014). The sub-ice platelet layer and its influence on freeboard to thickness conversion of Antarctic sea ice. *The Cryosphere*, **8(3)**, 1031-1039, doi: 10.5194/tc-8-1031-2014.
- Price, D., Rack, W., Haas, C., Langhorne, P. J., and Marsh, O. (2013). Sea ice freeboard in McMurdo Sound, Antarctica, derived by surface-validated ICESat laser altimeter data. *Journal of Geophysical Research: Oceans*, **118(7)**, 3634-3650, doi: 10.1002/jgrc.20266.
- Pringle, D. J., Eicken, H., Trodahl, H. J., and Backstrom, L. G. E. (2007). Thermal conductivity of landfast Antarctic and Arctic sea ice. *Journal of Geophysical Research: Oceans*, **112(C4)**, doi: 10.1029/2006JC003641.
- Prowse, T., Alfredsen, K., Beltaos, S., Bonsal, B., Duguay, C., Korhola, A., McNamara, J., Pienitz, R., Vincent, W. F., Vuglinsky, V., and Weyhenmeyer, G. A. (2011). Past and Future Changes in Arctic Lake and River Ice. *AMBIO*, **40(1)**, 53-62, doi: 10.1007/s13280-011-0216-7.
- Prowse, T. D., Furgal, C., Chouinard, R., Melling, H., Milburn, D., and Smith, S. L. (2009). Implications of Climate Change for Economic Development in Northern Canada: Energy, Resource, and Transportation Sectors. *AMBIO: A Journal of the Human Environment*, **38(5)**, 272-281, doi: 10.1579/0044-7447-38.5.272.

- Purdie, C. R., Langhorne, P. J., Leonard, G. H., and Haskell, T. G. (2006). Growth of first-year landfast Antarctic sea ice determined from winter temperature measurements. *Annals of Glaciology*, **44**, 170-176, doi: 10.3189/172756406781811853.
- Rabe, B., Karcher, M., Schauer, U., Toole, J. M., Krishfield, R. A., Pisarev, S., Kauker, F., Gerdes, R., and Kikuchi, T. (2011). An assessment of Arctic Ocean freshwater content changes from the 1990s to the 2006-2008 period. *Deep Sea Research Part I: Oceanographic Research Papers*, **58(2)**, 173 - 185, doi: 10.1016/j.dsr.2010.12.002.
- Rampal, P., Weiss, J., and Marsan, D. (2009). Positive trend in the mean speed and deformation rate of Arctic sea ice, 1979-2007. *Journal of Geophysical Research: Oceans*, **114(C5)**, doi: 10.1029/2008JC005066.
- Rapley, C. G. (1984). First observations of the interaction of ocean swell with sea ice using satellite radar altimeter data. *Nature*, **307(5947)**, 150-152, doi: 10.1038/307150a0.
- Rempel, R. C. and Parker, A. K. (1964). An information note on an airborne laser terrain profiler for micro-relief studies. Proceedings 3rd Symposium on Remote Sensing of Environment, 321-337.
- Renner, A. H. H., Gerland, S., Haas, C., Spreen, G., Beckers, J. F., Hansen, E., Nicolaus, M., and Goodwin, H. (2014). Evidence of Arctic sea ice thinning from direct observations. *Geophysical Research Letters*, **41(14)**, 5029-5036, doi: 10.1002/2014GL060369.
- Renner, A. H. H., Hendricks, S., Sebastian Gerland, S., Beckers, J. F., Haas, C., and Krumpfen, T. (2013). Large-scale ice thickness distribution of first-year sea ice in spring and summer north of Svalbard. *Annals of Glaciology*, **54(62)**, 13-18, doi: 10.3189/2013AoG62A146.
- Renner, A. H. H., Dumont, M., Beckers, J. F., Gerland, S., and Haas, C. (2013). Improved characterisation of sea ice using simultaneous aerial photography and sea ice thickness measurements. *Cold Regions Science and Technology*, **92**, 37 - 47, doi: 10.1016/j.coldregions.2013.03.009.
- Ricker, R., Hendricks, S., and Beckers, J. F. (2016). The Impact of Geophysical Corrections on Sea-Ice Freeboard Retrieved from Satellite Altimetry. *Remote Sensing*, **8(4)**, doi: 10.3390/rs8040317.

- Ricker, R., Hendricks, S., Perovich, D. K., Helm, V., and Gerdes, R. (2015). Impact of snow accumulation on CryoSat-2 range retrievals over Arctic sea ice: An observational approach with buoy data. *Geophysical Research Letters*, **42(11)**, 4447-4455, doi: 10.1002/2015GL064081.
- Ricker, R., Hendricks, S., Helm, V., Skourup, H., and Davidson, M. (2014). Sensitivity of CryoSat-2 Arctic sea-ice freeboard and thickness on radar-waveform interpretation. *The Cryosphere*, **8(4)**, 1607-1622, doi: 10.5194/tc-8-1607-2014.
- Riegl (2010). Riegl LMS Q120 Datasheet. Riegl Laser Measurement Systems GmbH. Accessed online at: http://www.riegl.com/uploads/tx_pxpriegl/downloads/10_DataSheet_LMS-Q120_20-04-2010.pdf.
- Rigor, I. G. and Wallace, J. M. (2004). Variations in the age of Arctic sea-ice and summer sea-ice extent. *Geophysical Research Letters*, **31(9)**, L09401, doi: 10.1029/2004GL019492.
- Rose, S. K., Forsberg, R., and Toudal Pedersen, L. (2013). Measurements of sea ice by satellite and airborne altimetry. Technical University of Denmark.
- Rosmorduc, V., Benveniste, J., Bronner, E., Dinardo, S., Lauret, O., Maheu, C., Milagro, M., Picot, N., Ambrozio, A., Escolà, R., Garcia-Mondejar, A., Restano, M., Schrama, E., Terra-Homem, M. (2016). Radar Altimetry Tutorial. Accessed at: <http://www.altimetry.info>.
- Rouse, W. R., Blanken, P. D., Bussières, N., Walker, A. E., Oswald, C. J., Schertzer, W. M., and Spence, C. (2008). An Investigation of the Thermal and Energy Balance Regimes of Great Slave and Great Bear Lakes. *Journal of Hydrometeorology*, **9(6)**, 1318-1333, doi: 10.1175/2008JHM977.1.
- Rouse, W. R., Oswald, C. M., Binyamin, J., Blanken, P. D., Schertzer, W. M., and Spence, C. (2003). Interannual and Seasonal Variability of the Surface Energy Balance and Temperature of Central Great Slave Lake. *Journal of Hydrometeorology*, **4(4)**, 720-730, doi: 10.1175/1525-7541(2003)004<0720:IASVOT>2.0.CO.
- von Saldern, C., Haas, C., and Dierking, W. (2006). Parameterization of Arctic sea-ice surface roughness for application in ice type classification. *Annals of Glaciology*, **44(1)**, 224-230, doi: 10.3189/172756406781811411.

- Sarmiento, S. E. and Khan, S. D. (2010). Spatial and Temporal Variability of Great Slave Lake Levels From Satellite Altimetry. *Geoscience and Remote Sensing Letters, IEEE*, **7(3)**, 426-429, doi: 10.1109/LGRS.2009.2038178.
- Schertzer, W. M., Rouse, W. R., Blanken, P. D., and Walker, A. E. (2003). Over-lake Meteorology and Estimated Bulk Heat Exchange of Great Slave Lake in 1998 and 1999. *Journal of Hydrometeorology*, **4(4)**, 649-659, doi: 10.1175/1525-7541(2003)004<0649:OMAEBH>2.0.CO;2.
- Schweiger, A. I., Lindsay, R., Zhang, J., Steele, M., Stern, H., and Kwok, R. (2011). Uncertainty in modeled Arctic sea ice volume. *Journal of Geophysical Research: Oceans*, **116(C8)**, doi: 10.1029/2011JC007084.
- Screen, J. A. (2017). Simulated Atmospheric Response to Regional and Pan-Arctic Sea Ice Loss. *Journal of Climate*, **30(11)**, 3945-3962, doi: 10.1175/JCLI-D-16-0197.1.
- Serreze, M. C. and Stroeve, J. (2015). Arctic sea ice trends, variability and implications for seasonal ice forecasting. *Philosophical Transactions of the Royal Society of London A: Mathematical, Physical and Engineering Sciences*, **373(2045)**, doi: 10.1098/rsta.2014.0159.
- Serreze, M. C., Barrett, A. P., Slater, A. G., Woodgate, R. A., Aagaard, K., Lammers, R. B., Steele, M., Moritz, R., Meredith, M., and Lee, C. M. (2006). The large-scale freshwater cycle of the Arctic. *Journal of Geophysical Research: Oceans*, **111(C11)**, doi: 10.1029/2005JC003424.
- Shokr, M. and Sinha, N. (2015). Sea Ice: Physics and Remote Sensing. American Geophysical Union, doi: /10.1002/9781119028000.
- Skourup, H., Farrell, S., Hendricks, S., Ricker, R., Armitage, T. W. K., Ridout, A., Andersen, O. B., Haas, C., Baker, S. (2017). An assessment of state-of-the-art mean sea surface and geoid models of the arctic ocean: Implications for sea ice freeboard retrieval. *Journal of Geophysical Research: Oceans*, **122**, 8593 – 8613, doi: 10.1002/2017JC013176
- Smith, I. J., Langhorne, P. J., Frew, R. D., Vennell, R., and Haskell, T. G. (2012). Sea ice growth rates near ice shelves. *Cold Regions Science and Technology*, **83**, 57 - 70, doi: 10.1016/j.coldregions.2012.06.005.

- Smith, L. C. and Stephenson, S. R. (2013). New Trans-Arctic shipping routes navigable by midcentury. *Proceedings of the National Academy of Sciences*, **110(13)**, E1191-E1195, doi: 10.1073/pnas.1214212110.
- Spren, G., Kwok, R., and Menemenlis, D. (2011). Trends in Arctic sea ice drift and role of wind forcing: 1992-2009. *Geophysical Research Letters*, **38(19)**, doi: 10.1029/2011GL048970.
- Spren, G., Kern, S., Stammer, D., and Hansen, E. (2009). Fram Strait sea ice volume export estimated between 2003 and 2008 from satellite data. *Geophysical Research Letters*, **36(19)**, doi: 10.1029/2009GL039591.
- Steele, M. and Dickinson, S. (2016). The phenology of Arctic Ocean surface warming. *Journal of Geophysical Research: Oceans*, **121(9)**, 6847-6861, doi: 10.1002/2016JC012089.
- Steele, M., Zhang, J., and Ermold, W. (2010). Mechanisms of summertime upper Arctic Ocean warming and the effect on sea ice melt. *Journal of Geophysical Research: Oceans*, **115(C11)**, doi: 10.1029/2009JC005849.
- Stephenson, S., Smith, L., Brigham, L., and Agnew, J. (2013). Projected 21st-century changes to Arctic marine access. *Climatic Change*, **118(3-4)**, 885-899, doi: 10.1007/s10584-012-0685-0.
- Stroeve, J. C., Kattsov, V., Barrett, A., Serreze, M., Pavlova, T., Holland, M., and Meier, W. N. (2012). Trends in Arctic sea ice extent from CMIP5, CMIP3 and observations. *Geophysical Research Letters*, **39(16)**, doi: 10.1029/2012GL052676.
- Stroeve, J. C., Markus, T., Maslanik, J. A., Cavalieri, D. J., Gasiewski, A. J., Heinrichs, J. F., Holmgren, J., Perovich, D. K., and Sturm, M. (2006). Impact of Surface Roughness on AMSR-E Sea Ice Products. *IEEE Transactions on Geoscience and Remote Sensing*, **44(11)**, 3103-3117, doi: 10.1109/TGRS.2006.880619.
- Stroeve, J., Holland, M. M., Meier, W., Scambos, T., and Serreze, M. (2007). Arctic sea ice decline: Faster than forecast. *Geophysical Research Letters*, **34(9)**, doi: 10.1029/2007GL029703.
- Sturm, M., Holmgren, J., and Perovich, D. K. (2002). Winter snow cover on the sea ice of the Arctic Ocean at the Surface Heat Budget of the Arctic Ocean (SHEBA): Temporal evolution and spatial variability. *Journal of Geophysical Research: Oceans*, **107(C10)**, SHE 23-1-SHE 23-17, doi: 10.1029/2000JC000400.

- Sturm, M., Perovich, D. K., and Holmgren, J. (2002). Thermal conductivity and heat transfer through the snow on the sea ice of the Beaufort Sea. *Journal of Geophysical Research*, **107(C21)**, 8043, doi: 10.1029/2000JC000409.
- Surdu, C. M., Duguay, C. R., and Fernández Prieto, D. (2016). Evidence of recent changes in the ice regime of lakes in the Canadian High Arctic from spaceborne satellite observations. *The Cryosphere*, **10(3)**, 941-960, doi: 10.5194/tc-10-941-2016.
- Takenobu, T., Massom, R., Tateyama, K., Tamura, T., and Fraser, A. (2011). Properties of snow overlying the sea ice off East Antarctica in late winter, 2007. *Deep Sea Research Part II: Topical Studies in Oceanography*, **58(9-10)**, 1137 - 1148, doi: 10.1016/j.dsr2.2010.12.002.
- Tamura, T., Ohshima, K. I., and Nihashi, S. (2008). Mapping of sea ice production for Antarctic coastal polynyas. *Geophysical Research Letters*, **35(7)**, doi: 10.1029/2007GL032903.
- Tan, B., Li, Z.-J., Lu, P., Haas, C., and Nicolaus, M. (2012). Morphology of sea ice pressure ridges in the northwestern Weddell Sea in winter. *Journal of Geophysical Research: Oceans*, **117(C6)**, doi: 10.1029/2011JC007800.
- Thomas, D. N. (2017). Sea Ice. John Wiley & Sons, Ltd, doi: /10.1002/9781118778371.
- Thomas, D. N. and Dieckmann, G. (2010). Sea Ice. Wile-Blackwell Pub., Chichester, U.K., doi: 10.1002/9781444317145.
- Tilling, R. L., Ridout, A., Shepherd, A., and Wingham, D. J. (2015). Increased Arctic sea ice volume after anomalously low melting in 2013. *Nature Geosci*, **8(8)**, 643-646, doi: 10.1038/ngeo2489.
- Timco, G. W. and Weeks, W. F. (2010). A review of the engineering properties of sea ice. *Cold Regions Science and Technology*, **60(2)**, 107 - 129, doi: 10.1016/j.coldregions.2009.10.003.
- Tiuri, M., Sihvola, A., Nyfors, E., and Hallikainen, M. (1984). The complex dielectric constant of snow at microwave frequencies. *IEEE J. Ocean. Eng.*, **9**, 377-382
- Tschudi, M. A., Stroeve, J. C., and Stewart, J. S. (2016). Relating the Age of Arctic Sea Ice to its Thickness, as Measured during NASA's ICESat and IceBridge Campaigns. *Remote Sensing*, **8(6)**, doi: 10.3390/rs8060457.

- U.S.A.C.E. (2002). Engineering and Design: Ice Engineering Manual. EM: 1110-2-1612, U.S. Army Corps of Engineers, Washington, D.C. Accessed online at: http://www.publications.usace.army.mil/Portals/76/EngineerManuals/EM_1110-2-1612.pdf.
- Ulaby, F., Moore, R. K., and Fung, A. K. (1986). Microwave remote sensing: active and passive. III Artech House, Dedham, MA.
- Ulaby, F. T., Stiles, W. H., and Abdelrazik, M. (1984). Snowcover Influence on Backscattering from Terrain. *Geoscience and Remote Sensing, IEEE Transactions on*, **GE-22(2)**, 126-133, doi: 10.1109/TGRS.1984.350604.
- Ulaby, F. T., Moore, R. K., and Fung, A. K. (1982). Physical mechanisms and empirical models for scattering and emission. Microwave remote sensing: active and passive. Vol. II: Radar remote sensing and surface scattering and emission theory. Addison-Wesley Publishing Co.
- Ulander, L. M. H. (1987). Interpretation of Seasat radar-altimeter data over sea ice using near-simultaneous SAR imagery. *International Journal of Remote Sensing*, **8(11)**, 1679-1686, doi: 10.1080/01431168708954807.
- Vaughan, D. G., Comiso, J. C., Allison, I., Carrasco, J., Kaser, G., Kwok, R., Mote, P., Murray, T., Paul, F., Ren, J., Rignot, E., Solomina, O., Steffen, K., Zhang, T., and 4 (2013). Observations: Cryosphere. In: Stocker, T. F., Qin, D., Plattner, G.-K., Tignor, M., Allen, S. K., Boschung, J., Nauels, A., Xia, Y., Bex, V., and Midgley, P. M. editor. *Climate Change 2013: The Physical Science Basis. Contribution of Working Group I to the Fifth Assessment Report of the Intergovernmental Panel on Climate Change*, 317-382. Cambridge University Press, doi: 10.1017/CBO9781107415324.012.
- Wadhams, P. and Doble, M. J. (2008). Digital terrain mapping of the underside of sea ice from a small AUV. *Geophysical Research Letters*, **35(1)**, L01501, doi: 10.1029/2007GL031921.
- Wadhams, P., Tucker, W. B., Krabill, W. B., Swift, R. N., Comiso, J. C., and Davis, N. R. (1992). Relationship between sea ice freeboard and draft in the Arctic Basin, and implications for ice thickness monitoring. *Journal of Geophysical Research: Oceans*, **97(C12)**, 20325-20334, doi: 10.1029/92JC02014.

- Walsh, J. E. (2014). Intensified warming of the Arctic: Causes and impacts on middle latitudes. *Global and Planetary Change*, **117**, 52 - 63, doi: 10.1016/j.gloplacha.2014.03.003.
- Wang, M. and Overland, J. E. (2012). A sea ice free summer Arctic within 30 years: An update from CMIP5 models. *Geophysical Research Letters*, **39(18)**, doi: 10.1029/2012GL052868.
- Wang, Q., Ilicak, M., Gerdes, R., Drange, H., Aksenov, Y., Bailey, D. A., Bentsen, M., Biastoch, A., Bozec, A., Böning, C., Cassou, C., Chassignet, E., Coward, A. C., Curry, B., Danabasoglu, G., Danilov, S., Fernandez, E., Fogli, P. G., Fujii, Y., Griffies, S. M., Iovino, D., Jahn, A., Jung, T., Large, W. G., Lee, C., Lique, C., Lu, J., Masina, S., Nurser, A. J. G., Rabe, B., Roth, C., y Mélia, D. S., Samuels, B. L., Spence, P., Tsujino, H., Valcke, S., Voldoire, A., Wang, X., and Yeager, S. G. (2016). An assessment of the Arctic Ocean in a suite of interannual CORE-II simulations. Part I: Sea ice and solid freshwater. *Ocean Modelling*, **99**, 110 - 132, doi: 10.1016/j.ocemod.2015.12.008.
- Warren, S. G. and Brandt, R. E. (2008). Optical constants of ice from the ultraviolet to the microwave: A revised compilation. *Journal of Geophysical Research: Atmospheres*, **113(D14)**, 10, doi: 10.1029/2007JD009744.
- Warren, S. G., Rigor, I. G., Untersteiner, N., Radionov, V. F., Bryazgin, N. N., and Aleksandrov, Y. I. (1999). Snow Depth on Arctic Sea Ice. *Journal of Climate*, **12**, 1814 - 1829, doi: 10.1175/1520-0442.
- Wavemetrics (2014). Igor Pro User Manual: Curve-Fitting. Wavemetrics.
- Webster, M. A., Rigor, I. G., Nghiem, S. V., Kurtz, N. T., Farrell, S. L., Perovich, D. K., and Sturm, M. (2014). Interdecadal changes in snow depth on Arctic sea ice. *Journal of Geophysical Research: Oceans*, **119(8)**, 5395-5406, doi: 10.1002/2014JC009985.
- Wernecke, A. and Kaleschke, L. (2015). Lead detection in Arctic sea ice from CryoSat-2: quality assessment, lead area fraction and width distribution. *The Cryosphere Discussions*, **9(2)**, 2167-2200, doi: 10.5194/tcd-9-2167-2015.
- Wessel, P. and Smith, W. H. F. (1996). A global, self-consistent, hierarchical, high-resolution shoreline database. *Journal of Geophysical Research: Solid Earth*, **101(B4)**, 8741-8743, doi: 10.1029/96JB00104.

- Willatt, R., Laxon, S., Giles, K., Cullen, R., Haas, C., and Helm, V. (2011). Ku-band radar penetration into snow cover on Arctic sea ice using airborne data. *Annals of Glaciology*, **52(57)**, 197-205
- Willatt, R. C., Giles, K. A., Laxon, S. W., Stone-Drake, L., and Worby, A. P. (2010). Field Investigations of Ku-Band Radar Penetration Into Snow Cover on Antarctic Sea Ice. *Geoscience and Remote Sensing, IEEE Transactions on*, **48(1)**, 365-372, doi: 10.1109/TGRS.2009.2028237.
- Wingham, D. J., Francis, C. R., Baker, S., Bouzinac, C., Brockley, D., Cullen, R., de Chateau-Thierry, P., Laxon, S. W., Mallow, U., Mavrocordatos, C., Phalippou, L., Ratier, G., Rey, L., Rostan, F., Viau, P., and Wallis, D. W. (2006). CryoSat: A mission to determine the fluctuations in Earth's land and marine ice fields. *Advances in Space Research*, **37(4)**, 841 - 871, doi: 10.1016/j.asr.2005.07.027.
- Wingham, D. J., Phalippou, L., Mavrocordatos, C., and Wallis, D. (2004). The mean echo and echo cross product from a beamforming interferometric altimeter and their application to elevation measurement. *IEEE Transactions on Geoscience and Remote Sensing*, **42(10)**, 2305-2323, doi: 10.1109/TGRS.2004.834352.
- Wingham, D. J., Forsberg, R., Laxon, S. W., Lemke, P., Miller, H., Raney, K., Sandven, S., Scharoo, R., Vincent, P., and Rebhan, H. (2001). CryoSat Calibration and Validation Concept. CS-PL-UCL-SY-0004, E.S.A. and C.P.O.M.
- Wingham, D., Rapley, C., and Griffiths, H. (1986). New techniques in satellite altimeter tracking systems. IEEE International Geoscience and Remote Sensing Symposium, IGARSS 1986, ESA SP-254, 1339-1344.
- Xie, H., Tekeli, A. E., Ackley, S. F., Yi, D., and Zwally, H. J. (2013). Sea ice thickness estimations from ICESat Altimetry over the Bellingshausen and Amundsen Seas, 2003-2009. *Journal of Geophysical Research: Oceans*, **118(5)**, 2438-2453, doi: 10.1002/jgrc.20179.
- Yi, D., Zwally, H. J., and Robbins, J. W. (2011). ICESat observations of seasonal and interannual variations of sea-ice freeboard and estimated thickness in the Weddell Sea, Antarctica (2003- 2009). *Annals of Glaciology*, **52(57 Pt 1)**, 43-51, doi: 10.3189/ 172756411795931480.

- Zwally, H. J., Yi, D., Kwok, R., and Zhao, Y. (2008). ICESat measurements of sea ice freeboard and estimates of sea ice thickness in the Weddell Sea. *Journal of Geophysical Research: Oceans*, **113(C2)**, doi: 10.1029/2007JC004284.
- Zygmuntowska, M. and Khvorostovsky, K. (2014). Analysis of CryoSat's radar altimeter waveforms over different Arctic sea ice regimes. University of Bergen.
- Zygmuntowska, M., Rampal, P., Ivanova, N., and Smedsrud, L. H. (2014). Uncertainties in Arctic sea ice thickness and volume: new estimates and implications for trends. *The Cryosphere*, **8(2)**, 705-720, doi: 10.5194/tc-8-705-2014.
- Zygmuntowska, M., Khvorostovsky, K., Helm, V., and Sandven, S. (2013). Waveform classification of airborne synthetic aperture radar altimeter over Arctic sea ice. *The Cryosphere*, **7(4)**, 1315-1324, doi: 10.5194/tc-7-1315-2013.

Appendix A: Other Publications

- Casey, J. A., Beckers, J. F., Busche, T., and Haas, C. (2013). Comparison of in situ and airborne measurements of multiyear sea ice thickness with dual-frequency, polarimetric SAR observations, *IEEE IGARSS224-227*, doi:/10.1109/IGARSS.2013.6721132.
- Casey, J. A., Beckers, J. F., Busche, T., and Haas, C. (2014). Towards the retrieval of multi-year sea ice thickness and deformation state from polarimetric C- and X-band SAR observations, *IEEE IGARSS*, 1190-1193, doi:/10.1109/IGARSS.2014.6946644.
- Fors, A. S., Brekke, C., Gerland, S., Doulgeris, A. P., and Beckers, J. F. (2016). Late Summer Arctic Sea Ice Surface Roughness Signatures in C-Band SAR Data. *IEEE Journal of Selected Topics in Applied Earth Observations and Remote Sensing*, 9(3), 1199-1215, doi:/10.1109/JSTARS.2015.2504384.
- Haas, C. and Beckers, J. F. (2014). CryoVEx 2014 Final Report, ESA contract 4000110552/14/MP/vb, accessible online at <https://earth.esa.int/web/guest/campaigns/>
- Haas, C. and Beckers, J. F. (2017). Sea Ice and Lake Ice Thickness Observations with CryoSat. *CMOS BULLETIN*, 45(1), 11–15.
- Haas C., Beckers, J. F., King, J., Silis, A., Stroeve, J., Wilkinson, J., Notenboom, B., Schweiger, A., and Hendricks, S. (2017). Ice and snow thickness variability and change in the high Arctic Ocean observed by in-situ measurements. *Geophysical Research Letters*, 44, 10,462–10,469, doi: 10.1002/2017GL075434
- Hatam, I., Charchuk, R., Lange, B., Beckers, J. F., Haas, C., and Lanoil, B. (2014). Distinct bacterial assemblages reside at different depths in Arctic multiyear sea ice. *FEMS Microbiology Ecology*, 90(1), 115, doi:/10.1111/1574-6941.12377.
- Hatam, I., Lange, B., Beckers, J. F., Haas, C., and Lanoil, B. (2016). Bacterial communities from Arctic seasonal sea ice are more compositionally variable than those from multi-year sea ice. *ISME J*, 10, 2543--2552
- Jackson, K., Wilkinson, J., Maksym, T., Meldrum, D., Beckers, J. F., Haas, C., and Mackenzie, D. (2013). A Novel and Low-Cost Sea Ice Mass Balance Buoy. *Journal of Atmospheric and Oceanic Technology*, 30(11), 2676-2688, doi:/10.1175/JTECH-D-13-00058.1.

- King, J., Howell, S., Derksen, C., Rutter, N., Toose, P., Beckers, J. F., Haas, C., Kurtz, N., and Richter-Menge, J. (2015). Evaluation of Operation IceBridge quick-look snow depth estimates on sea ice. *Geophysical Research Letters*, 42(21), 9302--9310, doi:/10.1002/2015GL066389.
- Lange, B. A., Michel, C., Beckers, J. F., Casey, J. A., Flores, H., Hatam, I., Meisterhans, G., Niemi, A., and Haas, C. (2015). Comparing Springtime Ice-Algal Chlorophyll a and Physical Properties of Multi-Year and First-Year Sea Ice from the Lincoln Sea. *PLOS ONE*, 10(4), 1-26, doi:/10.1371/journal.pone.0122418.
- Lange, B. A., Flores, H., Michel, C., Beckers, J. F., Bublitz, A., Casey, J. A., Castellani, G., Hatam, I., Reppchen, A., Rudolph, S. A., and Haas, C. (2017). Pan-Arctic sea ice-algal chl a biomass and suitable habitat are largely underestimated for multiyear ice. *Global Change Biology*, doi: 10.1111/gcb.13742.
- Renner, A. H. H., Dumont, M., Beckers, J. F., Gerland, S., and Haas, C. (2013). Improved characterisation of sea ice using simultaneous aerial photography and sea ice thickness measurements. *Cold Regions Science and Technology*, 92, 37 - 47, doi:/10.1016/j.coldregions.2013.03.009.
- Renner, A. H. H., Hendricks, S., Sebastian Gerland, S., Beckers, J. F., Haas, C., and Krumpen, T. (2013). Large-scale ice thickness distribution of first-year sea ice in spring and summer north of Svalbard. *Annals of Glaciology*, 54(62), 13-18, doi:/10.3189/2013AoG62A146.
- Renner, A. H. H., Gerland, S., Haas, C., Spreen, G., Beckers, J. F., Hansen, E., Nicolaus, M., and Goodwin, H. (2014). Evidence of Arctic sea ice thinning from direct observations. *Geophysical Research Letters*, 41(14), 5029 - 5036, doi:/10.1002/2014GL060369.
- Ricker, R., Hendricks, S., and Beckers, J. F. (2016). The impact of geophysical corrections on sea-ice freeboard retrieved from satellite altimetry. *Remote Sensing*, 8(4), doi:/10.3390/rs8040317